



Faculté des Sciences Appliquées  
Département d'Architecture, Géologie,  
Environnement et Constructions  
Secteur MS<sup>2</sup>F



# **Modeling of fracture in heavy steel welded beam-to-column connection submitted to cyclic loading by finite elements**

Thèse présentée en vue de l'obtention du grade de  
Docteur en Sciences de l'Ingénieur  
par Cédric LEQUESNE  
Année académique 2008-2009

Membres du Jury :

- Prof. André Plumier (SE Sector, ArGEnCo Department, University of Liege, Belgium)
- Mr. Adam Bannister (Corus, Rotherham, UK)
- Prof. Jean-Louis Chaboche (ONERA, France)
- Dr. Hervé Degée (SE sector, ArGEnCo department, University of Liege, Belgium)
- Prof. Ludovic Noels (Aerospace and Mechanical Engineering department, University of Liege, Belgium)

Promoteurs: Dr. Anne Marie Habraken (MS<sup>2</sup>F Sector, ArGEnCo Department, Université de Liege, Belgium)

Coordonnées de l'auteur :

Cédric LEQUESNE  
Département ArGEnCo  
Université de Liège  
Chemin des Chevreuils, 1  
4000 Liège  
Belgique  
Tel: +.32.4.366.91.40  
e-mail : Cedric.Lequesne@ulg.ac.be



# Acknowledgments

I would like to express my gratitude to Dr. Anne Marie Habraken, Dr. André Plumier and Dr. Catherine Doneux from the ArGEnCo Department of the University of Liege for their guidance in this research and their patience.

I would like to thank Dr. Christophe Henrard, Dr. Frederic Pascon and Dr. Laurent Duchêne from the ArGEnCo Department, who helped me understand the LAGAMINE Code. Moreover I have greatly appreciated the cooperation with the other members of the Lagamine team.

I will always remember the help and the friendship of office mates during the period of my PhD research: Dr. Viviane Warnotte, Abdeljalil Kalifa Marmi, Dr. Ahmed El Bartali and Amine Ben Bettaieb. Next, I am grateful to the other members of the MS<sup>2</sup>F and SE sectors of the ArGEnCo Department because the good atmosphere they provided allowed me to work on enjoyable conditions.

I have benefited from the corrections of Ellen Henrard in writing this thesis. I thank her very much for this.

This work has been done thanks to funding of the European Community (VERAPS project n° RFS-CR-03035) and the assistance of the project partners. It has been a pleasure and an honor to work with Adam Bannister and Yuri Tkach from Corus, Manuel Gomez from ISQ, Prof. Helmut Saal and Wolfram Hölbling from Karlsruhe University.

Lastly I finish in thanking my family for their support and I dedicate my thesis to Mary Devel, my love, who has always trusted in me.

# Contents

<b>CHAPTER 1</b> .....	<b>1</b>
<b>INTRODUCTION</b> .....	<b>1</b>
1.1 CONTEXT.....	2
1.2 VERAPS PROJECT .....	2
1.3 OBJECTIVES.....	3
1.4 SCOPE OF THE STUDY .....	4
1.4.1 <i>Connection description</i> .....	4
1.4.2 <i>Welding</i> .....	4
1.4.3 <i>Materials</i> .....	5
1.4.4 <i>Large scale test</i> .....	5
1.4.5 <i>Damage and Crack process</i> .....	6
1.5 METHODS.....	7
1.6 OUTLINE OF THIS THESIS .....	9
<b>CHAPTER 2</b> .....	<b>11</b>
<b>NUMERICAL TOOLS DESCRIPTION</b> .....	<b>11</b>
2.1 INTRODUCTION.....	12
2.2 MECHANICAL DEFINITIONS .....	12
2.2.1 <i>Strain</i> .....	12
2.2.2 <i>Cauchy's stress</i> .....	13
2.2.3 <i>Jaumann's derivative</i> .....	14
2.3 THE FINITE ELEMENT CODE LAGAMINE .....	14
2.3.1 <i>Description</i> .....	14
2.3.2 <i>Concepts of the finite element code</i> .....	14
2.3.2.1 The equilibrium condition .....	14
2.3.2.2 Temporal integration.....	16
2.3.2.3 Computation of the nodal force and the stiffness matrix .....	19
2.4 THE SOLID ELEMENT BWD3D.....	20
2.5 THE CONSTITUTIVE LAW .....	21
2.5.1 <i>The elastic law</i> .....	21
2.5.2 <i>The plastic law</i> .....	21
2.5.2.1 The yield locus .....	21
2.5.2.2 The flow rules.....	23
2.5.3 <i>ARB law and its parameters</i> .....	31
2.5.3.1 Description .....	31
2.5.3.2 Computation of the plastic modulus, $E_p$ .....	31
2.5.3.3 Link between the kinematic modulus and the plastic modulus.....	32
2.5.3.4 Computation of the tangent matrix .....	32
2.5.4 <i>Identification of the parameters</i> .....	33
2.5.4.1 The tensile test presentations.....	33
2.5.4.2 Treatment of the experimental results .....	35
2.6 CONCLUSION.....	40
<b>CHAPTER 3</b> .....	<b>41</b>
<b>FATIGUE DAMAGE MODELING</b> .....	<b>41</b>
3.1 INTRODUCTION.....	42
3.2 INTRODUCTION TO THE CONCEPT OF FATIGUE DAMAGE .....	42
3.3 MANSION-COFFIN'S MODEL .....	44

3.3.1	<i>Model origins and evolution</i> .....	44
3.3.2	<i>Palmgren-Miner's Rules</i> .....	44
3.3.3	<i>Procedure to assess lifetime with a finite element code</i> .....	45
3.4	MULTIAXIAL FATIGUE CRITERIA .....	45
3.5	FATIGUE CONTINUUM DAMAGE MODEL (CDM) .....	47
3.5.1	<i>One-dimensional fatigue CDM description</i> .....	47
3.5.2	<i>Description of multiaxial fatigue CDM</i> .....	48
3.6	COMPARISON BETWEEN MANSON-COFFIN'S LAW AND CDM.....	48
3.7	IDENTIFICATION OF THE FATIGUE DAMAGE PARAMETERS .....	48
3.7.1	<i>Method used to identify the parameters</i> .....	48
3.7.2	<i>Experimental data and Wöhler's curves</i> .....	49
3.7.3	<i>Identification</i> .....	50
3.8	IMPLEMENTATION IN THE LAGAMINE CODE .....	52
3.9	CONCLUSION.....	53
<b>CHAPTER 4</b>	.....	<b>55</b>
<b>CRACK PROPAGATION MODELING</b>	.....	<b>55</b>
4.1	INTRODUCTION TO FAILURE MECHANICS .....	56
4.2	INTRODUCTION TO THE COHESIVE ZONE MODEL (CZM) .....	60
4.2.1	<i>Introduction</i> .....	60
4.2.2	<i>Process zone</i> .....	62
4.2.3	<i>Implicit thickness</i> .....	63
4.2.4	<i>Jump displacement</i> .....	64
4.3	THE CONSTITUTIVE LAWS OF THE COHESIVE ZONE MODEL .....	66
4.3.1	<i>Description of the cohesive components</i> .....	66
4.3.2	<i>Xu and Needleman's law</i> .....	66
4.3.2.1	<i>Cohesive stresses</i> .....	67
4.3.2.2	<i>Fatigue damage coupling</i> .....	68
4.3.2.3	<i>Loading and unloading cases</i> .....	69
4.3.2.4	<i>Viscosity</i> .....	70
4.3.2.5	<i>Cohesive stiffness matrix</i> .....	71
4.3.3	<i>Crisfield's law</i> .....	74
4.3.3.1	<i>Description</i> .....	74
4.3.3.2	<i>Viscosity</i> .....	76
4.3.3.3	<i>Fatigue Damage</i> .....	76
4.4	IMPLEMENTATION OF THE TWO-DIMENSIONAL COHESIVE ELEMENT (CZMEL) .....	77
4.4.1	<i>Element description</i> .....	77
4.4.2	<i>The isoparametric and the local axes</i> .....	78
4.4.3	<i>Interpolation functions</i> .....	80
4.4.4	<i>Computation of the separation</i> .....	81
4.4.5	<i>Computation of the nodal forces and the tangent stiffness matrix</i> .....	81
4.5	IMPLEMENTATION OF THE THREE DIMENSIONAL COHESIVE ELEMENT (CZM3D).....	83
4.5.1	<i>Element description</i> .....	83
4.5.2	<i>The isoparametric and local axes</i> .....	84
4.5.3	<i>Interpolation functions</i> .....	87
4.5.4	<i>Computation of the separation</i> .....	88
4.5.5	<i>Computation of the nodal force and the tangent stiffness matrix</i> .....	88
4.6	COUPLING WITH FATIGUE DAMAGE .....	89
4.7	IDENTIFICATION OF PARAMETERS.....	89
4.7.1	<i>Identification method</i> .....	89
4.7.2	<i>Three-point bend testing</i> .....	90
4.7.3	<i>Identification of the J-integral-Crack growth plot from Charpy-V notch test</i> .....	94
4.7.4	<i>Parametric study</i> .....	96
4.7.4.1	<i>Modeling</i> .....	96

4.7.4.2	Computation of the growth in crack's length.....	97
4.7.4.3	The initial cohesive parameters.....	97
4.7.4.4	Varying the maximum cohesive stress .....	98
4.7.4.5	Varying the cohesive energy .....	99
4.7.4.6	Varying the initial slope .....	100
4.7.4.7	Cohesive constitutive law's effect .....	101
4.7.4.8	Results and discussion .....	102
4.7.5	<i>Parameter identification</i> .....	103
4.7.5.1	Modeling.....	103
4.7.5.2	Computation of the growth in crack length.....	104
4.7.5.3	Results and Discussion .....	104
4.8	CONCLUSIONS .....	106
<b>CHAPTER 5 .....</b>		<b>109</b>
<b>WELDING SIMULATION.....</b>		<b>109</b>
5.1	INTRODUCTION.....	110
5.2	WELDING PROCESS .....	110
5.2.1	<i>Description</i> .....	110
5.2.2	<i>Thermal phenomena</i> .....	113
5.2.3	<i>Metallurgical phenomena</i> .....	113
5.2.4	<i>The physical aspect</i> .....	114
5.3	COUPLING STRATEGY .....	115
5.4	THERMAL ANALYSIS.....	116
5.4.1	<i>The heat equations</i> .....	116
5.4.2	<i>Heat source modeling</i> .....	117
5.5	MECHANICAL ANALYSIS.....	119
5.6	THE FINITE ELEMENT MODELING .....	120
5.6.1	<i>The thermal analysis</i> .....	120
5.6.2	<i>The temperature transfer</i> .....	121
5.6.3	<i>The birth technique</i> .....	123
5.6.4	<i>The mechanical analysis</i> .....	124
5.7	MODELING OF BEAM-TO-COLUMN CONNECTION WELDING .....	124
5.7.1	<i>Welding description</i> .....	124
5.7.2	<i>The residual stress measurement</i> .....	128
5.7.3	<i>The material parameters</i> .....	130
5.7.4	<i>FEM modeling description</i> .....	135
5.7.5	<i>Results and discussion</i> .....	137
5.8	CONCLUSIONS .....	138
<b>CHAPTER 6 .....</b>		<b>141</b>
<b>BEAM-TO-COLUMN CONNECTION SIMULATIONS .....</b>		<b>141</b>
6.1	INTRODUCTION.....	142
6.2	PRESENTATION OF THE VERAPS CONNECTIONS .....	142
6.2.1	<i>Introduction</i> .....	142
6.2.1.1	The moment resisting frame (MRF).....	142
6.2.1.2	The connection ductility of a steel MRF .....	143
6.2.2	<i>The connection description</i> .....	145
6.2.2.1	The bars .....	146
6.2.2.2	The stiffeners.....	147
6.2.2.3	Connection details.....	149
6.2.2.4	The welding .....	151
6.2.3	<i>The test procedure</i> .....	152
6.2.4	<i>Test results</i> .....	155
6.3	FEM SIMULATIONS .....	156

6.3.1	<i>Mesh Generator</i> .....	156
6.3.1.1	Characteristics .....	156
6.3.1.2	Adaptation to the VERAPS connection.....	159
6.3.2	<i>Simulations without damage</i> .....	162
6.3.2.1	Static loading.....	162
6.3.2.2	Cyclic loading .....	166
6.3.3	<i>Cyclic loading with fatigue damage</i> .....	168
6.3.4	<i>Cyclic loading with the cohesive zone model and fatigue damage</i> .....	172
6.4	CONCLUSION.....	175
<b>CHAPTER 7</b> .....		<b>177</b>
<b>CONCLUSIONS AND PERSPECTIVES</b> .....		<b>177</b>
<b>APPENDIX 1</b> .....		<b>181</b>
<b>ITERATIVE SOLVERS</b> .....		<b>181</b>
A1.1	INTRODUCTION .....	182
A1.2	DIRECT METHODS IN LAGAMINE FINITE ELEMENT CODE.....	182
A1.3	STATIONARY METHODS .....	183
A1.4	KRYLOV SUBSPACE METHODS .....	185
A1.4.1	<i>Some definitions</i> .....	185
A1.4.2	<i>The conjugate gradient method</i> .....	185
A1.4.2.1	Principles of the method.....	185
A1.4.2.2	Krylov's subspace.....	186
A1.4.2.3	Convergence consideration .....	187
A1.4.2.4	Algorithm .....	189
A1.4.3	<i>Arnoldi's method</i> .....	189
A1.4.4	<i>GMRES method</i> .....	190
A1.5	PRECONDITIONING .....	192
A1.6	IMPLEMENTATION IN LAGAMINE .....	194
A1.6.1	<i>GMRES module description</i> .....	194
A1.6.2	<i>Input parameters</i> .....	194
A1.7	VALIDATION OF THE GMRES METHOD IN LAGAMINE.....	194
A1.7.1	<i>Indentation test</i> .....	194
A1.7.2	<i>Incremental forming modeling</i> .....	195
A1.8	CONCLUSIONS .....	196
<b>APPENDIX 2</b> .....		<b>197</b>
<b>ADAPTIVE REMESHING</b> .....		<b>197</b>
<b>APPENDIX 3</b> .....		<b>205</b>
<b>REFERENCES</b> .....		<b>205</b>



# List of figures

Figure 1-1: Flowchart of the VERAPS project .....	3
Figure 1-2: Welded beam-to-column connection.....	4
Figure 1-3: Welding by multipass with dimensions in millimeters .....	5
Figure 1-4: Presentation of the three materials in a welded connection .....	5
Figure 1-5: Loading definition .....	6
Figure 1-6: Crack initiation .....	6
Figure 1-7: Possible crack paths.....	7
Figure 1-8: Flow chart of the study .....	9
Figure 2-1: Internal force descriptions.....	13
Figure 2-2: 2D Finite element description, isoparametric and global coordinate definition .....	15
Figure 2-3: Newton-Raphson method description .....	16
Figure 2-4: General flowchart of the LAGAMINE code.....	19
Figure 2-5: Yield locus with Von Mises' criterion .....	22
Figure 2-6: Yield locus with Tresca criterion .....	22
Figure 2-7: Isotropic hardening effect on the yield locus .....	24
Figure 2-8: Isotropic hardening effect on the uniaxial stress-strain curve.....	24
Figure 2-9: Kinematic hardening effect on the yield locus .....	25
Figure 2-10: Kinematic hardening effect on the uniaxial stress-strain curve .....	25
Figure 2-11: Geometric interpretation of the generalized algorithm for stress updating.....	30
Figure 2-12: Radial return method .....	31
Figure 2-13: Input points in the ARB law.....	32
Figure 2-14: Position of the samples in the beam-to-column connection.....	33
Figure 2-15: Experimental tensile test plot for BM for core positions .....	34
Figure 2-16: Experimental tensile test plot for BM at flange positions .....	34
Figure 2-17: Experimental tensile test plot for WM .....	35
Figure 2-18: Identification of the yield stress .....	36
Figure 2-19: Tensile plot for BM in the core position .....	37
Figure 2-20: Tensile plot for BM in the flange position .....	37
Figure 2-21: Tensile plot for WM .....	38
Figure 3-1: Description of the stress or strain cycle as a function of time.....	43
Figure 3-2: Flow chart of steps to assess the lifetime of a structure undergoing a cyclic loading [TEN04] .....	45
Figure 3-3: Description of the computation of the residual stress tensor.....	47
Figure 3-4: Position of the sample for the LCF test from a) the BM and b) the WM.....	49
Figure 3-5: Evolution of the maximum stress per cycle due to imposed cyclic strain .....	50
Figure 3-6: Wöhler's curve for the BM position K.....	51
Figure 3-7: Wöhler's curve for the BM position L .....	51
Figure 3-8: Wöhler's curve for the WM position .....	52
Figure 4-1: Fracture mode: mode I: opening mode; mode II: sliding mode; mode III: tearing mode (from [CHA96]) .....	56
Figure 4-2: Mode I loaded crack .....	57
Figure 4-3: Integral contour .....	58

Figure 4-4: Definition of the effective CTOD as proposed by Rice .....	59
Figure 4-5: Fracture samples used to characterize fracture toughness estimated by J-integral (from [WIL99]) .....	60
Figure 4-6: Typical form of cohesive stress-separation law .....	61
Figure 4-7: Various cohesive zone models .....	62
Figure 4-8: Process zone description in the cohesive zone model .....	63
Figure 4-9: Simple uniaxial problem to illustrate the jump displacement .....	64
Figure 4-10: The cohesive separation response driven by the imposed displacement $U$ .....	65
Figure 4-11: Relative normal and shear cohesive stress-separation curve for uncoupled modeling .....	68
Figure 4-12: Cohesive loading curve coupled with fatigue damage .....	69
Figure 4-13: Normal traction curve in case of loading and unloading .....	70
Figure 4-14: Crisfield's cohesive zone model .....	75
Figure 4-15: Coupling between cohesive zone model and fatigue damage suggested by a) [BOU06] and b) [ROE03] .....	77
Figure 4-16: Element description .....	78
Figure 4-17: Local axes .....	80
Figure 4-18: Local separation .....	81
Figure 4-19: Description of CZM3D .....	84
Figure 4-20: Local axes definition .....	87
Figure 4-21: Local axis along the CZM3D .....	87
Figure 4-22: Transfer of fatigue damage from solid elements to cohesive elements .....	89
Figure 4-23: Extraction locations of the three-point bend specimens .....	91
Figure 4-24: Geometry of the specimen .....	91
Figure 4-25: Variable Measured during the experiment .....	91
Figure 4-26: Definition of $U_p$ .....	92
Figure 4-27: Force displacement plot from the CTOD test on the base metal .....	93
Figure 4-28: Crack growth in function of the J-integral from the three-point bend testing on the base metal .....	93
Figure 4-29: Charpy test description .....	94
Figure 4-30: Extraction location for the weld metal V notch specimen .....	95
Figure 4-31: Crack growth in function of the J-integral for the base metal .....	95
Figure 4-32: Finite element modeling of the CTOD test .....	96
Figure 4-33: Computation methods of the growth in crack's length for 2D simulations .....	97
Figure 4-34: Evolution of tool force as a function of the load line displacement by varying $\sigma_{max}$ .....	98
Figure 4-35: Evolution of the J-integral as a function of the crack's growth by varying $\sigma_{max}$ .....	99
Figure 4-36: Evolution of tool force as a function of the load line displacement by varying $\phi_n$ .....	100
Figure 4-37: Evolution of the J-integral in function of the crack growth in varying $\phi_n$ .....	100
Figure 4-38: Evolution of tool force as a function of the load line displacement by varying $k_n$ .....	101
Figure 4-39: Evolution of the J-integral as a function of the crack growth by varying $k_n$ .....	101
Figure 4-40: Effect of the constitutive law on the force displacement plot .....	102
Figure 4-41: 3D Finite element modeling of the CTOD test .....	103
Figure 4-42: Computation methods of the crack length's growth for 3D simulation .....	104
Figure 4-43: Force displacement comparison plot between experimental test and finite element modeling for BM .....	105

Figure 4-44: J-integral versus crack growth plot Comparison between experimental test and finite element modeling for BM .....	106
Figure 4-45: Comparison of J-integral versus crack growth plot between experimental test and finite element modeling for WM.....	106
Figure 5-1: Diagram of SMAW process (from www.esab.com) .....	111
Figure 5-2: Diagram of GMAW (from www.substech.com).....	112
Figure 5-3: Diagram of SAW (from robot-welding.com).....	112
Figure 5-4: Scheme of GTAW (from common/Wikimedia.org) .....	113
Figure 5-5: Material description after a welding process.....	114
Figure 5-6: Coupling between physical phenomenon during welding .....	114
Figure 5-7: Computation strategy of residual stress.....	116
Figure 5-8: Division of the surfaces according to the flux exchange along the solid $\Omega$ .....	117
Figure 5-9: Friedman Models of the heat source .....	118
Figure 5-10: Double ellipsoid heat source with the power distribution.....	119
Figure 5-11: Computation of the imposed nodal heat.....	121
Figure 5-12: Interpolation for temperature transfer .....	122
Figure 5-13: Computation of the diagonal of the rectangle which contains the structure $\Omega$ .....	123
Figure 5-14: Birth technique method (top view).....	124
Figure 5-15: Birth technique method in two passes.....	124
Figure 5-16: View of the fabrication of connection N°5 [BAN07] .....	125
Figure 5-17: VERAPS connection design from [BAN07].....	126
Figure 5-18: Pass description of the welding for the VERAPS n°5 connection from [BAN07] .....	127
Figure 5-19: Welding of VERAPS connection.....	127
Figure 5-20: Position of residual stress measurement.....	129
Figure 5-21: Longitudinal stress measurements.....	129
Figure 5-22: Transversal stress measurement .....	130
Figure 5-23: Stress-plastic strain curve as a function of temperature for the base metal .....	131
Figure 5-24: Stress-plastic strain curve as a function of temperature for the weld metal.....	132
Figure 5-25: Thermal dilatation as a function of temperature .....	133
Figure 5-26: Specific heat as a function of temperature .....	134
Figure 5-27: Young Modulus as a function of temperature .....	134
Figure 5-28: Conductivity as a function of temperature .....	135
Figure 5-29: Description of beam-to-column flange finite element modeling .....	136
Figure 5-30: Contour plot of the residual stress analysis .....	137
Figure 5-31: Comparison of the longitudinal residual stress between the measurement and simulation of the surface of the beam .....	138
Figure 5-32: Comparison of the transversal residual stress between the measurement and simulation of the surface of the beam .....	138
Figure 6-1: Building frame.....	142
Figure 6-2: Solutions of structural systems to withstand to earthquakes.....	143
Figure 6-3: Components of a frame connection.....	144
Figure 6-4: Weld connection failure .....	145
Figure 6-5: Test specimen (from [BAN07]) .....	146
Figure 6-6: Cross section description.....	147
Figure 6-7: Details of the connections from [BAN07] .....	148

Figure 6-8: Connection Detail with a) bolted shear tab and b) welded and bolted shear tab from [BAN07].....	150
Figure 6-9: Definition of connection rotation from FEMA 350 [FEM00] .....	153
Figure 6-10: Identification of $K_e$ for the specimen 1 .....	155
Figure 6-11 Simple bloc .....	157
Figure 6-12: Methods to pass from one to three element subdivisions.....	158
Figure 6-13: Transition block to be finer in the $e_y$ direction .....	158
Figure 6-14: Simple area .....	158
Figure 6-15: Transition block to be finer in the $e_y$ direction .....	159
Figure 6-16: Mesh of two beam-to-column connections tested by Karlsruhe .....	160
Figure 6-17: Mesh of the connection around the welding .....	160
Figure 6-18: Boundary condition of the connection modeling .....	161
Figure 6-19: Position of the different sets of hardening coefficient .....	162
Figure 6-20: Beam end moment vs. imposed displacement curve for specimen 1 .....	163
Figure 6-21: Beam end moment vs. imposed displacement curve for specimen 5 .....	163
Figure 6-22: Beam end moment vs. imposed displacement curve for specimen 6.....	164
Figure 6-23: Longitudinal stress in the beam for specimen 1 (100 mm displacement) .....	165
Figure 6-24: Longitudinal stress in the column for specimen 1 (100 mm displacement).....	165
Figure 6-25: Equivalent von Mises Stress for specimen 1 (100 mm displacement).....	166
Figure 6-26: Comparison of the beam end's moment rotation between FEM analysis and experimental measurement (specimen 3).....	167
Figure 6-27: Buckling observation at the end of step 5 (specimen 3).....	168
Figure 6-28: Fatigue damage at the end of the step 1 in the weld access hole .....	169
Figure 6-29: Evolution of the fatigue damage near the lower weld flange.....	170
Figure 6-30: Location of elements where the fatigue damage where recorded .....	171
Figure 6-31: Evolution of damage in weld metal elements along the transverse direction of the beam .....	171
Figure 6-32: Location of the cohesive elements .....	173
Figure 6-33: Zone in the connection where crack was observed .....	173
Figure 6-34: Crack initiation after 10 cycles (displacement x50).....	174
Figure 6-35: Longitudinal stress for the beam flange plot after 10 cycles (displacement x1).....	175
Figure A1-1 : Sparse matrix example .....	183
Figure A1-2 : Example of ILU(0) factorization .....	193
Figure A1-3 : Example of ILU(1) factorization .....	193
Figure A1-4 : Indentation test modeling mesh.....	195
Figure A1-5 : SPIF process modeling mesh.....	196

# List of tables

Table 2-1: Elastic parameters .....	36
Table 2-2: Values for tensile properties for BM in the core position .....	38
Table 2-3: Values for tensile properties for BM in flange position .....	39
Table 2-4: Values for tensile properties for WM in the flange position .....	40
Table 3-1: Parameters of CDM for the different materials .....	52
Table 4-1: Association between separation and cohesive stress components and the crack mode	66
Table 4-2: Coefficient of the power law for the J- $\Delta a$ curve for the BM.....	93
Table 4-3: Parameters of the power law of the J-integral versus crack growth plot for the weld metal .....	95
Table 4-4: Penalty parameters.....	96
Table 4-5: Summary of the parameters tested.....	98
Table 4-6: Parameters of Xu and Needleman’s law.....	102
Table 4-7: Cohesive parameters Identified for BM .....	105
Table 4-8: Cohesive parameters Identified for WM .....	105
Table 5-1: Welding heat source data.....	128
Table 5-2: Flow stress as a function of strain and temperature for the base Metal.....	131
Table 5-3: Flow stress as a function of strain and temperature for the weld metal .....	132
Table 5-4: Thermo elastic parameters as a function of temperature .....	133
Table 5-5: Heat source parameters .....	136
Table 6-1: Cross section dimensions.....	147
Table 6-2: Joint design description .....	150
Table 6-3: Welding parameters .....	152
Table 6-4: Cyclic rotation imposed on the connection according to FEMA 350 .....	154
Table 6-5: Results of VERAPS experiments .....	156
Table 6-6: Loading definition of the connection 3.....	166
Table A1-1: Iterative resolution parameters for indentation simulation .....	195
Table A1-2: Comparison of CPU time for indentation simulation SPIF modeling .....	195
Table A1-3: Comparison of CPU time for SPIF simulation.....	196
Table A1-4: Iterative resolution parameters for the SPIF simulation.....	196

# Abbreviations and symbols

## Abbreviations

BM	Base metal
CDM	Continuum damage model
CTOD	Crack Tip Opening Displacement
CZM	Cohesive zone model
FE	Finite element
HAZ	Heat affected zone
ISQ	Instituto de Soldadura e Qualidade from Lisbon (Portugal)
ULg	University of Liege
VERAPS	Validation and enhancement of risk assessment procedure for seismic conditions
WM	Weld metal

## Symbols

$x$	Scalar
$\underline{x}$	Vector
$\underline{\underline{X}}$	Matrix or 2 <sup>nd</sup> order tensor
$x_i$	Component $i$ of vector $\underline{x}$
$X_{ij}$	Component $ij$ of matrix or tensor $\underline{\underline{X}}$
$\underline{x}^T, \underline{\underline{X}}^T$	Transposed vector $\underline{x}$ or tensor $\underline{\underline{X}}$
$\text{Tr}(\underline{\underline{X}})$	Trace of tensor $\underline{\underline{X}}$
$\underline{\underline{X}}^{-1}$	Inverse of a tensor
$\dot{x}, \dot{\underline{x}}, \dot{\underline{\underline{X}}}$	Derivative of the scalar $x$ , the vector $\underline{x}$ and the tensor $\underline{\underline{X}}$ respectively with respect to time
$\underline{x} \wedge \underline{y}$	Cross product between vectors $\underline{x}$ and $\underline{y}$
$\underline{\underline{X}}:\underline{\underline{Y}}$	Double tensor contraction
$\langle x \rangle$	$\langle x \rangle = 0$ if $x \leq 0$ , else $\langle x \rangle = x$ .

# **Chapter 1**

# **Introduction**

## 1.1 Context

In seismic zones, the steel moment resisting frame building contains heavy welded beam-to-column connections. The ductility of steel makes it possible to avoid the appearance of cracks in the connections by energy dissipation due to plastic strain. However, earthquakes in the 1990s in the USA and Japan resulted in widespread and unpredicted damage in welded beam-to-column connections in rigid steel frame buildings. These failures explain why the engineering community has decided to investigate the reasons for this unexpected behavior and explore alternative connection types. Research in many countries has resulted in a number of changes to building design codes and specifications. However, performance is affected by many factors such as dimensions of beam-to-column components, connection design, manufacturing quality and the mechanical properties of the different regions of the joint. A procedure for analyzing these factors was recently published under the auspice of the International Institute of Welding (IIW), called the Risk Assessment Procedure (RAP). It determines the risk of fracture in seismically affected moment connections, covering design, material, fabrication and loading issues.

European steelmakers produce heavy sections used in multi-storey buildings in seismic zones. In order to maintain the competitiveness of the European Union in this market, it is important that methods verified for specifying steel sections, defining connections and assessing safety in service should be available for steel users.

## 1.2 VERAPS Project

The VERAPS project (Validation and Enhancement of Risk Assessment Procedure for Seismic connections) [BAN07] aims to validate and enhance the RAP for connections in seismic areas. To achieve this, it further develops modeling methods for predicting connection behavior. The objectives are therefore to assess the cyclic plastic rotation capacity of heavy welded beam-to-column connections as a function of mechanical properties of the beams, columns and weld materials and type of joint preparation. Fabrication, testing, modeling methods and reliability analyses were combined to achieve this aim. In this project, several numerical tools were developed and material data were gathered to contribute to the assessment of connection behavior.

The partners of the project were:

- Corus Ltd UK of the Swinden Technology Center (England),
- Versuchsanstalt für Stahl, Holz und Steine, University of Karlsruhe (Germany),
- Instituto de Soldadura e Qualidade (ISQ) in Lisbon (Portugal),
- ArGEnCo Department, University of Liège (ULg) (Belgium).

Figure 1-1 describes the distribution of the partner's tasks in the VERAPS project. Firstly, Corus provided the steel. Then, eight large scale tests on welded beam-to-column connections were carried out at the University of Karlsruhe according to the design performed by the University of Liege and Karlsruhe.



Next, ISQ measured the residual stresses generated by the welding process in the connection zone. The measurements of the material properties were performed by ISQ and Corus, where the samples from the connections were machined.

These measurements and finite element simulation results enabled Corus to analyze the connection performance according to the RAP procedure.

The work of the University of Liege was to develop a finite element model of Karlsruhe's tests which had to simulate the experiments accurately and enable project members to achieve a series of tests completing the test campaign by modeling other connection designs.

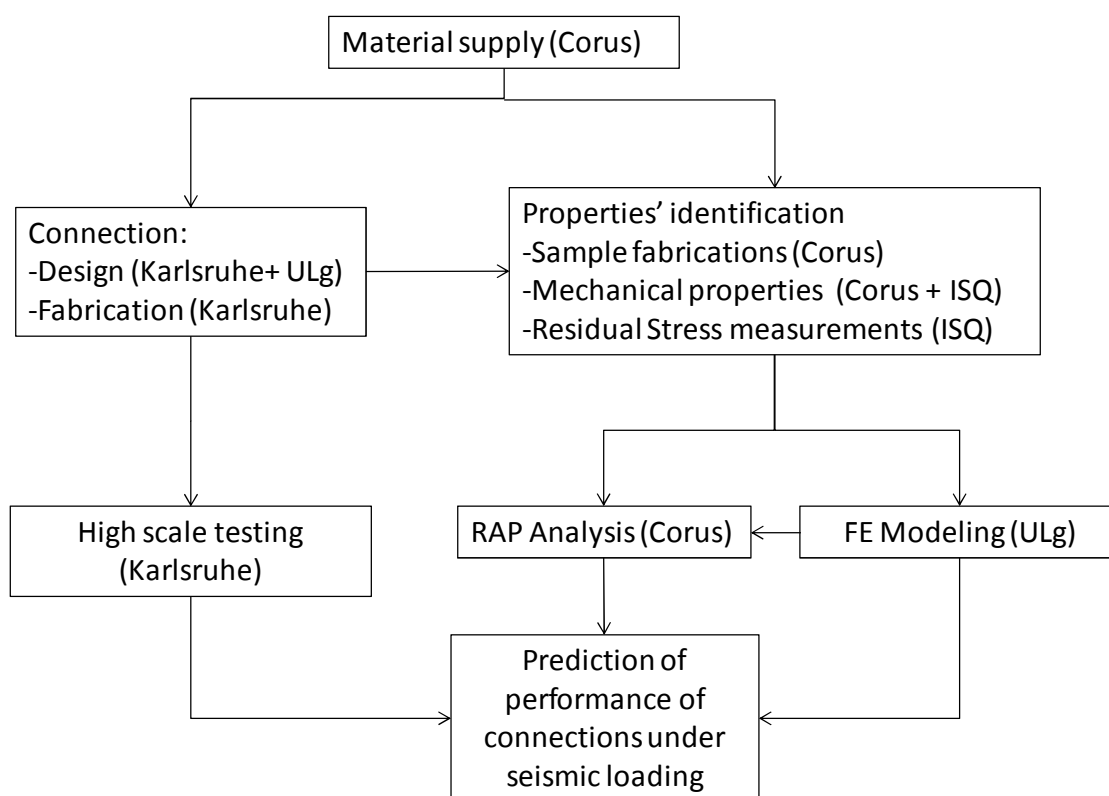


Figure 1-1: Flowchart of the VERAPS project

### 1.3 Objectives

The current PhD research included in the VERAPS project aims to model the crack's propagation in heavy welded beam-to-column connections by finite elements submitted to cyclic quasi-static loading. This modeling approach is validated by tests performed by the University of Karlsruhe and the validated model has made it possible to predict the behavior of non-tested connections and to explore a larger field of possibilities. The model should require only a few material parameters and should be available to industrial engineers.

## 1.4 Scope of the study

### 1.4.1 Connection description

The structure under investigation, described in Figure 1-2, was a welded connection between a beam and a column. The beam was a horizontal I-beam. The column is a vertical I-beam. The steel of the beams, columns and plates was S 355 grade. The dimensions of these beam flanges are considerable.

The welding was applied between the beam and column flanges. At the end of the beam web, holes were made to enable access to the weld. Moreover, as it was a weld made on site, a backup tab was placed to maintain the beam during the welding process and to prevent weld from flowing down when it is in a liquid state. This backup tab was removed after the end of the welding.

The shear tab was bolted or welded to the beam web and welded to the column flange. The beam web is not directly connected to the column flange.

In this type of setup, the geometry of each piece influences the rotation capacity.

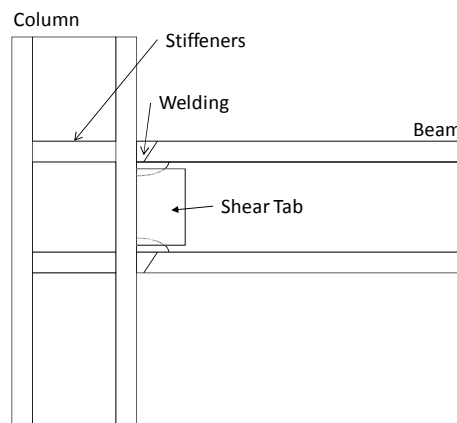


Figure 1-2: Welded beam-to-column connection

### 1.4.2 Welding

The welding linked the beam flange to the column flange. The shape of this welding is described in Figure 1-3. The angle of bevel,  $\alpha$ , was about 35 to 45 °. It is performed by arc welding. Due to dilation and contraction during the manufacturing, the welding process generates non-negligible residual stresses. During the thermal cycle, steel undergoes not only liquid-solid phase transformation but also solid phase transformation, which affects the material properties. Here the welding was performed using a multipass method because the thickness of the beam flange is high and multipass processes make it possible to reduce the residual stresses. The residual stresses have an impact on the crack strength.

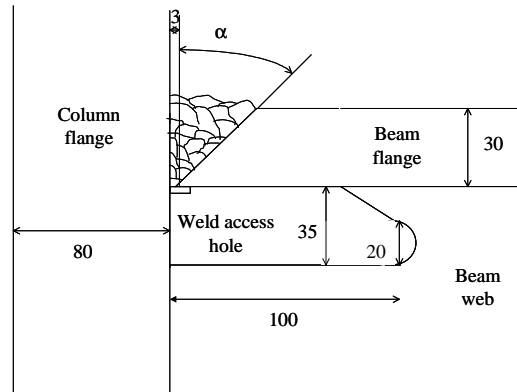


Figure 1-3: Welding by multipass with dimensions in millimeters

### 1.4.3 Materials

After the welding process, the structure is composed of three materials (see Figure 1-4):

- the **B**ase **M**etal (BM): steel from the beam and the column before welding,
- the **W**elded **M**etal (WM),
- the **H**eat **A**ffected **Z**one (HAZ): base metal around the welding where the microstructure is modified by the heat; therefore, its material properties are different, particularly for the toughness [ROD04].

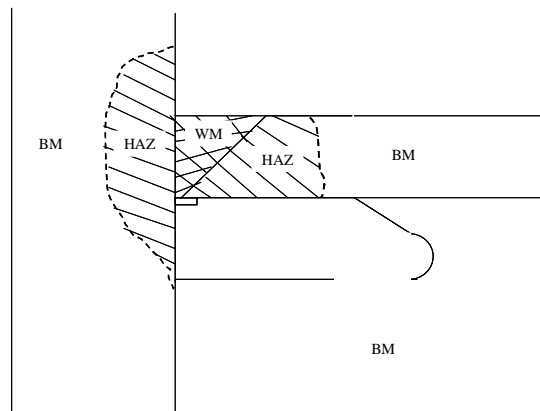


Figure 1-4: Presentation of the three materials in a welded connection

It should be noted that the HAZ was not taken into account in this research. The first reason for this choice is that no metallurgical aspect was studied as this would have required an excessive number of material parameters and heavy thermo-mechanical metallurgical finite element codes [HAB89; ALI00; CAS06]. The second reason is due to the size of the HAZ. Experimental tests, which would make it possible to identify the mechanical behavior of the HAZ, would be highly complicated because of the relatively limited size of the zone.

### 1.4.4 Large scale test

Eight beam-to-column connections were manufactured. The RAP parameters, such as the moment ratio between the beam and the column, the welding process and initial defects were

varied. The connections were submitted to cyclic loading with variable amplitude until macroscopic cracks appeared as according to FEMA 350 [FEM00] (see Figure 1-5). The aim was to evaluate the rotation capacity and the crack propagation strength of the connection to quantify resistance to an earthquake. The cyclic loading was defined to generate a cyclic moment in the connection.

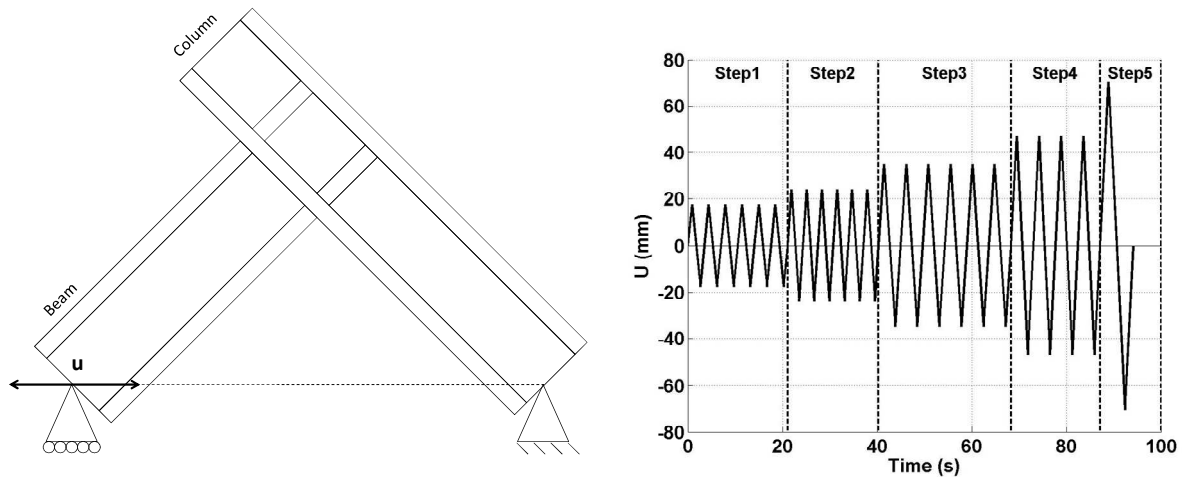


Figure 1-5: Loading definition

### 1.4.5 Damage and Crack process

Matos described this process well in [MAT01]. The crack process is defined by two stages: the initiation stage and the propagation stage. In most cases, initiation happens at the root of the welding along the column. Indeed this is the region where the residual stresses are the highest and the initial defects, where cracks are initiated, are often found like as well as a lack of fusion. The crack size increased up to until about 8 to 10 mm.

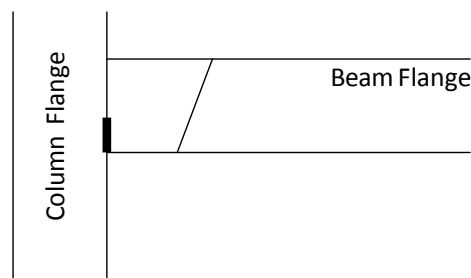


Figure 1-6: Crack initiation

For propagation, the structure studied was observed to exhibit five possible paths (see Figure 1-7):

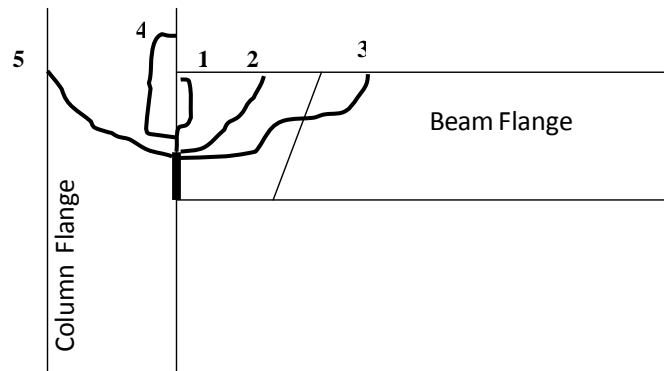


Figure 1-7: Possible crack paths

- Vertically along the beam and the column,
- Through the welding,
- Through the beam,
- Divot,
- Through the column.

The fracture could be brittle with cleavage fracture especially when the residual stresses are significant. It was observed for some connection in Northridge after the earthquake. However in the case of the VERAPS connection the fracture were ductile with inelastic behavior. The damage is generated by two mechanisms: fatigue due to the cyclic loading and the high level of loading during the last cycle. The fracture is influenced by the residual stresses demonstrated by the fact that the crack path follows the normal to the direction of the maximum principal stress.

## 1.5 Methods

The aim of this study was to develop a three-dimensional finite element model of the large scale test performed at the University of Karlsruhe. The finite element code used was the Lagrangian non-linear finite element code Lagamine, developed at the ULg since the 1980s. One feature of this code is that it can model high levels of displacement and strain states. Moreover, it is open source, so one can add and modify subroutines. It contains an important library of elements and constitutive laws.

The study has been divided into several steps. The division of the study performed by the author are shown in Figure 1-8 and grouped by color. No experimental tests have been performed by the author. The experimental data come from the experiments carried out by the partners of the VERAPS project.

Corus and ISQ have performed tensile tests on the base metal and the welding metal. The experimental results were then processed in order to identify the elastoplastic constitutive law of each material by the inverse method.

The crack process was modeled by the Cohesive Zone Model (CZM), which was used to simulate initiation and propagation. Thus a new element and a new constitutive law were created firstly in

two dimensions and then in three dimensions. Then, the identification of the cohesive parameters was performed by the inverse method. Corus performed three point bend testing and Charpy tests on samples extracted from the connection. The experimental tests were modeled by finite elements with a cohesive zone model and the model's parameters were identified.

A crack's propagation is affected by fatigue damage due to cyclic loading. The fatigue damage for this study was computed by the Continuum Damage Model developed by Lemaitre and Chaboche. This damage evolution law was implemented in the Lagamine code during this research. Thus, the fatigue damage and monotonic damage could be coupled. ISQ performed cyclic tensile tests on samples extracted from the connection. Their data were processed to identify the CDM parameters. In addition, the fatigue damage can give an estimation of the crack path, which cannot be identified by the cohesive zone model. The goal of this development was to compute the level of fatigue damage to couple it with the cohesive zone model. One could link to a remeshing procedure adding new cohesive zone elements according to the damage's characterization and modeling the whole process in one simulation. However, in three dimensions, this approach is quite complex and it was decided to work in two steps: characterizing the damage with a first computation without cohesive elements, then performing a second simulation with cohesive elements defined according the first simulation's results.

As the residual stresses have an impact on the crack's propagation, it was important to evaluate their values. With this aim in view, a welding simulation was performed by a thermo-mechanical finite element model. The welding process parameters were communicated by the University of Karlsruhe. Then some thermo-mechanical properties were provided by Corus. Finally, the results of these simulations were compared to the residual stress measurement performed by ISQ. The aim was to obtain a balanced residual stress field to be entered into the connection modeling at the beginning of the simulation and to observe its impact on the strength of the cracked components.

As the connections tested by the University of Karlsruhe had different dimensions and different designs, a module for 3D mesh generation of the welded beam-to-column connection was programmed with the Fortran 90 in order to generate the mesh only by providing the design of the structure. In the first step some computations without damage or residual stresses were performed to validate the mesh by comparing the moment rotation curve with the experimental one. Then, to identify the crack path, modeling without the cohesive zone model was performed by incorporating the fatigue damage model. The crack path may be the zone where fatigue is at its highest. Finally, a computation with the cohesive zone model coupled with the fatigue continuum damage model was performed to predict the crack's propagation.

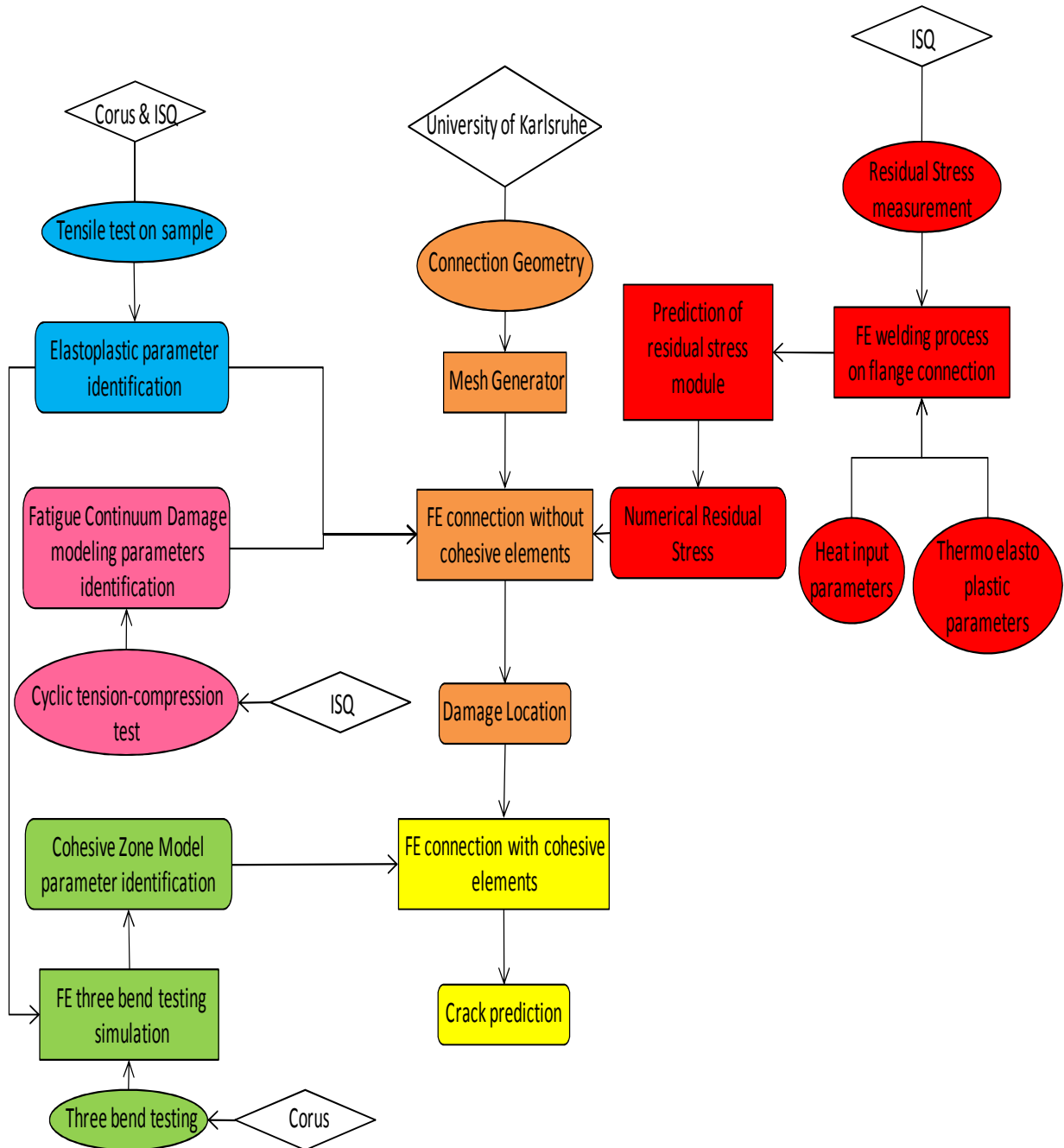


Figure 1-8: Flow chart of the study

## 1.6 Outline of this thesis

This thesis is organized according to the flow chart reported in Figure 1-8. Firstly, in Chapter 2, the numerical tools used in this study are described. The Lagamine code is presented along with the solid element and the elastoplastic law used. In this part, no development is performed during the study except for the treatment of the tensile test data, which used to calibrate the elastoplastic model.

In Chapter 3, the fatigue damage modeling is presented. The continuum damage model and some other classic models are described and compared. This chapter explains the identification method for the parameters after treatment of the experimental data. The computation of the damage variable from the integration of the damage evolution law is described in the finite element code.

Chapter 4 outlines on the modeling of crack propagation. After the illustration of the classic fracture mechanic model, the theory of the cohesive zone model is explained according to a literature review. Then, the implementation of the cohesive element in 2D and 3D is shown. Finally, the results and method of the inverse approach are described to calibrate the model for the base and weld metals.

The welding simulations performed to evaluate the residual stress fields are presented in Chapter 5. Firstly, the strategies used in the model to tackle the difficulties of the simulation are set out. After this step, the results are shown and are compared with the measurements performed by ISQ.


Next, Chapter 6 focused on the large scale test performed at the University of Karlsruhe. First, the welded beam-to-column connections and the test characteristics are described. Then, the strategy to generate the 3D mesh of the structure is set out. Lastly, the results of the simulation of this test are presented.

Finally the thesis ends with the conclusions and the perspectives of this research, followed by appendices. The first appendix contains a description of iterative methods used to solve linear equation systems. These methods help to speed up the three-dimensional simulations. The second appendix describes an adaptive remeshing method which has been developed. This method has been adapted to incremental forming simulations with 4-node shell elements. This development helps to better understand the Lagamine code and to explore a remeshing method.



# **Chapter 2**

## **Numerical tools description**



## 2.1 Introduction

Since the overall aim of this thesis is to develop a numerical model, in such a context it is important to describe the finite element code in which some developments have been implemented. After several reminders of mechanical definitions, this chapter presents the finite element code Lagamine, used in this study, and its features. Then the solid element, BWD3D, which is used in connection modeling, is discussed. Finally the last section defines the elasto-plastic model used and explains the identification of its parameters needed to model the material behavior of the materials (base metal and weld metal) from tensile experiments. The developments of a traditional isotropic elasto-plastic law are well-known, such as the radial return integration scheme. However, it was decided to recall this theory for the interest of the Lagamine group, who uses the ARB law coupled with kinematic hardening extensively. This law, initially implemented by R. Charlier [CHA87] with isotropic hardening, has not yet been described in a thesis in the case when coupled with kinematic hardening. The current description thus helps to understand the work of L. Kaiping [CES97].

## 2.2 Mechanical definitions

### 2.2.1 Strain

The engineering strain is expressed as the ratio of total deformation values compared to the initial dimensions of the material body in which the forces are applied. The engineering normal strain or engineering tensile strain,  $\epsilon_{\text{ing}}$ , of a material line element or an axially loaded fiber is expressed as the change in length,  $\Delta l$ , per unit of the original length,  $l_0$ , of the line element or the fiber. Thus, we have

$$\epsilon_{\text{ing}} = \frac{\Delta l}{l_0} = \frac{l - l_0}{l_0} \quad (2.1)$$

where  $l$  is the current length of the fiber.

The displacement vector,  $\underline{u}$ , is the difference between the current position vector,  $\underline{x}$ , and the initial position vector,  $\underline{x}_0$ :

$$\underline{u} = \underline{x} - \underline{x}_0. \quad (2.2)$$

The velocity vector is obtained from the derivative of the displacement as a function of time:

$$\underline{v} = \frac{\partial \underline{u}}{\partial t}. \quad (2.3)$$

From infinitesimal theory, Cauchy's strain tensor can be defined by

$$\underline{\underline{\epsilon}} = \frac{1}{2} (\underline{\underline{\nabla}} \underline{u} + \underline{\underline{\nabla}} \underline{u}^T). \quad (2.4)$$

The strain tensor can be further divided into two parts:

$$\underline{\underline{\epsilon}} = \underline{\underline{\epsilon}}^e + \underline{\underline{\epsilon}}^p \quad (2.5)$$

where  $\underline{\underline{\epsilon}}^e$  is the elastic component of the strain and  $\underline{\underline{\epsilon}}^p$  is the plastic component. The equivalent plastic strain rate is defined by the following:

$$\dot{\underline{\underline{\epsilon}}}_{\text{eq}}^p = \sqrt{\frac{2}{3} \dot{\underline{\underline{\epsilon}}}_{\text{p}} : \dot{\underline{\underline{\epsilon}}}_{\text{p}}}. \quad (2.6)$$

## 2.2.2 Cauchy's stress

For a load applied in one direction, the engineering stress,  $\sigma_{\text{ing}}$ , is the ratio between the applied force,  $F$  and the initial surface,  $S_0$ .

$$\sigma_{\text{ing}} = \frac{F}{S_0} \quad (2.7)$$

Considering a structure, cut by a plane  $\pi$ , and where an infinitesimal internal force,  $d\underline{F}$ , is applied to an infinitesimal surface,  $dS$ , along the outward normal to  $\pi$ , called  $\underline{n}$ , the following relation can be defined by:

$$\frac{d\underline{F}}{dS} = \underline{\underline{\sigma}} \cdot \underline{n} \quad (2.8)$$

where  $\underline{\underline{\sigma}}$  is a second-order tensor called Cauchy's stress. Note that, here,  $S$  is the current cross section of the structure and not the initial one.

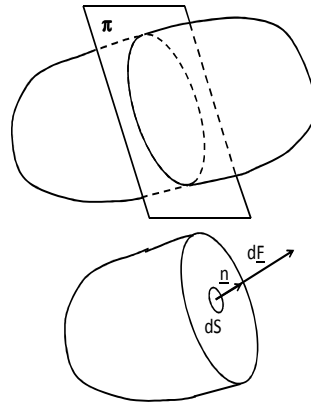


Figure 2-1: Internal force descriptions

One defines the equivalent von Mises' stress by:

$$\sigma_{\text{eq}} = \sqrt{\frac{3}{2} \hat{\underline{\underline{\sigma}}} : \hat{\underline{\underline{\sigma}}}} \quad (2.9)$$

where  $\hat{\underline{\underline{\sigma}}}$  corresponds to the deviatoric component of the stress.

$$\hat{\underline{\underline{\sigma}}} = \underline{\underline{\sigma}} - \sigma_{\text{H}} \underline{\underline{I}} \quad \text{where} \quad \sigma_{\text{H}} = \frac{1}{3} \text{Tr}(\underline{\underline{\sigma}}) \quad (2.10)$$

In the equation above,  $\sigma_{\text{H}}$  is called the hydrostatic stress.

One defines the stress triaxiality by:

$$\underline{T}_F = \frac{\underline{\sigma}_H}{\underline{\sigma}_{eq}} \quad (2.11)$$

### 2.2.3 Jaumann's derivative

The constitutive law is not dependent on any reference frame modification; therefore, the variables used must be objective. An objective second-order tensor,  $\underline{T}$ , defined in an initial reference frame, is a tensor which follows

$$\underline{T}' = \underline{R} \underline{T} \underline{R}^T \quad (2.12)$$

where  $\underline{T}'$  is the representation of the tensor  $\underline{T}$  in a new reference frame and  $\underline{R}$  is the rotational matrix to pass from the initial reference frame to the new one.

Cauchy's stress, strain and strain rate are objective variables. However, the stress rate is not objective. That's why Jaumann's derivative, noted  $\nabla$ , is used, which makes it possible to correct parasite rotations in the stress rate:

$$\begin{aligned} \underline{\overset{\nabla}{\sigma}} &= \underline{\dot{\sigma}} - \underline{\Omega} \underline{\sigma} + \underline{\sigma} \underline{\Omega} \\ \text{where } \underline{\dot{\sigma}} &= \frac{\partial \underline{\sigma}}{\partial t} \quad \text{and} \quad \underline{\Omega} = \frac{1}{2} (\underline{\nabla} \underline{v} - \underline{\nabla} \underline{v}^T). \end{aligned} \quad (2.13)$$

## 2.3 The finite element code LAGAMINE

### 2.3.1 Description

During this research, the finite element code LAGAMINE developed in-house was used. It is a non-linear Lagrangian code that has been under development at the Department ArGENCo of the University of Liege since 1982 and was started by Prof. Cescotto in order to simulate the rolling process [CES85].

The code can carry out thermal, mechanical and metallurgical analyses. Therefore, the code has been applied to numerous forming process such as forging [HAB90], continuous casting [CAS04], deep drawing [DUC05b], powder compaction [MOS99] and incremental forming [HEN07]. To perform this, the code contains an extensive library of elements and constitutive laws for large strains and large displacements.

### 2.3.2 Concepts of the finite element code

#### 2.3.2.1 The equilibrium condition

The displacement field which minimizes the total energy of the system is the one that respects equilibrium. This minimization is performed by checking the virtual work principle,

$$\int_V \underline{\sigma}^T \delta \underline{\epsilon} dV = \int_V \underline{\rho} \underline{b}^T \cdot \delta \underline{u} dV + \int_S \underline{\rho} \underline{t}^T \delta \underline{u} dS \quad (2.14)$$

where  $(\underline{\sigma})_{6 \times 1}$  is the stress vector which contains the components of the stress tensor that respect internal equilibrium,  $(\underline{\delta \epsilon})_{6 \times 1}$  is the virtual strain vector which contains the components of the strain tensor and verifies kinematic compatibility,  $(\underline{\delta u})_{3 \times 1}$  is the virtual displacement,  $\rho$  is the density,  $(\underline{b})_{3 \times 1}$  is a volumetric load,  $(\underline{t})_{3 \times 1}$  is a surface load,  $V$  is the current volume of the system and  $S$  is the current surface.

This variation principle is the simplest one, where only one unknown (the displacement field) needs to be identified. In this principle, direct links between displacement history and strains are defined as well as between strains and stresses. More advanced principles exist: for instance, in section 2.4, the solid element BWD3D relies on the three-field Hu-Washizu variation principle.

The spatial discretization of the virtual displacement field,  $\underline{\delta u}$ , in finite elements is defined by

$$\underline{\delta u} = \underline{H} \underline{\delta U} \quad (2.15)$$

where  $(\underline{\delta U})_{3 \times N}$  contains the admissible virtual displacement of  $N$  nodes, and  $(\underline{H})_{3 \times 3N}$  is the interpolation matrix.

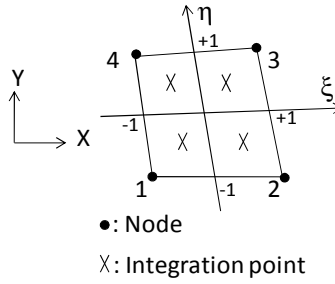


Figure 2-2: 2D Finite element description, isoparametric and global coordinate definition

The virtual strain field is computed by

$$\underline{\delta \epsilon} = \underline{B} \underline{\delta U} \quad (2.16)$$

where  $(\underline{B})_{6 \times 3N}$  contains the gradient of the interpolation function. The matrixes,  $\underline{B}$  and  $\underline{H}$ , depend on the element used.

Thus equation (2.14) becomes

$$\int_V \underline{\sigma}^T \underline{B} \underline{\delta U} dV = \int_V \rho \underline{b}^T \cdot \underline{H} \underline{\delta U} dV + \int_S \rho \underline{t}^T \underline{H} \underline{\delta U} dS. \quad (2.17)$$

As  $\underline{\delta U}$  is a virtual nodal displacement, it can be removed from the integral. So, one defines the following vectors:

- the nodal internal force vector,  $\underline{F}_{int}$ , equivalent in term of energy to the stress:

$$\underline{F}_{int} = \int_V \underline{B}^T \underline{\sigma} dV; \quad (2.18)$$

- the nodal external force vector,  $\underline{F}_{ext}$ , equivalent in terms of energy to the applied loading:

$$\underline{F}_{\text{ext}} = \int_V \rho \underline{H}^T \underline{b} dV + \int_S \rho \underline{H}^T \underline{t} dS. \quad (2.19)$$

Therefore, the virtual work principle becomes

$$(\underline{F}_{\text{int}} - \underline{F}_{\text{ext}}) \delta \underline{U} = 0. \quad (2.20)$$

As the previous relation is true regardless of which the arbitrary field  $\delta \underline{U}$  is chosen, the equilibrium condition of a finite element problem can be expressed as:

$$\underline{F}_{\text{int}} = \underline{F}_{\text{ext}} \quad (2.21)$$

### 2.3.2.2 Temporal integration

Lagamine's code users often choose an implicit integration scheme though it is possible to apply explicit integration. This is because the advantages of the implicit integration scheme are that it is more stable and larger increment can be used.

The implicit methods is an incremental one, that is, in radial loading cases the loading,  $\underline{P}$ , or displacement,  $\underline{U}$ , are imposed step by step. At the first time step,  $\lambda_{p1} \underline{P}$  and  $\lambda_{u1} \underline{U}$  are applied to the initial balanced configuration. By a Newton-Raphson method, a new balanced configuration is determined. Then a second time step begins where  $\lambda_{p2} \underline{P}$  and  $\lambda_{u2} \underline{U}$  are applied to the previous balanced configuration. This procedure is continued until one reaches

$$\sum_k \lambda_{pk} = 1 \quad \text{and} \quad \sum_k \lambda_{uk} = 1 \quad (2.22)$$

The Newton-Raphson method (see Figure 2-3) is an iterative procedure which is used to find the zero of the out-of-balance force vector,  $\underline{F}_{\text{OBF}}$ , in order to pass from a balanced configuration A to a balanced configuration B at the  $N_{\text{inc}}^{\text{th}}$  increment.

$$\underline{F}_{\text{OBF}} = \underline{F}_{\text{int}} - \underline{F}_{\text{ext}} \quad (2.23)$$

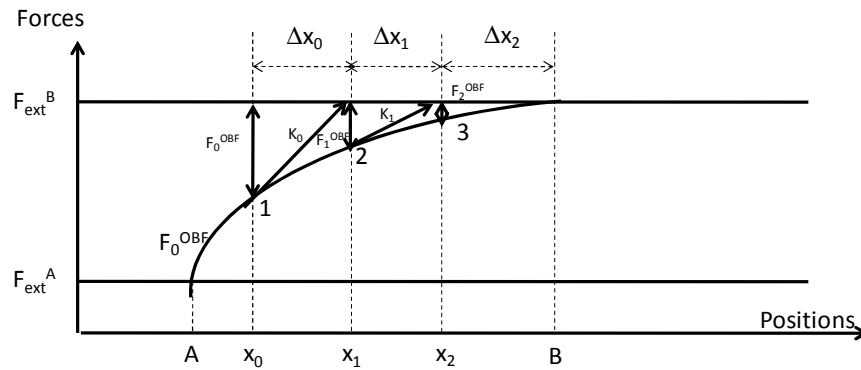


Figure 2-3: Newton-Raphson method description

Firstly an approximation is made of the new nodal positions. It can be derived from the nodal position of the previous balance configuration,  $\underline{x}_A$ , plus the constrained displacement.

$$\underline{x}_0 = \underline{x}_A + \left( \sum_k^{N_{\text{inc}}} \lambda_k \right) \underline{U} \quad (2.24)$$

Another solution can be obtained from the nodal velocity of the previous configuration,  $\underline{v}_A$ .

$$\underline{x}_0 = \underline{x}_A + \underline{v}_A \Delta t + \left( \sum_k^{N_{mc}} \lambda_k \right) \underline{U} \quad (2.25)$$

where  $\Delta t$  is the time step.

By a first-order Taylor development of Equation (2.23), one obtains

$$\underline{F}_{\text{OBF}}(\underline{x}_i + \Delta \underline{x}) = \underline{F}_{\text{OBF}}(\underline{x}_i) + \left( \frac{\partial \underline{F}_{\text{OBF}}}{\partial \underline{x}} \right)_{\underline{x}_i} \Delta \underline{x} \quad (2.26)$$

where  $\underline{x}_i$  is the nodal position of the previous iteration and  $\Delta \underline{x}$  is a nodal position correction.

One defines the tangent stiffness matrix,  $\underline{\underline{K}}$ , by the following:

$$\underline{\underline{K}} = \left( \frac{\partial \underline{F}_{\text{OBF}}}{\partial \underline{x}} \right)_{\underline{x}_i} \quad (2.27)$$

As the aim is to nullify the out-of-balance force, where  $\underline{F}_{\text{OBF}}(\underline{x}_i + \Delta \underline{x}) = \underline{0}$ , Equation (2.26) becomes

$$\Delta \underline{x} = -\underline{\underline{K}}^{-1} \underline{F}_{\text{OBF}}(\underline{x}_i). \quad (2.28)$$

The computation of the inverse tangent stiffness matrix can take some time depending on the number of degrees of freedom. Before the current thesis began, only direct methods have been implemented by LU factorization. For large simulations, an iterative method was therefore implemented during this research to reduce the computation time (see Appendix 1).

Consequently, the nodal position,  $\underline{x}_i$ , of the next configuration is:

$$\underline{x}_{i+1} = \underline{x}_i + \Delta \underline{x} \quad (2.29)$$

Then one iterates with the algorithm described until reaching a convergence tolerance. An increment is determined converged if

$$\frac{\|\underline{F}_{\text{OBF}}\|}{\|\underline{R}\|} < \varepsilon_f \quad (2.30)$$

where  $\underline{R}$  is the reaction which contains all force components of fixed or constrained nodes and  $\varepsilon_f$  is a level of a tolerance (about  $1 \times 10^{-5}$ ). The symbol  $\|\underline{x}\|$  defines the norm of the vector  $\underline{x}$ . There are three different definitions for this norm used in the Lagamine code:

$$\begin{aligned} \|\underline{x}\|_1 &= \frac{1}{N_x} \sqrt{\sum_i^{N_x} x_i^2}, \\ \|\underline{x}\|_2 &= \frac{1}{N_x} \sum_i^{N_x} |x_i|, \\ \|\underline{x}\|_3 &= \max_i (|x_i|) \end{aligned} \quad (2.31)$$

where  $N_x$  is the length of  $\underline{x}$ .

To avoid jump displacements, another convergence tolerance is used in the Lagamine code:

$$\frac{\|\Delta \underline{x}\|}{\|\underline{x}_i - \underline{x}_A\|} < \varepsilon_u \quad (2.32)$$

where  $\varepsilon_u$  is a level of tolerance (about  $1 \times 10^{-3}$ ).

Figure 2-4 summarizes the Lagamine flowchart for implicit schemes.



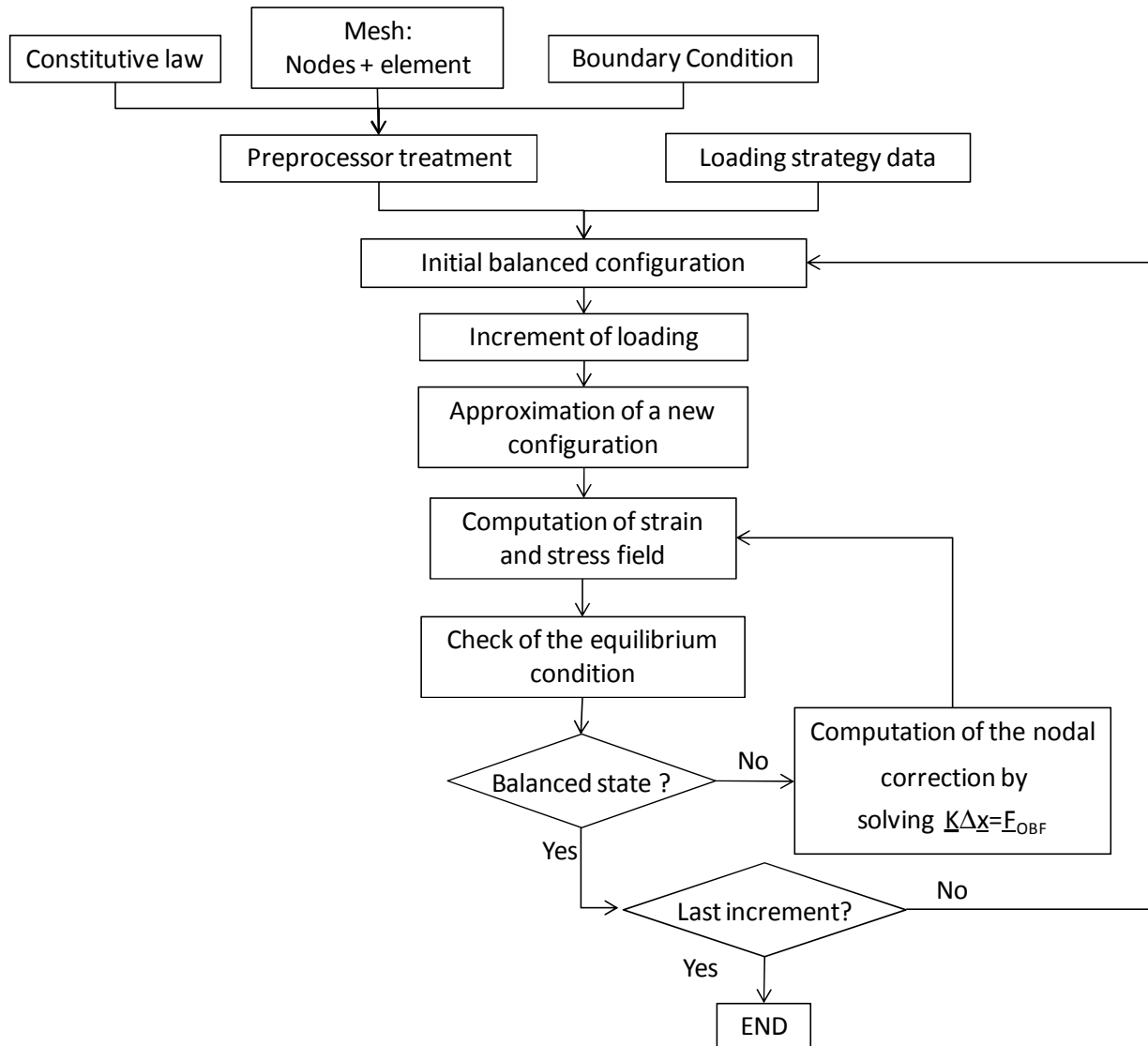


Figure 2-4: General flowchart of the LAGAMINE code

### 2.3.2.3 Computation of the nodal force and the stiffness matrix

The nodal internal force vector,  $\underline{F}_{\text{int}}$ , is computed for each element by numerical integration according to a Gauss' scheme:

$$\underline{F}_{\text{int}} = \sum_{\text{ip}} \underline{B}^T \underline{\sigma} W \det(\underline{J}) \quad (2.33)$$

where ip is an integration point,  $W$  is the weight of the integration point and  $(\underline{J}_{3 \times 3})$  is the Jacobian matrix defining the mapping from the global coordinate axes  $(x, y, z)$  to the isoparametric coordinate axes  $(\xi, \eta, \gamma)$  (see Figure 2-2):

$$\underline{\underline{J}} = \begin{bmatrix} \frac{\partial x}{\partial \xi} & \frac{\partial x}{\partial \eta} & \frac{\partial x}{\partial \gamma} \\ \frac{\partial y}{\partial \xi} & \frac{\partial y}{\partial \eta} & \frac{\partial y}{\partial \gamma} \\ \frac{\partial z}{\partial \xi} & \frac{\partial z}{\partial \eta} & \frac{\partial z}{\partial \gamma} \end{bmatrix}. \quad (2.34)$$

To obtain the stiffness matrix,  $\underline{\underline{K}}$ , it is sufficient to differentiate the nodal internal force vector:

$$d\underline{\underline{F}}_{\text{int}} = \underline{\underline{K}} d\underline{\underline{x}} \quad (2.35)$$

The derivative of (2.33) gives

$$d\underline{\underline{F}}_{\text{int}} = \sum_{\text{ip}} \underline{\underline{B}}^T \det(\underline{\underline{J}}) d\underline{\underline{\sigma}} W + \sum_{\text{ip}} d(\underline{\underline{B}}^T \det(\underline{\underline{J}})) \underline{\underline{\sigma}} W. \quad (2.36)$$

The first term defines the classic stiffness of the small strain cases, which is computed from the derivative of the stress. The second term defines the large displacement effect: the influence of the element volume modification on the nodal forces.

## 2.4 The solid element BWD3D

In this research, the solid element chosen was the element BWD3D. It is an 8-node 3D brick element with a mixed formulation especially adapted to large strains and large displacements. This element can be coupled with any 3D mechanical constitutive law, and its strain and stress tensors are expressed in global axes.

This element uses a reduced integration scheme (that is, only one integration point in its center) and an hourglass control technique. It is based on the three-field Hu-Washizu variation principle with the ‘‘assumed strain method’’ [SIM86; BEL91].

One feature of the BWD3D element is a new shear locking treatment based on the Wang-Wagoner’s method [WAN04]. This method identifies the hourglass modes responsible for shear locking and removes them. The two bending hourglass modes and the non-physical hourglass modes are eliminated. The volumetric locking treatment is also based on the elimination of inconvenient hourglass modes.

A second feature of this element is its use of a corotational reference system. In order to identify the hourglass modes, which is crucial to the method, the formulation of the element’s kinematics must be expressed in a corotational reference system, closely linked to element’s coordinates. This reference system must have its origin at the center of the element and its reference axes are needed to be aligned (as much as possible, depending on the element’s shape) with element edges. A fortunate consequence of this corotational reference system is a simple and accurate treatment of the hourglass stress objectivity, by using initial and final time step rotation matrices.

The shear locking and the volumetric locking methods proposed by Wang and Wagoner, coupled with the corotational reference system, have been successfully implemented in the BWD3D

element. The Wang-Wagoner's method, contrary to some other shear locking methods (see for example, Li and Cescotto [LI97]) has deep physical roots, which makes it very efficient for various FE analyses. Further details about the hourglass and the locking treatment in the BWD3D can be found in [DUC05a; DUC05b]. A more complete description can also be found in [DUC08].

## 2.5 The constitutive law

### 2.5.1 The elastic law

Elastic strain is a variation in the atomic positions and is a reversible process. For the metallic material, elastic behavior is generally linear and according to its forming process, it can be isotropic. Therefore, it can be described by the Hooke's law:

$$\left\{ \begin{array}{l} \underline{\underline{\sigma}} = \lambda \text{Tr}(\underline{\underline{\epsilon}}^e) \underline{\underline{I}} + 2\mu \underline{\underline{\epsilon}}^e \\ \text{or } \underline{\underline{\epsilon}}^e = \frac{1+\nu}{E} \underline{\underline{\sigma}} - \frac{\nu}{E} \text{Tr}(\underline{\underline{\sigma}}) \underline{\underline{I}} \end{array} \right. \quad (2.37)$$

where  $\lambda$  and  $\mu$  are Lamé's coefficients,  $E$  is Young's modulus and  $\nu$  is Poisson's ratio. The relationships between the elastic parameters are

$$\begin{aligned} \lambda &= \frac{\nu E}{(1+\nu)(1-2\nu)}; \mu = G = \frac{E}{2(1+\nu)} \\ E &= \mu \frac{3\lambda + 2\mu}{\lambda + \mu}; \nu = \frac{\lambda}{2(\lambda + \mu)} \end{aligned} \quad (2.38)$$

where  $G$  is known as Coulomb's modulus.

### 2.5.2 The plastic law

In metal, plastic strain is often due to the motion of the dislocations, which is an irreversible process. Other phenomena, such as twinning and grain boundary slip, can also occur. These phenomena appear only when the stress level reaches and passes a limit  $\sigma_y$ , called yield stress.

#### 2.5.2.1 The yield locus

In a multiaxial case, the yield limit is described by a surface in the principal stress spaces ( $\sigma_1, \sigma_2, \sigma_3$ ) called the yield locus  $f(\underline{\underline{\sigma}})$  which depends on the stress state:

- If  $f(\underline{\underline{\sigma}}) < 0$ , the state is elastic,
- If  $f(\underline{\underline{\sigma}}) = 0$ , the state is elastoplastic and loading and unloading can occur,
- The case  $f(\underline{\underline{\sigma}}) > 0$  is impossible because the stress cannot cross the surface.

There are different functions,  $f$ , describing the yield locus in the literature [BUN00]. This chapter will describe only three possible yield loci because these are often those used in the industrial world, as a result, in this study.

#### *Von Mises' yield criterion*

As plastic strains are due to intracrystalline shear and slip driven by shear stress, the von Mises' yield criterion considers the yield stress to be linked to the elastic shear energy. So, the yield locus depends on the second invariant of the stress tensor. Therefore, it is defined by

$$f = \frac{1}{2} \hat{\underline{\underline{\sigma}}} : \hat{\underline{\underline{\sigma}}} - k_0^2 = 0 \text{ where } k_0 = \frac{\sigma_y}{\sqrt{3}}. \quad (2.39)$$

The criterion is described in Figure 2-5.

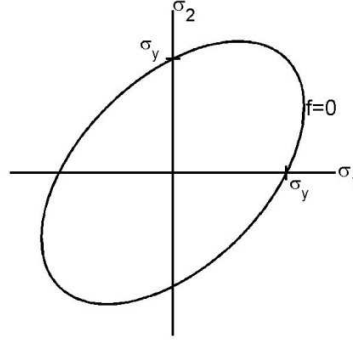


Figure 2-5: Yield locus with Von Mises' criterion

### *Tresca's yield criterion*

In this case, the criterion is not linked to shear energy but rather depends on the maximum shear stress:

$$f = \sup_{i \neq j} (|\sigma_i - \sigma_j|) - \sigma_y = 0 \quad (2.40)$$

where  $\sigma_i$  and  $\sigma_j$  are the eigenvalues of the stress tensor.

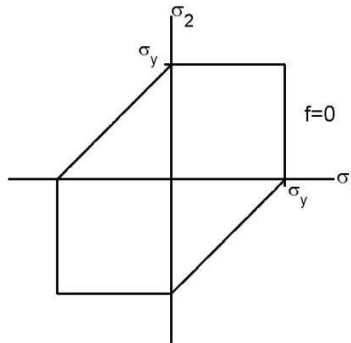


Figure 2-6: Yield locus with Tresca criterion

The criterion is described in Figure 2-6.

### *Hill's yield criterion*

The previous criteria consider the yielding to be isotropic. In the case of anisotropic orthotropic material, Hill's 1948 [HIL48] yield criterion is the most used in commercial codes:

$$F(\sigma_{11} - \sigma_{22})^2 + G(\sigma_{33} - \sigma_{22})^2 + H(\sigma_{33} - \sigma_{11})^2 + 2L\sigma_{12}^2 + 2M\sigma_{23}^2 + 2N\sigma_{13}^2 - 2\sigma_y^2 = 0 \quad (2.41)$$

where F, G, H, L, M, N, are Hill's coefficients.

### 2.5.2.2 The flow rules

#### *General rules*

Loading and unloading can occur according to the product of the yield normal and the stress rate, as expressed in the condition below.

$$f = \begin{cases} \frac{\partial f}{\partial \underline{\underline{\sigma}}} : d\underline{\underline{\sigma}} > 0 : \text{loading} \\ \frac{\partial f}{\partial \underline{\underline{\sigma}}} : d\underline{\underline{\sigma}} = 0 : \text{neutral loading} \\ \frac{\partial f}{\partial \underline{\underline{\sigma}}} : d\underline{\underline{\sigma}} < 0 : \text{unloading} \end{cases} \quad (2.42)$$

It is assumed that the plastic strain rate is normal to the yield locus (i.e. associated plasticity):

$$\underline{\underline{\epsilon}}^p = \begin{cases} \lambda \frac{\partial f}{\partial \underline{\underline{\sigma}}} & \text{if } \frac{\partial f}{\partial \underline{\underline{\sigma}}} : d\underline{\underline{\sigma}} > 0 \\ 0 & \text{if } \frac{\partial f}{\partial \underline{\underline{\sigma}}} : d\underline{\underline{\sigma}} \leq 0 \end{cases} \quad (2.43)$$

where  $\lambda$  is the multiplier of the normal to the yield locus.

In addition to these conditions, as the loading point has to remain on the yield locus, the consistency condition described by

$$\dot{f} = \frac{df}{dt} = 0 \quad (2.44)$$

has to be respected.

Hardening, which may exist in two forms, describes the evolution of the yield locus. Firstly, the yield locus can grow in an isotropic manner, where the yield stress under tension increases as much as yield stress under compression (see Figure 2-7 and Figure 2-8). This is known as the isotropic hardening.

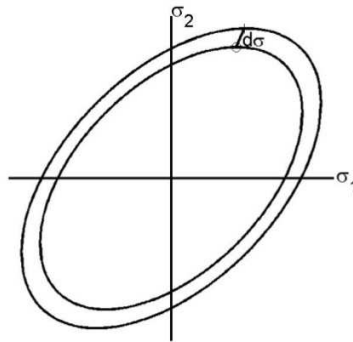


Figure 2-7: Isotropic hardening effect on the yield locus

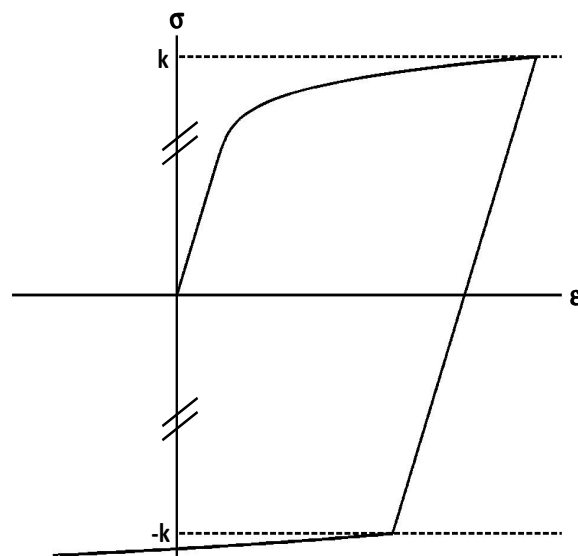


Figure 2-8: Isotropic hardening effect on the uniaxial stress-strain curve

In a second approach the yield stress under tension can be greater than in compression during a cyclic loading (Bauschinger effect). Thus the yield locus moves by translation in the stress space (see Figure 2-9 and Figure 2-10). This is known as the kinematic hardening.

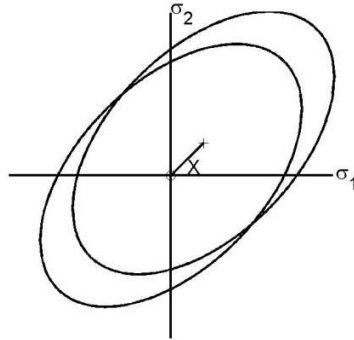


Figure 2-9: Kinematic hardening effect on the yield locus

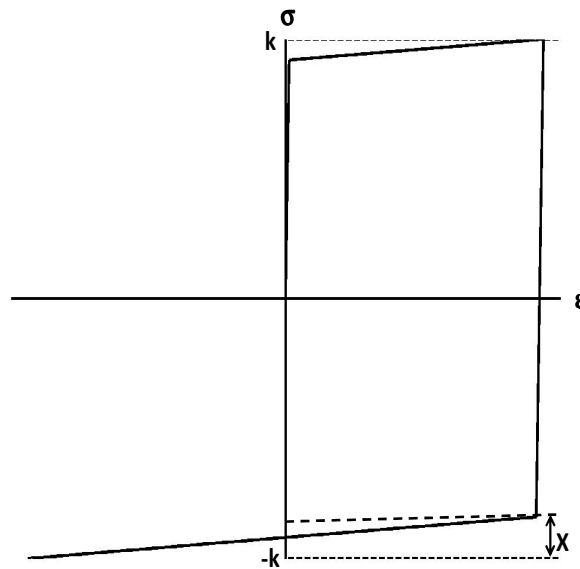


Figure 2-10: Kinematic hardening effect on the uniaxial stress-strain curve

Numerous different functions exist for each type of hardening. In general, the material presents both types of hardening, which is a mixed hardening model is also used.

### ***The isotropic hardening model***

This approach was introduced in the Charlier's thesis [CHA87]. After the evolution of the hardening, von Mises' in a criterion in isotropic hardening case can be written by:

$$f = \frac{1}{2} \underline{\hat{\sigma}} : \underline{\hat{\sigma}} - k^2 = 0 \quad (2.45)$$

where  $k$  is the hardening variable, which depends on the equivalent plastic strain.

The consistency equation (2.44) has to be respected, which gives:

$$\dot{f} = \frac{\partial f}{\partial \underline{\hat{\sigma}}} : \underline{\hat{\sigma}} + \frac{\partial f}{\partial k} : \dot{k} = \underline{\hat{\sigma}} : \underline{\hat{\sigma}} + 2k\dot{k} = 0 \quad (2.46)$$

Equation (2.45) dictates that

$$k = \sqrt{\frac{1}{2} \hat{\underline{\underline{\sigma}}} : \hat{\underline{\underline{\sigma}}} = \frac{\sigma_{\text{eq}}}{\sqrt{3}}. \quad (2.47)$$

If one differentiates this equation, the hardening updating rule can be obtained,

$$\dot{k} = \frac{\dot{\sigma}_{\text{eq}}}{\sqrt{3}} = \frac{1}{\sqrt{3}} \frac{\partial \sigma_{\text{eq}}}{\partial \underline{\underline{\epsilon}}_{\text{eq}}^{\text{p}}} \dot{\underline{\underline{\epsilon}}}_{\text{eq}}^{\text{p}} \quad (2.48)$$

where  $\dot{\underline{\underline{\epsilon}}}_{\text{eq}}^{\text{p}}$  has been defined in section 2.2.1.

The plastic modulus,  $E^{\text{p}}$ , is defined by

$$E^{\text{p}} = \frac{\partial \sigma_{\text{eq}}}{\partial \underline{\underline{\epsilon}}_{\text{eq}}^{\text{p}}}. \quad (2.49)$$

The corresponding plasticity condition (Equation (2.43)) linked to the definitions of the yield locus (2.45) and the equivalent plastic strain rate are used to compute the derivative of the plastic strain:

$$\dot{\underline{\underline{\epsilon}}}_{\text{eq}}^{\text{p}} = \sqrt{\frac{2}{3}} \dot{\lambda}^2 \frac{\partial f}{\partial \underline{\underline{\sigma}}} \frac{\partial f}{\partial \underline{\underline{\sigma}}} = \dot{\lambda} \sqrt{\frac{2}{3} \hat{\underline{\underline{\sigma}}} : \hat{\underline{\underline{\sigma}}}} = \dot{\lambda} \frac{2}{3} \sigma_{\text{eq}}. \quad (2.50)$$

Using these relations (2.47) to (2.50), Equation (2.46) becomes

$$\hat{\underline{\underline{\sigma}}} : \hat{\underline{\underline{\sigma}}} - \frac{4}{9} \sigma_{\text{eq}}^2 E^{\text{p}} \dot{\lambda} = 0. \quad (2.51)$$

Taking the deviatoric component of the strain and stress tensors with the additive split of strain tensors, Equation (2.5), the Hooke's law, Equation (2.37), becomes

$$\hat{\underline{\underline{\sigma}}} = 2G \hat{\underline{\underline{\epsilon}}}^{\text{e}} = 2G(\hat{\underline{\underline{\epsilon}}} - \hat{\underline{\underline{\epsilon}}}^{\text{p}}). \quad (2.52)$$

If one differentiates this equation using the normal condition (Equation (2.43)), one obtains:

$$\hat{\underline{\underline{\sigma}}}^{\text{v}} = 2G \left( \dot{\hat{\underline{\underline{\epsilon}}}} - \dot{\lambda} \frac{\partial f}{\partial \hat{\underline{\underline{\sigma}}}} \right) = 2G(\dot{\hat{\underline{\underline{\epsilon}}}} - \dot{\lambda} \hat{\underline{\underline{\sigma}}}). \quad (2.53)$$

Equations (2.51) and (2.53) give the derivative of the multiplier of the normal,  $\dot{\lambda}$ :

$$\dot{\lambda} = \frac{3G}{2\sigma_{\text{eq}}^2 \left( G + \frac{1}{3} E^{\text{p}} \right)} \hat{\underline{\underline{\sigma}}} : \dot{\hat{\underline{\underline{\epsilon}}}}. \quad (2.54)$$

### ***The kinematic hardening model***

von Mises' criterion coupled with a kinematic hardening model can be written as

$$f = \frac{1}{2} (\hat{\underline{\underline{\sigma}}} - \hat{\underline{\underline{X}}}) : (\hat{\underline{\underline{\sigma}}} - \hat{\underline{\underline{X}}}) - k_0^2 = 0 \quad (2.55)$$

where  $\underline{\underline{X}}$  is the back stress tensor, which indicates the current position of the yield locus center.



The consistency condition and the previous equation give

$$df = \frac{\partial f}{\partial \underline{\underline{\hat{\sigma}}}} : \underline{\underline{\dot{\hat{\sigma}}}} + \frac{\partial f}{\partial \underline{\underline{\hat{X}}}} : \underline{\underline{\dot{\hat{X}}}} = (\underline{\underline{\hat{\sigma}}} - \underline{\underline{\hat{X}}}) : \underline{\underline{\dot{\hat{\sigma}}}} - (\underline{\underline{\hat{\sigma}}} - \underline{\underline{\hat{X}}}) : \underline{\underline{\dot{\hat{X}}}} = 0. \quad (2.56)$$

According to Prager, the evolution of the back stress tensor is linear with the plastic strain tensor. This means that the yield locus moves in the normal direction to the yield locus at the current stress point:

$$\underline{\underline{\dot{X}}} = C \underline{\underline{\dot{\epsilon}^p}} \quad (2.57)$$

where C is the kinematic modulus.

For the evolution of the deviatoric stress, one differentiates Equation (2.52) and uses the normal condition (2.43):

$$\underline{\underline{\dot{\hat{\sigma}}}} = 2G \left( \underline{\underline{\dot{\epsilon}}} - \dot{\lambda} \frac{\partial f}{\partial \underline{\underline{\hat{\sigma}}}} \right) = 2G \left( \underline{\underline{\dot{\epsilon}}} - \dot{\lambda} (\underline{\underline{\hat{\sigma}}} - \underline{\underline{\hat{X}}}) \right) \quad (2.58)$$

Using the relationship (2.56) and (2.58) makes it possible to obtain the derivative of  $\lambda$  as

$$\dot{\lambda} = \frac{2G}{(2G + C)} \frac{(\underline{\underline{\hat{\sigma}}} - \underline{\underline{\hat{X}}}) : \underline{\underline{\dot{\epsilon}}}}{(\underline{\underline{\hat{\sigma}}} - \underline{\underline{\hat{X}}}) : (\underline{\underline{\hat{\sigma}}} - \underline{\underline{\hat{X}}})}. \quad (2.59)$$

### ***The mixed hardening model***

In general, metals present both isotropic and kinematic hardening. As a result, the yield locus can grow and move; therefore, the yield locus is defined by:

$$f = \frac{1}{2} (\underline{\underline{\hat{\sigma}}} - \underline{\underline{\hat{X}}}) : (\underline{\underline{\hat{\sigma}}} - \underline{\underline{\hat{X}}}) - k^2 = 0. \quad (2.60)$$

This hardening phenomenon can be modeled by a mixed law with the isotropic and kinematic hardening models. If we choose the following hardening functions,

$$\begin{aligned} \underline{\underline{\dot{X}}} &= m C \underline{\underline{\dot{\epsilon}^p}} \\ k &= \sigma_y + \int (1 - m) E^p d\epsilon_{eq}^p \end{aligned} \quad (2.61)$$

where m is the mixing parameter. It is equal to:

$$m = \begin{cases} 0 & \text{isotropic hardening} \\ 1 & \text{kinematic hardening.} \\ ]0; 1[ & \text{mixed hardening} \end{cases} \quad (2.62)$$

The consistency condition (2.44) becomes

$$df = \frac{\partial f}{\partial \underline{\underline{\hat{\sigma}}}} : \overset{\nabla}{\underline{\underline{\hat{\sigma}}}} + \frac{\partial f}{\partial \underline{\underline{\hat{X}}}} : \dot{\underline{\underline{\hat{X}}}} + \frac{\partial f}{\partial k} \dot{k} = 0. \quad (2.63)$$

As previously, the derivative of the multiplier,  $\dot{\lambda}$ , is

$$\dot{\lambda} = \frac{2G}{\left(2G + mC + \frac{2}{3}(1-m)E^p\right)} \frac{(\underline{\underline{\hat{\sigma}}} - \underline{\underline{\hat{X}}}) : \dot{\underline{\underline{\hat{\sigma}}}}}{(\underline{\underline{\hat{\sigma}}} - \underline{\underline{\hat{X}}}) : (\underline{\underline{\hat{\sigma}}} - \underline{\underline{\hat{X}}})}. \quad (2.64)$$

### ***The integration of the constitutive law: The radial return method***

There are different methods to perform the integration of the constitutive elastoplastic law. Let the current balanced state A pass to a state B during one time step,  $\Delta t$ . The total strain,  $\underline{\underline{\epsilon}}_B$ , is known. Jaumann's derivative follows Hooke's law:

$$\overset{\nabla}{\underline{\underline{\sigma}}}_B = \underline{\underline{C}}_B^e \dot{\underline{\underline{\epsilon}}}_B^e = \underline{\underline{C}}_B^e (\dot{\underline{\underline{\epsilon}}}_B - \dot{\underline{\underline{\epsilon}}}_B^p) \quad (2.65)$$

where  $(C_{ijkl}^e)$  correspond to the fourth-order tensor to the Hooke's law (see (2.37)).

The stress rate is computed by the Jaumann's correction:

$$\overset{\nabla}{\underline{\underline{\sigma}}}_B = \overset{\nabla}{\underline{\underline{\sigma}}}_B + \underline{\underline{\Omega}}_A \underline{\underline{\sigma}}_B - \underline{\underline{\sigma}}_A \underline{\underline{\Omega}}_A = \left[ \underline{\underline{C}}_B^e \dot{\underline{\underline{\epsilon}}}_B + \underline{\underline{\Omega}}_A \underline{\underline{\sigma}}_B - \underline{\underline{\sigma}}_A \underline{\underline{\Omega}}_A \right] - \left[ \underline{\underline{C}}_B^p \dot{\underline{\underline{\epsilon}}}_B^p \right] \quad (2.66)$$

The strain can be:

- permanently elastic,
- elastic and then elastoplastic,
- permanently elastoplastic.

The first term in Equation (2.66) corresponds to an elastic case and the second corresponds to "plastic corrective stress". To begin the integration, one computes only the first term by assuming the plastic strain rate is null; therefore, a trial stress called  $\underline{\underline{\sigma}}_{B0}$  is computed. At the initial state, when no hardening has occurred, the trial stress is computed by

$$\left\{ \begin{array}{l} \dot{\underline{\underline{\epsilon}}}_{B0}^e = \dot{\underline{\underline{\epsilon}}}_B ; \dot{\underline{\underline{\epsilon}}}_{B0}^p = 0 ; \dot{\underline{\underline{X}}}_{B0} = 0 ; \dot{k}_{B0} = 0 \\ \overset{\nabla}{\underline{\underline{\sigma}}}_{B0} = \underline{\underline{C}}_{B0}^e \dot{\underline{\underline{\epsilon}}}_{B0}^e \\ \overset{\nabla}{\underline{\underline{\sigma}}}_{B0} = \overset{\nabla}{\underline{\underline{\sigma}}}_{B0} + \underline{\underline{\Omega}}_A \underline{\underline{\sigma}}_{B0} - \underline{\underline{\sigma}}_{B0} \underline{\underline{\Omega}}_A \\ \underline{\underline{\sigma}}_{B0} = \underline{\underline{\sigma}}_A + \overset{\nabla}{\underline{\underline{\sigma}}}_{B0} \Delta t \end{array} \right. \quad (2.67)$$

Afterwards, the consistency condition (Equation (2.44)) is checked:

- if  $f(\underline{\underline{\sigma}}_{B0}, \underline{\underline{X}}_{B0}, k_{B0}) \leq 0$ , the strain is purely elastic, therefore the trial stress is the updated stress and the problem is solved.
- if  $f(\underline{\underline{\sigma}}_{B0}, \underline{\underline{X}}_{B0}, k_{B0}) > 0$  the strain is elastoplastic, so a correction must be applied.

Now it is necessary to examine, if one part of the strain is elastic or not. A point C is identified by solving the following equation:

$$\begin{cases} f(\underline{\underline{\sigma}}_C, \mathbf{X}_A, k_A) = 0 \\ \underline{\underline{\sigma}}_C = \underline{\underline{\sigma}}_A + \beta \dot{\underline{\underline{\sigma}}}_{B0} \Delta t \end{cases} \quad (2.68)$$

If  $\beta=0$ , this corresponds to the case where A is on point C and no strain component is purely elastic. Otherwise,  $0 < \beta \leq 1$ .

Regarding the second term of Equation (2.66), the total strain is assumed to be null and the plastic strain rate is computed by

$$\dot{\underline{\underline{\epsilon}}}_{B}^p = \dot{\lambda} \frac{\partial f}{\partial \underline{\underline{\sigma}}} = \dot{\lambda} \underline{\underline{n}} \quad (2.69)$$

where  $\underline{\underline{n}}$  is the normal to the yield locus. The most famous methods (see Figure 2-11) compute the normal by:

$$\underline{\underline{n}} = (1 - \theta) \left( \frac{\partial f}{\partial \underline{\underline{\sigma}}} \right)_C + \theta \left( \frac{\partial f}{\partial \underline{\underline{\sigma}}} \right)_B. \quad (2.70)$$

If  $\theta = 0$ , the method is explicit, also called the forward Euler algorithm, which is numerically and conditionally stable. In this case, the time step must be small and, if not, other techniques must be used to reduce introduced error.

If  $0.5 \leq \theta \leq 1$ , the method becomes unconditionally stable. The case  $\theta = 0.5$  is the mid-point rule, which is often used for different constitutive laws in Lagamine.

If  $\theta = 1$ , the method is implicit and also called the backward Euler algorithm, or radial return method. In this case, point C is useless. This method is stable, accurate and has a good convergence rate of the global equilibrium iteration, which is why this method is used in this study.

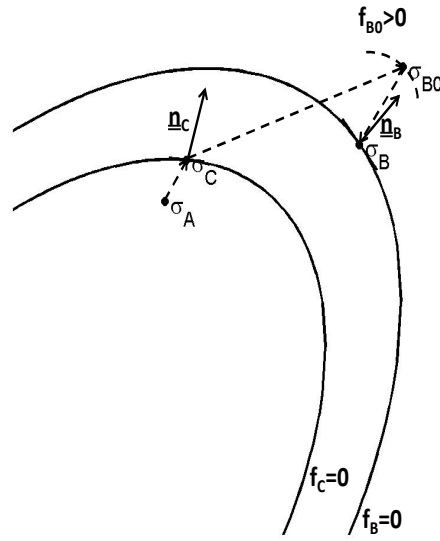


Figure 2-11: Geometric interpretation of the generalized algorithm for stress updating

For Equations (2.69) and (2.70) in the case of the radial return method, the algorithm used is the tangent cutting plane. In this algorithm, the trial stress is returned to the yield surface in successive iterations (see Figure 2-12). At each iteration, the yield locus is linearized around the current value of the stresses and state variables.

$$f_{i+1} = f_i + \left( \frac{\partial f}{\partial \underline{\hat{\sigma}}} \right)_i : \Delta \underline{\hat{\sigma}}_i + \left( \frac{\partial f}{\partial \underline{\hat{X}}} \right)_i : \Delta \underline{\hat{X}}_i + \left( \frac{\partial f}{\partial k} \right)_i \Delta k_i = 0 \quad (2.71)$$

Therefore, the value of  $\Delta \lambda_i$  can be computed without considering any modification of the total strain at each iteration.

$$\Delta \lambda_i = \frac{f_i}{\left( 2G + mC + \frac{2}{3}(1-m)E^p \right) \left( \underline{\hat{\sigma}}_{\underline{\hat{B}i}} - \underline{\hat{X}}_{\underline{\hat{B}i}} \right) : \left( \underline{\hat{\sigma}}_{\underline{\hat{B}i}} - \underline{\hat{X}}_{\underline{\hat{B}i}} \right)} \quad (2.72)$$

Thus, one can compute other variables for this iteration:

$$\begin{cases} \dot{\underline{\hat{\sigma}}}_{\underline{\hat{B}i}}^p = \Delta \lambda_i \left( \underline{\hat{\sigma}}_{\underline{\hat{B}i}} - \underline{\hat{X}}_{\underline{\hat{B}i}} \right) \\ \Delta \underline{\hat{\sigma}}_i = -2G \dot{\underline{\hat{\sigma}}}_{\underline{\hat{B}i}}^p \\ \dot{\underline{\hat{X}}}_i = Cm \dot{\underline{\hat{\sigma}}}_{\underline{\hat{B}i}}^p \\ \dot{k}_i = E^p (1-m) \dot{\underline{\hat{\sigma}}}_{\underline{\hat{B}i}}^p \end{cases} \quad (2.73)$$

Finally, the update for the stress tensor and the state variables at this iteration are



The input of the ARB law is made up the points of the stress-strain curve in the plastic components. The first point must correspond to the yield stress and gives Young's modulus by the ratio of the yield stress to the yield strain. The Lagamine preprocessor computes the tangent modulus,  $E^T$ , for all other points.

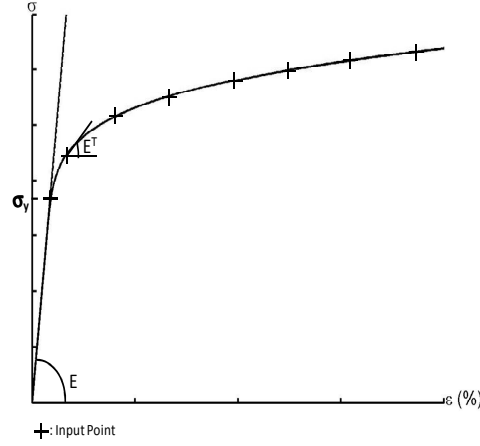


Figure 2-13: Input points in the ARB law

### 2.5.3.3 Link between the kinematic modulus and the plastic modulus

To compute the modulus  $C$  defined by (2.57), the ARB law [CES97] assumes that the projection of  $d\underline{\underline{\sigma}}$  on the normal of the yield locus is equal to the projection of  $d\underline{\underline{X}}$  which means

$$\frac{\partial f}{\partial \underline{\underline{\sigma}}} : d\underline{\underline{\sigma}} = \frac{\partial f}{\partial \underline{\underline{X}}} : d\underline{\underline{X}} \quad (2.78)$$

With the normal condition (2.43) and Prager's law (2.57) this equation can be modified to become:

$$d\underline{\underline{\varepsilon}}^p : d\underline{\underline{\sigma}} = C d\underline{\underline{\varepsilon}}^p : d\underline{\underline{\varepsilon}}^p = \frac{3}{2} C d\underline{\underline{\varepsilon}}_{eq}^p. \quad (2.79)$$

The product  $d\underline{\underline{\varepsilon}}^p : d\underline{\underline{\sigma}}$  corresponds to the plastic energy, which is equivalent to

$$d\underline{\underline{\varepsilon}}^p : d\underline{\underline{\sigma}} = d\underline{\underline{\varepsilon}}_{eq}^p d\underline{\underline{\sigma}}_{eq}. \quad (2.80)$$

Finally, the two last equations are used to determine the kinematic modulus, which is linearly dependent on the plastic modulus,  $E^p$ :

$$C = \frac{2}{3} \frac{d\underline{\underline{\sigma}}_{eq}}{d\underline{\underline{\varepsilon}}_{eq}^p} = \frac{2}{3} E^p. \quad (2.81)$$

### 2.5.3.4 Computation of the tangent matrix

The tangent matrix is simply computed by a perturbation in each direction.

## 2.5.4 Identification of the parameters

### 2.5.4.1 The tensile test presentations

Samples were taken from the beams, the columns and the welding (see Figure 2-14). The round bar tensile specimens were extracted from Section F located at the  $1/6$  of the flange's width and from the core positions of the column and beam. All weld round bar tensile specimens were machined from the cap and root positions of the beam-to-columns welds. Corus performed the tensile tests on the specimens from the BM, while ISQ performed them from the WM. They plotted the engineering stress as a function of the engineering strain.

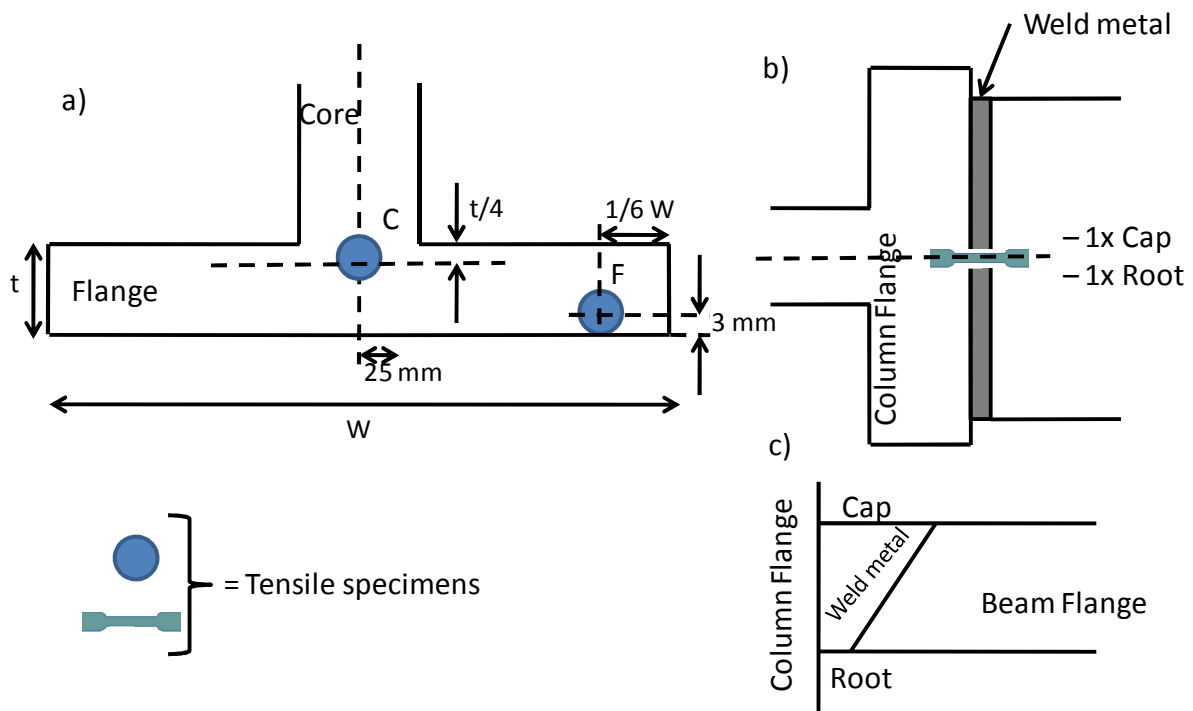


Figure 2-14: Position of the samples in the beam-to-column connection

The plots in Figure 2-15 and Figure 2-16 show that the behavior between the BM in the beam or in the column is equivalent. However the yield stress is different in the flange or in the core position. Therefore, three sets of ARB parameters have been identified for:

- the core position,
- the flange position,
- the weld position.

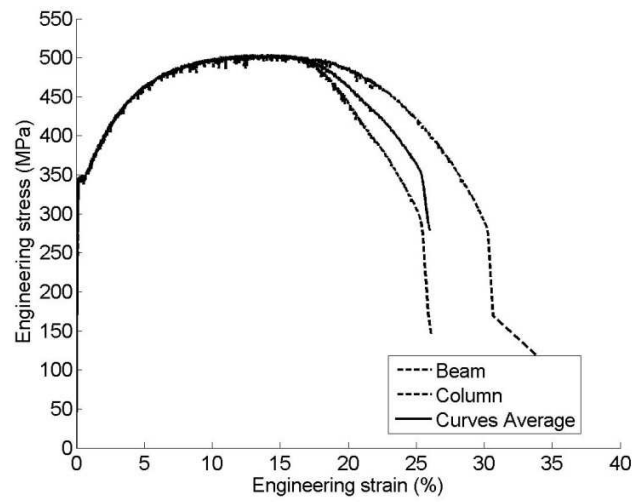


Figure 2-15: Experimental tensile test plot for BM for core positions

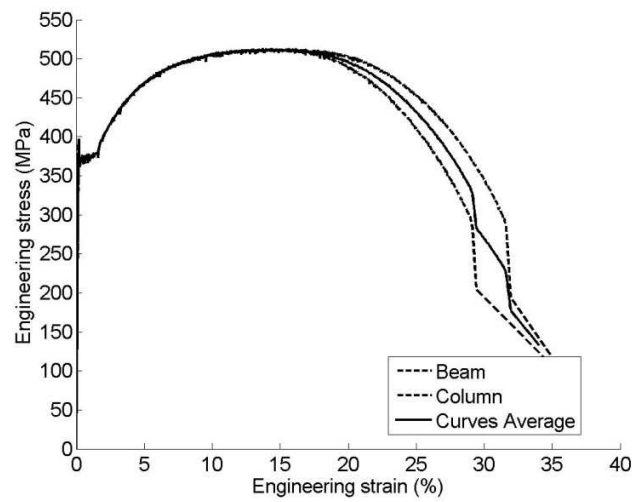


Figure 2-16: Experimental tensile test plot for BM at flange positions



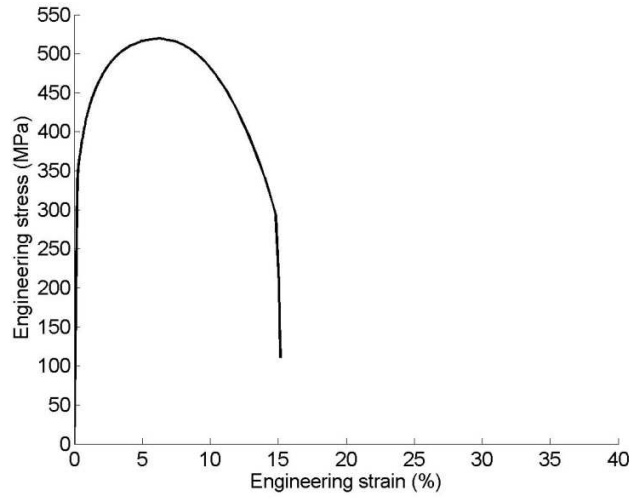


Figure 2-17: Experimental tensile test plot for WM

#### 2.5.4.2 Treatment of the experimental results

Firstly, for each position, the different experimental curves were averaged to obtain a single plot. Then the true stress and strain,  $\sigma$  and  $\epsilon$ , were obtained from the engineering stress and strain,  $\sigma_{\text{eng}}$  and  $\epsilon_{\text{eng}}$ , by the following equations:

$$\begin{cases} \epsilon_i = \ln(1 + \epsilon_{\text{eng}}) \\ \sigma = \sigma_{\text{eng}}(1 + \epsilon_{\text{eng}}) \end{cases} \quad (2.82)$$

Young's modulus of the experiment,  $E_i$ , was identified by the slope of the stress-strain plot in the linear component. However, the linearization shows that the stresses are not null when the strains are null.

$$\sigma = \epsilon_i E_i + \sigma_0 \quad (2.83)$$

where  $\epsilon_i$  is the initial strain and  $\sigma_0$  the value of the stress when  $\epsilon_i$  is null.

The problem likely came from the elastic strain of the tool. Thus, the strains are corrected to avoid this error.

$$\epsilon_{\text{mes}} = \epsilon_i + \frac{\sigma_0}{E_i} \quad (2.84)$$

Conventionally, the yield stress is the stress when the plastic strain is equal to 0.2%. The method used to identify the yield stress is illustrated in Figure 2-18.

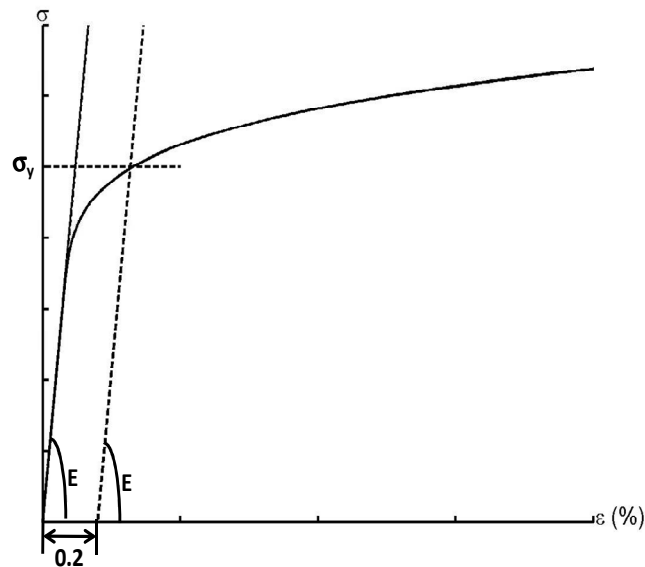


Figure 2-18: Identification of the yield stress

Finally, Young's modulus,  $E_i$ , measured experimentally was exceptionally low (about 118 GPa) due to the well known difficulty to accurately measure the low elastic strain. Thus the curves were modified by computing the elastic strain at each point and considering the Young's modulus,  $E$ , equal to 205 GPa as the usual value for this steel grade.

$$\varepsilon = \varepsilon^e + \varepsilon^p \text{ where } \begin{cases} \varepsilon^p = \varepsilon_{\text{mes}} - \frac{\sigma}{E_i} \\ \varepsilon^e = \frac{\sigma}{E} \end{cases} \quad (2.85)$$

As no experimental curve have successfully quantified a Bauschinger effect, the material was assumed to have isotropic hardening and the value of  $m$  was fixed to 0.

For all materials, Hooke's law parameters are listed in Table 2-1.

Table 2-1: Elastic parameters

E (GPa)	$\nu$
205	0.3

The results of the analysis of the tensile test data are given in Table 2-2 to Table 2-4 and in Figure 2-19 to Figure 2-21.

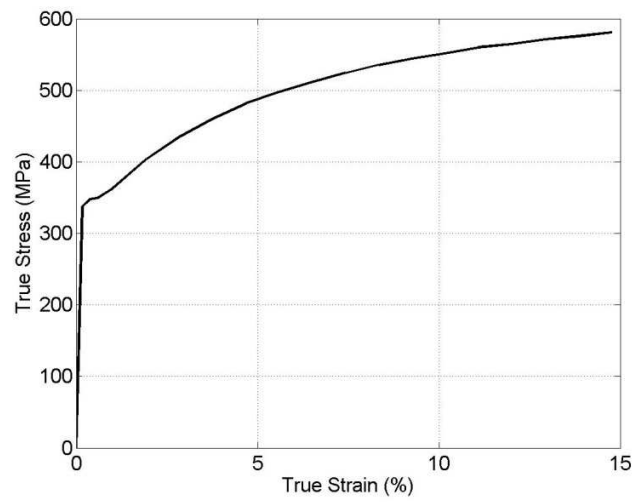


**Figure 2-19: Tensile plot for BM in the core position**

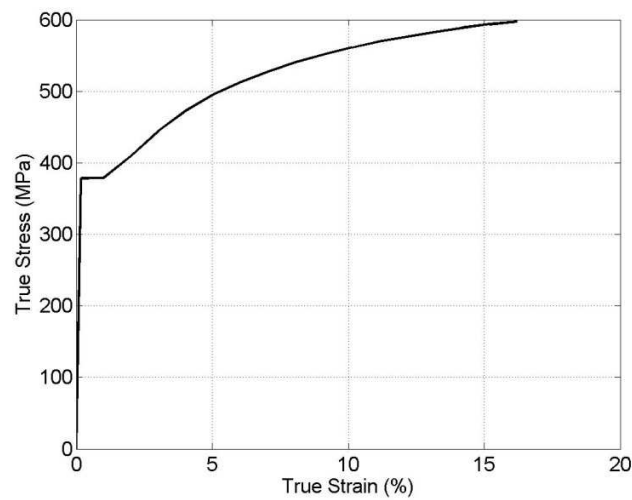


**Figure 2-20: Tensile plot for BM in the flange position**

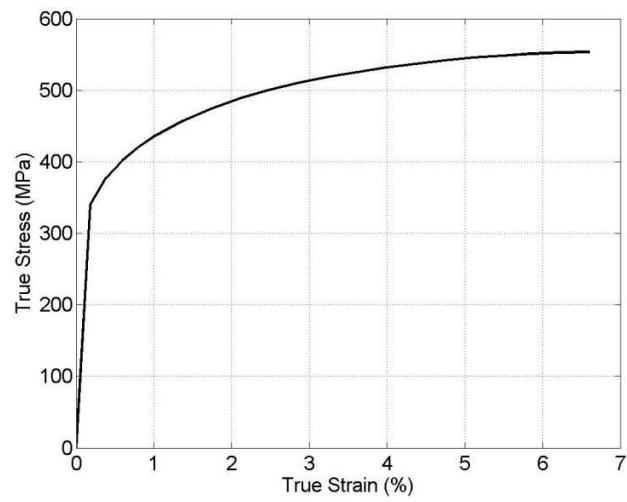


**Figure 2-21: Tensile plot for WM**

**Table 2-2: Values for tensile properties for BM in the core position**

$\epsilon$ (%)	$\sigma$ (MPa)
0.17	337
0.38	348
0.58	349
0.79	356
1.00	362
1.92	403
2.84	434
3.75	460
4.67	481
5.59	497
6.51	511
7.42	524
8.34	536
9.26	544
10.18	551
11.09	560
12.01	565
12.93	571
13.85	576
14.76	581

**Table 2-3: Values for tensile properties for BM in flange position**

$\varepsilon$ (%)	$\sigma$ (MPa)
0.18	379
0.39	379
0.59	379
0.80	379
1.00	379
2.01	410
3.03	445
4.04	473
5.05	496
6.07	513
7.08	528
8.10	541
9.11	551
10.12	561
11.14	570
12.15	576
13.16	583
14.18	589
15.19	594
16.21	597

**Table 2-4: Values for tensile properties for WM in the flange position**

$\epsilon$ (%)	$\sigma$ (MPa)
0.18	340
0.39	378
0.59	402
0.80	420
1.00	435
1.37	457
1.75	475
2.12	489
2.49	501
2.87	511
3.24	519
3.62	526
3.99	532
4.36	537
4.74	542
5.11	546
5.48	548
5.86	551
6.23	553
6.61	554

## 2.6 Conclusion

This chapter recalled general mechanical methods used in finite element codes. No original developments were made here, but as these tools will be used in the thesis, they were worth being discussed. The only contribution from the author here is the identification of material parameters based on experiments performed by Corus and ISQ, as well as a clear description of the available ARB law coupled with kinematic hardening. The extension to the thermo-mechanical 3D ARB law was implemented by the author and will be used in Chapter 5.

# **Chapter 3**

# **Fatigue Damage**

# **modeling**



### 3.1 Introduction

The beam-to-column connection studied was submitted to cyclic loading, which generates fatigue damage. This damage has an impact on the fracture strength of the structure. Therefore, it is important to compute it. The fatigue phenomenon has been studied for many years, and well-known works such as the experiments and the first analytical models of Kachanov [KAC86], Wöhler [WOH55], Palmgren-Miner [PAL24; MIN45], are still the basis of current research and fatigue design rules. In this chapter, the concept of damage is first defined. Then the two classic methods of fatigue crack prediction are outlined. The model chosen is the fatigue continuum damage mechanics of Lemaitre and Chaboche [LEM96] with the Sines' multiaxial criterion. This chapter presents the method used to identify the parameters of this model and its implementation in the finite element code Lagamine.

### 3.2 Introduction to the concept of fatigue damage

If one observes a representative volume element in a damaged structure, it will contain some micro-cracks or voids; therefore, the effective area,  $\tilde{S}$ , is inferior to the global area,  $S$ . The damaged area,  $S_D$ , which represents the sum of the micro-cracks or void area, is equal to the difference between  $\tilde{S}$  and  $S$ . A damage variable,  $D$ , represents the density of material discontinuity due to the damage. It is defined as the ratio of the damaged area,  $S_D$ , over the global area,  $S$ .

$$D = \frac{S_D}{S} = \frac{S - \tilde{S}}{S} \quad (3.1)$$

When  $D=0$ , the material is sound and when  $D=1$ , the material is fully cracked.

This damage variable is considered isotropic which means that it affects all components of any stress or strain tensor in all directions in the same manner. However, the micro-cracks tend to follow privileged direction (in metal, the direction orthogonal to the maximum principal stress's direction); therefore, the damage's actual effect is anisotropic. As anisotropic modeling can become overly complex, this thesis focused on isotropic modeling to provide the engineer solution with a according to the project's objectives.

Due to the damage's behavior, the stress state is modified. Indeed, in one dimension if the force,  $F$ , is applied to a area,  $S$ , of a representative volume element, the classic stress is

$$\sigma = \frac{F}{S}. \quad (3.2)$$

Due to the damage, the effective surface becomes

$$\tilde{S} = S(1 - D). \quad (3.3)$$

Therefore, the effective stress is defined by:

$$\tilde{\sigma} = \frac{F}{\tilde{S}} = \frac{\sigma}{(1 - D)}. \quad (3.4)$$

If one assumes that the strain is not affected by the damage, then the elastic strain is:



$$\varepsilon_e = \frac{\tilde{\sigma}}{E} = \frac{\sigma}{(1-D)E}. \quad (3.5)$$

Thus, the stiffness of the structure drops. In this study, it was preferred to keep the damage uncoupled with the stress because the drop in stiffness can cause numerical problems in finite element analyses due to singularities in the stiffness matrix. In this chapter, the stress is thus defined by (3.2).

The fatigue damage,  $D_f$ , represents the generation of micro-cracks in a structure which is under the influence of loading cycles, up to the initiation of a macroscopic crack. There are two domains in fatigue analysis:

- High-Cycle Fatigue (HCF): a high number of cycles occurs before fracture (>50 000 cycles), and the strains stay in elastic domain.
- Low-Cycle Fatigue (LCF): a low number of cycles occurs before fracture (<50 000 cycles) under plastic strains.

Each of these cycles is defined by the following mechanical quantities (see Figure 3-1):

- amplitude of stress or strain,  $\Delta\sigma$  or  $\Delta\varepsilon$ ,
- mean stress or strain,  $\sigma_m$  or  $\varepsilon_m$ ,
- ratio between the minimum stress or strain,  $\sigma_{\min}$  or  $\varepsilon_{\min}$ , and the maximum stress or strain,  $\sigma_{\max}$  or  $\varepsilon_{\max}$ , usually called R.

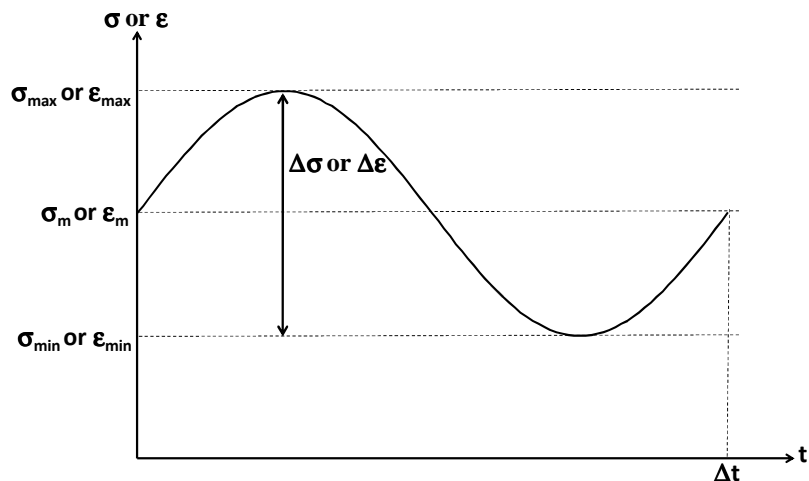


Figure 3-1: Description of the stress or strain cycle as a function of time

Microscopic models do exist, but they require many parameters, and in coupled approaches, they generate a softening law. The damage predicted often depends on the mesh size [HAB01]. This thesis introduces two models: Manson Coffin's model and the Continuum Damage Model.

### 3.3 Manson-Coffin's Model

#### 3.3.1 Model origins and evolution

This model has experimental origins. In the LCF domain, the yielding strain amplitude has a predominant effect on fatigue rupture, whereas in the HCF domain, the stress amplitude is predominant. To model this, Manson [MAN53] and Coffin [COF53] proposed the following law:

$$\frac{\Delta\varepsilon}{2} = \frac{\sigma_f}{E} (2N_f)^b + \varepsilon_f (2N_f)^c \quad (3.6)$$

where  $\Delta\varepsilon$  is the difference between the maximum and the minimum strain (see Figure 3-1) of the deformation,  $N_f$  is the number of cycles before crack,  $\sigma_f$ ,  $\varepsilon_f$ ,  $b$  and  $c$  are characteristic constants of the material and  $E$  is Young's modulus.

Morrow [MOR687] suggested that the effect of the mean stress,  $\sigma_m$ , could be considered by reducing the elastic term in the strain life equation by the mean stress:

$$\frac{\Delta\varepsilon}{2} = \frac{\sigma_f - \sigma_m}{E} (2N_f)^b + \varepsilon_f (2N_f)^c. \quad (3.7)$$

Manson and Halford [MAN81] modified both elastic and plastic terms of the strain life's equation to keep the elasto-plastic strain ratio independent from mean stress:

$$\frac{\Delta\varepsilon}{2} = \frac{\sigma_f - \sigma_m}{E} (2N_f)^b + \varepsilon_f \left( \frac{\sigma_f - \sigma_m}{\sigma_f} \right) (2N_f)^c. \quad (3.8)$$

In another work, Smith, Watson and Topper [SMI70] proposed an energetic form to represent the mean stress effect:

$$\sigma_{\max} \frac{\Delta\varepsilon}{2} = \frac{\sigma_f^2}{E} (2N_f)^b + \sigma_f \varepsilon_f (2N_f)^c \quad \text{where } \sigma_{\max} = \frac{1}{2} \Delta\sigma + \sigma_m. \quad (3.9)$$

#### 3.3.2 Palmgren-Miner's Rules

The previous model enables one to determine the life of the structure under constant loading amplitude. In the case of amplitude variation, it is necessary to use Palmgren-Miner's rule [CHE98], which is a linear additive rule used to compute damage evolution.

At different levels of the strain amplitude rate,  $\Delta\varepsilon_i$ , the damage accumulation is defined as:

$$D_f = \sum_i \frac{N_i(\Delta\varepsilon_i)}{N_{fi}(\Delta\varepsilon_i)} \quad (3.10)$$

where  $N_i$  is the number of cycles in the rate  $\Delta\varepsilon_i$  and  $N_{fi}$  is number of cycles before rupture in the rate,  $\Delta\varepsilon_i$ . The crack appears when  $D_f$  is greater than 1. This rule has been validated for elastic and HCF states but it has been observed experimentally that the rupture can initiate before  $D_f$  reaches 1 in the LCF case. Moreover, the variation in the amplitude must not be too significant [LEM96].

The Zhang's paper [ZAH09] presents the uses and the limitations of the Palmgren-Miner's rule in evaluating the damage in welded joints under variable amplitude.

### 3.3.3 Procedure to assess lifetime with a finite element code

The assessment procedure proposed by Teng et al. [TEN04] is shown in Figure 3-2. In the first step, finite element analyses determine the stress and strain in the structure. Then, in the second step, where the principal stress and strain are maximum, the stress and strain amplitudes are analyzed as a function of time. Equation (3.9) gives  $N_{fi}$  for each rate of different local amplitudes. Finally, with Palmgren-Miner rule, the lifetime of the structure can be determined.

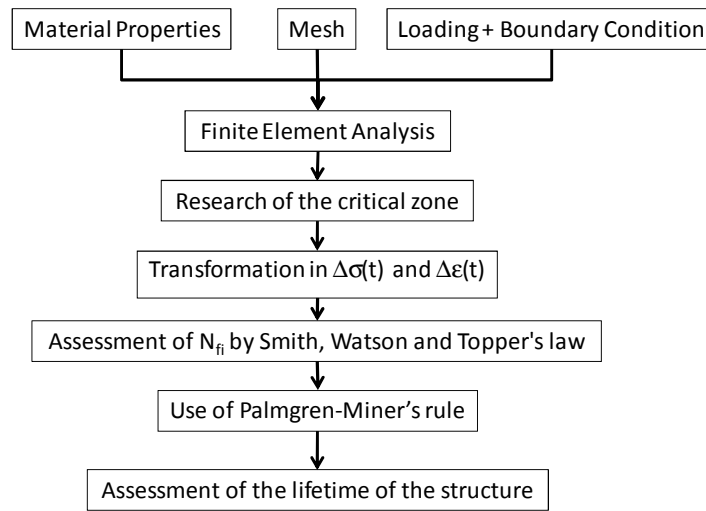


Figure 3-2: Flow chart of steps to assess the lifetime of a structure undergoing a cyclic loading [TEN04]

## 3.4 Multiaxial fatigue criteria

The previous laws neglect the fact that loading does not generate axial stress or strain but tensorial values. Still, the criterion of fatigue limit depends on the amplitude and the mean values per cycle. As experimentally observed, the mean shear does not affect the fatigue limit, as opposed to the mean tension. One defines:

- the second invariant of the amplitude of the deviator,  $\underline{\hat{\sigma}}$ , of the stress tensor:

$$A_{II} = \frac{1}{2} \sqrt{\frac{3}{2} (\hat{\sigma}_{ijmax} - \hat{\sigma}_{ijmin}) (\hat{\sigma}_{ijmax} - \hat{\sigma}_{ijmin})} \quad \text{where } \hat{\sigma}_{ij} = \sigma_{ij} - \sum_k \frac{1}{3} \sigma_{kk} \quad (3.11)$$

- the mean hydrostatic stress,  $\sigma_{Hm}$ :

$$\sigma_{Hm} = \frac{1}{3} \left[ \frac{1}{T} \int \text{Tr}(\underline{\underline{\sigma}}(t)) dt \right] \quad (3.12)$$

- the hydrostatic stress maximum,  $\sigma_{Hmax}$ :

$$\sigma_{Hmax} = \frac{1}{3} \max_t \text{Tr}(\underline{\underline{\sigma}}(t)) \quad (3.13)$$

where  $\hat{\sigma}_{ijmax}$  and  $\hat{\sigma}_{ijmin}$  are the maximum and minimum components of the deviatoric stress respectively and T is the time period of the cycle.

The multiaxial fatigue criterion is defined by a damage yield locus, noted  $f_D$ , as in plasticity:

$$f_D = A_{II} - A_{II}^* \quad (3.14)$$

where  $A_{II}^*$  represents the fatigue limit. Therefore if the loading,  $A_{II}$ , is smaller than the threshold value, the structure does not undergo any damage. Different criteria exist:

- Sines' [SIN59] criterion:

$$A_{II}^* = \sigma_{10} (1 - 3b\sigma_{Hm}) \quad (3.15)$$

- Crossland's [CRO56] criterion:

$$A_{II}^* = \sigma_{10} \frac{1 - 3b\sigma_{Hmax}}{1 - b\sigma_{10}} \quad (3.16)$$

where  $\sigma_{10}$  is the maximum stress limit before the appearance of fatigue damage with null mean stress. An infinite number of cycles characterized by  $\sigma_{10}$  can be applied without any fracture event. The difference in accuracy in between the two models depends on the material (see [PAP97]).

Dang Van [DAN93; LEH08] proposes another type of criterion which is based on the critical plane approach in the stress domain and uses a combination of the mesoscopic shear stress and mesoscopic hydrostatic stress applied to this critical plane. To use this criterion, the mesoscopic stress tensor must be computed:

$$\underline{\underline{\sigma}}^{meso}(t) = \underline{\underline{\sigma}}(t) + \text{dev}(\underline{\underline{\rho}}) \quad (3.17)$$

where t is the time and  $\underline{\underline{\rho}}$  represents the residual stress tensor. The latter is equal to the radius of the circle,  $\mathcal{C}$ , which contains the loading path during the cycle of the stress components. Its center defines the mean stress component. Therefore, the residual stress tensor is equal to the difference between the two extreme loading solutions see Figure 3-3:

$$\rho_{ij} = \frac{1}{2} \max_{t_n, t_m} (\sigma_{ij}(t_n) - \sigma_{ij}(t_m)). \quad (3.18)$$

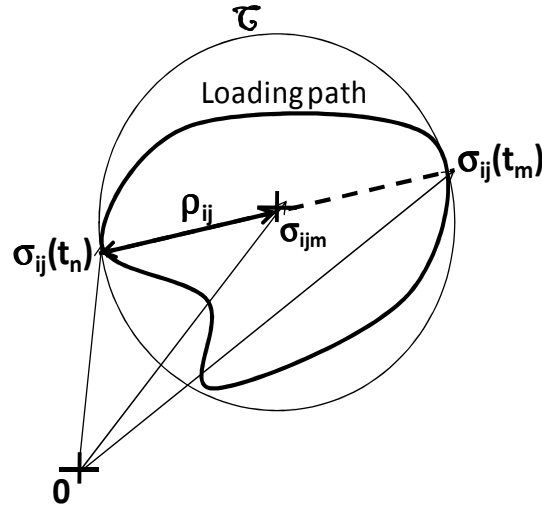


Figure 3-3: Description of the computation of the residual stress tensor

The shear stress amplitude,  $\tau_a$ , to be used in Dang Van's criterion is found by computing the mesoscopic principal stresses,  $\sigma_I^{\text{meso}}$ ,  $\sigma_{II}^{\text{meso}}$ ,  $\sigma_{III}^{\text{meso}}$  (where  $\sigma_I^{\text{meso}} > \sigma_{II}^{\text{meso}} > \sigma_{III}^{\text{meso}}$ ):

$$\tau_a(t) = \frac{\sigma_I^{\text{meso}}(t) - \sigma_{III}^{\text{meso}}(t)}{2}. \quad (3.19)$$

Finally, Dang Van's criterion is:

$$f_D = \max_t (\tau_a(t) - a_H \sigma_H^{\text{meso}}(t)) - \tau_{af} \quad (3.20)$$

where  $\sigma_H^{\text{meso}}(t)$  is the mesoscopic hydrostatic stress, and  $a_H$  and  $\tau_{af}$  are material parameters.

## 3.5 Fatigue Continuum damage model (CDM)

### 3.5.1 One-dimensional fatigue CDM description

For uniaxial loading, Lemaître and Chaboche [LEM96] stated that the evolution law for the fatigue damage variable during one cycle is the following:

$$\left\{ \begin{array}{l} \frac{\partial D_f}{\partial N} = \left[ 1 - (1 - D_f)^{\beta+1} \right]^\alpha \cdot \left[ \frac{\sigma_{\max} - \sigma_m}{M(1 - D_f)} \right]^\beta \\ \alpha = 1 - a \left\langle \frac{\sigma_{\max} - \sigma_l}{\sigma_u - \sigma_{\max}} \right\rangle \\ \sigma_l = \sigma_{l0} + (1 - b \sigma_{l0}) \sigma_m \\ M = M_0 (1 - b \sigma_m) \end{array} \right. \quad (3.21)$$

This evolution law depends on the maximum stress  $\sigma_{\max}$  and the mean stress  $\sigma_m$  as defined in Figure 3-1.  $\sigma_u$  is the ultimate tensile stress of the material.  $M_0$ ,  $b$ ,  $\alpha$  and  $\beta$  are other material

parameters. The symbol,  $\langle x \rangle$ , corresponds to the following definition: if  $x$  is negative then its value is null and if  $x$  is positive, then its value is  $x$ . The fatigue continuum damage model makes it possible to compute the non-linear evolution of the damage with different levels of loading amplitude [CHE98; BOG08; SHA09].

### 3.5.2 Description of multiaxial fatigue CDM

Lemaître and Chaboche [LEM96] proposed the following extension of their previous damage evolution law in three dimensions:

$$\frac{\partial D_f}{\partial N} = \begin{cases} 0 & \text{if } f_D < 0 \\ \left[ 1 - (1 - D_f)^{\beta+1} \right]^\alpha \left( \frac{\tilde{A}_{II}}{M} \right)^\beta & \text{if } f_D \geq 0 \end{cases} \quad (3.22)$$

$$\tilde{A}_{II} = \frac{A_{II}}{1 - D_f} ; M = M_0 (1 - 3b\sigma_{Hm}) ; \alpha = 1 - a \left\langle \frac{A_{II} - A_{II}^*}{\sigma_u - \sigma_{eqmax}} \right\rangle$$

where  $\sigma_{eqmax}$  is the maximum von Mises' stress per cycle.  $A_{II}$  has already been defined in (3.11).

## 3.6 Comparison between Manson-Coffin's law and CDM

Manson-Coffin's model is interesting because its material parameters are easy to determine and its approach is simple. However, this model does not represent the case where maximum principal stress components change direction because the model is uniaxial.

Palmgren-Miner's rule is only accurate for material, that has a linear damage evolution. Moreover, the variation in amplitude should not be too significant.

CDM does not have these drawbacks. It assesses a damage variable, which can be used in crack propagation analysis taking into account all components of the stress tensor. With regards to the multiaxial criterion, different models exist. Sines' criterion has been chosen due to its simplicity and the fact that the experiments performed are insufficient to identify a more sophisticated model such as Dang Van's.

Here, it will be defined how the Lemaître and Chaboche's model was identified from the data provided.

## 3.7 Identification of the fatigue damage parameters

### 3.7.1 Method used to identify the parameters

The parameters of CDM can be identified from the well-known Wöhler's curves. The Wöhler's curves define the evolution of the number of cycles before fracture,  $N_f$ , as a function of the value of the stress amplitude for a chosen fixed mean stress. They are obtained from one-dimensional fatigue tests. In the one-dimensional case, equation (3.21) gives the number of cycles before fracture as a function of the maximum and the mean stress by integrating from  $D_f=0$  to  $D_f=1$ .

$$N_f = \frac{1}{(\beta+1)(1-\alpha)} \left( \frac{\sigma_{\max} - \sigma_m}{M} \right)^{-\beta} \quad (3.23)$$

The CDM parameters can be identified by a least-square method in comparing the experimental Wöhler's curves and CDM curves.

### 3.7.2 Experimental data and Wöhler's curves

The experimental test was performed by ISQ. Some samples were taken of different locations of the connection to have BM and WM samples (see Figure 3-4). All BM samples were extracted from the column flange. Six samples were taken at 25 mm from the mid axis of the flange along the transverse position, called position K. Six other BM samples were taken at 1/6 of the flange's length, W, from the outer flange, called position L, along the longitudinal direction. The WM samples were taken near the mid axis of the column's flange. Three samples came from the weld cap and three from the weld root.

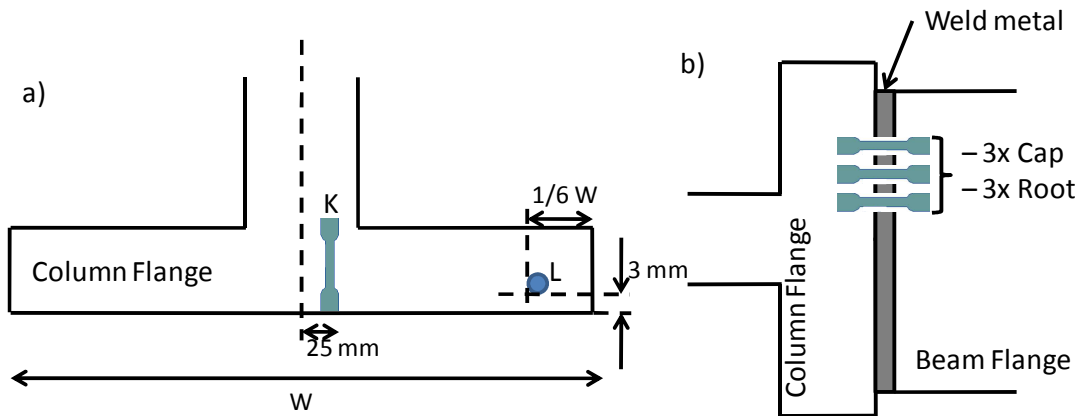


Figure 3-4: Position of the sample for the LCF test from a) the BM and b) the WM

Each sample was submitted to cyclic tensile tests at different levels of strain amplitude in the LCF range with a null strain average at imposed displacement. For the first hundred cycles, the strain and stress were recorded as a function of time. The evolution of the number of cycles before fracture,  $N_f$ , is a function of the value of the strain amplitude.

A first pre-treatment was performed to obtain the Wöhler's curves. During cyclic tensile loading, hardening proprieties varied. Indeed the level of the stress amplitude increased though the strain amplitude remained constant until stabilizing. This phenomenon is called cyclic hardening. After a number of cycles, the stress amplitude began to decrease. This phenomenon is due to the damage event which occurs and decreases the strength of the material, so the stress drops. Thus the value of the amplitude of stress was found from the value in the stabilized zone (see Figure 3-5).

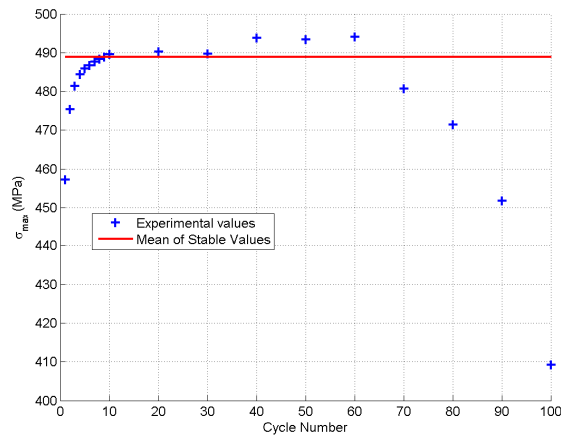


Figure 3-5: Evolution of the maximum stress per cycle due to imposed cyclic strain

### 3.7.3 Identification

The first step in identifying the CDM parameters was to smooth the experimental curves. Indeed the scattering of the experimental points require this step to help the least-square method to converge. An approximate model of a power law is used to smooth the experimental values.

In this identification method the author applied following approach:  $\sigma_u$  is obtained from the tensile test (see Chapter 2.5.4),  $b$  was chosen equal to the inverse of  $\sigma_u$ , and initial values for steel, found in Lemaître and Chaboche's book are used [LEM96]. Then, the parameters were modified manually to try to fit the provided curve and finally they were identified by Matlab optimizer, which uses the least-square method. The results are shown in Figure 3-6 to Figure 3-8 and Table 3-1 for the different materials.

With regards to the BM, the parameters found for K and L samples were closed; therefore, the isotropic model could be validated.



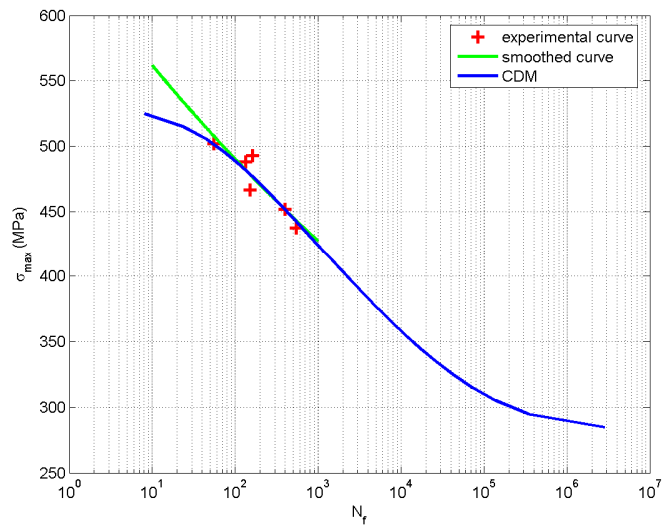


Figure 3-6: Wöhler's curve for the BM position K

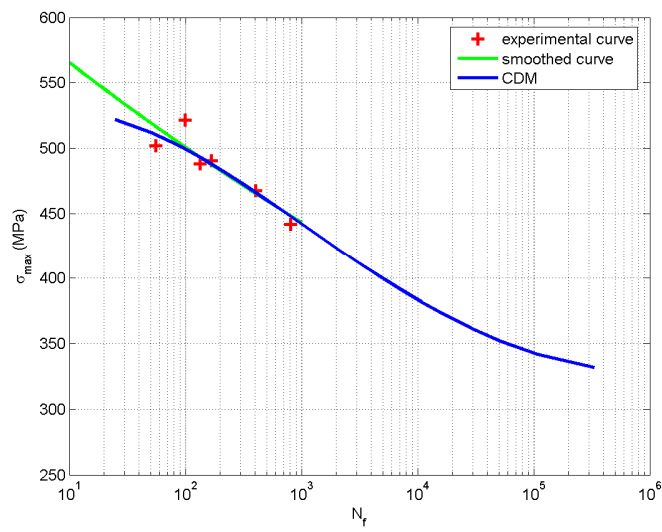


Figure 3-7: Wöhler's curve for the BM position L

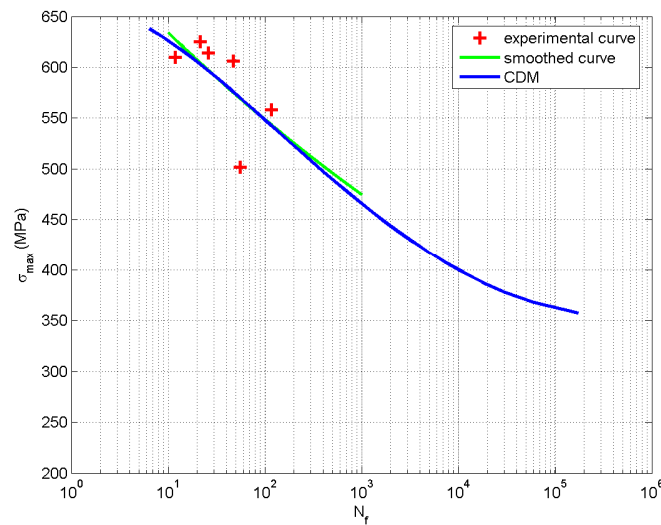


Figure 3-8: Wöhler's curve for the WM position

Table 3-1: Parameters of CDM for the different materials

	$\sigma_{10}$ (MPa)	$\sigma_u$ (MPa)	$\beta$	a	b (MPa)	$M_0$ (MPa)
BM Position K	275.5	530.7	7.054	0.9	0.001884	1568
BM Position L	252.8	528.1	7.803	0.9	0.001893	1542
WM	228.8	643.2	5.598	0.9	0.001555	2134

### 3.8 Implementation in the Lagamine code

The fatigue CDM model was implemented in the Lagamine code. A subroutine, called FATDAM, computes the following at the end of each cycle for each integration point:

- the maximum von Mises' stress,
- the mean of the hydrostatic stress,
- the maximum and minimum deviatoric stress components.

The time period of the cycle is an input parameter of this function. Therefore, the fatigue damage rate can be computed by equation (3.22) with Sines' criterion and the fatigue damage. Sines' criterion was chosen because primarily it is easy to program and the experiments performed were insufficient to compare its validity with other criteria.

The integration of equation (3.22) was performed numerically by the common fourth-order Runge–Kutta method. The damage variable was computed from the derivative by knowing the value from the previous iteration:

$$\begin{cases} \frac{\partial D}{\partial N} = f(N, D) \\ D_0 = D(N_0) \\ D_{n+1} = D_n + \frac{\Delta N}{6}(k_1 + 2k_2 + 2k_3 + k_4) \end{cases} \quad (3.24)$$

where

$$\begin{cases} k_1 = f(N_n + \Delta N, D_n) \\ k_2 = f(N_n + \frac{\Delta N}{2}, D_n + \frac{\Delta N}{2}k_1) \\ k_3 = f(N_n + \frac{\Delta N}{2}, D_n + \frac{\Delta N}{2}k_2) \\ k_4 = f(N_n + \Delta N, D_n + \Delta Nk_3) \end{cases} \quad (3.25)$$

and where  $\Delta N$  is a cyclic increment.

However as the slope of the damage evolution is infinite at the beginning for LCF, the method diverges for the computation of the first cycle. The solution for this divergence was to compute the first cycles analytically when the damage becomes significant with the following equation:

$$\begin{cases} N_f = \frac{1}{(1+\beta)(1-\alpha)} \left( \frac{A_{II}}{M} \right)^{-\beta} \\ D_{f1} = 1 - \left[ 1 - \left( \frac{1}{N_f} \right)^{\frac{1}{1-\alpha}} \right]^{\frac{1}{1-\beta}} \end{cases} \quad (3.26)$$

where  $\alpha$ ,  $M$   $A_{II}$  are computed according to equations (3.11) and (3.22).

### 3.9 Conclusion

The fatigue CDM was chosen because the model takes LCF and HCF levels into account and can compute the damage for non-linear cyclic amplitude. It was implemented in the Lagamine code for multiaxial analysis with Sines' criterion.

The parameters were identified by LCF tests driven by strain with a null average. Some tests should have been performed with different levels of averaged but were not done. The number of points was insufficient to validate the values of these parameters particularly at the HCF level. However, they make it possible to reproduce the available experimental results and their levels of magnitude were in keeping with values in [LEM96].



# **Chapter 4**

# **Crack propagation**

# **modeling**



## 4.1 Introduction to failure mechanics

Fracture mechanics describes the behavior of solids or structures which contain macroscopic geometric discontinuity. The fracture theory is used to predict the evolution of a macroscopic crack up to the complete rupture of the structure. Depending on the loading, three modes of fracture can be differentiated, as illustrated in Figure 4-1.

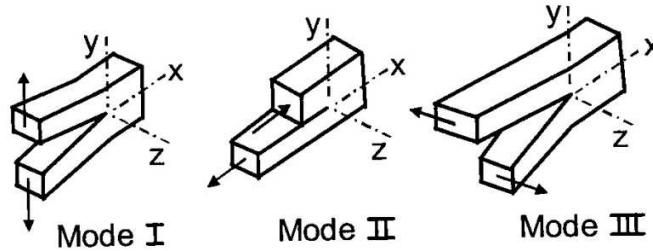


Figure 4-1: Fracture mode: mode I: opening mode; mode II: sliding mode; mode III: tearing mode (from [CHA96])

The analyses of crack propagation are usually carried out under several idealized conditions, as in the case of linear elastic fracture mechanics or a limited yielding state. In such a case, the details of the local crack tip field are uniquely characterized by a single macroscopic parameter for each mode: the stress intensity factor ( $K_{I,II,III}$ ) or the corresponding material energy release rate ( $G_{I,II,III}$ ) which determines the critical conditions of crack growth. The numeral I, II or III corresponds to the loading mode.

In practice, mode I is the most severe one. Typical stress-strain zones appear at the crack tip in a cracked specimen. For mode I, the stress and strain fields near the crack tip are defined by the stress intensity factor:

$$\underline{\underline{\sigma}} = \frac{K_I}{\sqrt{2\pi r}} \underline{\underline{\tilde{\sigma}}}(\theta) \quad \underline{\underline{\varepsilon}} = \frac{K_I}{\sqrt{2\pi r}} \underline{\underline{\tilde{\varepsilon}}}(\theta) \quad (4.1)$$

where  $r$  and  $\theta$  are the polar coordinates (see Figure 4-2) with  $r$  being the distance from the crack tip and  $\theta$  the angle relative to the crack plane;  $\underline{\underline{\tilde{\sigma}}}(\theta)$  and  $\underline{\underline{\tilde{\varepsilon}}}(\theta)$  are functions depending on the angle  $\theta$ . Similarly, the same expressions can be obtained for mode II and mode III.  $K_I$  is a function depending on the type of loading ( $\sigma_{22}^\infty$  for mode I) and on the half-length of the crack,  $a$ . For instance, the stress intensity factor according to Westergaard [LEM96] for a large sheet containing a small crack with a length of  $2a$  and tensile loading in a perpendicular direction is

$$K_I = \sigma_{22}^\infty \sqrt{\pi a}. \quad (4.2)$$

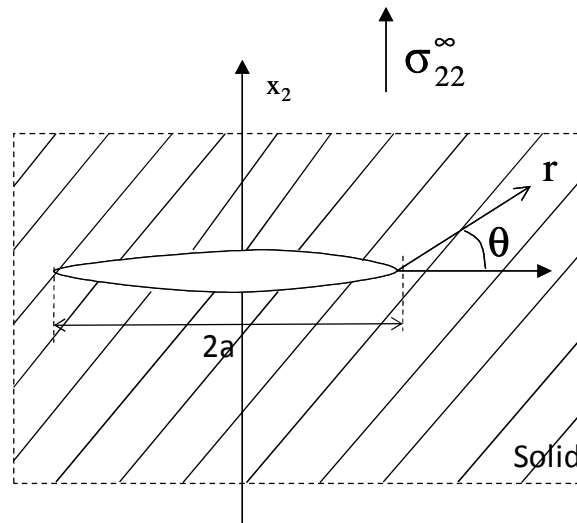


Figure 4-2: Mode I loaded crack

The stress intensity factor  $K_I$  depends on the geometry as well. Other relationships for different geometries are given in [LEM96].

This stress intensity factor is related to  $G$ , the energy released per unit of length of the extension of the crack front per unit thickness of the body, also called the crack extension force. For mode I, its definition is

$$G_I = \frac{K_I^2}{E} \quad (\text{plane stress}) \quad G_I = \frac{K_I^2(1-\nu^2)}{E} \quad (\text{plane strain}). \quad (4.3)$$

However the previous concepts, based on purely elastic theory, are not valid in the case of ductile fracture. Rice [RIC68] introduced an independent J-integral, better adapted to plastic cases, which characterizes the stress singularity near the crack tip:

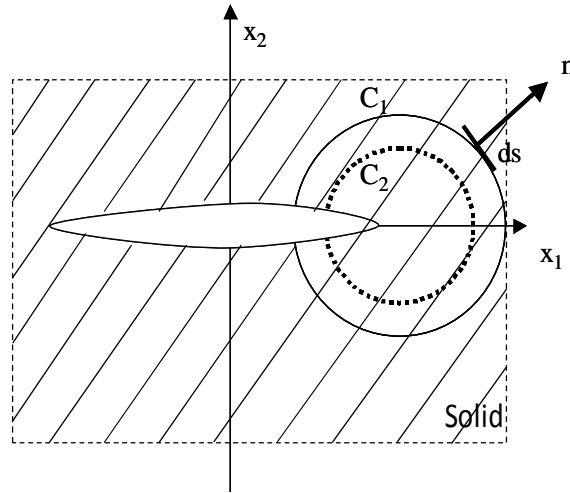


Figure 4-3: Integral contour

$$J = \int_C \left( w n_1 - \sigma_{ij} n_j \frac{\partial u_i}{\partial x_1} \right) ds ; w = \int_0^\varepsilon \sigma_{ij} d\varepsilon_{ij} \quad (4.4)$$

where  $u_i$  is the displacement component,  $n_j$  is the component of the normal to the contour  $C$  and  $x_1$  is the horizontal position (see Figure 4-3).  $J$  is independent of the contour chosen ( $C_1$  or  $C_2$ ). However, if the loading is non-linear or cyclic, this independence is lost.

Wells [WEL61] argued that an initially sharp crack blunts with plastic deformation resulting in a finite displacement at the crack tip, as illustrated in Figure 4-4. This blunting increases in the same proportion as the toughness of the material. This crack tip blunting, called the Crack Tip Opening Displacement (CTOD), refers to the progressive increase in the displacement at the crack tip during blunting and crack propagation. Rice [RIC68] suggested defining the CTOD as the displacement at the intersection the crack flanks of a  $90^\circ$  vertex centered at the tip as illustrated in Figure 4-4. Lemaître and Chaboche [LEM96] compute the CTOD with

$$\delta_{CTOD} = \frac{\sqrt{2} K_I^2}{E \sigma_y} \quad (4.5)$$

where  $E$  is Young's Modulus and  $\sigma_y$  the yield stress.



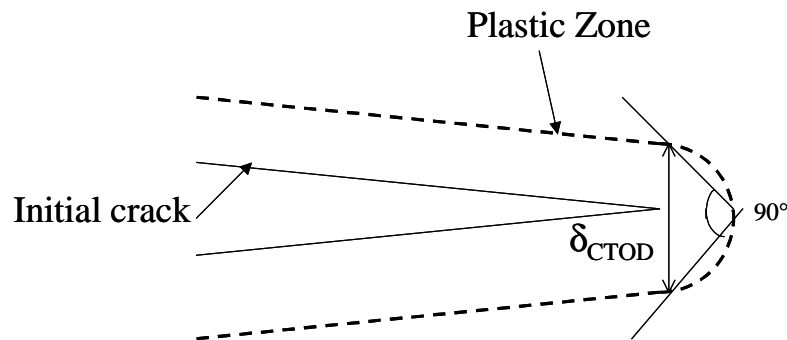


Figure 4-4: Definition of the effective CTOD as proposed by Rice

These different fracture parameters assume the existence of an infinite stress level near the crack tip. The crack begins to propagate as soon as the parameter chosen reaches a critical value ( $K_{IC}$ ,  $J_{IC}$ ,  $\delta_{CTODc}$  or  $G_{IC}$ ). These boundary values define the crack propagation strength of the material and are experimentally determined. For further details, the measurement methods are summarized in [WIL99] and [BSI91]. The sample geometries commonly used are presented in Figure 4-5. In small-scale yielding situations, where the plastic zone does not influence the elastic stress field, the J-integral is equal to G and relation (4.3) gives the link between the J-integral and K stress intensity factor. However, these parameters depend not only on the material but also on the geometry [BRO95]. For example, the J-integral varies with the type of specimen as

$$J_{CCP} \geq J_{DENT} \geq J_{SENT} \geq J_{SENB} \geq J_{CT} \quad (4.6)$$

CCP, DENT, SENT, SENB and CT sample are defined in Figure 4-5. SENB specimens were used in the VERAPS project to evaluate the toughness of the materials.

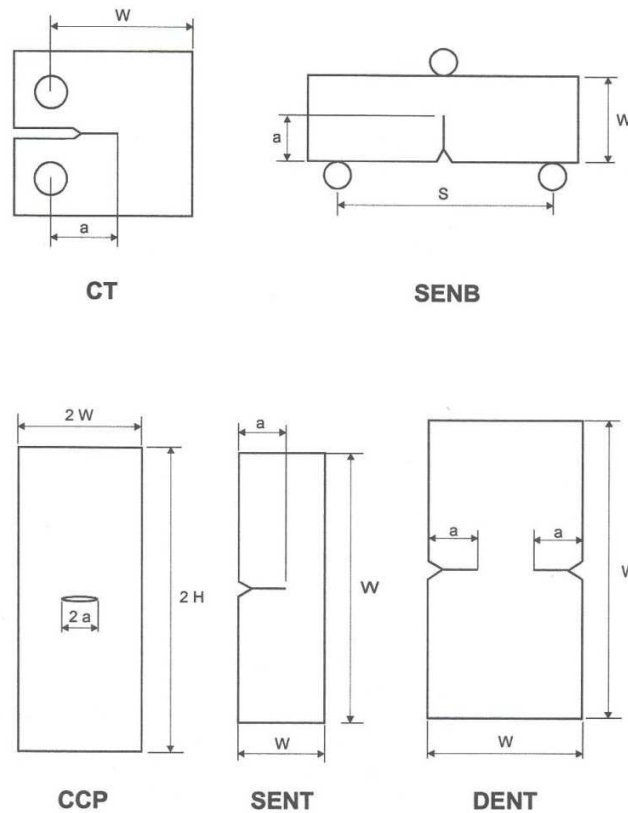


Figure 4-5: Fracture samples used to characterize fracture toughness estimated by J-integral (from [WIL99])

## 4.2 Introduction to the Cohesive Zone Model (CZM)

### 4.2.1 Introduction

Dugdale [DUG60] and Barenblatt [BAR62] in the early sixties introduced the concept of the Cohesive Zone Model (CZM). This model has since been used for monolithic and composite material. During crack propagation, there is a fracture process occurring behind the crack tip, where microcracks and microvoids nucleate, grow and then coalesce. Thus the behavior of this zone is different from the sound bulk material due to its progressive degradation. The cohesive zone model describes this behavior. The potential crack is modeled by two interface areas connected by cohesive stresses. The degradation process is described by the constitutive law linking cohesive stress,  $T$ , and separation,  $\Delta u$  (see Figure 4-6). According to a literature review, there are different forms of this law but they have common features. Cohesive stress, during the increase in the separation, begins to increase until reaching a maximum stress value  $\sigma_{\max}$ , then decreases and vanishes after full rupture. The area under the cohesive stress-separation curve is the cohesive energy,  $\phi$ , which takes into account the creation of two new surfaces and the micro-damage phenomena. In general, cohesive energy is believed to be equivalent to the work of fracture  $G_{10}$  or  $J_{10}$  [SHE02]. Particular separations can be defined:  $\delta_0$ , which is the separation when the cohesive stress is maximum, and  $\delta_c$ , when it vanishes.

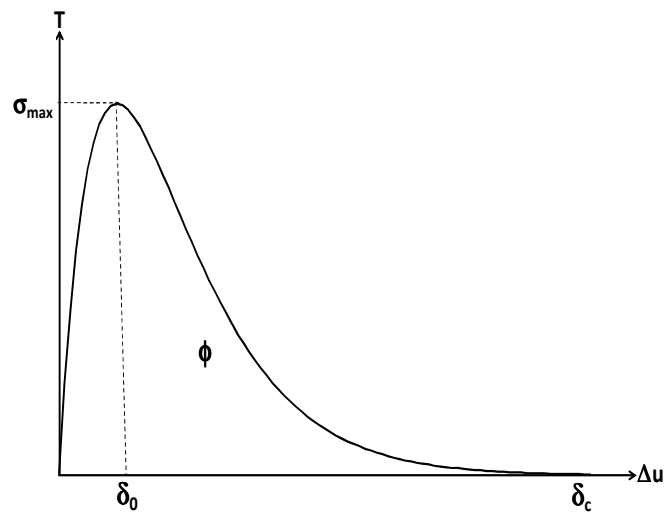


Figure 4-6: Typical form of cohesive stress-separation law

Figure 4-7 describes some of the available cohesive laws. Needleman [NEE90] was the first who used polynomial and exponential models to study the void nucleation at the interface of particles in matrix metal. Tvergaard & Hutchinson [TVE92] proposed a trapezoidal shape to study elastoplastic material. Geubelle et al. [GEU98] used a bilinear model to analyze the initiation and the propagation of transverse matrix crack. Camacho and Ortiz [CAM96] modeled the propagation of multiple crack and delamination in a composite by a linear law. Schreurs et al. [ERI05] performed modeling of fatigue on solder bumps in microelectronics.

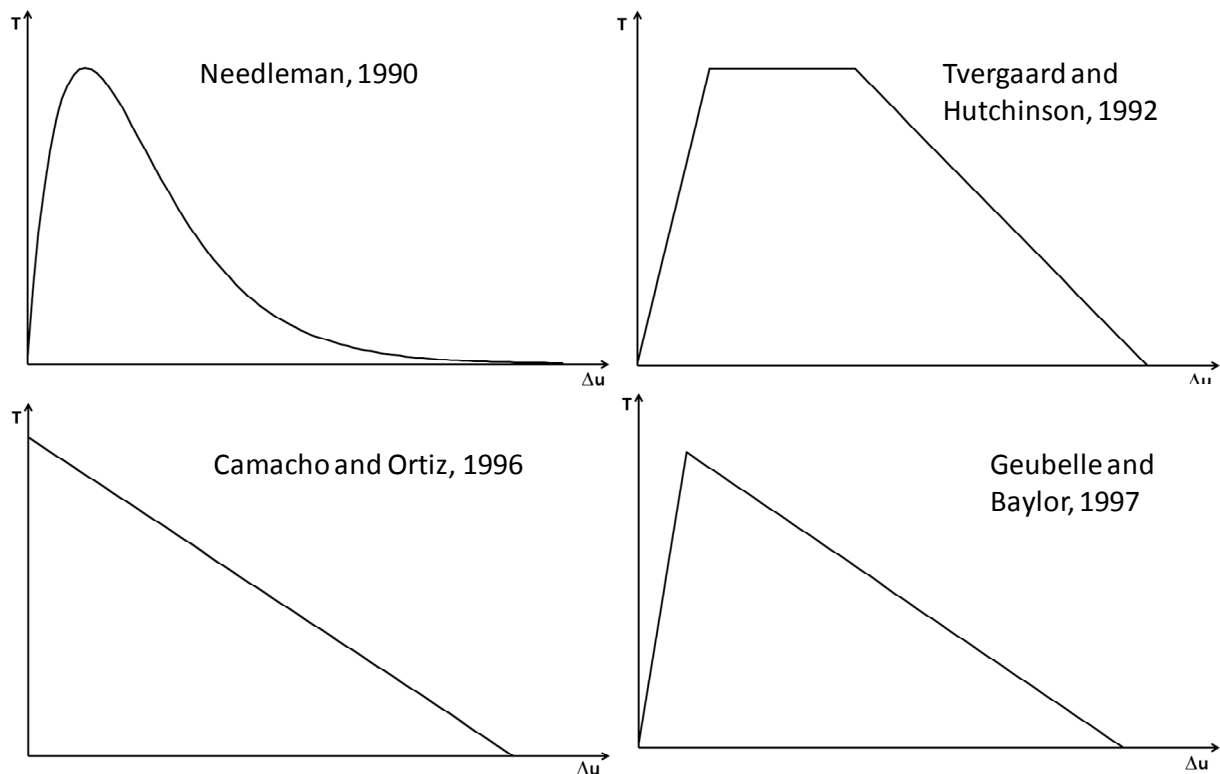


Figure 4-7: Various cohesive zone models

### 4.2.2 Process zone

The constitutive law of the cohesive zone involves two steps (see Figure 4-6). The microstructural analysis of the crack propagation also defines two different zones (see Figure 4-8). Li and Chandra [LI 03] proposed the concept for the first step (point A to point B) of the “forward zone” and for the second step (point B to C) of the “wake zone”.

In the forward zone, where the separation is less than  $\delta_0$ , extrinsic energy dissipation occurs due to microstructural damage (e.g. microcrack initiation and growth, microvoid coalescence, phase transformation or yielding) which generally promotes the crack’s growth.

On the contrary, in the wake zone, where the separation is greater than  $\delta_0$ , intrinsic energy dissipation occurs. This is caused by micromechanism phenomena which impede the crack’s propagation (e.g. crack deflection, friction or crack closure).

Both zones consume energy: the first part is dissipated by the material and the rest by the cohesive zone. The notion of these process zones is important in the use of the cohesive zone model. Indeed the accuracy of the computation depends directly on the number of elements in each zone.

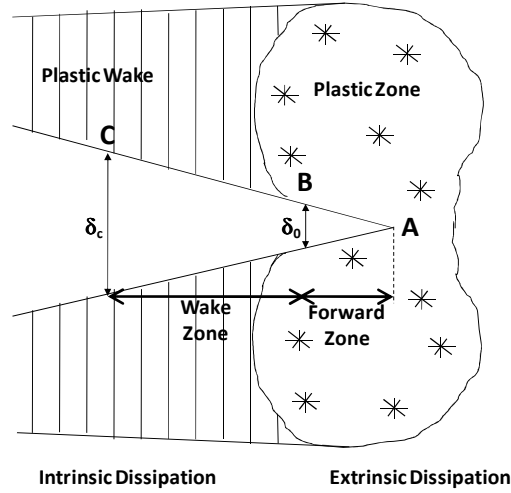


Figure 4-8: Process zone description in the cohesive zone model

Rice [RIC80] and Molinari [MOL07] proposed the following relationship to evaluate the size of the process zone,  $R_{PZ}$ , from the crack tip:

$$R_{PZ} = \frac{9\pi}{32} \frac{E}{1-\nu^2} \frac{G_c}{\sigma_{\max}^2}. \quad (4.7)$$

This length incorporates both the wake zone and the forward zone. As a result, the criterion works well on brittle material. For proper functioning, it is advised that the finite element size should be smaller than the process zone.

### 4.2.3 Implicit thickness

The cohesive zone model allows the stick layer of a composite to be simulated. A contradiction appears as the cohesive zone models a layer with zero thickness. However, it is possible to define an implicit thickness. Suquet [SUQ87] suggested computing the strain,  $\varepsilon$ , by

$$\varepsilon = \frac{\Delta u}{h} \quad (4.8)$$

where  $h$  is the implicit thickness of the element.

If a bulk material exhibits elastic behavior, then the stress as a function of the deformation is

$$\sigma = E\varepsilon. \quad (4.9)$$

By analogy the separation depends on the cohesive stress by

$$T = k\Delta u \quad (4.10)$$

where  $k$  is the stiffness of the cohesive zone before the degradation process begins.

The latter three equations allow identifying the implicit thickness,  $h$ , by considering the stress equality:

$$h = \frac{E}{k}. \quad (4.11)$$

In this case, the choice of the initial stiffness is important because it can generate an implicit thickness. As the cohesive zone model aims to model cracking, the initial stiffness must be as high as possible to have the lowest possible implicit thickness. In the case of finite element simulations,  $h$  must be smaller than the smallest size of the cohesive element.

#### 4.2.4 Jump displacement

The use of the cohesive zone model can induce some instability called solution jumps. This problem has been addressed by Gao [GAO04], Chaboche [CHA01] and Hamitouche [HAM08]. This phenomenon can be explained by the following simple one-dimensional problem. Let two simple elastic solid volumes with length,  $a$ , be linked by a cohesive zone (see Figure 4-9).

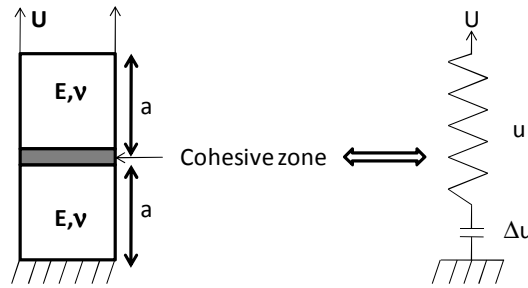


Figure 4-9: Simple uniaxial problem to illustrate the jump displacement

The cohesive zone is defined by the following bilinear law [MI 98]:

$$T = \begin{cases} \frac{\sigma_{\max}}{\delta_0} \Delta u & \text{if } \Delta u < \delta_0 & \text{(a)} \\ \sigma_{\max} \frac{\delta_c - \Delta u}{\delta_c - \delta_0} & \text{if } \delta_0 \leq \Delta u \leq \delta_c & \text{(b)} \\ 0 & \text{if } \Delta u > \delta_c & \text{(c)} \end{cases} \quad (4.12)$$

The solids are elastic, so the total elongation,  $u$ , and the stress,  $\sigma$ , are related by:

$$\sigma = \frac{E}{2a} u \quad (4.13)$$

where  $E$  is Young's modulus.

The constraint displacement,  $U$ , is the sum of the solid elongation,  $u$ , and the cohesive separation,  $\Delta u$ :

$$U = u + \Delta u. \quad (4.14)$$

Equations (4.12),(a) to (4.14) and the continuity of stress can be used to write the relationship between the constraint displacement,  $U$ , and the cohesive separation,  $\Delta u$ , before it reaches  $\delta_0$ :

$$U = \left( \frac{1}{\Lambda} + 1 \right) \Delta u \text{ with } \Lambda = \frac{E\delta_0}{2a\sigma_{\max}}. \quad (4.15)$$

The displacement imposed induces the cohesive separation,  $\Delta u$ . This separation can be computed from the curves in Figure 4-10. The separation,  $\Delta u$ , which corresponds to the displacement imposed, is the abscissa of the intersection point between the curves of the cohesive law and the Equation (4.16), which was compiled from equations (4.13) and (4.14).

$$\sigma = \frac{E}{2a}(U - \Delta u) \quad (4.16)$$

In the first step, where the separation,  $\Delta u_1$ , is less than  $\delta_0$  (for example  $U=U_1$ ), an intersection point can always be found. However when the cohesive separation reaches,  $\delta_0$  ( $U=U_2$ ), two situations may occur:

- If the elastic stiffness is large enough (see Figure 4-10 (a)) to maintain the intersection between the cohesive and the elastic law, then the response is always stable because an intersection point can always be found (for example,  $U=U_3$ ).
- Otherwise, (see Figure 4-10(b)) when  $U$  increases, the solution jumps ( $\Delta u_3=U$  and  $T=0$ ) and the crack occurs without a smoothing component. This is the jump displacement case.

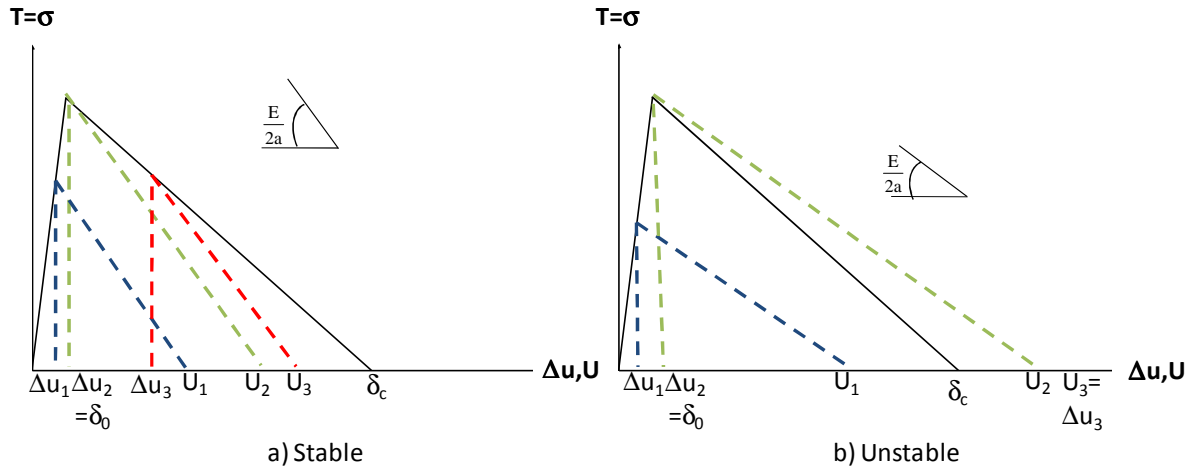


Figure 4-10: The cohesive separation response driven by the imposed displacement  $U$

Consequently, the condition of stability can only be met, when the cohesive separation reaches  $\delta_0$ , the constraint displacement is inferior to  $\delta_c$ . From Equation (4.15), this condition becomes

$$\Lambda \leq \frac{1}{\alpha - 1} \text{ and } \alpha = \frac{\delta_c}{\delta_0} \quad (4.17)$$

The stiffness ratio condition can also be written as a comparison of energy:

$$\Lambda \leq \frac{1}{\alpha - 1} \Leftrightarrow \frac{1}{2} \frac{2a}{E} \sigma_{\max}^2 > \frac{1}{2} \sigma_{\max} \delta_c - \frac{1}{2} \sigma_{\max} \delta_0 = \phi - \frac{1}{2} \sigma_{\max} \delta_0 = \phi_d \quad (4.18)$$

where  $\phi$  is the cohesive energy needed to reach total debonding. This stability criterion requires the elastic energy to be less than the effective cohesive energy,  $\phi_d$ . Otherwise all elastic energy stored in the cohesive zone is distributed through the solid elements and the separation jumps.

This phenomenon explains the convergence problems found in simulations with the cohesive zone. Different authors ([GAO04], [CHA01] and [HAM08]) suggested adding viscosity in the cohesive behavior in order to smooth this phenomenon. In this case, a part of the elastic energy is converted into kinetic energy and the crack rate is limited. This model will be described in more details later.

### 4.3 The constitutive laws of the cohesive zone model

In this section, two constitutive laws are described to compare their application to the cohesive zone model. The first one is Xu and Needleman's law. It is an exponential law which has often been used according to the literature review [XU 93; KEL99]. It was the first law implemented in the finite element code Lagamine for the cohesive zone model. However, this law does not allow the stiffness of the cohesive zone to be calibrated before the degradation process begins (see Section 4.2.3). Therefore, it was decided to implement Crisfield's law and compare the two, as described further in the following section.

#### 4.3.1 Description of the cohesive components

The cohesive zone model makes it possible to model cracks in a mixed mode. Each mode of fracture (I, II or III) is associated with a separation component and a cohesive stress component (see Table 4-1). The components constitute the separation vector,  $\underline{\Delta u}$ , and the cohesive stress vector,  $\underline{T}$ . These components are oriented along the local triad ( $\underline{e}_p, \underline{e}_s, \underline{e}_n$ ) in 3D or ( $\underline{e}_t, \underline{e}_n$ ) in 2D where  $\underline{e}_n$  corresponds to the normal of the mid-plane between the crack interfaces while  $\underline{e}_t, \underline{e}_p$  and  $\underline{e}_s$  correspond to tangential directions.

$$\underline{\Delta u} = \begin{cases} \Delta u_p \underline{e}_p + \Delta u_s \underline{e}_s + \Delta u_n \underline{e}_n & (3D) \\ \Delta u_t \underline{e}_t + \Delta u_n \underline{e}_n & (2D) \end{cases}; \underline{T} = \begin{cases} T_p \underline{e}_p + T_s \underline{e}_s + T_n \underline{e}_n & (3D) \\ T_t \underline{e}_t + T_n \underline{e}_n & (2D) \end{cases} \quad (4.19)$$

**Table 4-1: Association between separation and cohesive stress components and the crack mode**

Mode (see Figure 4-1)	2D		3D	
	Separation	Cohesive stress	Separation	Cohesive stress
I	$\Delta u_n$	$T_n$	$\Delta u_n$	$T_n$
II	$\Delta u_t$	$T_t$	$\Delta u_p$	$T_p$
III			$\Delta u_s$	$T_s$

#### 4.3.2 Xu and Needleman's law

During this research, Xu and Needleman's model [XU 93] was firstly chosen for the cohesive zone, because it has already been used for such application as the ductile fracture of metal [SHE02]. Xu and Needleman introduced an exponential law, which comes from a pseudo-potential.



$$\phi(\Delta u_n, \Delta u_t) = \phi_n + \phi_n \exp\left(-\frac{\Delta u_n}{\delta_{n0}}\right) \left\{ \left(1-r + \frac{\Delta u_n}{\delta_{n0}}\right) \left(\frac{1-q}{r-1}\right) - \left[ q + \left(\frac{r-q}{r-1}\right) \frac{\Delta u_n}{\delta_{n0}} \right] \exp\left(-\frac{\Delta u_t^2}{\delta_{t0}^2}\right) \right\} \quad (4.20)$$

$$\text{where } \phi_n = \sigma_{\max0} \exp(1) \delta_{n0}, \phi_t = \sqrt{\frac{\exp(1)}{2}} \tau_{\max0} \delta_{t0}, q = \frac{\phi_t}{\phi_n} \text{ and } r = \frac{\Delta u_n^*}{\delta_{n0}}$$

$\Delta u_n$  and  $\Delta u_t$  are the normal and the shear components, respectively, of the separation between the two interfaces.  $\phi_n$  and  $\phi_t$  are the normal and shear energies released by the normal and shear crack processes.  $\sigma_{\max0}$  and  $\tau_{\max0}$  are the normal and shear maximum stresses.  $\delta_{n0}$  and  $\delta_{t0}$  are the normal and shear separation when the stresses are at a maximum. Finally,  $\Delta u_n^*$  is the normal separation after the shear separation is completed and the normal stress is null (in literature, generally  $r=0$  [RAH00; ROE03]).

#### 4.3.2.1 Cohesive stresses

The normal and the shear components of the cohesive stress,  $T_n$  and  $T_t$ , are obtained from the derivation of the pseudo-potential by the components of the separation.

$$\underline{T} = \begin{cases} T_t = -\frac{\partial \phi}{\partial \Delta u_t} \\ T_n = -\frac{\partial \phi}{\partial \Delta u_n} \end{cases} \quad (4.21)$$

Thus (4.20) + (4.21) become

$$\begin{aligned} T_t &= \left(\frac{\phi_n}{\delta_{n0}}\right) \left(\frac{2\delta_{n0}}{\delta_{t0}}\right) \frac{\Delta u_t}{\delta_{t0}} \left\{ q + \left[\frac{r-q}{r-1}\right] \left(\frac{\Delta u_n}{\delta_{n0}}\right) \right\} \exp\left(-\frac{\Delta u_n}{\delta_{n0}}\right) \exp\left(-\frac{\Delta u_t^2}{\delta_{t0}^2}\right) \\ T_n &= \left(\frac{\phi_n}{\delta_{n0}}\right) \exp\left(-\frac{\Delta u_n}{\delta_{n0}}\right) \left\{ \frac{\Delta u_n}{\delta_{n0}} \exp\left(-\frac{\Delta u_t^2}{\delta_{t0}^2}\right) + \left(\frac{1-q}{r-1}\right) \left(1 - \exp\left(-\frac{\Delta u_t^2}{\delta_{t0}^2}\right)\right) \left(r - \frac{\Delta u_n}{\delta_{n0}}\right) \right\}. \end{aligned} \quad (4.22)$$

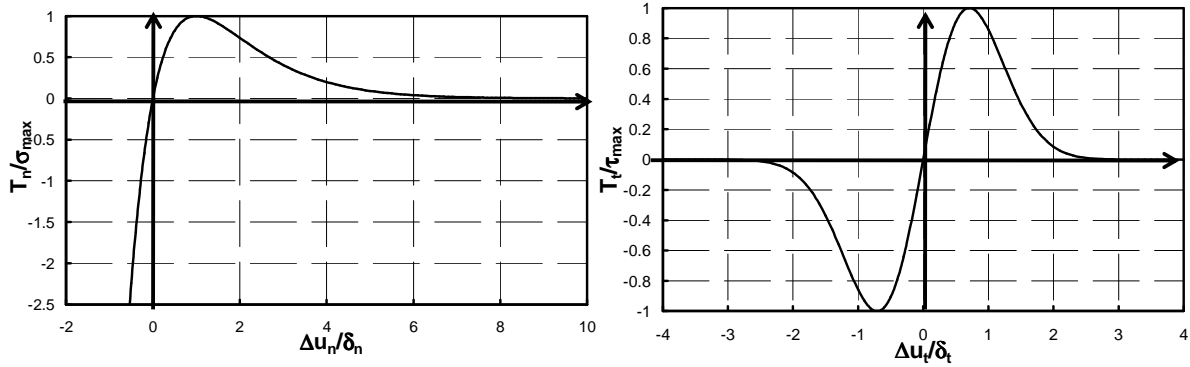


Figure 4-11: Relative normal and shear cohesive stress-separation curve for uncoupled modeling

Figure 4-11 shows the tension-separation curves in the case of uncoupled modeling for the normal and tangential modes.

In the case of three-dimensional analyses, the two-dimensional model is extended directly. The cohesive shear stress,  $T_t$ , is projected on the local axes to obtain the components of the shear stresses,  $T_p$  and  $T_s$ , by Equation (4.23).

$$\underline{T} = \begin{Bmatrix} T_p \\ T_s \\ T_n \end{Bmatrix} = \begin{Bmatrix} \frac{\Delta u_p}{\sqrt{\Delta u_p^2 + \Delta u_s^2}} T_t \\ \frac{\Delta u_s}{\sqrt{\Delta u_p^2 + \Delta u_s^2}} T_t \\ T_n \end{Bmatrix} \quad \text{where } \Delta u_t = \sqrt{\Delta u_p^2 + \Delta u_s^2} \quad (4.23)$$

#### 4.3.2.2 Fatigue damage coupling

In the case studied by the author, the system would be undergoing cyclic loading and unloading; therefore it was necessary to take into account the fatigue damage expressed by a scalar  $D_f$ . The fatigue Continuum Damage Model (see Chapter 3) describes this damage. Thus, it is coupled with the cohesive zone model by the following way proposed by Roe and Sigmund [ROE03] by modifying the value of the maximum cohesive stresses:

$$\sigma_{\max} = \sigma_{\max 0} (1 - D_f) \quad (4.24)$$

$$\tau_{\max} = \tau_{\max 0} (1 - D_f) \quad (4.25)$$

where  $\sigma_{\max 0}$  and  $\tau_{\max 0}$  are the initial normal and shear maximum cohesive stresses, respectively, with no fatigue damage.

Due to fatigue damage, the energy needed to crack material is reduced, and the new curves are defined on Figure 4-12.

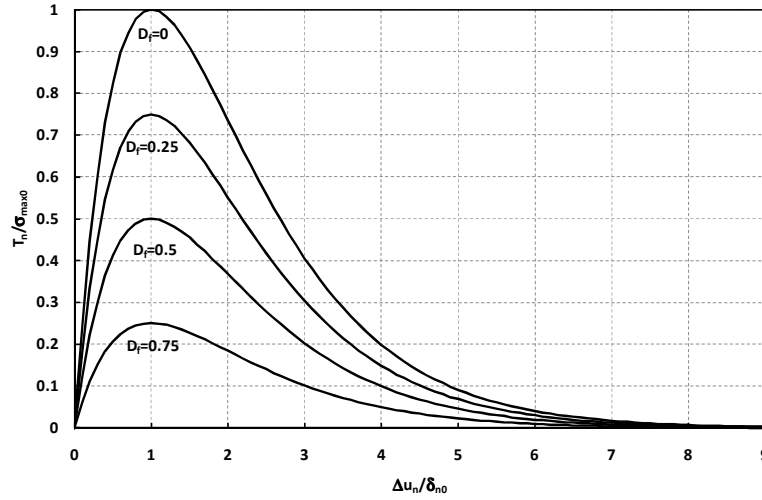


Figure 4-12: Cohesive loading curve coupled with fatigue damage

### 4.3.2.3 Loading and unloading cases

During unloading (step 3 in Figure 4-13), Roe and Sigmund [ROE03] suggested that the cohesive stress is linear, as in elasticity. Its behavior remains linear during reloading (step 4 in Figure 4-13) until the separation reaches the values when unloading began. Then the behavior follows the constitutive law defined by Equation (4.22) (step 5). To determine the linear cases due to loading or unloading and which crack mode, three new variables are computed:

$$\left\{ \begin{array}{l} \omega_j = \frac{|\Delta u_j|}{\delta_{t0}} \text{ where } j=t, p \text{ or } s \\ \omega_n = \frac{\langle \Delta u_n \rangle}{\delta_{n0}} \\ \omega_{oi} = \max_t \{ \omega_i(t) \} \text{ with } i=t, p, s \text{ or } n \end{array} \right. \quad (4.26)$$

where  $\omega_{oi}$  is the maximum value of  $\omega_i$  during the loading phase, which defines the monotonic damage state of the material. The linear behavior takes places when  $\omega_i$  is less than  $\omega_{oi}$ ; therefore, the constitutive law becomes

$$\text{if } (\omega_i \leq \omega_{oi}), \text{ then } T_i = \Delta u_i \frac{T_{i,\max}}{\Delta u_{i,\max}} \text{ where } i= t, s, p \text{ or } n \quad (4.27)$$

where  $T_{i,\max}$  represents the cohesive stress component and,  $\Delta u_{i,\max}$  represents the separation component before unloading begins.

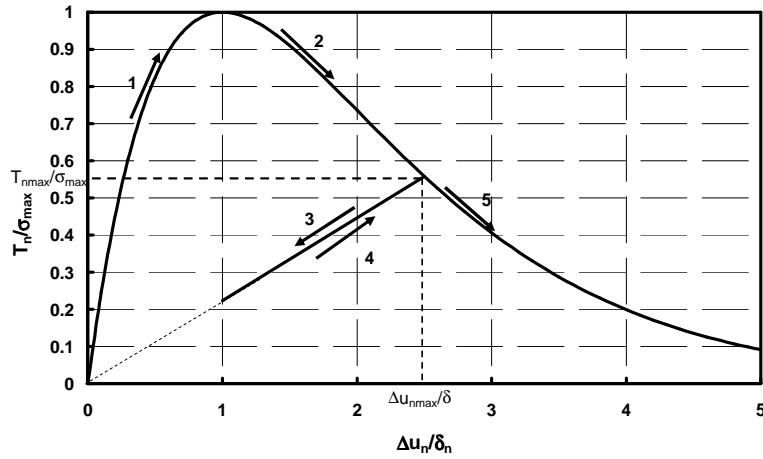


Figure 4-13: Normal traction curve in case of loading and unloading

If the two new crack surfaces begin to touch each other (i.e.  $\Delta u_n \leq 0$ ), then the cohesive zone will be compressed and the law becomes:

$$T_{n,comp} = \frac{\phi_n}{\delta_{n0}} \exp\left(-\frac{\Delta u_n}{\delta_{n0}}\right) \left\{ \frac{\Delta u_n}{\delta_{n0}} \exp\left(-\frac{\Delta u_t^2}{\delta_{t0}^2}\right) + \left(\frac{1-q}{r-1}\right) \left(1 - \exp\left(-\frac{\Delta u_t^2}{\delta_{t0}^2}\right)\right) \left(r - \frac{\Delta u_n}{\delta_{n0}}\right) \right\} + \dots$$

$$\alpha \sigma_{max0} e \frac{\Delta u_n}{\delta_{n0}} \exp\left(-\frac{\Delta u_n}{\delta_{n0}}\right) \text{ if } \Delta u_n < 0 \quad (4.28)$$

where  $\alpha$  is a penalty coefficient. The value of  $\alpha$  should be around 10 [ROE03] to have an significant stiffness and simulate contact by a penalty model.

#### 4.3.2.4 Viscosity

To avoid convergence problems in finite element simulations due to jump displacement (see Section 4.2.4), Gao and Bower, [GAO04] suggested adding some viscosity terms such as:

– in 2D cases,

$$T_t = \left(\frac{\phi_n}{\delta_{n0}}\right) \left(\frac{2\delta_{n0}}{\delta_{t0}}\right) \frac{\Delta u_t}{\delta_{t0}} \left\{ q + \left[\frac{r-q}{r-1}\right] \left(\frac{\Delta u_n}{\delta_{n0}}\right) \right\} \exp\left(-\frac{\Delta u_n}{\delta_{n0}}\right) \exp\left(-\frac{\Delta u_t^2}{\delta_{t0}^2}\right) \left\{ 1 + \zeta_t \frac{d}{dt} \left(\frac{\Delta u_t}{\delta_{t0}}\right) \right\}$$

$$T_n = \left(\frac{\phi_n}{\delta_{n0}}\right) \exp\left(-\frac{\Delta u_n}{\delta_{n0}}\right) \left\{ \frac{\Delta u_n}{\delta_{n0}} \exp\left(-\frac{\Delta u_t^2}{\delta_{t0}^2}\right) + \left(\frac{1-q}{r-1}\right) \left(1 - \exp\left(-\frac{\Delta u_t^2}{\delta_{t0}^2}\right)\right) \left(r - \frac{\Delta u_n}{\delta_{n0}}\right) \right\} \times \dots \quad (4.29)$$

$$\left\{ 1 + \zeta_n \frac{d}{dt} \left(\frac{\Delta u_n}{\delta_{n0}}\right) \right\}$$

– in 3D cases,

$$\begin{aligned}
T_p &= \left( \frac{\phi_n}{\delta_{n0}} \right) \left( \frac{2\delta_n}{\delta_{t0}} \right) \frac{\Delta u_p}{\delta_{t0}} \left\{ q + \left[ \frac{r-q}{r-1} \right] \left( \frac{\Delta u_n}{\delta_{n0}} \right) \right\} \exp \left( -\frac{\Delta u_n}{\delta_{n0}} \right) \exp \left( -\frac{\Delta u_t^2}{\delta_{t0}^2} \right) \times \dots \\
&\quad \left\{ 1 + \zeta_t \frac{d}{dt} \left( \frac{\Delta u_p}{\delta_{t0}} \right) \right\} \\
T_s &= \left( \frac{\phi_n}{\delta_n} \right) \left( \frac{2\delta_n}{\delta_{t0}} \right) \frac{\Delta u_s}{\delta_{t0}} \left\{ q + \left[ \frac{r-q}{r-1} \right] \left( \frac{\Delta u_n}{\delta_n} \right) \right\} \exp \left( -\frac{\Delta u_n}{\delta_n} \right) \exp \left( -\frac{\Delta u_t^2}{\delta_{t0}^2} \right) \times \dots \\
&\quad \left\{ 1 + \zeta_t \frac{d}{dt} \left( \frac{\Delta u_s}{\delta_{t0}} \right) \right\} \\
T_n &= \left( \frac{\phi_n}{\delta_{n0}} \right) \exp \left( -\frac{\Delta u_n}{\delta_{n0}} \right) \left\{ \frac{\Delta u_n}{\delta_{n0}} \exp \left( -\frac{\Delta u_t^2}{\delta_{t0}^2} \right) + \left( \frac{1-q}{r-1} \right) \left( 1 - \exp \left( -\frac{\Delta u_t^2}{\delta_{t0}^2} \right) \right) \left( r - \frac{\Delta u_n}{\delta_{n0}} \right) \right\} \times \dots \\
&\quad \left\{ 1 + \zeta_n \frac{d}{dt} \left( \frac{\Delta u_n}{\delta_{n0}} \right) \right\}
\end{aligned} \tag{4.30}$$

where  $\zeta_n$  and  $\zeta_t$  are viscosity-like parameters that govern viscous energy dissipation under normal and tangential loading, respectively.

This viscosity term is added only if the normal separation is positive.

#### 4.3.2.5 Cohesive stiffness matrix

The definition of the cohesive stiffness matrix takes into account viscosity, as described below:

	2D	3D
$\underline{\underline{C}} =$	$\begin{bmatrix} \frac{\partial T_t}{\partial \Delta u_t} & \frac{\partial T_t}{\partial \Delta u_n} \\ \frac{\partial T_n}{\partial \Delta u_t} & \frac{\partial T_n}{\partial \Delta u_n} \end{bmatrix}$	$\begin{bmatrix} \frac{\partial T_p}{\partial \Delta u_p} & \frac{\partial T_p}{\partial \Delta u_s} & \frac{\partial T_p}{\partial \Delta u_n} \\ \frac{\partial T_s}{\partial \Delta u_p} & \frac{\partial T_s}{\partial \Delta u_s} & \frac{\partial T_s}{\partial \Delta u_n} \\ \frac{\partial T_n}{\partial \Delta u_p} & \frac{\partial T_n}{\partial \Delta u_s} & \frac{\partial T_n}{\partial \Delta u_n} \end{bmatrix}$

(4.31)

The components of this matrix are determined by the Equations in (4.31). Here, their analytical forms will be given:

– For 2D cases:

Case:  $\omega_t = \omega_{0t}$

$$\begin{cases} C_{11} = 2 \frac{\phi_n}{\delta_{t0}^2} \left\{ q + \left( \frac{r-q}{r-1} \right) \left( \frac{\Delta u_n}{\delta_{n0}} \right) \right\} \exp \left( -\frac{\Delta u_n}{\delta_{n0}} \right) \exp \left( -\frac{\Delta u_t^2}{\delta_{t0}^2} \right) \left( 1 - 2 \frac{\Delta u_t^2}{\delta_{t0}^2} \right) \left\{ 1 + \zeta_t \frac{d}{dt} \left( \frac{\Delta u_t}{\delta_{t0}} \right) \right\} + T_t \frac{\zeta_t}{\delta_{t0} \Delta t} \\ C_{12} = 2 \frac{\phi_n}{\delta_{t0} \delta_{n0}} \left( \frac{\Delta u_t}{\delta_{t0}} \right) \exp \left( -\frac{\Delta u_n}{\delta_{n0}} \right) \exp \left( -\frac{\Delta u_t^2}{\delta_{t0}^2} \right) \left\{ \left( \frac{r-q}{r-1} \right) \left( 1 - \frac{\Delta u_n}{\delta_{n0}} \right) - q \right\} \left\{ 1 + \zeta_t \frac{d}{dt} \left( \frac{\Delta u_t}{\delta_{t0}} \right) \right\} \end{cases} \quad (4.32)$$

Case:  $\omega_t \leq \omega_{0t}$

$$\begin{cases} C_{11} = \frac{T_{tmax}}{\Delta u_{tmax}} \\ C_{12} = 0 \end{cases}$$

Case:  $\omega_n = \omega_{n0}$

$$\begin{cases} C_{21} = 2 \frac{\phi_n}{\delta_{t0} \delta_{n0}} \left( \frac{\Delta u_t}{\delta_{t0}} \right) \exp \left( -\frac{\Delta u_n}{\delta_{n0}} \right) \exp \left( -\frac{\Delta u_t^2}{\delta_{t0}^2} \right) \left\{ -\frac{\Delta u_n}{\delta_{n0}} + \left( \frac{1-q}{r-1} \right) \left( r - \frac{\Delta u_n}{\delta_{n0}} \right) \right\} \left\{ 1 + \zeta_n \frac{d}{dt} \left( \frac{\Delta u_n}{\delta_{n0}} \right) \right\} \\ C_{22} = \frac{\phi_n}{\delta_{n0}^2} \exp \left( -\frac{\Delta u_n}{\delta_{n0}} \right) \left\{ \left( 1 - \frac{\Delta u_n}{\delta_{n0}} \right) \exp \left( -\frac{\Delta u_t^2}{\delta_{t0}^2} \right) + \left( \frac{1-q}{r-1} \right) \left( 1 - \exp \left( -\frac{\Delta u_t^2}{\delta_{t0}^2} \right) \right) \left( -1 + r - \frac{\Delta u_n}{\delta_{n0}} \right) \right\} \left\{ 1 + \zeta_n \frac{d}{dt} \left( \frac{\Delta u_n}{\delta_{n0}} \right) \right\} + T_n \frac{\zeta_n}{\delta_{n0} \Delta t} \end{cases}$$

Case:  $\omega_n \leq \omega_{n0}; \Delta u_n \geq 0$

$$\begin{cases} C_{21} = 0 \\ C_{22} = \frac{T_{nmax}}{\Delta u_{nmax}} \end{cases} \quad (4.33)$$

Case:  $\omega_n \leq \omega_{n0}; \Delta u_n < 0$

$$\begin{cases} C_{21} = 2 \frac{\phi_n}{\delta_{t0} \delta_{n0}} \left( \frac{\Delta u_t}{\delta_{t0}} \right) \exp \left( -\frac{\Delta u_n}{\delta_{n0}} \right) \exp \left( -\frac{\Delta u_t^2}{\delta_{t0}^2} \right) \left\{ -\frac{\Delta u_n}{\delta_{n0}} + \left( \frac{1-q}{r-1} \right) \left( r - \frac{\Delta u_n}{\delta_{n0}} \right) \right\} \\ C_{22} = \frac{\phi_n}{\delta_{n0}^2} \exp \left( -\frac{\Delta u_n}{\delta_{n0}} \right) \left\{ \left( 1 - \frac{\Delta u_n}{\delta_{n0}} \right) \exp \left( -\frac{\Delta u_t^2}{\delta_{t0}^2} \right) + \left( \frac{1-q}{r-1} \right) \left( 1 - \exp \left( -\frac{\Delta u_t^2}{\delta_{t0}^2} \right) \right) \left( -1 + r - \frac{\Delta u_n}{\delta_{n0}} \right) \right\} + \frac{\alpha \epsilon \sigma_{max}}{\delta_{n0}} \left( 1 - \frac{\Delta u_n}{\delta_{n0}} \right) \exp \left( -\frac{\Delta u_n}{\delta_{n0}} \right) \end{cases}$$

– For 3D cases:

Case:  $\omega_p = \omega_{p0}$

$$\begin{cases} C_{11} = 2 \frac{\phi_n}{\delta_{i0}^2} \exp\left(-\frac{\Delta u_n}{\delta_{n0}}\right) \exp\left(-\frac{\Delta u_t^2}{\delta_{i0}^2}\right) \left(q + \frac{\Delta u_n}{\delta_{n0}} \left(\frac{r-q}{r-1}\right)\right) \left(1 - 2 \frac{\Delta u_p^2}{\delta_{i0}^2}\right) \left\{1 + \zeta_t \frac{d}{dt} \left(\frac{\Delta u_p}{\delta_{i0}}\right)\right\} + T_p \frac{\zeta_t}{\delta_{i0} \Delta t} \\ C_{12} = -4 \frac{\phi_n}{\delta_{i0}^2} \exp\left(-\frac{\Delta u_n}{\delta_{n0}}\right) \exp\left(-\frac{\Delta u_t^2}{\delta_{i0}^2}\right) \left(q + \frac{\Delta u_n}{\delta_{n0}} \left(\frac{r-q}{r-1}\right)\right) \left(\frac{\Delta u_s \Delta u_p}{\delta_{i0}^2}\right) \left\{1 + \zeta_t \frac{d}{dt} \left(\frac{\Delta u_p}{\delta_{i0}}\right)\right\} \\ C_{13} = 2 \frac{\phi_n}{\delta_{i0}^2 \delta_{n0}} \exp\left(-\frac{\Delta u_n}{\delta_{n0}}\right) \exp\left(-\frac{\Delta u_t^2}{\delta_{i0}^2}\right) \Delta u_p \left(1 - q - \frac{\Delta u_n}{\delta_{n0}} \left(\frac{r-q}{r-1}\right)\right) \left\{1 + \zeta_t \frac{d}{dt} \left(\frac{\Delta u_p}{\delta_{i0}}\right)\right\} \end{cases} \quad (4.34)$$

Case:  $\omega_p \leq \omega_{p0}$

$$\begin{cases} C_{11} = \frac{T_{pmax}}{\Delta u_{pmax}} \\ C_{12} = 0 \\ C_{13} = 0 \end{cases}$$

Case:  $\omega_s = \omega_{s0}$

$$\begin{cases} C_{21} = -4 \frac{\phi_n}{\delta_{i0}^2} \exp\left(-\frac{\Delta u_n}{\delta_{n0}}\right) \exp\left(-\frac{\Delta u_t^2}{\delta_{i0}^2}\right) \left(q + \frac{\Delta u_n}{\delta_{n0}} \left(\frac{r-q}{r-1}\right)\right) \left(\frac{\Delta u_s \Delta u_p}{\delta_{i0}^2}\right) \left\{1 + \zeta_t \frac{d}{dt} \left(\frac{\Delta u_s}{\delta_{i0}}\right)\right\} \\ C_{22} = 2 \frac{\phi_n}{\delta_{i0}^2} \exp\left(-\frac{\Delta u_n}{\delta_{n0}}\right) \exp\left(-\frac{\Delta u_t^2}{\delta_{i0}^2}\right) \left(q + \frac{\Delta u_n}{\delta_{n0}} \left(\frac{r-q}{r-1}\right)\right) \left(1 - 2 \frac{\Delta u_s^2}{\delta_{i0}^2}\right) \left\{1 + \zeta_t \frac{d}{dt} \left(\frac{\Delta u_s}{\delta_{i0}}\right)\right\} + T_s \frac{\zeta_t}{\delta_{i0} \Delta t} \\ C_{23} = 2 \frac{\phi_n}{\delta_{i0}^2 \delta_{n0}} \exp\left(-\frac{\Delta u_n}{\delta_{n0}}\right) \exp\left(-\frac{\Delta u_t^2}{\delta_{i0}^2}\right) \Delta u_s \left(1 - q - \left(\frac{r-q}{r-1}\right)\right) \left\{1 + \zeta_t \frac{d}{dt} \left(\frac{\Delta u_s}{\delta_{i0}}\right)\right\} \end{cases} \quad (4.35)$$

Case:  $\omega_s \leq \omega_{s0}$

$$\begin{cases} C_{21} = 0 \\ C_{22} = \frac{T_{smax}}{\Delta u_{smax}} \\ C_{23} = 0 \end{cases}$$

Case:  $\omega_n = \omega_{n0}$

$$\begin{cases} C_{31} = 2 \frac{\phi_n}{\delta_{n0} \delta_{t0}^2} \exp\left(-\frac{\Delta u_n}{\delta_{n0}}\right) \exp\left(-\frac{\Delta u_t^2}{\delta_{t0}^2}\right) \Delta u_p \left(-\frac{\Delta u_n}{\delta_{n0}} + \left(r - \frac{\Delta u_n}{\delta_{n0}}\right) \frac{(1-q)}{(r-1)}\right) \left\{1 + \zeta_n \frac{d}{dt} \left(\frac{\Delta u_n}{\delta_{n0}}\right)\right\} \\ C_{32} = 2 \frac{\phi_n}{\delta_{n0} \delta_{t0}^2} \exp\left(-\frac{\Delta u_n}{\delta_{n0}}\right) \exp\left(-\frac{\Delta u_t^2}{\delta_{t0}^2}\right) \Delta u_s \left(-\frac{\Delta u_n}{\delta_{n0}} + \left(r - \frac{\Delta u_n}{\delta_{n0}}\right) \frac{(1-q)}{(r-1)}\right) \left\{1 + \zeta_n \frac{d}{dt} \left(\frac{\Delta u_n}{\delta_{n0}}\right)\right\} \\ C_{33} = \frac{\phi_n}{\delta_{n0}^2} \exp\left(-\frac{\Delta u_n}{\delta_{n0}}\right) \left( \exp\left(-\frac{\Delta u_t^2}{\delta_{t0}^2}\right) \left(1 - \frac{\Delta u_n}{\delta_{n0}} + \frac{(1-q)}{(r-1)}\right) - \frac{(1-q)}{(r-1)} \left(1 - \exp\left(-\frac{\Delta u_t^2}{\delta_{t0}^2}\right) \left(r - \frac{\Delta u_n}{\delta_{n0}}\right)\right) \right) \left\{1 + \zeta_n \frac{d}{dt} \left(\frac{\Delta u_n}{\delta_{n0}}\right)\right\} + T_n \frac{\zeta_n}{\delta_{n0} \Delta t} \end{cases}$$

Case:  $\omega_n < \omega_{n0}; \Delta u_n \geq 0$

$$\begin{cases} C_{31} = 0 \\ C_{32} = 0 \\ C_{33} = \frac{T_{nmax}}{\Delta u_{nmax}} \end{cases} \quad (4.36)$$

Case:  $\omega_n < \omega_{n0}; \Delta u_n < 0$

$$\begin{cases} C_{31} = 2 \frac{\phi_n}{\delta_{n0} \delta_{t0}^2} \exp\left(-\frac{\Delta u_n}{\delta_{n0}}\right) \exp\left(-\frac{\Delta u_t^2}{\delta_{t0}^2}\right) \Delta u_p \left(-\frac{\Delta u_n}{\delta_{n0}} + \left(r - \frac{\Delta u_n}{\delta_{n0}}\right) \frac{(1-q)}{(r-1)}\right) \\ C_{32} = 2 \frac{\phi_n}{\delta_{n0} \delta_{t0}^2} \exp\left(-\frac{\Delta u_n}{\delta_{n0}}\right) \exp\left(-\frac{\Delta u_t^2}{\delta_{t0}^2}\right) \Delta u_s \left(-\frac{\Delta u_n}{\delta_{n0}} + \left(r - \frac{\Delta u_n}{\delta_{n0}}\right) \frac{(1-q)}{(r-1)}\right) \\ C_{33} = \frac{\phi_n}{\delta_{n0}^2} \exp\left(-\frac{\Delta u_n}{\delta_{n0}}\right) \left\{ \left(1 - \frac{\Delta u_n}{\delta_{n0}}\right) \exp\left(-\frac{\Delta u_t^2}{\delta_{t0}^2}\right) + \frac{(1-q)}{(r-1)} \left(1 - \exp\left(-\frac{\Delta u_t^2}{\delta_{t0}^2}\right)\right) \left(-1 + r - \frac{\Delta u_n}{\delta_{n0}}\right) \right\} + \frac{\alpha e \sigma_{max}}{\delta_{n0}} \left(1 - \frac{\Delta u_n}{\delta_{n0}}\right) \exp\left(-\frac{\Delta u_n}{\delta_{n0}}\right) \end{cases}$$

### 4.3.3 Crisfield's law

#### 4.3.3.1 Description

Unlike Xu and Needleman's model, Crisfield's model has a bilinear shape. It is used to define the initial stiffness  $\underline{\underline{E}}_{co}$ .

$$\underline{\underline{E}}_{co} = \begin{bmatrix} \frac{\tau_{max}}{\delta_{t0}} & 0 & 0 \\ 0 & \frac{\tau_{max}}{\delta_{t0}} & 0 \\ 0 & 0 & \frac{\sigma_{max}}{\delta_{n0}} \end{bmatrix} \quad (4.37)$$

where  $\sigma_{max}$  and  $\tau_{max}$  are the maximum normal and shear stresses,  $\delta_{n0}$  and  $\delta_{t0}$  are the normal and shear separations when the normal and shear stresses reach their maximum values,  $\sigma_{max}$  and  $\tau_{max}$ .



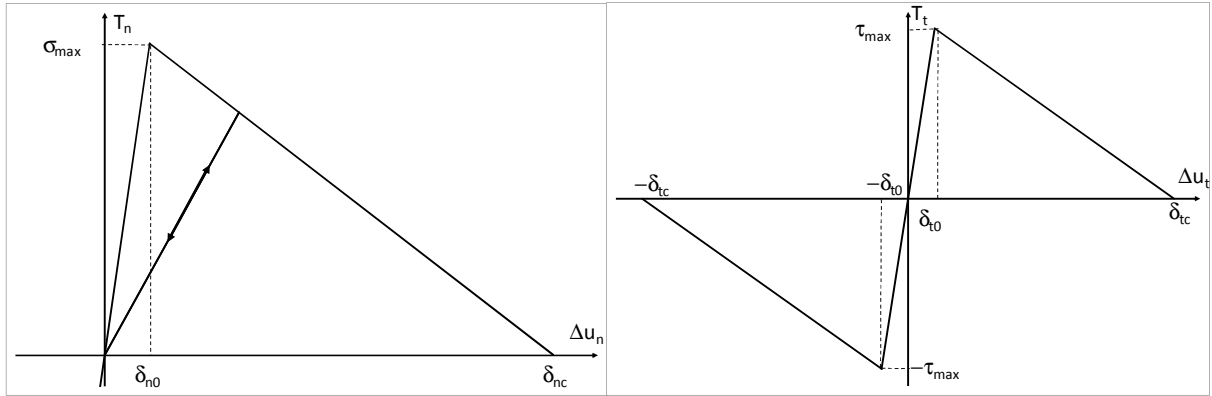


Figure 4-14: Crisfield's cohesive zone model

A monotonic damage tensor,  $\underline{D}_{\text{mono}}$ , is defined as a function of the separation,  $\underline{\Delta u}$ . At the beginning of the loading phase, the damage is equal to zero. If one separation component,  $\Delta u_i$ , is beyond the separation,  $\delta_{i0}$ , where the stress is equal to the maximum stress, then the damage begins to grow until the separation is equal to a critical displacement,  $\delta_c$ , and the damage is equal to 1. In unloading, the damage stops growing. Then, in reloading, the damage grows again when the separation reaches the value reached when the unloading began.

For the mixed fracture mode, the damage tensor is defined by

$$\underline{D}_{\text{mono}} = \frac{\langle \omega_0 \rangle}{1 + \langle \omega_0 \rangle} \underline{F} \quad \text{with} \quad \left\{ \begin{array}{l} \omega = \left[ \left( \frac{\langle \Delta u_n \rangle}{\delta_{n0}} \right)^\alpha + \left( \frac{|\Delta u_p|}{\delta_{p0}} \right)^\alpha + \left( \frac{|\Delta u_s|}{\delta_{s0}} \right)^\alpha \right]^{\frac{1}{\alpha}} - 1 \\ \omega_0 = \max_t(\omega) \\ \underline{F} = \begin{bmatrix} \frac{\delta_{tc}}{\delta_{tc} - \delta_{t0}} & 0 & 0 \\ 0 & \frac{\delta_{tc}}{\delta_{tc} - \delta_{t0}} & 0 \\ 0 & 0 & \frac{\delta_{nc}}{\delta_{nc} - \delta_{n0}} \end{bmatrix} \end{array} \right. \quad (4.38)$$

where  $\delta_{tc}$  and  $\delta_{nc}$  are the separations when the normal and the shear stresses are null,  $\alpha$  is a material parameter and  $t$  the time.

The condition when the monotone damage rate is positive is

$$\text{if } (\omega - \omega_0 > 0), \text{ then } \begin{cases} \dot{\underline{D}}_{\text{mono}} > 0 \\ \omega_0 = \omega \end{cases} \quad (4.39)$$

Otherwise,  $\dot{\underline{D}}_{\text{mono}} = 0$ , since no decrease in damage is possible.

Thus, the constitutive law of the cohesive zone model is (see Figure 4-14)

$$\underline{\underline{T}} = \left[ \underline{\underline{I}} - \underline{\underline{D}}_{\text{mono}} \right] \underline{\underline{E}}_{\text{co}} \underline{\underline{\Delta u}}. \quad (4.40)$$

In compression ( $\Delta u_n < 0$ ), the damage tensor becomes null to model penalty contact.

In this case, the cohesive energies needed for mode I,  $\phi_n$ , and mode II or III,  $\phi_t$ , to crack the material are defined by

$$\begin{aligned} \phi_t &= \frac{1}{2} \tau_{\text{max}} \delta_{\text{tc}} \\ \phi_n &= \frac{1}{2} \sigma_{\text{max}} \delta_{\text{nc}}. \end{aligned} \quad (4.41)$$

As a result, the cohesive stiffness matrix is

$$\underline{\underline{C}} = \begin{cases} \left[ \underline{\underline{I}} - \underline{\underline{D}}_{\text{mono}} \right] \underline{\underline{E}}_{\text{co}} & \text{if } \dot{\underline{\underline{D}}}_{\text{mono}} = \underline{\underline{0}} \\ \left[ \underline{\underline{I}} - \underline{\underline{D}}_{\text{mono}} \right] \underline{\underline{E}}_{\text{co}} - \frac{1}{(1+\omega)^{\alpha+1}} \underline{\underline{F}} \underline{\underline{E}}_{\text{co}} \begin{bmatrix} \Delta u_p^\alpha & \Delta u_s^{\alpha-1} \Delta u_p & \Delta u_n^{\alpha-1} \Delta u_p \\ \Delta u_s \Delta u_p^{\alpha-1} & \Delta u_s^\alpha & \Delta u_n^{\alpha-1} \Delta u_s \\ \Delta u_n \Delta u_p^{\alpha-1} & \Delta u_n \Delta u_s^{\alpha-1} & \Delta u_n^\alpha \end{bmatrix} \begin{bmatrix} \frac{1}{\delta_{t0}^\alpha} & 0 & 0 \\ 0 & \frac{1}{\delta_{t0}^\alpha} & 0 \\ 0 & 0 & \frac{1}{\delta_{n0}^\alpha} \end{bmatrix} & \text{if } \dot{\underline{\underline{D}}}_{\text{mono}} > \underline{\underline{0}} \end{cases} \quad (4.42)$$

#### 4.3.3.2 Viscosity

To suppress jump displacement, the bilinear law can be affected by a viscosity parameter. [HAM08] proposes to take the viscosity in a damage tensor,  $\underline{\underline{D}}_v$  into account:

$$\underline{\underline{D}}_v = \begin{bmatrix} \zeta_t \frac{\Delta \dot{u}_p}{\Delta u_p} & 0 & 0 \\ 0 & \zeta_t \frac{\Delta \dot{u}_s}{\Delta u_s} & 0 \\ 0 & 0 & \zeta_n \frac{\Delta \dot{u}_n}{\Delta u_n} \end{bmatrix} \quad (4.43)$$

where  $\zeta_n$  and  $\zeta_t$  are viscosity-like parameters that govern viscous energy dissipation under normal and tangential loading, respectively.

Therefore, Equation (4.40) is modified as follow:

$$\underline{\underline{T}} = \left[ \underline{\underline{I}} - \underline{\underline{D}} \right] \underline{\underline{E}}_{\text{co}} \underline{\underline{\Delta u}} \text{ where } \underline{\underline{D}} = \underline{\underline{D}}_{\text{mono}} + \underline{\underline{D}}_v. \quad (4.44)$$

#### 4.3.3.3 Fatigue Damage

Fatigue damage can be taken into account in the same way as performed in [BOU06]. To do so, one adds the fatigue damage parameter,  $D_f$ , computed by the CDM to the damage tensor,  $\underline{\underline{D}}$ , (see Chapter 3).

$$\underline{\underline{T}} = \left[ \underline{\underline{I}} - \underline{\underline{D}} \right] \underline{\underline{E}}_{\text{co}} \underline{\underline{\Delta u}} \text{ where } \underline{\underline{D}} = \underline{\underline{D}}_{\text{mono}} + \underline{\underline{D}}_v + D_f \underline{\underline{I}} \quad (4.45)$$

However, in this way the fatigue damage reduce the separation when the material is totally debonding (see Figure 4-15 a)). Therefore, the stiffness of the cohesive law when the cohesive stress decreases, which is negative, strongly decreases which can affect the convergence of the computation. Consequently, it was decided to couple the fatigue damage in the same way as in Chapter 4.3.2.2 (see Figure 4-15 b)).

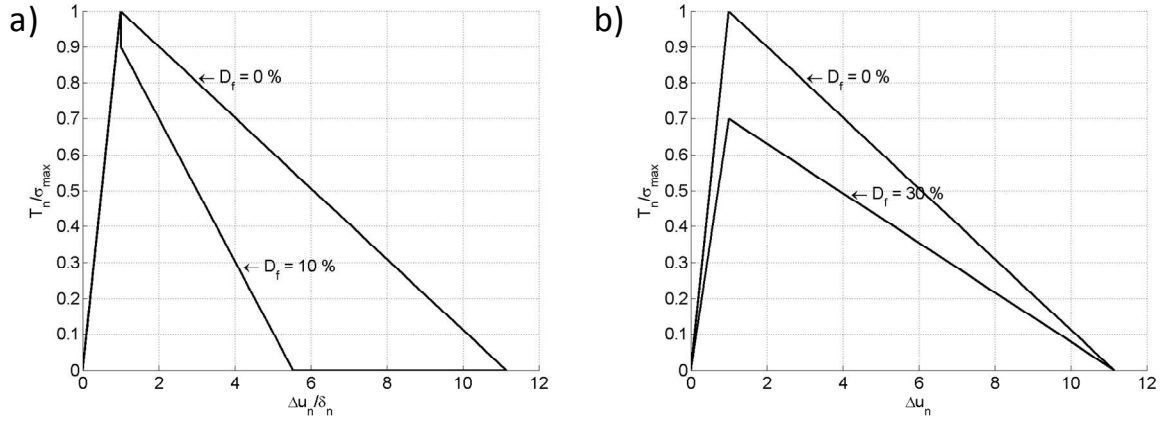


Figure 4-15: Coupling between cohesive zone model and fatigue damage suggested by a) [BOU06] and b) [ROE03]

## 4.4 Implementation of the two-dimensional cohesive element (CZMEL)

### 4.4.1 Element description

The CZMEL element models one side of the interface called the solid interface while a foundation segment models the other side of the interface (see Figure 4-16). These elements contain two nodes, each of which has two translational degrees of freedom. The nodal position vector, for the CZMEL element  $(\underline{x}_n^s)_{4 \times 1}$  and the foundation  $(\underline{x}_n^f)_{4 \times 1}$  in the global coordinates  $(x, y)$  can be written as

$$\begin{aligned} \underline{x}_n^s &= (x_1^s, y_1^s, x_2^s, y_2^s)^T, \\ \underline{x}_n^f &= (x_1^f, y_1^f, x_2^f, y_2^f)^T. \end{aligned} \quad (4.46)$$

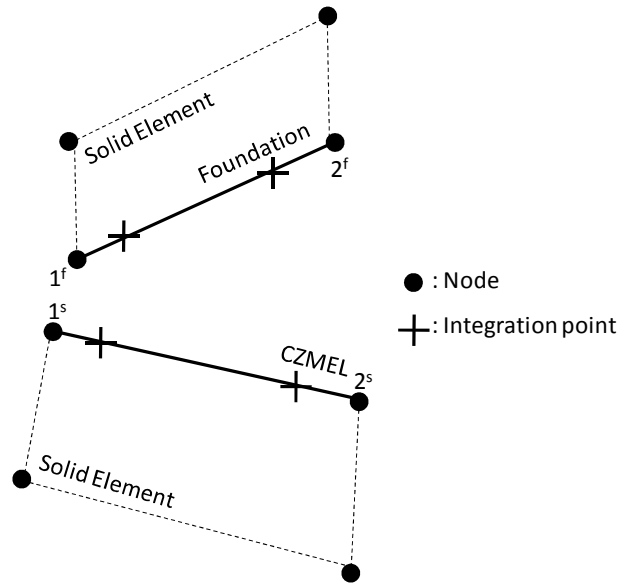


Figure 4-16: Element description

Before the crack occurs the coordinates of the foundation segment and CZMEL element are identical. As the crack progress, separation induces different values for these coordinates.

#### 4.4.2 The isoparametric and the local axes

The mid-plane node positions,  $(\underline{x}_n^m)_{4 \times 1}$ , are the average of the foundation and solid interface node positions.

$$\underline{x}_n^m = \frac{1}{2}(\underline{x}_n^s + \underline{x}_n^f) \quad (4.47)$$

In mode I, a symmetric axis can pass along the mid-plane. That's why only half of the structure and one interface side are sufficient to model this case by finite element simulations. In this model, the interface is the foundation segment and the symmetric axis and the mid-plane are merged with the solid interface (see Figure 4-17). Thus:

$$\underline{x}_n^m = \underline{x}_n^s. \quad (4.48)$$

The isoparametric axis,  $\underline{e}_\xi$ , is an unit vector tangent to the mid-plane. Along this axis, an isoparametric coordinate,  $\xi$ , is defined. Its value is equal to -1 at the first nodal position, 0 in the middle of the axis and 1 at the last nodal position.

The local axes are defined along the mid-plane between the two interfaces (see Figure 4-17). The tangent axis  $\underline{e}_t$  is aligned with to the local isoparametric axis  $\underline{e}_\xi$  and  $\underline{e}_n$  is normal to this axis.

Let the first direction be:

$$\underline{e}_t = \underline{e}_\xi = \frac{1}{\sqrt{\left(\frac{\partial x}{\partial \xi}\right)^2 + \left(\frac{\partial y}{\partial \xi}\right)^2}} \begin{bmatrix} \frac{\partial x}{\partial \xi} \\ \frac{\partial y}{\partial \xi} \end{bmatrix} \quad (4.49)$$

where

$$\begin{cases} \frac{\partial x}{\partial \xi} = \frac{\partial(\phi_i x_i^m)}{\partial \xi} = \frac{\partial \phi_i}{\partial \xi} x_i^m \\ \frac{\partial y}{\partial \xi} = \frac{\partial(\phi_i y_i^m)}{\partial \xi} = \frac{\partial \phi_i}{\partial \xi} y_i^m \end{cases} \quad (4.50)$$

In the same way, for the second direction, let

$$\underline{e}_n = \frac{1}{\sqrt{\left(\frac{\partial x}{\partial \xi}\right)^2 + \left(\frac{\partial y}{\partial \xi}\right)^2}} \begin{bmatrix} -\frac{\partial y}{\partial \xi} \\ \frac{\partial x}{\partial \xi} \end{bmatrix} \quad (4.51)$$

The rotational matrix,  $(\underline{\mathbf{R}})_{2 \times 2}$ , which is used to pass from the global axes to the local axes, has the following form:

$$\begin{bmatrix} \underline{e}_t \\ \underline{e}_n \end{bmatrix} = \underline{\mathbf{R}} \begin{bmatrix} \underline{e}_x \\ \underline{e}_y \end{bmatrix} \quad \text{where } \underline{\mathbf{R}} = \frac{1}{|\underline{\mathbf{J}}|} \begin{bmatrix} \frac{\partial x}{\partial \xi} & \frac{\partial y}{\partial \xi} \\ -\frac{\partial y}{\partial \xi} & \frac{\partial x}{\partial \xi} \end{bmatrix} \quad \text{and } |\underline{\mathbf{J}}| = \sqrt{\left(\frac{\partial x}{\partial \xi}\right)^2 + \left(\frac{\partial y}{\partial \xi}\right)^2} \quad (4.52)$$

where  $|\underline{\mathbf{J}}|$  is the determinant of the Jacobian matrix.

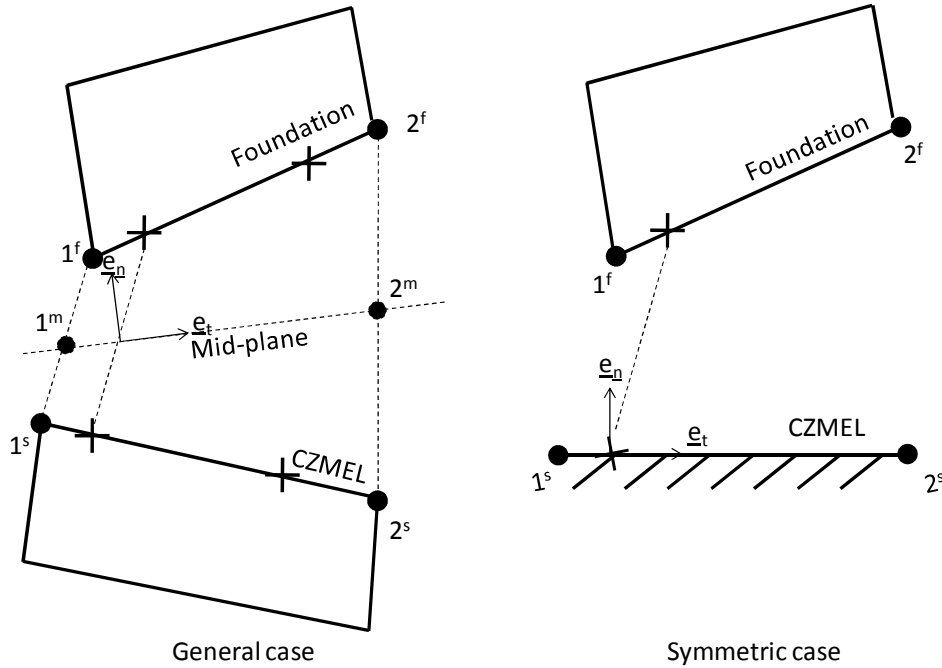


Figure 4-17: Local axes

### 4.4.3 Interpolation functions

To compute the position of any point which belongs to the element or the foundation segment, linear interpolation functions are used in terms of the isoparametric coordinate,  $\xi$ .

One defines the linear interpolation function as:

$$\begin{aligned}\phi_1 &= \frac{1}{2}(1 + \xi) \\ \phi_2 &= \frac{1}{2}(1 - \xi).\end{aligned}\quad (4.53)$$

These linear functions are implemented into the interpolation matrix,  $(\underline{\underline{N}})_{2 \times 4}$ :

$$\underline{\underline{N}} = \begin{bmatrix} \phi_1 & 0 & \phi_2 & 0 \\ 0 & \phi_1 & 0 & \phi_2 \end{bmatrix}. \quad (4.54)$$

The relationship between the continuous position field, either of the CZMEL element  $(\underline{x})_{2 \times 1}$  or the foundation segment  $(\underline{x}^f)_{2 \times 1}$ , and the nodal positions is

$$\begin{aligned}\underline{x}^s &= \begin{bmatrix} x^s \\ y^s \end{bmatrix} = \underline{\underline{N}} \underline{x}_n^s, \\ \underline{x}^f &= \begin{bmatrix} x^f \\ y^f \end{bmatrix} = \underline{\underline{N}} \underline{x}_n^f.\end{aligned}\quad (4.55)$$

#### 4.4.4 Computation of the separation

The separation field in global axes  $(\Delta \underline{x})_{2 \times 1}$  is computed by

$$\Delta \underline{x} = \underline{x}^f - \underline{x}^s = \underline{N}(\underline{x}_n^f - \underline{x}_n^s) \quad (4.56)$$

where  $\underline{N}$  is computed at the same isoparametric coordinate  $\xi$  on the solid and the foundation.

One switches to the local axes with the rotational matrix (see Figure 4-18):

$$\Delta \underline{u} = \begin{bmatrix} \Delta u_t \\ \Delta u_n \end{bmatrix} = \underline{R} \Delta \underline{x} = \underline{R} \underline{N}(\underline{x}_n^f - \underline{x}_n^s) \quad (4.57)$$

where  $\underline{R}$  is computed along the mid-plane at the same  $\xi$ .

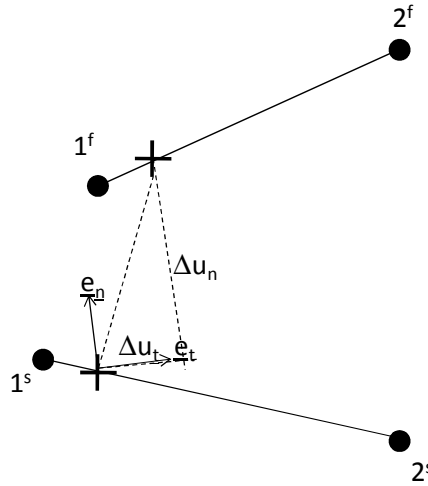


Figure 4-18: Local separation

#### 4.4.5 Computation of the nodal forces and the tangent stiffness matrix

The nodal forces on the solid,  $(\underline{F}^s)_{4 \times 1}$ , and on the foundation,  $(\underline{F}^f)_{4 \times 1}$ , generated by the cohesive stresses are defined by:

$$\begin{aligned} \underline{F}_n^s &= -\int_{l^s} \underline{N}^T \underline{R}^T \underline{T} dl = -\int_{-1}^1 \underline{N}^T \underline{R}^T \underline{T} |\underline{J}| d\xi \\ \underline{F}_n^f &= \int_{l^f} \underline{N}^T \underline{R}^T \underline{T} dl = \int_{-1}^1 \underline{N}^T \underline{R}^T \underline{T} |\underline{J}| d\xi \end{aligned} \quad (4.58)$$

where  $l^s$  and  $l^f$  are the CZMEL element and foundation segment lengths respectively.

The integration is numerical following the Gauss' scheme with 1 to 9 integration points. Finally, Equation (4.58) becomes:

$$\begin{aligned}\underline{\underline{F}}_n^s &= -\sum_{\text{IP}} \underline{\underline{N}}^T \underline{\underline{R}}^T \underline{\underline{T}} | \underline{\underline{J}} | \underline{\underline{W}} \\ \underline{\underline{F}}_n^f &= \sum_{\text{IP}} \underline{\underline{N}}^T \underline{\underline{R}}^T \underline{\underline{T}} | \underline{\underline{J}} | \underline{\underline{W}}\end{aligned}\quad (4.59)$$

To obtain the compliance stiffness matrix, one differentiates Equation (4.59).

$$\begin{aligned}d\underline{\underline{F}}_n^s &= -\sum_{\text{IP}} \underline{\underline{N}}^T d(\underline{\underline{R}}^T | \underline{\underline{J}} |) \underline{\underline{T}} \underline{\underline{W}} - \sum_{\text{IP}} \underline{\underline{N}}^T \underline{\underline{R}}^T d\underline{\underline{T}} | \underline{\underline{J}} | \underline{\underline{W}} \\ d\underline{\underline{F}}_n^f &= \sum_{\text{IP}} \underline{\underline{N}}^T d(\underline{\underline{R}}^T | \underline{\underline{J}} |) \underline{\underline{T}} \underline{\underline{W}} + \sum_{\text{IP}} \underline{\underline{N}}^T \underline{\underline{R}}^T d\underline{\underline{T}} | \underline{\underline{J}} | \underline{\underline{W}}\end{aligned}\quad (4.60)$$

Stress matrix                      Classical matrix

It is appropriate to differentiate  $\underline{\underline{R}}$  and  $| \underline{\underline{J}} |$  simultaneously, because  $| \underline{\underline{J}} |$  appears in the denominator of most  $\underline{\underline{R}}$  terms. There are two terms in the derivative of the nodal forces on the solid and the foundation:

- $(d\underline{\underline{F}}_c^i)_{4 \times 1}$  which comes from the derivative of the rotation and Jacobian's determinant and which yields the stress matrix;
- $(d\underline{\underline{F}}_h^i)_{4 \times 1}$  which comes from the derivative of the cohesive stress and which yields the classic matrix.

The derivative of the cohesive stresses is directly linked to the derivative of the separation (see Section 4.3) by

$$d\underline{\underline{T}} = \underline{\underline{C}} d(\Delta \underline{\underline{u}}). \quad (4.61)$$

By neglecting rotation variation for one step,

$$d(\Delta \underline{\underline{u}}) = \underline{\underline{R}} d(\Delta \underline{\underline{x}}). \quad (4.62)$$

So, from Equation (4.57), the last equation becomes:

$$d(\Delta \underline{\underline{u}}) = \underline{\underline{R}} d(\underline{\underline{N}} \Delta \underline{\underline{x}}_n) = \underline{\underline{R}} \underline{\underline{N}} d(\underline{\underline{x}}_n^f - \underline{\underline{x}}_n^s). \quad (4.63)$$

So, the classic matrix becomes

$$\begin{aligned}d\underline{\underline{F}}_h^s &= -\sum_{\text{IP}} \underline{\underline{N}}^T \underline{\underline{R}}^T \underline{\underline{C}} \underline{\underline{R}} \underline{\underline{N}} d(\Delta \underline{\underline{x}}_n) | \underline{\underline{J}} | \underline{\underline{W}} = \sum_{\text{IP}} \underline{\underline{N}}^T \underline{\underline{R}}^T \underline{\underline{C}} \underline{\underline{R}} \underline{\underline{N}} | \underline{\underline{J}} | \underline{\underline{W}} d\underline{\underline{x}}_n^s - \sum_{\text{IP}} \underline{\underline{N}}^T \underline{\underline{R}}^T \underline{\underline{C}} \underline{\underline{R}} \underline{\underline{N}} | \underline{\underline{J}} | \underline{\underline{W}} d\underline{\underline{x}}_n^f \\ &\qquad\qquad\qquad \text{Solid/Solid} \qquad\qquad\qquad \text{Solid/Foundation} \\ d\underline{\underline{F}}_h^f &= \sum_{\text{IP}} \underline{\underline{N}}^T \underline{\underline{R}}^T \underline{\underline{C}} \underline{\underline{R}} \underline{\underline{N}} d(\Delta \underline{\underline{x}}_n) | \underline{\underline{J}} | \underline{\underline{W}} = -\sum_{\text{IP}} \underline{\underline{N}}^T \underline{\underline{R}}^T \underline{\underline{C}} \underline{\underline{R}} \underline{\underline{N}} | \underline{\underline{J}} | \underline{\underline{W}} d\underline{\underline{x}}_n^s + \sum_{\text{IP}} \underline{\underline{N}}^T \underline{\underline{R}}^T \underline{\underline{C}} \underline{\underline{R}} \underline{\underline{N}} | \underline{\underline{J}} | \underline{\underline{W}} d\underline{\underline{x}}_n^f \\ &\qquad\qquad\qquad \text{Foundation/Solid} \qquad\qquad\qquad \text{Foundation/Foundation}\end{aligned}\quad (4.64)$$

To obtain the stress matrix one has to differentiate  $d(\underline{\underline{R}}^T \underline{\underline{J}})$ . One can demonstrate that



$$\underline{\underline{R}}^T \underline{\underline{J}} = \underline{\underline{B}}_t \underline{\underline{x}}_n^m \underline{\underline{e}}_x^T + \underline{\underline{B}}_n \underline{\underline{x}}_n^m \underline{\underline{e}}_y^T$$

$$\text{where } \underline{\underline{B}}_t = \begin{bmatrix} \frac{\partial \phi_1}{\partial \xi} & 0 & \frac{\partial \phi_2}{\partial \xi} & 0 \\ 0 & \frac{\partial \phi_1}{\partial \xi} & 0 & \frac{\partial \phi_2}{\partial \xi} \end{bmatrix} \text{ and } \underline{\underline{B}}_n = \begin{bmatrix} 0 & -\frac{\partial \phi_1}{\partial \xi} & 0 & -\frac{\partial \phi_2}{\partial \xi} \\ \frac{\partial \phi_1}{\partial \xi} & 0 & \frac{\partial \phi_2}{\partial \xi} & 0 \end{bmatrix}. \quad (4.65)$$

Thus

$$d(\underline{\underline{R}}^T \underline{\underline{J}}) = \underline{\underline{B}}_t d\underline{\underline{x}}_n^m \underline{\underline{e}}_x^T + \underline{\underline{B}}_n d\underline{\underline{x}}_n^m \underline{\underline{e}}_y^T. \quad (4.66)$$

The stress matrix is defined by the following equation:

$$d\underline{\underline{F}}_c^s = -\sum_{IP} \underline{\underline{N}}^T (\underline{\underline{B}}_t d\underline{\underline{x}}_n^m \underline{\underline{e}}_x^T + \underline{\underline{B}}_n d\underline{\underline{x}}_n^m \underline{\underline{e}}_y^T) \underline{\underline{T}} \underline{\underline{W}} = -\sum_{IP} \underline{\underline{N}}^T (\underline{\underline{T}}_t \underline{\underline{B}}_t + \underline{\underline{T}}_n \underline{\underline{B}}_n) d\underline{\underline{x}}_n^m \underline{\underline{W}}$$

$$d\underline{\underline{F}}_c^f = \sum_{IP} \underline{\underline{N}}^T (\underline{\underline{B}}_t d\underline{\underline{x}}_n^m \underline{\underline{e}}_x^T + \underline{\underline{B}}_n d\underline{\underline{x}}_n^m \underline{\underline{e}}_y^T) \underline{\underline{T}} \underline{\underline{W}} = \sum_{IP} \underline{\underline{N}}^T (\underline{\underline{T}}_t \underline{\underline{B}}_t + \underline{\underline{T}}_n \underline{\underline{B}}_n) d\underline{\underline{x}}_n^m \underline{\underline{W}}. \quad (4.67)$$

Finally,

$$d\underline{\underline{F}}_c^s = -\sum_{IP} \frac{1}{2} \underline{\underline{N}}^T (\underline{\underline{T}}_t \underline{\underline{B}}_t + \underline{\underline{T}}_n \underline{\underline{B}}_n) \underline{\underline{W}} d\underline{\underline{x}}_n^s - \sum_{IP} \frac{1}{2} \underline{\underline{N}}^T (\underline{\underline{T}}_t \underline{\underline{B}}_t + \underline{\underline{T}}_n \underline{\underline{B}}_n) \underline{\underline{W}} d\underline{\underline{x}}_n^f$$

Solid/Solid Solid/Foundation

$$d\underline{\underline{F}}_c^f = \sum_{IP} \frac{1}{2} \underline{\underline{N}}^T (\underline{\underline{T}}_t \underline{\underline{B}}_t + \underline{\underline{T}}_n \underline{\underline{B}}_n) \underline{\underline{W}} d\underline{\underline{x}}_n^s + \sum_{IP} \frac{1}{2} \underline{\underline{N}}^T (\underline{\underline{T}}_t \underline{\underline{B}}_t + \underline{\underline{T}}_n \underline{\underline{B}}_n) \underline{\underline{W}} d\underline{\underline{x}}_n^f$$

Foundation/Solid Foundation/Foundation

$$(4.68)$$

For symmetry axes, the previous relationship can be simplified as follows.

$$d\underline{\underline{F}}_c^s = -\sum_{IP} \frac{1}{2} \underline{\underline{N}}^T (\underline{\underline{T}}_t \underline{\underline{B}}_1 + \underline{\underline{T}}_n \underline{\underline{B}}_2) d\underline{\underline{x}}_n^s \underline{\underline{W}}$$

Solid/Solid

$$d\underline{\underline{F}}_c^f = \sum_{IP} \frac{1}{2} \underline{\underline{N}}^T (\underline{\underline{T}}_t \underline{\underline{B}}_1 + \underline{\underline{T}}_n \underline{\underline{B}}_2) d\underline{\underline{x}}_n^s \underline{\underline{W}}.$$

Foundation/Solid

$$(4.69)$$

## 4.5 Implementation of the three dimensional cohesive element (CZM3D)

### 4.5.1 Element description

A three-dimensional cohesive element has been developed in the Lagamine code. In this element, each crack interface's side is modeled by 4 nodes (see Figure 4-19). They are called, respectively,

- CZM3D or solid element,
- foundation segment.

CZM3D and foundation are 4-node plane elements. As a result, they can contain 1, 4 or 9 integration points.

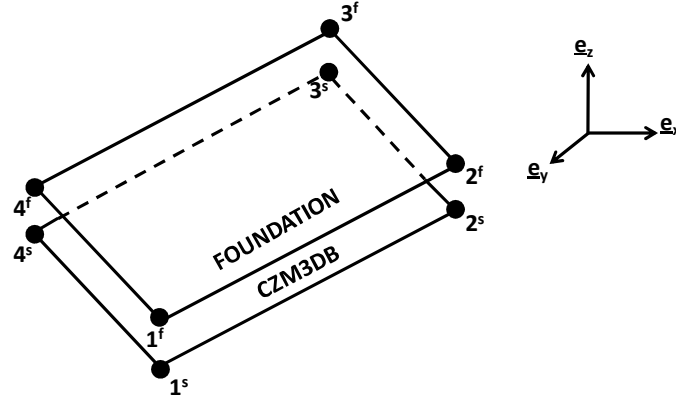


Figure 4-19: Description of CZM3D

The nodal position vector for the element  $(\underline{x}_n^s)_{12 \times 1}$  and the foundation  $(\underline{x}_n^f)_{12 \times 1}$  in the global coordinates  $(x, y)$  can be written

$$\begin{aligned} \underline{x}_n^s &= (x_1^s, y_1^s, z_1^s, x_2^s, y_2^s, z_2^s, x_3^s, y_3^s, z_3^s, x_4^s, y_4^s, z_4^s)^T \\ \underline{x}_n^f &= (x_1^f, y_1^f, z_1^f, x_2^f, y_2^f, z_2^f, x_3^f, y_3^f, z_3^f, x_4^f, y_4^f, z_4^f)^T. \end{aligned} \quad (4.70)$$

#### 4.5.2 The isoparametric and local axes

So that the separation associated with the cohesive stresses keeps its value during large strains and displacement, the normal vector of the CZM3D and the foundation to the surface always has to be directed outward from of the structure. This is achieved by defining the list of the element nodes so that the so-called corkscrew rule, applied to their sequence, may give the outer normal vector.

The mid-plane nodal positions,  $(\underline{x}_n^m)_{12 \times 1}$ , are obtained by calculating the average of the foundation and solid interface nodal positions according to Equation (4.47).

The directions  $\underline{e}_\xi$  and  $\underline{e}_\eta$  of the  $\xi$  and  $\eta$  isoparametric lines are defined by

$$\begin{aligned}
\underline{e}_\xi &= \frac{1}{\sqrt{\left(\frac{\partial x}{\partial \xi}\right)^2 + \left(\frac{\partial y}{\partial \xi}\right)^2 + \left(\frac{\partial z}{\partial \xi}\right)^2}} \begin{bmatrix} \frac{\partial x}{\partial \xi} \\ \frac{\partial y}{\partial \xi} \\ \frac{\partial z}{\partial \xi} \end{bmatrix} \\
\underline{e}_\eta &= \frac{1}{\sqrt{\left(\frac{\partial x}{\partial \eta}\right)^2 + \left(\frac{\partial y}{\partial \eta}\right)^2 + \left(\frac{\partial z}{\partial \eta}\right)^2}} \begin{bmatrix} \frac{\partial x}{\partial \eta} \\ \frac{\partial y}{\partial \eta} \\ \frac{\partial z}{\partial \eta} \end{bmatrix} \\
\text{with : } &\begin{cases} x = \phi_i x_i, \dots, \\ \frac{\partial x}{\partial \xi} = \frac{\partial \phi_i}{\partial \xi} x_i, \dots, \\ \frac{\partial x}{\partial \eta} = \frac{\partial \phi_i}{\partial \eta} x_i, \dots, \end{cases}
\end{aligned} \tag{4.71}$$

where  $x_i$ ,  $y_i$  and  $z_i$  are the global positions of the nodes and  $\phi_i$  is the interpolation function.

The rotational matrix is determined by connecting the global triad ( $\underline{e}_x$ ,  $\underline{e}_y$ ,  $\underline{e}_z$ ) to the local one ( $\underline{e}_p$ ,  $\underline{e}_r$ ,  $\underline{e}_n$ ). The local axes are defined along the mid-plane between the two interfaces or along the CZM3D element in symmetric cases (see Figure 4-20).

The local vector,  $\underline{e}_p$ , is equal to the isoparametric vector  $\underline{e}_\xi$ .

$$\underline{e}_p = \underline{e}_\xi = \begin{bmatrix} \mathbf{P}_x \\ \mathbf{P}_y \\ \mathbf{P}_z \end{bmatrix} \tag{4.72}$$

The local vector  $\underline{e}_n$  is obtained by the cross product between  $\underline{e}_\xi$  and  $\underline{e}_\eta$ .

$$\underline{e}_n^s = \underline{e}_\xi \Lambda \underline{e}_\eta = \frac{1}{|\underline{J}|} \begin{bmatrix} \frac{\partial y}{\partial \xi} \frac{\partial z}{\partial \eta} - \frac{\partial y}{\partial \xi} \frac{\partial z}{\partial \eta} \\ -\frac{\partial x}{\partial \xi} \frac{\partial z}{\partial \eta} + \frac{\partial x}{\partial \xi} \frac{\partial z}{\partial \eta} \\ \frac{\partial x}{\partial \xi} \frac{\partial y}{\partial \eta} - \frac{\partial x}{\partial \xi} \frac{\partial y}{\partial \eta} \end{bmatrix} = \begin{bmatrix} N_x \\ N_y \\ N_z \end{bmatrix} \quad (4.73)$$

$$\text{with } |\underline{J}| = \sqrt{\left(\frac{\partial x}{\partial \xi}\right)^2 + \left(\frac{\partial y}{\partial \xi}\right)^2 + \left(\frac{\partial z}{\partial \xi}\right)^2} \cdot \sqrt{\left(\frac{\partial x}{\partial \eta}\right)^2 + \left(\frac{\partial y}{\partial \eta}\right)^2 + \left(\frac{\partial z}{\partial \eta}\right)^2}$$

$|\underline{J}|$  is the determinant of the Jacobian matrix of the transformation from global coordinates (x, y, z) to local coordinates ( $\xi$ ,  $\eta$ ).

Finally, the local vector,  $\underline{e}_s$ , is obtained by the cross product between  $\underline{e}_p$  and  $\underline{e}_n$ .

$$\underline{e}_s = \underline{e}_n \Lambda \underline{e}_p = \begin{bmatrix} S_x \\ S_y \\ S_z \end{bmatrix} \quad (4.74)$$

The rotational matrix,  $\underline{R}$ , which is used to pass from global axes, ( $\underline{e}_x$ ,  $\underline{e}_y$ ,  $\underline{e}_z$ ), to local axes, ( $\underline{e}_p$ ,  $\underline{e}_s$ ,  $\underline{e}_n$ ), is defined by

$$\begin{bmatrix} \underline{e}_p \\ \underline{e}_s \\ \underline{e}_n \end{bmatrix} = \begin{bmatrix} P_x & P_y & P_z \\ S_x & S_y & S_z \\ N_x & N_y & N_z \end{bmatrix} \begin{bmatrix} \underline{e}_x \\ \underline{e}_y \\ \underline{e}_z \end{bmatrix} = \underline{R} \begin{bmatrix} \underline{e}_x \\ \underline{e}_y \\ \underline{e}_z \end{bmatrix} \quad (4.75)$$

where  $P_i$ ,  $S_i$  and  $N_i$  are defined in (4.72), (4.74) and (4.73) respectively.

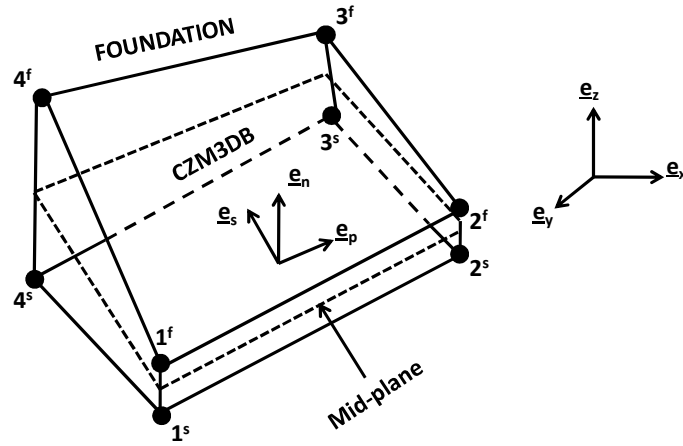


Figure 4-20: Local axes definition

### 4.5.3 Interpolation functions

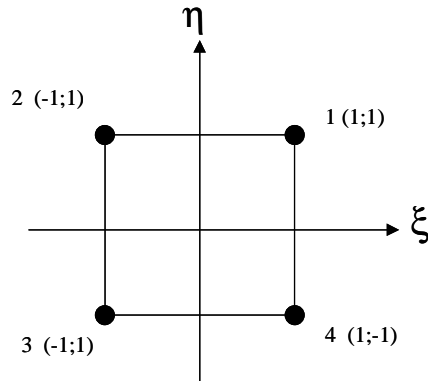


Figure 4-21: Local axis along the CZM3D

To compute the relative continuous position field in the element and in the foundation, a linear interpolation is used in terms of isoparametric coordinates,  $\xi$  and  $\eta$  (see Figure 4-21). Let the linear interpolation function be defined as:

$$\begin{aligned}
\phi_1 &= \frac{1}{4}(1-\xi)(1-\eta), \\
\phi_2 &= \frac{1}{4}(1+\xi)(1-\eta), \\
\phi_3 &= \frac{1}{4}(1+\xi)(1+\eta), \\
\phi_4 &= \frac{1}{4}(1-\xi)(1+\eta).
\end{aligned} \tag{4.76}$$

Then, these linear functions are introduced into the interpolation matrix ( $\underline{\underline{N}}$ )<sub>3x12</sub>:

$$\underline{\underline{N}} = \begin{bmatrix} \phi_1 & 0 & 0 & \phi_2 & 0 & 0 & \phi_3 & 0 & 0 & \phi_4 & 0 & 0 \\ 0 & \phi_1 & 0 & 0 & \phi_2 & 0 & 0 & \phi_3 & 0 & 0 & \phi_4 & 0 \\ 0 & 0 & \phi_1 & 0 & 0 & \phi_2 & 0 & 0 & \phi_3 & 0 & 0 & \phi_4 \end{bmatrix}. \tag{4.77}$$

Finally, the relationship between the continuous position field and the nodal position becomes

$$\begin{aligned}
\underline{\underline{x}}^s &= \begin{bmatrix} x^s \\ y^s \\ z^s \end{bmatrix} = \underline{\underline{N}} \underline{\underline{x}}_n^s, \\
\underline{\underline{x}}^f &= \begin{bmatrix} x^f \\ y^f \\ z^f \end{bmatrix} = \underline{\underline{N}} \underline{\underline{x}}_n^f.
\end{aligned} \tag{4.78}$$

#### 4.5.4 Computation of the separation

The separation field in the global axes is computed by

$$\Delta \underline{\underline{x}} = \underline{\underline{x}}^f - \underline{\underline{x}}^s = \underline{\underline{N}} (\underline{\underline{x}}_n^f - \underline{\underline{x}}_n^s) \tag{4.79}$$

where  $\underline{\underline{N}}$  is computed using the same isoparametric coordinates,  $\xi$  and  $\eta$ , on the solid and the foundation segment. One switches to the local axis with the rotational matrix:

$$\underline{\underline{u}} = \begin{bmatrix} \Delta u_p \\ \Delta u_s \\ \Delta u_n \end{bmatrix} = \underline{\underline{R}} \Delta \underline{\underline{x}} = \underline{\underline{R}} \underline{\underline{N}} (\underline{\underline{x}}_n^f - \underline{\underline{x}}_n^s) \tag{4.80}$$

where  $\underline{\underline{R}}$  is computed along the mid-plane at the same isoparametric coordinates for  $\xi$  and  $\eta$ .

#### 4.5.5 Computation of the nodal force and the tangent stiffness matrix

The nodal cohesive forces are computed by Equation (4.59) on the CZM3D element ( $\underline{\underline{F}}^s$ ) and foundation ( $\underline{\underline{F}}^f$ ). The stiffness matrix is the derivative of the nodal forces with respect to the nodal displacements of the CZM3D element in Equation (4.60).

As for 2D, two sub-matrices appear then: a classic matrix, obtained by derivation of the stresses, and a stress matrix, obtained by derivation of the geometry. The classic matrix is computed according to Equation (4.64). The stress matrix is obtained by derivation of  $(\underline{\mathbf{R}}^T \underline{\mathbf{J}})$ , but will not be discussed in this thesis.

Note: Stiffness can also be computed by perturbation of each degree of freedom too.

## 4.6 Coupling with fatigue damage

The fatigue damage was computed according to the fatigue Continuum Damage Model of Lemaître and Chaboche discussed in Chapter 3. Depending on the cohesive law used, the coupling in the constitutive cohesive law was described in sections 4.3.2.2 and 4.3.3.3. However, the fatigue damage was computed from the stress tensor components and as a result in the solid elements. The method to transfer the fatigue damage from the solid elements to the cohesive elements is illustrated in Figure 4-22. The fatigue damage transferred to integration points of the cohesive element was the mean of the fatigue damages computed in the integration points of the solid element linked to the cohesive element and to the foundation segment. In the studied cases, the solid elements contained only one integration point for two-dimensional and three-dimensional simulations.

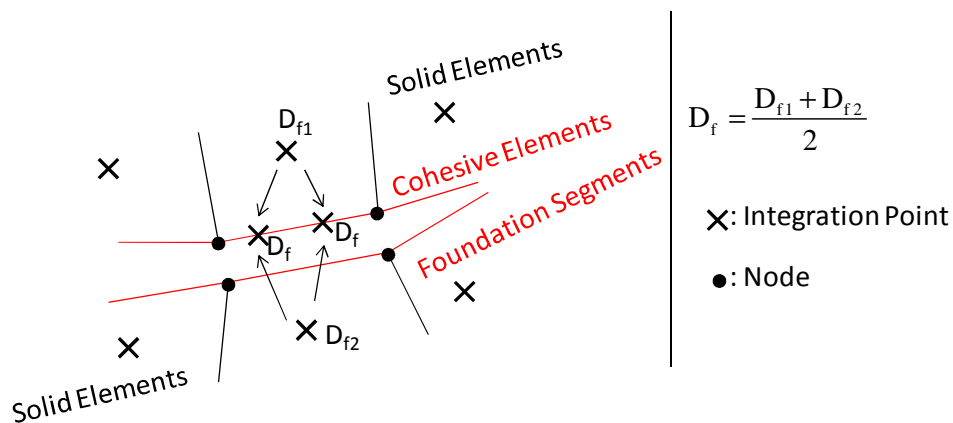


Figure 4-22: Transfer of fatigue damage from solid elements to cohesive elements

## 4.7 Identification of parameters

### 4.7.1 Identification method

The method used to identify the cohesive parameters was the inverse method. A three-point bend testing was performed on a specimen, which was extracted from the base metal. The welding metal was identified by the Charpy-V test.

Next, the three point bend testing was modeled by finite elements simulations with cohesive elements by knowing the mechanical parameters (see Chapter 2.5.4). In the first step, the effect of each material cohesive parameter variation was tested by two-dimensional analyses. Then, the parameter identification was performed by three-dimensional analyses because the crack's

growth is an average along the thickness of the sample. Finally, an initial set of cohesive parameters was chosen and the output data of the test were compared with the simulated ones.

The aim of this study was to identify the mode I. Modes II and III will be neglected in this study because they were expected to be minor in the crack mechanism studied and no experimental test was available to identify them. Cohesive parameters were thus considered to be equivalent for mode I, II and III in this study (i.e. isotropic behavior).

#### **4.7.2 Three-point bend testing**

The three point bend testing analyzed was performed by Corus according to the [BSI91] standards on the base metal. This test was used to identify the critical Rice integral,  $J_{IC}$ , experimentally for a metallic material under displacement due to monotonic loading at a quasi-static rate. The method uses fatigued, pre-cracked specimens which have been loaded by three rollers to fracture or maximum force at room temperature. The specimens were extracted from the column flange, the locations of which are defined in Figure 4-23. The geometry of the specimen is given in Figure 4-24. The initial crack length,  $a_0$ , is equal to the half of the sample thickness. The results of this test provided the J-integral,  $J$ , as a function of the crack's growth,  $\Delta a$ , and the force,  $F$ , as a function of the load line displacement,  $v_{LL}$  (see Figure 4-25).



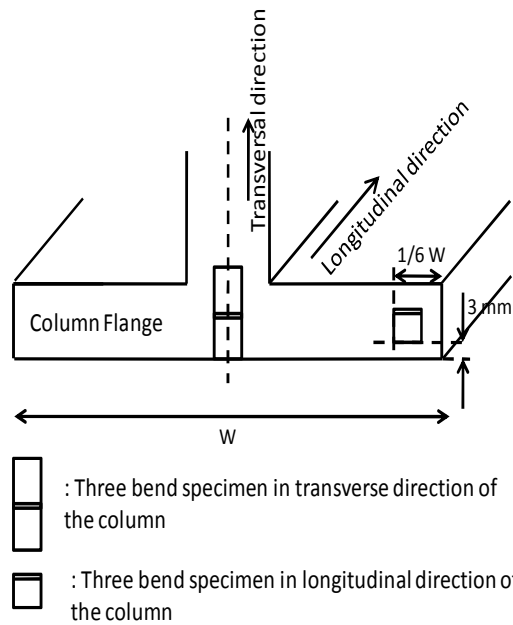
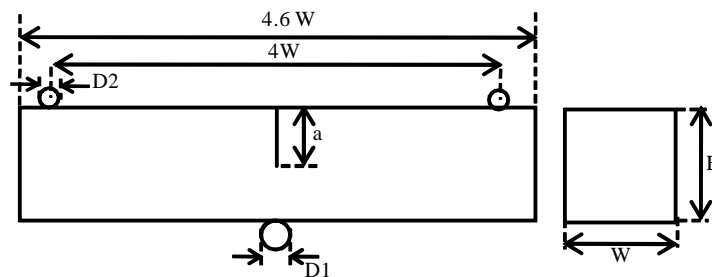


Figure 4-23: Extraction locations of the three-point bend specimens



$W = B = 25 \text{ mm}$

$a_0 = W/2; D1 = W/4; D2 = W/6$

Figure 4-24: Geometry of the specimen

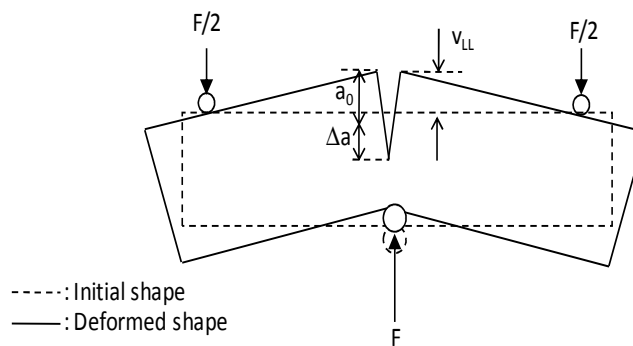


Figure 4-25: Variable Measured during the experiment

For different specimens, the force,  $F$ , versus the load line displacement,  $v_{LL}$ , was measured (see Figure 4-25). The crack's growth,  $\Delta a$ , was measured at nine equally distant on the thickness points, where the outer points were located at 1% of the thickness from the specimen's surface. This growth value was obtained firstly by averaging the two measurements at the outer points and then averaging this value with the inner points.

The J-integral was computed from the force-load line displacement plot. International Standard ISO 12135 provides a method to compute an equivalent J-integral for experimental tests. In the case of a three-point bend specimen, it is computed from the force displacement plot by Equation (4.81):

$$J = \left[ \frac{FS}{BW^{1.5}} g_1 \left( \frac{a_0}{W} \right) \right]^2 \left[ \frac{(1-\nu^2)}{E} \right] + \left[ \frac{\eta_p U_p}{B(W-a_0)} \right]$$

$$\text{with } g_1 \left( \frac{a}{W} \right) = \frac{3 \left( \frac{a_0}{W} \right)^{0.5} \left[ 1.99 - \left( \frac{a_0}{W} \right) \left( 1 - \frac{a_0}{W} \right) \left( 2.15 - \frac{3.93a_0}{W} + \frac{2.7a_0^2}{W^2} \right) \right]}{2 \left( 1 + \frac{2a_0}{W} \right) \left( 1 - \frac{a_0}{W} \right)^{1.5}} \quad (4.81)$$

where  $F$  is the force submitted by the downward roller,  $\nu$  is Poisson's ratio,  $E$  is Young's modulus,  $a_0$  is the initial crack length,  $B$ ,  $W$  and  $S$  are the geometrical parameters of the specimen (see Figure 4-24),  $U_p$  is the plastic component of area under the force ( $F$ ) versus the load-line displacement ( $v_{LL}$ ) plot (see Figure 4-26) and  $\eta_p$  is the 'eta' rotation factor, which is equal to 2 for three-point bend specimens for an  $a_0/W$  ratio ranging from 0.45 to 0.7.

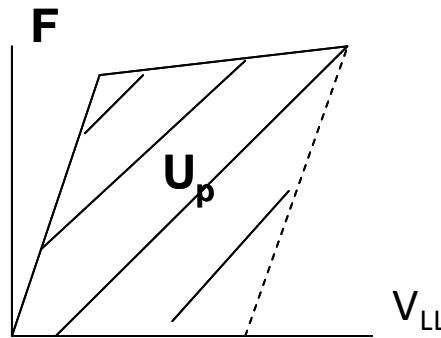


Figure 4-26: Definition of  $U_p$

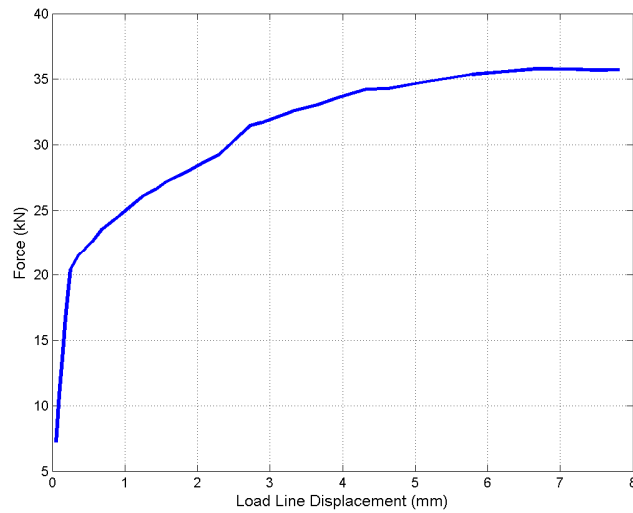
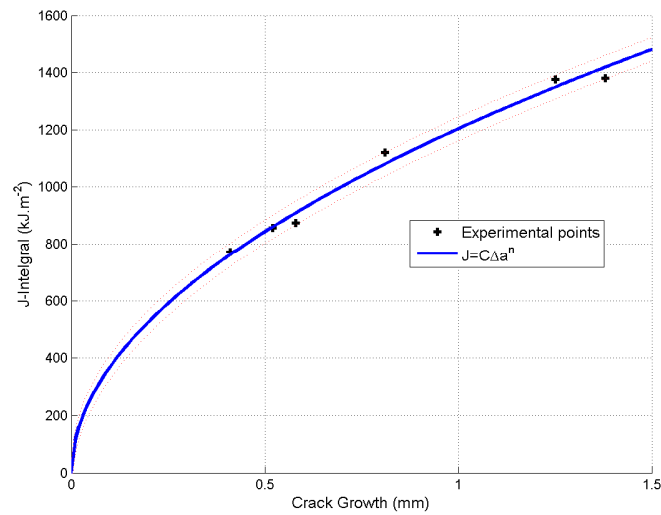
For the base metal, Figure 4-27 and Figure 4-28 provide the test results from a three-point bend testing on a sample extracted in the transversal direction. The experimental points of the J-integral versus crack growth curve can be fitted with a power law as described in [WIL99]:

$$J = C\Delta a^n \quad (4.82)$$

The values for this relationship are given in Table 4-2 and the fitted curve is in Figure 4-28.

**Table 4-2: Coefficient of the power law for the J- $\Delta a$  curve for the BM**

C (kJ.m <sup>-2</sup> )	n
1203	0.51

**Figure 4-27: Force displacement plot from the CTOD test on the base metal****Figure 4-28: Crack growth in function of the J-integral from the three-point bend testing on the base metal**

### 4.7.3 Identification of the J-integral-Crack growth plot from Charpy-V notch test

No three-point bend testing was performed on the weld metal. However, [WAL01] proposes a method to identify the J-integral versus crack growth plot using a Charpy-V notch test. This test measures the energy required to crack a notch specimen by impact (see Figure 4-29). A striker, which is mounted on the end of a pendulum and for which initial kinematic energy is known, impacts the notched specimen. The notch can have either V shape or U shape. The variation in the kinematic energy after the impact gives the energy required to yield the material and crack the specimen, called Charpy energy, noticed CVN.

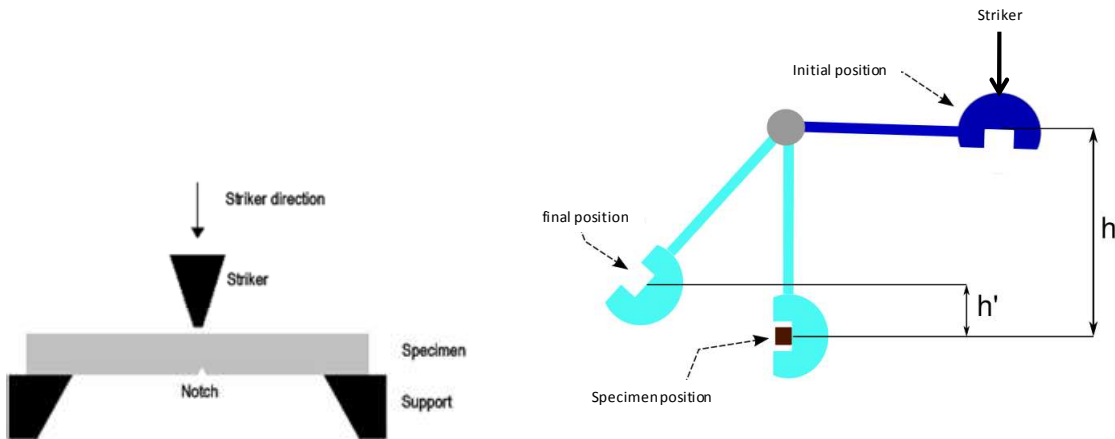


Figure 4-29: Charpy test description

[WAL01] analyzed 112 multispecimens J-integral versus crack growth curves from a wide variety of materials. A simple power-law description of the curves was correlated to the Charpy-V notch energy,  $CVN_{US}$ .

$$J_I = J_{Imm} \Delta a^m \text{ where } \begin{cases} J_{Imm} = 0.53 CVN_{US}^{1.28} \exp\left(-\frac{T-20}{400}\right) \\ m = 0.133 CVN_{US}^{0.256} \exp\left(-\frac{T-20}{2000}\right) - \frac{\sigma_y}{4664} + 0.03 \end{cases} \quad (4.83)$$

where  $T$  is the temperature of the sample.

Corus performed a Charpy-V notch test on weld metal. The specimens were extracted in the welding zone at the root and cap positions (see Figure 4-30). They proposed the coefficients in Table 4-3 of the power law description of the J-integral versus crack growth curve. The plot obtained shows that the weld metal crack strength was weaker than the base metal. Indeed, the weld metal was less ductile according to the tensile test (see Chapter 2.5.4). As no other data are available, these experimental data were used for the parametric identification.

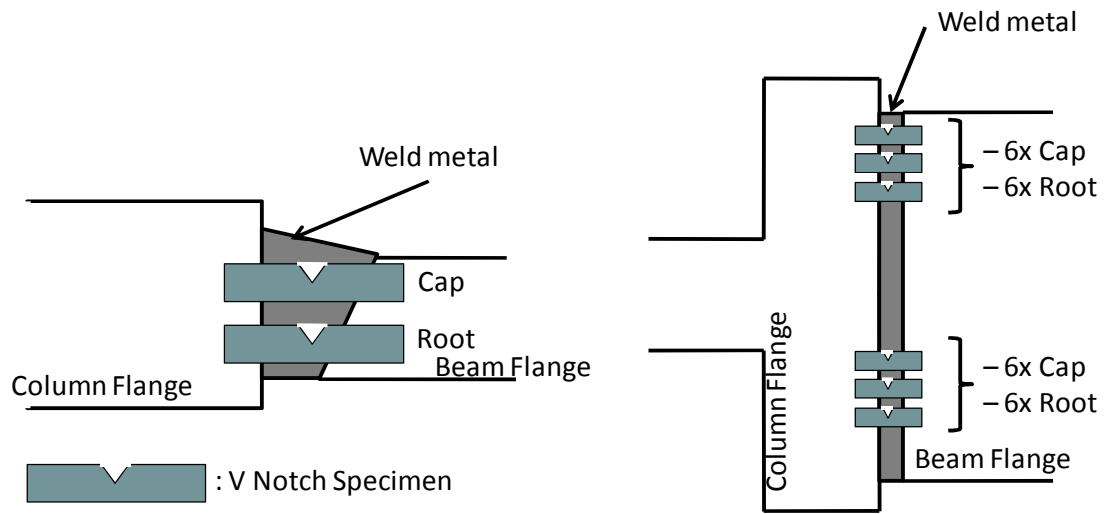


Figure 4-30: Extraction location for the weld metal V notch specimen

Table 4-3: Parameters of the power law of the J-integral versus crack growth plot for the weld metal

$J_{Imm}$ ( $\text{kJ}\cdot\text{m}^{-2}$ )	m
237.84	0.379

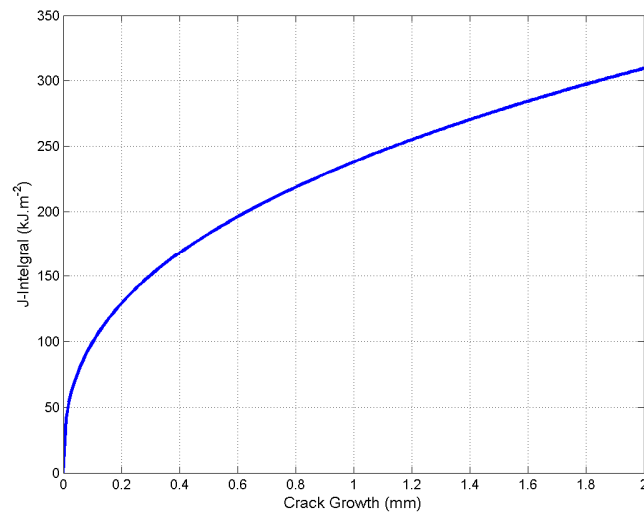


Figure 4-31: Crack growth in function of the J-integral for the base metal

## 4.7.4 Parametric study

### 4.7.4.1 Modeling

The aim of these analyses was to understand the effect of variations in each parameter on the model. The analysis is two dimensional in a plane stress state which is equivalent to the center of the specimen. Due to the symmetry of the geometry and the loading, only half of the specimen was modeled. Therefore, all nodes along the symmetric axis were fixed in the horizontal direction. The three-point bend specimen was modeled (see Figure 4-32) by a 4-nodes mixed solid element: BLZ2D [ZHU95]. The constitutive law was elasto-plastic with isotropic hardening and von Mises' criterion. The mechanical parameters are listed in 0 and were taken from the base metal parameters. The three rollers were modeled by non-deformable, circular foundations and the contact zones were modeled by CNTPC element with a penalty method [HAB98]. The parameters of this contact law can be found in Table 4-4. The fatigued pre-crack was modeled by letting the nodes free along the symmetric axis. The crack path was assumed to be along the symmetric axis because this is where the longitudinal stresses are the highest; therefore, the cohesive zone elements were located on this axis.

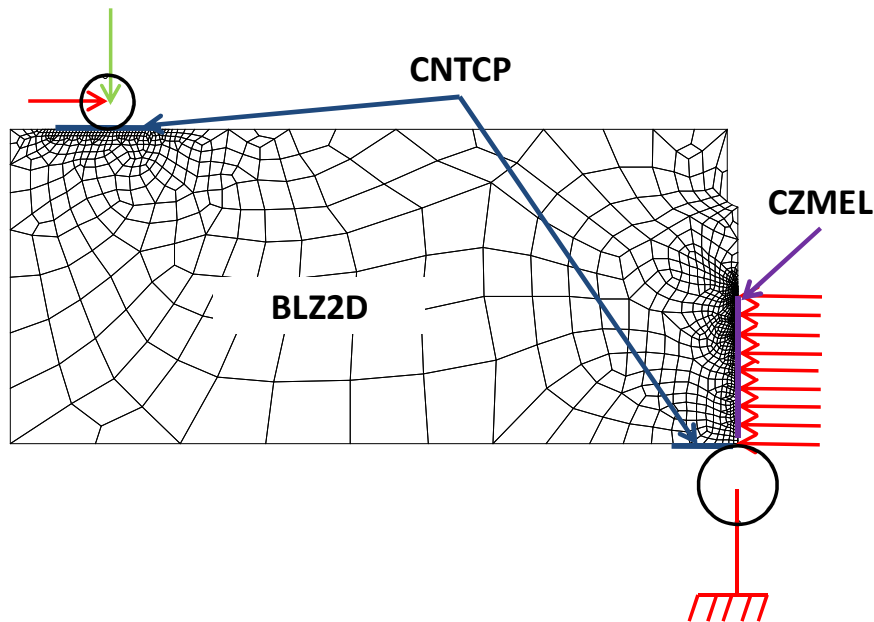


Figure 4-32: Finite element modeling of the CTOD test

Table 4-4: Penalty parameters

Penalty coefficient on the contact pressure (MPa.mm <sup>-1</sup> )	Penalty coefficient on the shear frictional stress (MPa.mm <sup>-1</sup> )	Coulomb's friction coefficient
1x10 <sup>5</sup>	1x10 <sup>5</sup>	0.05

Note: Due to this symmetric state, the stress values were identical to that of in whole simulation but the energy required to crack was halved. Thus, the separations parameters,  $\delta_{n0}$  and  $\delta_{nc}$ , were also halved in the simulations.

#### 4.7.4.2 Computation of the growth in crack's length

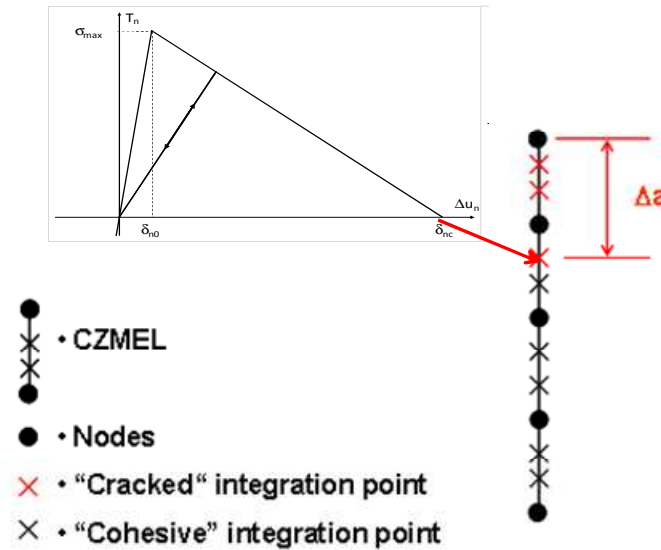


Figure 4-33: Computation methods of the growth in crack's length for 2D simulations

The computation method used to obtain the growth in the crack's length is shown in Figure 4-33. The crack propagated from the top CZMEL element to the bottom. At each time step, the cohesive stresses at each integration point were recorder. As soon as the cohesive stresses were zero, the integration point was considered to be cracked. The growth in the crack's length,  $\Delta a$ , represents the length of the segment which contains all the cracked integration points.

#### 4.7.4.3 The initial cohesive parameters

Crisfield's model was chosen because it can regulate the initial stiffness of the cohesive law and avoid introducing an implicit thickness. Crisfield's law uses three parameters: maximum stress,  $\sigma_{\max 0}$ , separation when cohesive stress is at its maximum,  $\delta_{n0}$ , and the separation limit before the stress is null,  $\delta_{nc}$ . However, it was preferable to focus on the cohesive energy,  $\phi_n$  and the initial slope of the cohesive plot,  $k_n$ , instead of  $\delta_{n0}$  and  $\delta_{nc}$  because the former parameter's interpretation is easier and more physical.

Shet et al. [SHE02] suggested varying the ratio  $\sigma_{\max 0}/\sigma_y$  from 1.5 to 3 where  $\sigma_y$  is the yield stress. The base metal seems very ductile; therefore one should choose as initial  $\sigma_{\max 0}$  3 times the yield stress. So, the initial  $\sigma_{\max 0}$  is equal to 1065 MPa.

Chen [CHE03] used the initial J-integral when the crack begins to propagate,  $J_{fi}$ , as the initial value of the cohesive energy. According to the experimental  $J_I-\Delta a$  plot,  $J_{fi}=133 \text{ kJ.m}^{-2}$ .

Bouvard [BOU06] recommended using a large initial slope value, to avoid modifying the elastic stiffness of the material and having too great implicit thickness at the interface (see 4.2.3). So initial slope was chosen as  $k_n=1 \times 10^7 \text{ MPa.mm}^{-1}$ .

Table 4-5: Summary of the parameters tested

	$\sigma_{\max 0}$ (MPa)	$\phi_n$ (kJ.m <sup>-1</sup> )	$k_n$ (MPa.mm <sup>-1</sup> )
Variation of $\sigma_{\max}$	1065	133	$1 \times 10^7$
	1242.5		
	1420		
Variation of $\phi_n$	1065	133	$1 \times 10^7$
		199	
		266	
Variation of $k_n$	1065	133	$1 \times 10^5$
			$1 \times 10^6$
			$1 \times 10^7$

#### 4.7.4.4 Varying the maximum cohesive stress

Three computations were performed by varying the maximum cohesive stress,  $\sigma_{\max 0}$ . Figure 4-34 shows the evolution of the tool force in function of the load line displacement. Figure 4-35 shows the evolution of the J-integral as a function of the crack's growth. As can be seen from these two figures, the maximum cohesive stress had an impact on the crack's growth rate but, it had no influence on the beginning of the crack's growth.

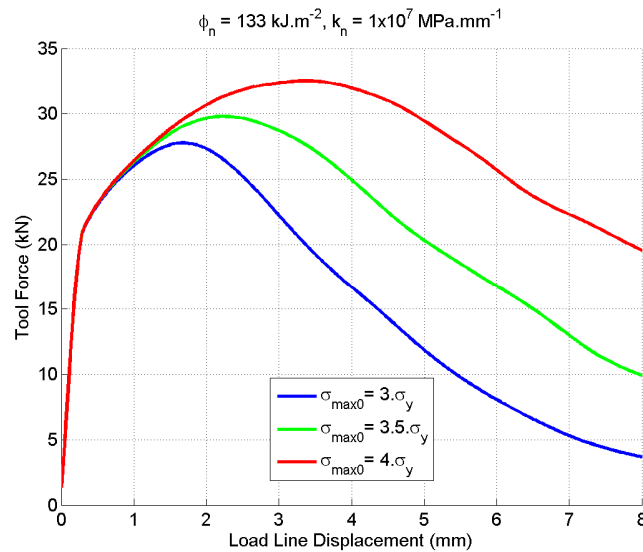


Figure 4-34: Evolution of tool force as a function of the load line displacement by varying  $\sigma_{\max}$



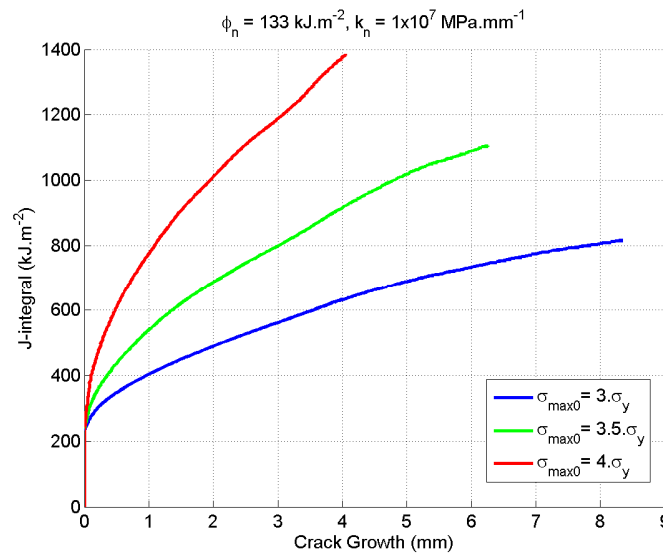


Figure 4-35: Evolution of the J-integral as a function of the crack's growth by varying  $\sigma_{max}$

#### 4.7.4.5 Varying the cohesive energy

Likewise, three computations were performed by varying the cohesive energy,  $\phi_n$ , in order to determine its effect on the crack's growth. Figure 4-36 shows the evolution of the tool force as a function of the load line displacement. Figure 4-37 shows the evolution of the J-integral as a function of the crack growth. Unlike the cohesive stress, the cohesive energy has a weak impact on the crack growth rate but it affected the onset of the crack's growth.

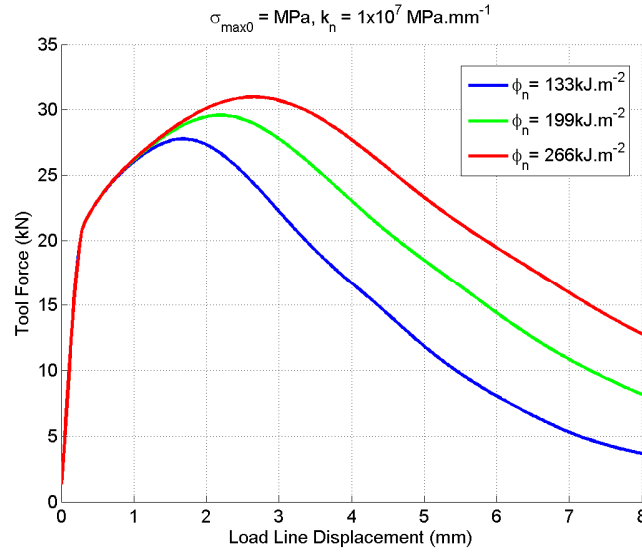


Figure 4-36: Evolution of tool force as a function of the load line displacement by varying  $\phi_n$

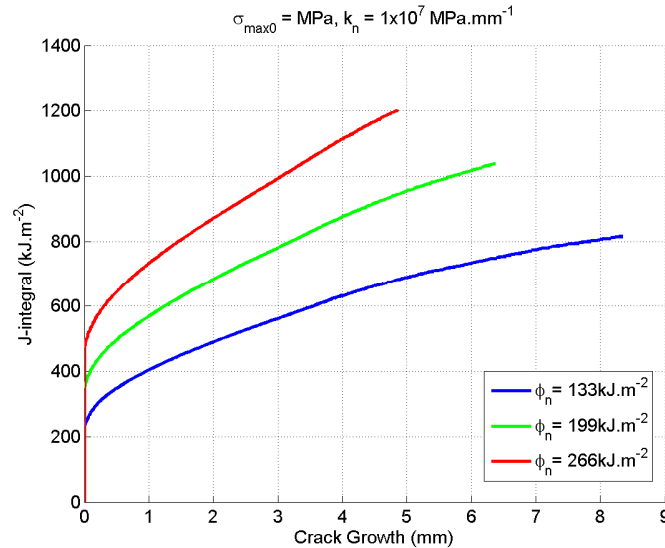


Figure 4-37: Evolution of the J-integral in function of the crack growth in varying  $\phi_n$

#### 4.7.4.6 Varying the initial slope

Another three computations were performed by varying the initial slope of the cohesive stress separation plot,  $k_n$ , between  $10^5$  and  $10^7$  MPa.mm<sup>-1</sup>. Figure 4-38 shows the evolution of the tool force as a function of the load line displacement. Figure 4-39 shows the evolution of the J-integral as a function of the crack's growth. As can be seen in the figures below, the initial slope barely affected the results up to a threshold before the structure lost stiffness due to the presence of the cohesive zone model. In conclusion, the initial slope must be high (i.e. greater than  $10^6$  MPa.mm<sup>-1</sup>) and, consequently, the cohesive separation when the cohesive stress is maximum,  $\delta_{n0}$ , must be low.

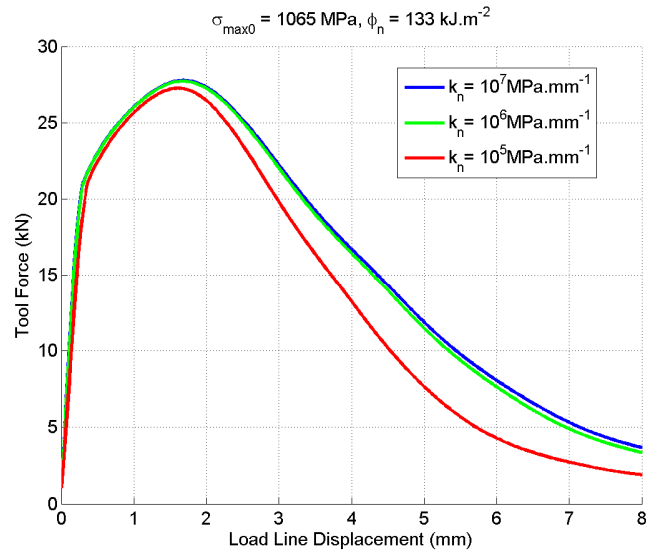


Figure 4-38: Evolution of tool force as a function of the load line displacement by varying  $k_n$

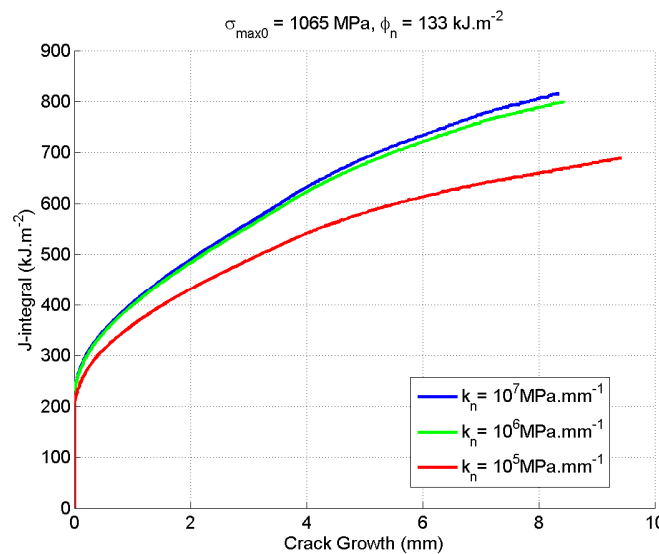


Figure 4-39: Evolution of the J-integral as a function of the crack growth by varying  $k_n$

#### 4.7.4.7 Cohesive constitutive law's effect

Finally, a simulation was performed using the Xu and Needleman's law instead of Crisfield's one. The parameters were chosen to have the equivalent maximum cohesive stress and the equivalent cohesive energy (see Table 4-6). These parameters are defined in Table 4-6. The computation of the crack's growth with Xu and Needleman is complex because the cohesive stresses are not null when the separation tend to infinity due to the exponential shape of the constitutive law. Thus, the J-integral/crack's growth plot depends on the threshold chosen by the user to consider a cracked integration point. The force displacement plot was compared with the

simulation with Crisfield's law (see Figure 4-40). The results were similar but Xu and Needleman's law imposes a weak initial slope, unlike Crisfield's law which allow this slope to be regulated it. Thus, the difference using Xu and Needleman's law is equivalent to a case where the initial slope has been decreased (see 4.7.4.6).

**Table 4-6: Parameters of Xu and Needleman's law**

$\sigma_{\max}$ (MPa)	$\delta_{n0}$ (mm)
1065	$2.297 \cdot 10^{-2}$

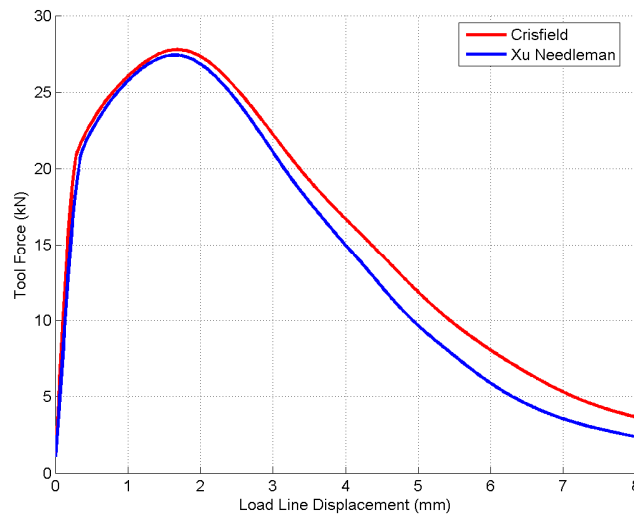


**Figure 4-40: Effect of the constitutive law on the force displacement plot**

#### 4.7.4.8 Results and discussion

This study helped to understand the effect of the variation of each parameter on the model of the crack's growth. It was found that the maximum cohesive stress can be used to adjust the crack's growth rate. The cohesive energy has only a weakly influence on the crack's growth rate but it can adjust the crack's growth initiation. The initial slope of the cohesive law must be high enough to prevent the use of the cohesive element from affecting the stiffness of the whole structure. That's why Crisfield's law was chosen as the most suitable law. However, the initial set of cohesive parameters gave different results from the experiments and the studied values did not give promise to find a good comparison with the experimental test. Indeed, the two-dimensional simulations do not take into account the stress triaxiality which can have an impact on the crack's propagation. Moreover, during the experiment the crack's growth was measured along the thickness of the sample. That's why, the calibration of the cohesive parameters was performed with three-dimensional analyses.

## 4.7.5 Parameter identification

### 4.7.5.1 Modeling

The aim of these 3D analyses was to identify the cohesive parameters of the model by the inverse method. The analysis was three dimensional because the crack's growth is obtained from an average measurement along the thickness. Due to the symmetry of geometry and loading, only a quarter of the three point bend specimen was modeled in order to reduce computation time (see Figure 4-41). The mesh was generated with the 3D mesh generator developed during this research (see Chapter 6.3.1).

All nodes which belonged to the plane where  $x=4.6W/2$  were fixed in the  $x$  direction and all nodes which belonged to the plane where  $z=W/2$  were fixed in the  $z$  direction. The specimen was modeled by 8-node mixed solid BWD3D elements (see Section 2.4).

The constitutive law applied was elasto-plastic with isotropic hardening and von Mises' criterion. The mechanical parameters used were listed in 2.5.4 for the base metal and the weld metal.

The three rollers were modeled by non-deformable cylinder-shaped foundations and the contact zones were modeled by CFI3D elements with a penalty method [HAB98]. The parameters of the contact law can be found in Table 4-4.

The fatigued pre-crack was modeled by letting the nodes free. The crack path was assumed to be along the symmetric plane because this is where the longitudinal stresses are the highest; therefore, the cohesive zone elements, CZM3D, were located at this place.

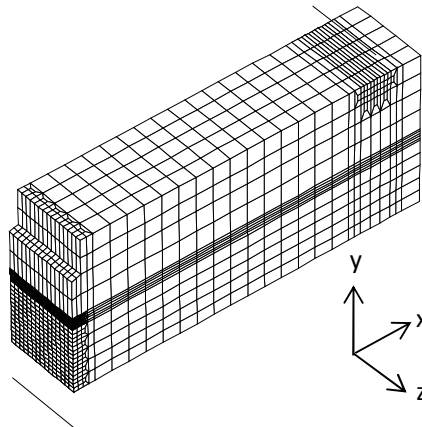


Figure 4-41: 3D Finite element modeling of the CTOD test

Due to the fact that the simulation was three dimensional, with a high number of nodes, and was repeated many times, the analysis was performed with an iterative solver method to speed up the computation time (see Appendix 1)

#### 4.7.5.2 Computation of the growth in crack length

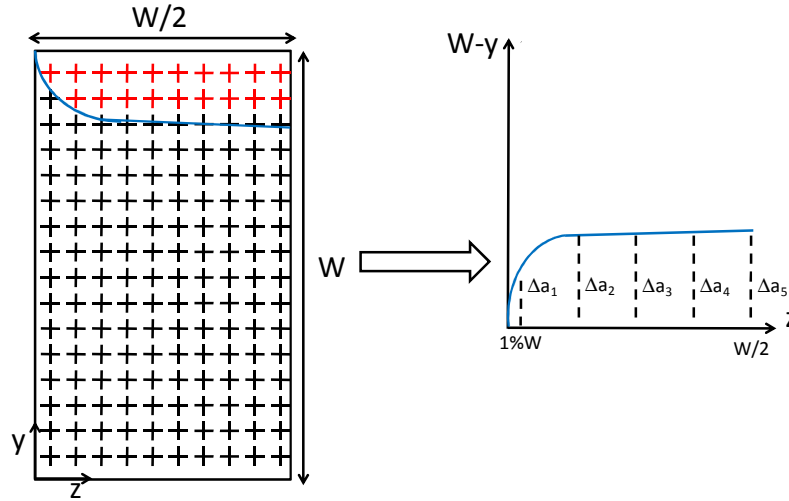


Figure 4-42: Computation methods of the crack length's growth for 3D simulation

The method used to compute the crack length's growth is illustrated in Figure 4-42. In this figure, the integration points of all CZM3D elements can be observed. The crack zone is the zone where the integration point has zero normal cohesive stress. The limit of this zone has been plotted. Five points were chosen on the plot according to the [BSI91] standards (five points instead of nine because only half of the specimen was modeled). The crack length's growth used was obtained from the average of five points where the outermost point has half the weight of the others.

$$\Delta a = \frac{\Delta a_1 + 2\Delta a_2 + 2\Delta a_3 + 2\Delta a_4 + 2\Delta a_5}{9} \quad (4.84)$$

#### 4.7.5.3 Results and Discussion

According to the results of the sensitivity study in Section 4.7.4, the cohesive parameters were modified until the force displacement curve and the J-integral/crack growth plot resembled the experiment plot (see Figure 4-43 to Figure 4-45). The parameters identified from this comparison are given in Table 4-7 and Table 4-8.

It was found that the value of the cohesive stress for the BM is considerable ( $\sigma_{\max}/\sigma_y=4.78$ ) while [LI03] recommended that the ratio  $\sigma_{\max}/\sigma_y$  must be less than 3 to prevent that all energy dissipation from occurring in plastic dissipation. The material seemed to be extremely ductile. In addition, the size of the cohesive elements may have been large which have affected the cohesive parameters but the mesh's refinement is limited by the computer's capability. In comparison, Cornec et al. [COR03] identified these cohesive parameters for the 20MnMoNi55 steel:  $\sigma_{\max}=1460$  MPa and  $\phi_n=120$  kJ.m<sup>-2</sup> with  $\sigma_y=465$  MPa. The ratio  $\sigma_{\max}/\sigma_y$  is equal to 3.1 for this grade.

Finally, it was determined that stress triaxiality (defined in Chapter 2.2.2) must have an impact on the parameters. Indeed, Chen [CHE05] explained that, as triaxiality differs along the thickness of

the sample, the cohesive parameters must be different. Tvergaard [TVE04] and Anvari [ANV06] propose using Gurson's model in order to take the ductile failure into account mixed with the cohesive zone model. Keller [KEL99] proposes using the Generalized Cohesive Zone Model, which uses a damage locus with equivalent cohesive parameters independent from triaxiality. However, the lack of experiments limited the author's numerical investigations and it was decided to use the parameters of in Table 4-7 and Table 4-8 for the rest of the research.

**Table 4-7: Cohesive parameters Identified for BM**

$\sigma_{\max}$ (MPa)	$k_n$ (MPa/mm)	$\phi_n$ (kJ.m <sup>-2</sup> )
1700	$1.10^7$	161

**Table 4-8: Cohesive parameters Identified for WM**

$\sigma_{\max}$ (MPa)	$k_n$ (MPa/mm)	$\phi_n$ (kJ.m <sup>-2</sup> )
1650	$1.10^7$	50

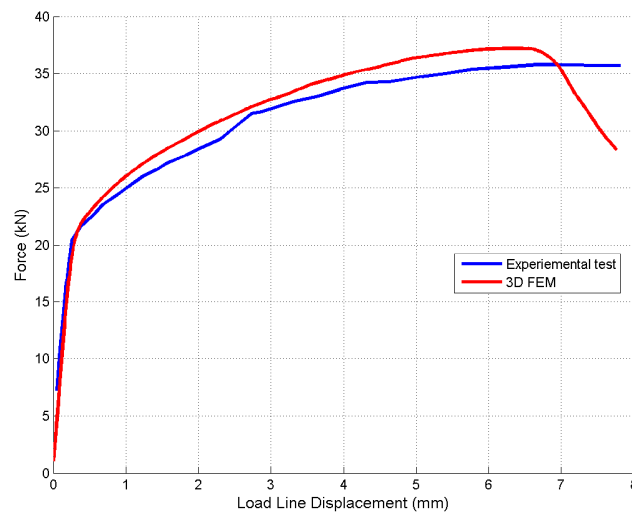


**Figure 4-43: Force displacement comparison plot between experimental test and finite element modeling for BM**

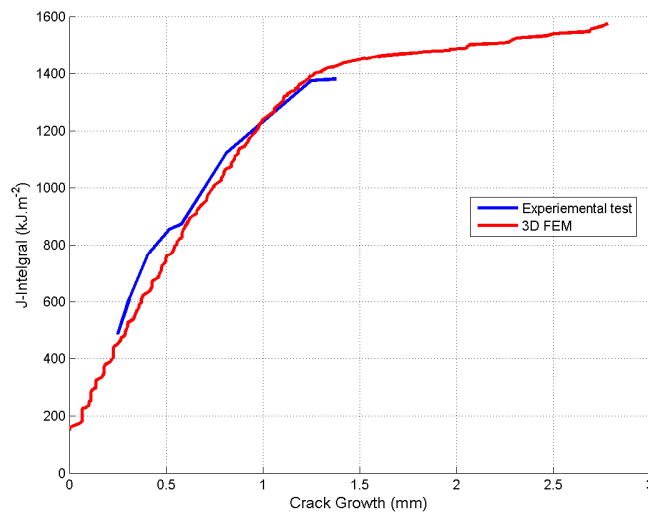


Figure 4-44: J-integral versus crack growth plot Comparison between experimental test and finite element modeling for BM

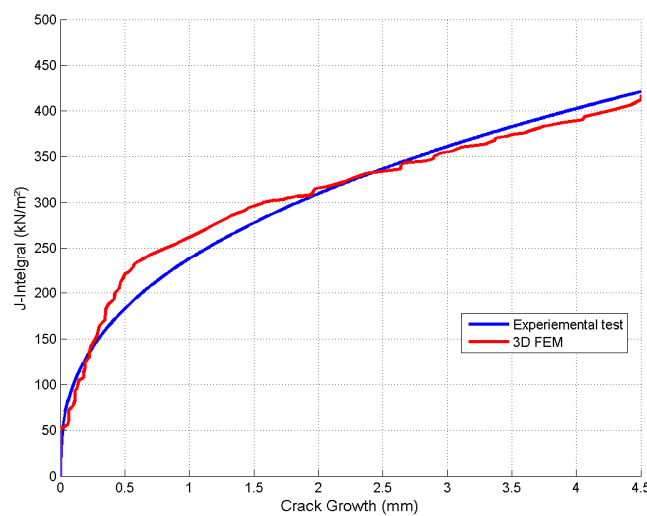


Figure 4-45: Comparison of J-integral versus crack growth plot between experimental test and finite element modeling for WM

## 4.8 Conclusions

Two new cohesive elements, CZMEL and CZM3D, and two cohesive laws, those of Xu and Needleman and Crisfield, were implemented in the Lagamine code. They were used to model crack initiation and propagation in a finite element analysis. As result of this analysis was that Crisfield's law was chosen for use in the rest of the study because the initial stiffness of the law can be regulated to avoid a drop of the structure's stiffness.



A method to identify the cohesive parameters of a material by an inverse method was established. The preliminary parametric study helped to understand the effect of varying each parameter on the crack's strength. It was found that in varying the maximum cohesive stress increased the crack propagation rate while the cohesive energy increased the energy required to induce the crack's propagation. Thus cohesive parameters were identified for the base metal and the weld metal. However, it is troubling to see the difference in the values identified by the author by comparing with the values identified for other steel grade in literature [COR03]. Likewise, the ratio,  $\sigma_{\max}/\sigma_y$ , equal to 4.8 is well above that recommended in the literature.



# **Chapter 5**

# **Welding simulation**



## 5.1 Introduction

A crack's strength and propagate path depend on residual stresses. These residual stresses are generated by the welding process as a result of the temperature gradients and metallurgical modifications. To reflect the impact of these values, the computation of the residual stresses was performed by modeling the welding process. However, this is a difficult task because it is necessary to consider many physical phenomena that occur during the welding process.

Thus, the goal of this chapter part was to compute a 3D balanced residual stress field generated by the welding process to enter at the beginning of the simulation of a cycle large scale beam-to-column test. Indeed, no analytical method exists for this geometry and for all components of the stress tensor. Some alternative analytical methods are summarized in [CLA04].

This chapter describes the welding process used in the VERAPS project and the physical phenomena resulting from it. Then the computation strategy and its simplifications are presented. Finally, there will be a discussion and illustration of some simulations that were performed and compared with experimental measurements performed on the connection after the welding.

## 5.2 Welding Process

### 5.2.1 Description

A welding process consists in joining materials by heating them to the melting temperature, sometimes by adding a filler material. The molten material when cooled down becomes a strong joint. The heat can be provided by a gas flame, an electric arc, a laser, an electron beam, friction, or ultrasound.

In our case, the type of welding process used was a metal arc weld with added of filler metal. This process creates and maintains an electric arc between the base metals to be joined and the electrode at the welding point. The electrodes can be consumable or non-consumable and the power supply can be direct (DC) or alternating (AC). The welding region can be protected by an inert gas called a shielding gas. Some different processes exist for this type of welding as it will be explained below.

The first is Manual Arc welding Metal (MMA), also known as Shielded Metal Arc Welding (SMAW). The consumable steel electrode, held by the operator, generates an electric arc with the metal structure, and is covered by a gas flux,  $\text{CO}_2$ , which protects the weld zone from oxidation and contamination.

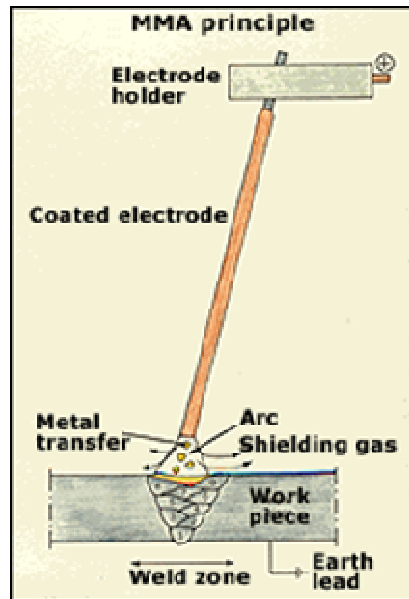


Figure 5-1: Diagram of SMAW process (from [www.esab.com](http://www.esab.com))

Gas Metal Arc Welding (GMAW) is a process characterized by the use of a long filler electrode and inert gas shielding of the welding pool. GMAW speeds are relatively high due to the automatically fed continuous electrode but this process requires more equipment than SMAW. The GMAW process is related to Flux Cored Arc Welding (FCAW) where the electrode consists of a powdered filler material contained in a tubular supply. FCAW is quicker than GMAC and its metal penetration is greater, but also more expensive. These processes can be automatic or semi-automatic.

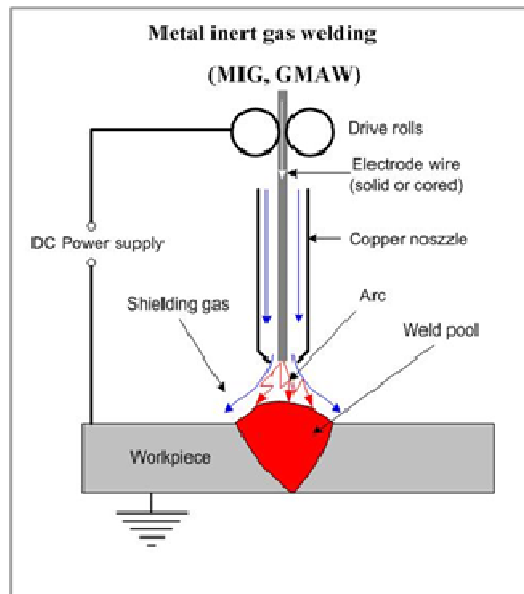


Figure 5-2: Diagram of GMAW (from [www.substech.com](http://www.substech.com))

Submerged Arc Welding (SAW) is the generation of an arc which is covered by a blanket of granular fusible flux consisting of lime, silica, manganese oxide, calcium fluoride, and other compounds. This method improves the arc quality because the flux shield is better between the contaminants than in the atmosphere. Working conditions are much improved over other arc welding processes since the flux hides the arc and no smoke is produced. As the arc is not visible, the process must be automatic.

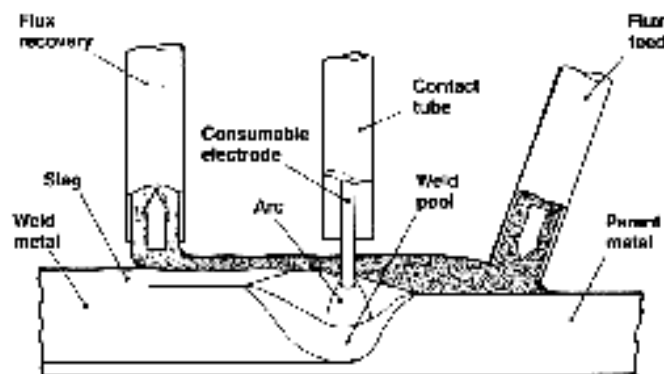


Figure 5-3: Diagram of SAW (from [robot-welding.com](http://robot-welding.com))

Finally, Gas Tungsten Arc Welding (GTAW) is a manual process which uses an inert tungsten electrode and a separate filler metal, shielded by an inert or semi-inert gas. The method gives a stabilized arc and high weld quality. It requires significant operator skill and can only be accomplished at relatively low speeds.

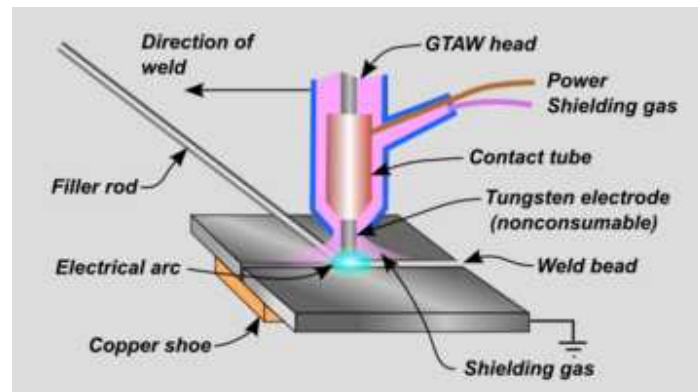


Figure 5-4: Scheme of GTAW (from common/Wikimedia.org)

### 5.2.2 Thermal phenomena

During the welding process, the materials absorb only a part of the thermal energy. This thermal energy generates a molten pool where the heat is transferred by convective exchange. In this molten pool, many physical phenomena happen with the surface tension, heat exchange and the electromagnetic force [SAIN06]. In other parts of the material, the heat transfer is conductive. The exchange with the environment is convective and radiative.

### 5.2.3 Metallurgical phenomena

The welding process affects the metallurgical state; therefore, the welded joint can become brittle or ductile according to the thermal history. As a result it is important to optimize the heat energy, the heat source velocity and the number of passes.

During the welding process, three materials are affected in different ways:

- the weld metal: this corresponds to the metal which is melted. The strength of this solidified material depends on the welding process and especially on its cooling rate.
- the heat affected zone: this around the weld metal. This zone is not melted but the heating and cooling cause modifications in the microstructure and the metallurgical state (i.e. solid phases of the steel) is deeply modified.
- the base metal: this zone is not affected by the process.

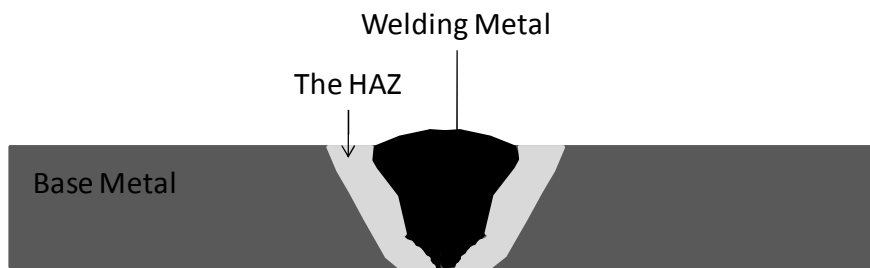


Figure 5-5: Material description after a welding process

### 5.2.4 The physical aspect

As described above, the welding process induces many physical phenomena such as mechanical deformation, thermal exchange, metallurgical transformation, and fluid mechanics. Each phenomenon affects the others with weak or strong coupling. These couplings are illustrated in Figure 5-6, followed by a description of their respective impact on the materials.

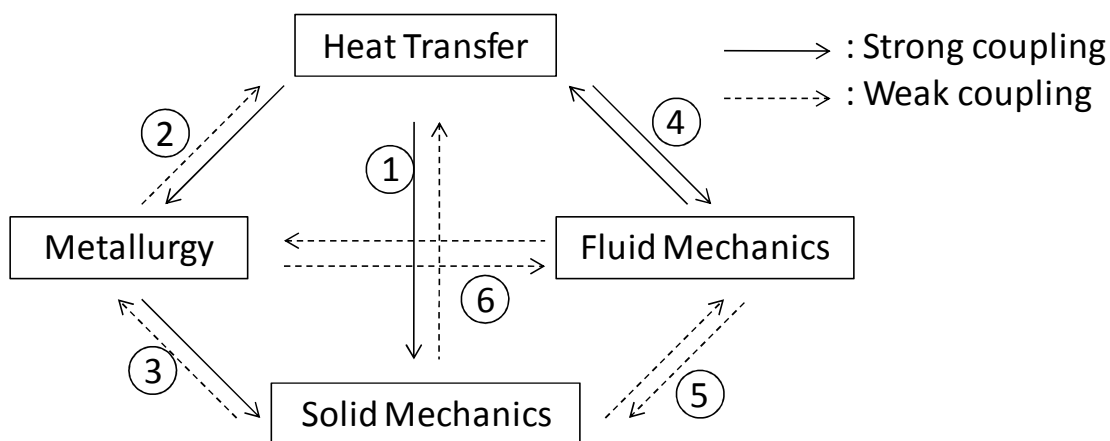


Figure 5-6: Coupling between physical phenomenon during welding

#### 1. Thermomechanical coupling:

- Thermal dilation: the dilation is due to the temperature variation and the flux gradient generated by the heat source of the welding. It generates distortions and residual stresses.
- Mechanical dissipation: the plastic deformation generates heat dissipation. However, the plastic strain rate is low; therefore, this dissipation has a weak impact on the thermal exchange.

#### 2. Thermometallurgical coupling:

- Metallurgical transformation: the heat and the cooling cause modifications in the steel's microstructure.



- Heat transformation and thermal properties: the phase transformation generates heat dissipation or absorption. Moreover, the thermal properties are modified by the metallurgical transformation.
3. Mechanometallurgical coupling:
    - Metallurgical distortion and mechanical properties: the phase transformation induces strain due to local volume modification. In addition, each phase has particular mechanical properties.
    - Stress-state effect on metallurgical transformation: the stress state affects the kinetics of the metallurgical transformation.
  4. Thermo-hydraulic coupling:
    - Modification of the flux: there is a significant temperature gradient in the weld pool between the center of the pool and the boundary. This gradient modifies the surface tension and causes modifications in the flux in the pool.
    - Convective exchange: the welding pool and the solid steel exchange heat by convection.
  5. Mechanohydraulic coupling:
    - Modification of the geometry of the molten pool: the strains induce modifications in the pool boundaries and in the flow in the pool.
    - Strain due to fluid pressure: the molten steel imposes pressure on the solid steel and affects the local stress fields.
    - These coupling phenomena are weak.
  6. Metallurgical hydraulic coupling:
    - Material mixing: the flow in the molten pool improves the mixing of steel components.
    - Macro-segregation: the flow depends on the chemical composition of the material.

### 5.3 Coupling strategy

It was chosen to neglect the hydraulic fields because the coupling phenomena are weak and their modeling requires two codes: a first one to model the solid steel's behavior by a finite element model and a second one to simulate the molten steel's behavior by a finite volume model.

Moreover, no metallurgical modeling has been performed. Although the Lagamine code can be used to carry out such a model [HAB89], such simulations require many material parameters and require additional experimental data. The goal of this study is to develop a simplified method to assess the residual stresses.

So only the thermal and the mechanical modeling remain. Their coupling can be strong or weak. Strong coupling takes the thermal dilation and the mechanical dissipation into account. At each increment, the temperature is computed, then the stress and strain fields and finally the mechanical dissipation. Weak coupling is only sequential and mechanical dissipation is

neglected. A thermal analysis is performed and the nodal thermal history is computed. Then a mechanical analysis is performed by imposing the thermal history.

Weak coupling was chosen because the mechanical dissipation in this case is low due to a low strain rate and the computation is quicker than for strong coupling. The coupling strategy adopted is described in Figure 5-7. This method can use different meshes for the thermal mesh and the mechanical mesh. Indeed, thermal analysis requires a fine mesh and a long time step as opposed to mechanical analysis, which requires a coarser mesh and a short time step.

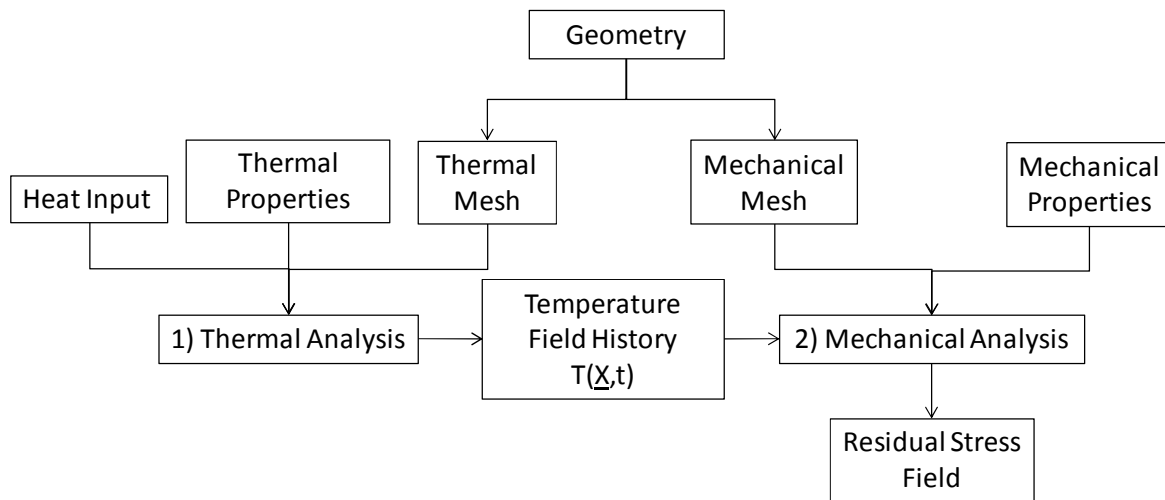


Figure 5-7: Computation strategy of residual stress

The decoupled approach is not new within the scientific community [ZHA00; CHA02; CHA04]. However within the Lagamine team, it had not yet been implemented. In their PhD theses, Habraken [HAB89] and Pascon [PAS03] each used thermo metallurgical mechanical analysis. However, they always used identical meshes for mechanical and thermal analyses.

## 5.4 Thermal analysis

### 5.4.1 The heat equations

The temperature field,  $T$ , on a volume  $\Omega$  follows the classic heat equation, which is derived from the Fourier's Law:

$$\rho C_p \frac{\partial T}{\partial t} = \text{div}(\lambda \underline{\nabla} T) + r \quad (5.1)$$

where  $\rho$  is the volumetric mass,  $C_p$  is the heat capacity,  $t$  is the time,  $\lambda$  is the conductivity, which can depend on the direction, and  $r$  is the heat source.

There are different kinds of boundary conditions which are described by Figure 5-8:

- On  $\Gamma_1$ , the system is free and exchanges convective and radiative flux with the environment;

- On  $\Gamma_2$ , a surface heat flux is imposed;
- On  $\Gamma_3$ , the temperature is imposed.

The above boundary conditions on surfaces outer  $\Gamma_1$ ,  $\Gamma_2$ ,  $\Gamma_3$  are modeled by the following equations:

$$\begin{cases} \lambda \nabla T \cdot \underline{n} + q_c + q_r = 0 & \text{on } \Gamma_1 \\ \lambda \nabla T \cdot \underline{n} + q_s = 0 & \text{on } \Gamma_2 \\ T = \bar{T} & \text{on } \Gamma_3 \end{cases} \quad (5.2)$$

where  $\underline{n}$  corresponds to the normal to  $\Gamma_1$  or  $\Gamma_2$ ,  $q_c$  is the convective flux loss,  $q_r$  is the radiative flux loss,  $q_s$  is the imposed surface heat flux and  $\bar{T}$  is the imposed temperature.

The convective flux loss can be modeled by

$$q_c = h(T - T_{\text{ext}}) \quad (5.3)$$

where  $h$  is the convective exchange constant and  $T_{\text{ext}}$  is the room temperature

The radiative flux loss can be modeled by

$$q_r = \varepsilon \sigma (T^4 - T_{\text{ext}}^4) \quad (5.4)$$

where  $\varepsilon$  is the emissivity and  $\sigma$  is Boltzman's constant;  $T$  must be expressed in radiant.

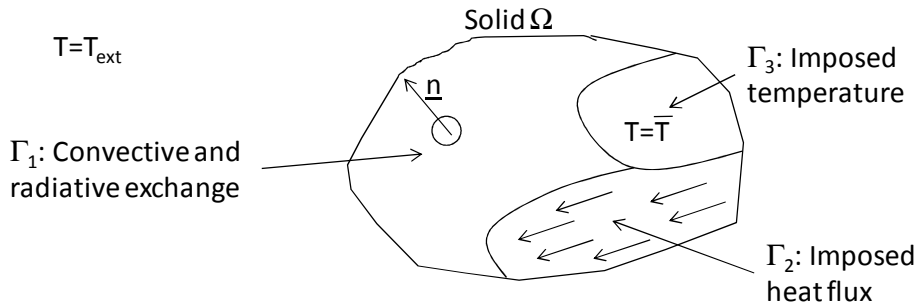


Figure 5-8: Division of the surfaces according to the flux exchange along the solid  $\Omega$

## 5.4.2 Heat source modeling

Pavli et al. [PAV69] were the first to propose a disc model for heat source (see Figure 5-9). The thermal surface flux exhibits a Gaussian distribution in the tangent plane to the heat source location.

$$q_s = q_0 \exp(-Cr^2) \quad (5.5)$$

where  $q_0$  is the maximum surface flux at the center of the heat source,  $C$  is the concentration coefficient and  $r$  is the distance from the heat source.

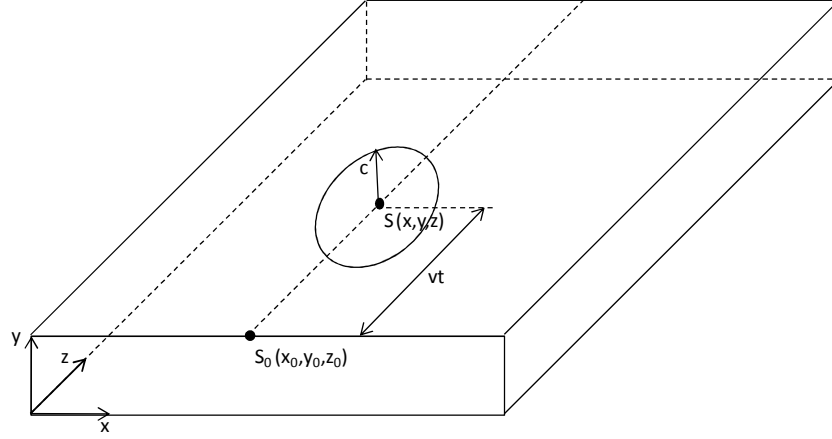


Figure 5-9: Friedman Models of the heat source

To take into account the motion of the heat source, Friedman [FRI75] and Krutz and Segerlind [KRU78] expressed the heat flux in a local coordinate system  $(x', z')$ . For example, if the heat source moves along the  $(x, z)$  plane along a line parallel to the axes,  $\underline{e}_z$ , the surface heat flux,  $q_s$ , is expressed as

$$q_s = \frac{3Q}{\pi c^2} \exp\left[-\frac{3}{c^2}(x'^2 + z'^2)\right] \text{ with } \begin{cases} x' = x - x_0 \\ z' = z - z_0 + vt \end{cases} \quad (5.6)$$

where  $Q$  is the welding heat input,  $c$  is the characteristic radius of the flux distribution,  $x_0$  and  $z_0$  define the initial position of the heat source,  $x$  and  $z$  define the position of the flux computation,  $v$  is the velocity of the heat source and  $t$  is time.

However, experimental observations show that a significant amount of heat flux is transferred by radiation and convection from the arc directly to the solid metal without passing through the molten pool. Therefore, the volumetric flux,  $q$ , becomes a hemispherical volume source defined by

$$q = \frac{6\sqrt{3}Q}{c^3\pi\sqrt{\pi}} \exp\left[-\frac{3}{c^2}(x'^2 + y'^2 + z'^2)\right] \text{ with } \begin{cases} x' = x - x_0 \\ y' = y - y_0 \\ z' = z - z_0 + vt \end{cases} \quad (5.7)$$

Furthermore, the molten pool has a different shape from a sphere, which is why Goldak et al. [GOL84] proposed an ellipsoidal power density distribution:

$$q = \frac{6\sqrt{3}Q}{abc\pi\sqrt{\pi}} \exp\left[-3\left(\frac{x'^2}{a^2} + \frac{y'^2}{b^2} + \frac{z'^2}{c^2}\right)\right] \text{ with } \begin{cases} x' = x - x_0 \\ y' = y - y_0 \\ z' = z - z_0 + vt \end{cases} \quad (5.8)$$

where  $a$ ,  $b$  and  $c$  are the semi-axes of the ellipsoid in the direction,  $x$ ,  $y$  and  $z$ , respectively,  $y_0$  is the initial  $y$  position of the heat source.

Then Goldack et al. [GOL84] noticed that after experimental calculations, the temperature gradient in front of the heat source is different from behind. That's why they proposed combining two different ellipsoids (see Figure 5-10): one is behind and the other in front of the heat sources.

$$q = \begin{cases} \frac{6\sqrt{3}Qf_f}{abc_f\pi\sqrt{\pi}} \exp\left[-3\left(\frac{x'^2}{a^2} + \frac{y'^2}{b^2} + \frac{z'^2}{c_f^2}\right)\right] & \text{if } z' \geq 0 \\ \frac{6\sqrt{3}Qf_b}{abc_b\pi\sqrt{\pi}} \exp\left[-3\left(\frac{x'^2}{a^2} + \frac{y'^2}{b^2} + \frac{z'^2}{c_b^2}\right)\right] & \text{if } z' < 0 \end{cases} \quad \text{with } \begin{cases} x' = x - x_0 \\ y' = y - y_0 \\ z' = z - z_0 + vt \end{cases} \quad (5.9)$$

where  $f_f$  and  $f_b$  are the heat fraction in front and behind the heat source, respectively, and  $c_f$  and  $c_b$  are the semi axes of the ellipsoid in  $z$  direction in front and behind the heat source, respectively. The energy distribution imposes the following relation:  $f_f + f_b = 2$ .

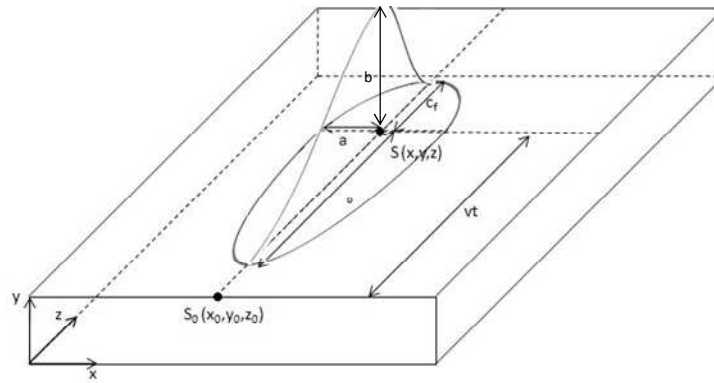


Figure 5-10: Double ellipsoid heat source with the power distribution

In arc welding, the energy input,  $Q$ , is defined by:

$$Q = \eta VI \quad (5.10)$$

where  $V$  is the electric tension,  $I$  is the electric intensity and  $\eta$  is the welding power efficiency.

## 5.5 Mechanical analysis

The total strain rate,  $\underline{\underline{\dot{\epsilon}}}$ , can be divided up as:

$$\underline{\underline{\dot{\epsilon}}} = \underline{\underline{\dot{\epsilon}}^e} + \underline{\underline{\dot{\epsilon}}^{vp}} + \underline{\underline{\dot{\epsilon}}^{th}} + \underline{\underline{\dot{\epsilon}}^{pt}} \quad (5.11)$$

where  $\underline{\underline{\dot{\epsilon}}^e}$  is the elastic strain rate,  $\underline{\underline{\dot{\epsilon}}^{vp}}$  is the viscoplastic strain rate,  $\underline{\underline{\dot{\epsilon}}^{th}}$  is the thermal dilation rate and  $\underline{\underline{\dot{\epsilon}}^{pt}}$  is the plastic strain rate due to microstructural transformation.

At the high levels of temperature, the behavior of the solid is elastoviscoplastic. However, the number of parameters required is more significant than with elastoplastic behavior because these parameters depend on both temperature and strain rates.

No experimental measurement was performed for parameter calibration. Corus provided tensile data as a function of temperature at a constant strain rate. Consequently, the viscoplastic strain rate is neglected and only the plastic strain rate,  $\underline{\underline{\dot{\epsilon}}}^p$ , is taken into account.

Moreover, as no metallurgical modeling was performed, one assumed that the plastic strain rate due to transformation is zero.

In conclusion, in this research the division of the total strain rate is:

$$\underline{\underline{\dot{\epsilon}}} = \underline{\underline{\dot{\epsilon}}}^e + \underline{\underline{\dot{\epsilon}}}^p + \underline{\underline{\dot{\epsilon}}}^{th} \quad (5.12)$$

So, the thermal dilation is computed by

$$\underline{\underline{\epsilon}}^{th} = \alpha(T)(T - T_{ext})\underline{\underline{I}} \quad (5.13)$$

where  $\alpha$  is the dilation coefficient,  $T_{ext}$  is the ambient temperature and  $\underline{\underline{I}}$  is the unity tensor.

The elastoplastic behavior can be modeled as in Section 2.5 by adding the thermal dilation and considering the mechanical parameters dependent on the temperature.

## 5.6 The finite element modeling

As it was presented in Section 5.3, two sequential computations were performed with the Lagamine code. Firstly, the temperature evolution in the structure was computed by imposing a heat flux described by Formula (5.9). Then a mechanical analysis was performed on the structure by imposing the temperature field computed by the first thermal analysis. Since the meshes were different in both analyses, the imposed temperature was computed by an interpolation method. Due to the geometry of the connection and in order to have a balanced stress field, the analyses were performed in 3D.

### 5.6.1 The thermal analysis

The structure was modeled by the thermomechanic mixed solid element BLZ3T [LI97]. The heat equation was integrated by the THLNS law (i.e. Fourier's conduction with physical parameters varying according to the temperature). Convection and radiative exchange were modeled by the CORA3 law.

In order to impose a double-ellipsoid Goldack's heat source, one computes the "nodal heat force" to obtain the equivalent volumetric heat flux of Goldack's model. This was computed in a preprocessor step, at each time increment, by the integration of the volumetric heat flux on the element by a Gauss' scheme:

$$Q_i = \sum_{k=1}^{NELEM} \sum_{j=1}^{NIP} B_{ij} q_j \det(\underline{\underline{J}}_j) W_j \quad (5.14)$$

where  $Q_i$  is the nodal heat input of node  $i$ , NELEM is the number of elements linked to node  $i$ ,  $B_{ij}$  is the derivative of the interpolation function,  $q_j$  is the heat flux computed by equation (5.9) at the interpolation point  $j$  of the element,  $J_j$  is the Jacobian matrix and  $W_j$  is the interpolation weight.

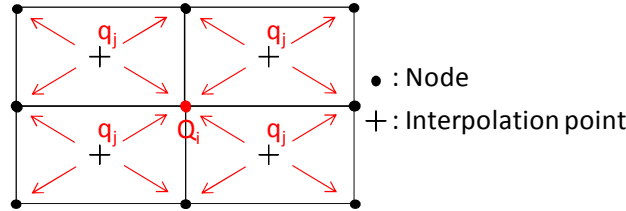


Figure 5-11: Computation of the imposed nodal heat

During the analysis all elements which model the weld metal were present. The advantage of this is that the weld metal and the base metal were preheated after the pass of the heat source. The drawback is some conduction flux appears in weld metal part which should no longer exist.

## 5.6.2 The temperature transfer

During a remeshing procedure, a transfer method of the data defined at the integration points and the nodes is necessary. In this study's case, only the nodal temperature was transferred from the thermal mesh to the mechanical mesh. There are different methods for data transfer in the literature, such as the least square method (adjustment between polynomial fit in each mesh or an extrapolation approach [DYD96; BAR98]). However, these classic methods would require significant development work and the computation time can be high.

That's why Habraken's transfer method [HAB89] was used. The interpolated value at node  $j$  in the mechanical mesh is obtained from the average of the value at the surrounding node,  $k$ , in the thermal mesh, weighted by the distance between nodes  $j$  and  $k$ , according to the following relation:

$$T_j = \begin{cases} \frac{\sum_k \frac{T_k}{R_{kj}^n} + \frac{CT_p}{R_{pj}^n}}{\sum_k \frac{1}{R_{kj}^n} + \frac{C}{R_{pj}^n}} & \text{if } R_{pj} > R_c \\ T_p & \text{if } R_{pj} \leq R_c \end{cases} \quad (5.15)$$

where  $T_j$  is the temperature of node  $j$  in the mechanical mesh (see Figure 5-12),  $T_k$  is the temperature of node  $k$  in the thermal mesh,  $T_p$  is the temperature of node  $p$  which is the closest node to node  $j$  in the thermal mesh,  $R_{kj}$  and  $R_{pj}$  are the distance between nodes  $k$  and  $j$  and between the nodes  $p$  and  $j$ , respectively,  $n$  is the interpolation exponent and  $C$  is an interpolation constant chosen by the user.

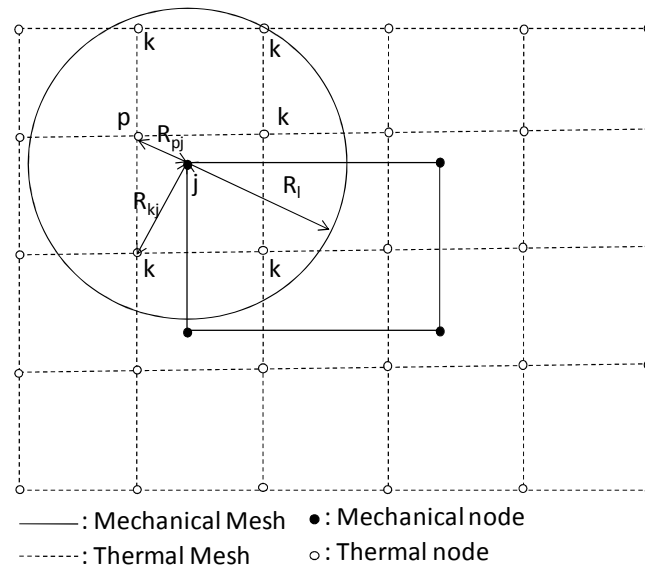


**Figure 5-12: Interpolation for temperature transfer**

The constant  $C$  is used to increase the influence of the closest node of the thermal mesh. According to numerical experiments, its default value is 5. The interpolation exponent  $n$  helps to refine the interpolation. Even values of this exponent give best result than odd values. However, if the exponent is too high, some temperature gradients in the mechanical mesh can appear in the constant temperature zone for by the thermal mesh.  $n=2$  was chosen in this thesis.

In the interpolation of Equation (5.15), only nodes  $k$  which have a distance  $R_{kj}$  less than  $R_l$  were taken into account as described by Figure 5-12.  $R_l$  is defined by the following choice:

$$R_l = 0.3D \quad (5.16)$$

where  $D$  is the diagonal length of the rectangle containing the structure (see Figure 5-13).



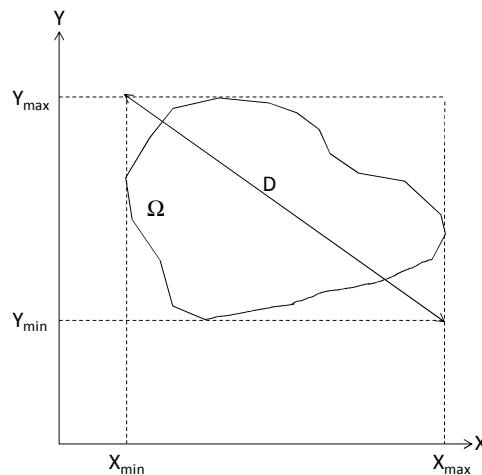


Figure 5-13: Computation of the diagonal of the rectangle which contains the structure  $\Omega$

If the distance between the closest node  $p$  and the new node  $j$  is less than a radius,  $R_c$ , then the temperature of the node  $j$  becomes equal to the temperature of the node  $p$ .  $R_c$  is defined in this the following simulation by:

$$R_c = 0.001D. \quad (5.17)$$

### 5.6.3 The birth technique

The birth technique simulates the weld metal supply by activating and deactivating some elements at defined steps. This procedure was applied only for the mechanical analysis. At the beginning all elements modeling the added weld metal existed but were deactivated. The deactivation resulted from a null stress field and nodal force. The birth technique is described in Figure 5-14 and Figure 5-15.

Physically speaking, in the blue zone, the weld metal has not been laid yet or is in a melted state; therefore, the stresses are null. In the red zone, the laid weld metal begins solidifying and having stiffness to generate stresses. Numerically speaking, in blue zone the temperature can increase and in the red zone the temperature drops. The birth technique dictates that the mechanical stress be computed only in the zone where the temperature decreases. Indeed, a temperature increase causes a decrease in stiffness and affects the convergence.

The nodes in the inactive elements (in blue) have artificial stiffness provided by STIFF elements to avoid numerical problems. The STIFF is a one-dimensional element which can model a spring or impose stiffness. The imposed value is  $0.1 \text{ N.mm}^{-1}$ . As soon as all the elements are in the double ellipsoid and behind the heat source, the element is activated and the STIFF element is turned off.

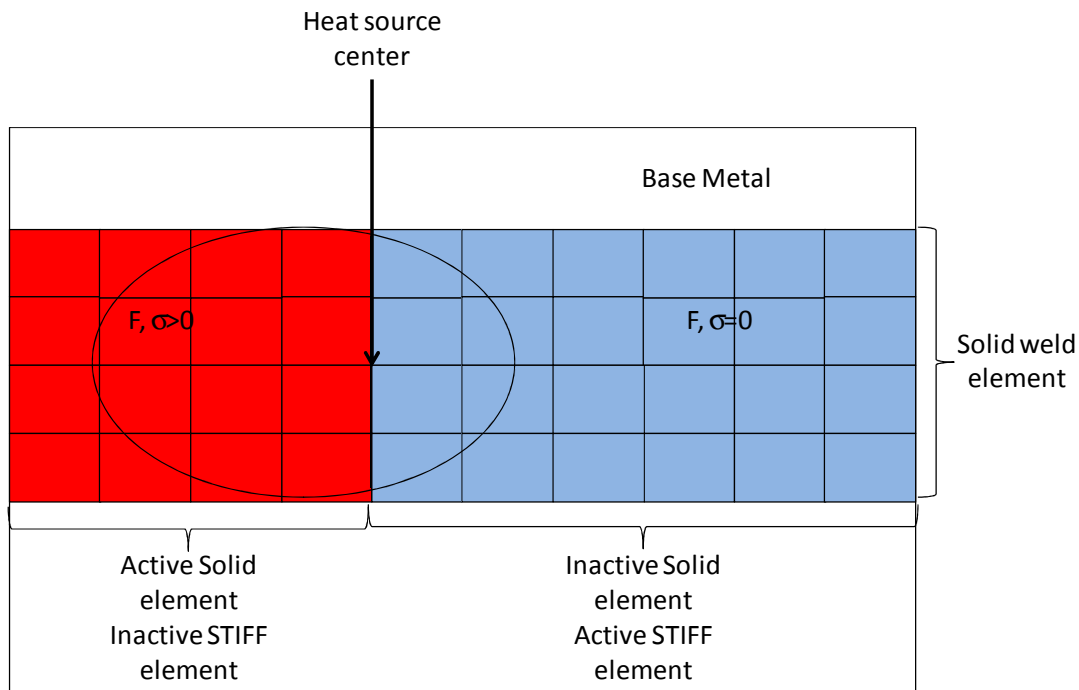


Figure 5-14: Birth technique method (top view)

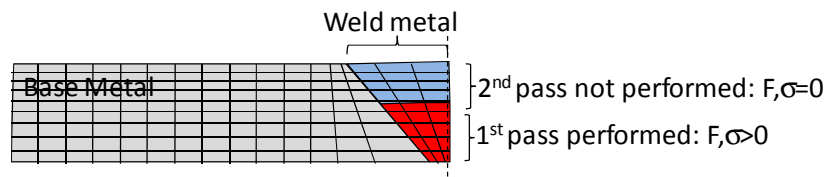


Figure 5-15: Birth technique method in two passes

## 5.6.4 The mechanical analysis

The structure was modeled by the thermomechanical mixed solid element BLZ3T. The mechanical behavior was modeled by the elastoplastic constitutive law, ARB3C. The ARB3C uses the same model as the ARB law described in Section 2.5.3 with dilation and the dependence on temperature for the parameters. However, this law did not exist for three-dimensional analyses; therefore, the ARB3C law was implemented during this research.

## 5.7 Modeling of beam-to-column connection welding

### 5.7.1 Welding description

In the VERAPS connection (see Chapter 6), the weld joints were between the beam flange and the column flange. In case of moment resisting frame connections, only applicable welding techniques are outside on site. Also, the relatively limited access for the welding rods and the arc to reach into the gap between beam and column is a factor. Only the welding of these joints was

modeled thought there are other weld joints between the shear panel and the beam web and the column flange, but no cracks or damage was noticed in these zones, so these welding processes were not simulated.

The weld connections were manufactured using a range of consumables to cover the full toughness range provided by three types of processes:

- Manual arc welding,
- Tubular cored metal arc welding with active gas shield,
- Metal arc welding without gas shield.

The beam flange and the beam webs were prepared according to the details given in [BAN07] and Figure 5-17. The column was positioned perpendicular to the ground, as shown in Figure 5-16, and maintained by two metallic bars. Then the beam end is bolted to the shear tab with low strength bolts that were not pre-stressed. Ceramic or metallic baking tabs were used. After welding, the backing bars were removed and any discontinuities in the root pass were removed by back gouging and back welding and an additional fillet weld with a minimum leg size of 6 mm was welded on the root side (see Figure 5-19).

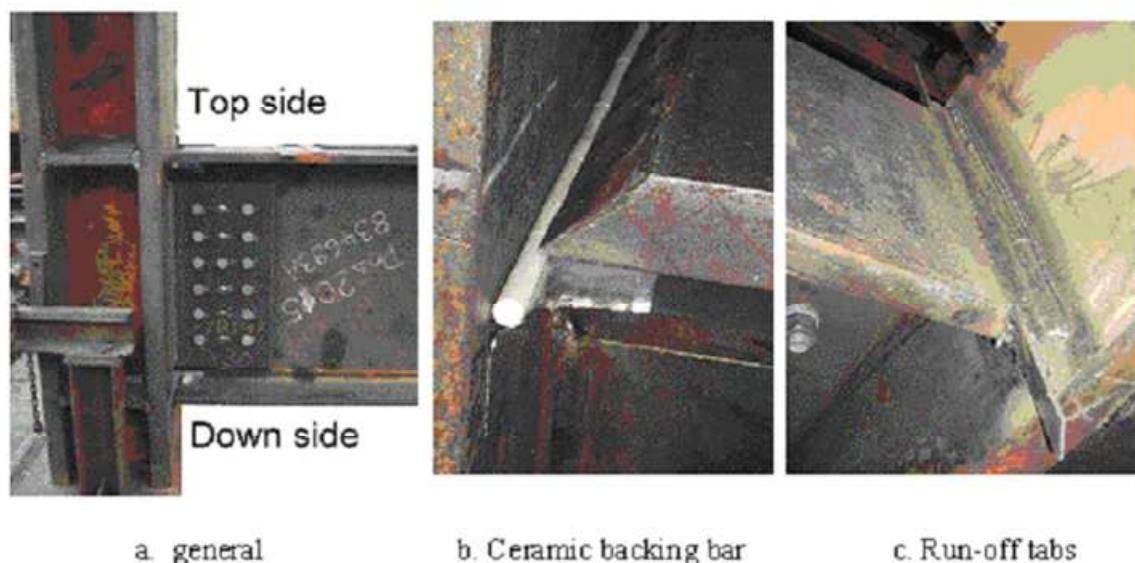
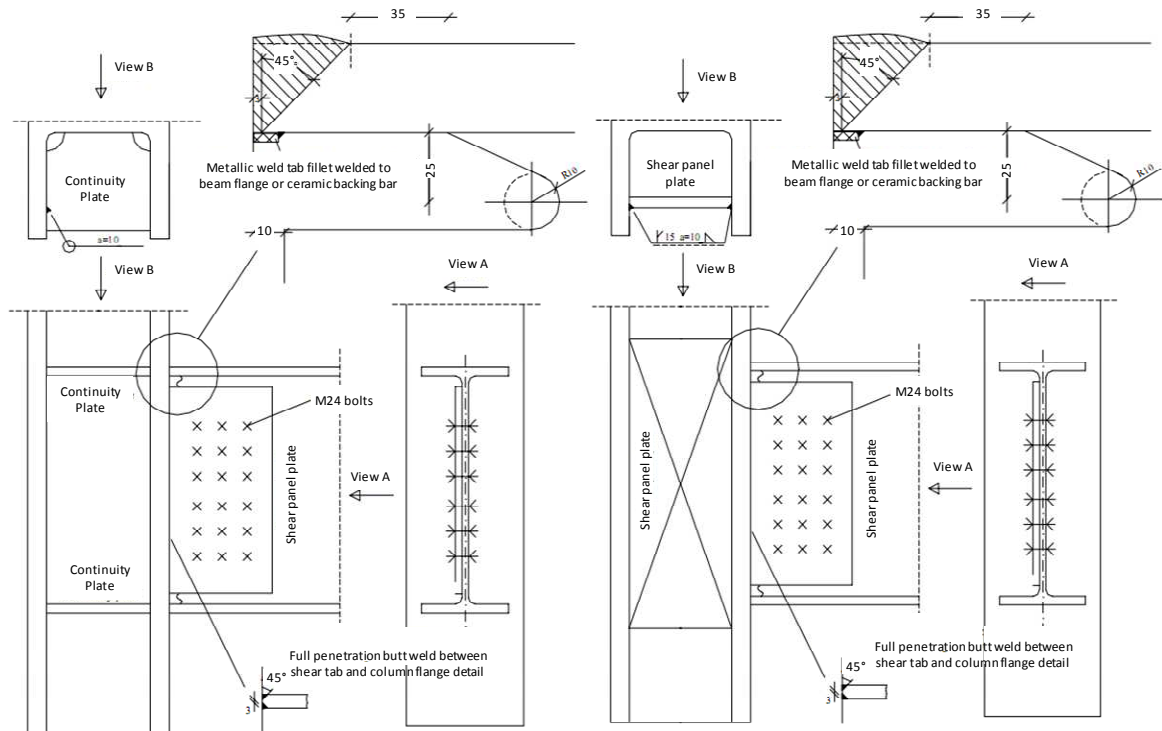


Figure 5-16: View of the fabrication of connection N°5 [BAN07]

The number of passes varied from 10 to 31 depending on flange thickness and heat input. An example is given in Figure 5-8 for specimen 5. Preheating the connection reduces the risk of hydrogen-induced cracks; therefore, the connection was preheated by a flame between 20 to 40°C.



a. Conventional continuity plates

b. Modified shear panel zone

Figure 5-17: VERAPS connection design from [BAN07]

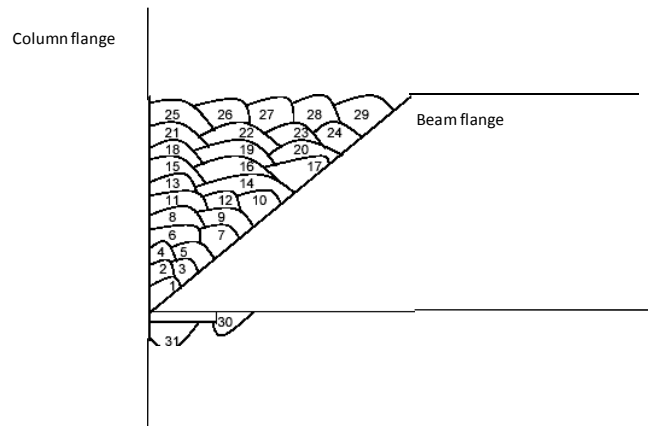


Figure 5-18: Pass description of the welding for the VERAPS n°5 connection from [BAN07]



Figure 5-19: Welding of VERAPS connection

Although 8 connections were fabricated (see Section 6.3.1), only the welding of connection n°5 was modeled due to the computation time. The average data of the heat source given by the University of Karlsruhe are provided in the table below.

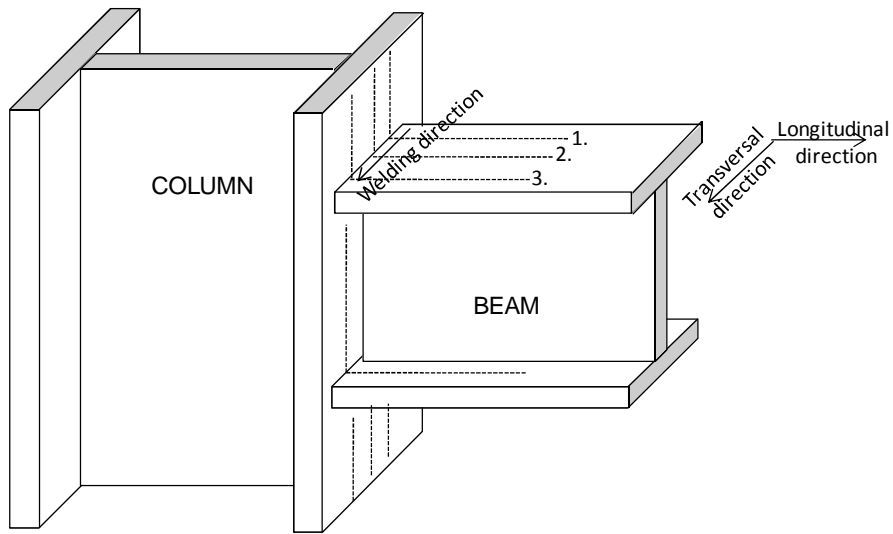
**Table 5-1: Welding heat source data**

$\eta UI$ (kW)	$v$ (mm.s <sup>-1</sup> )	Pass Number
5.4	3.3	18

### 5.7.2 The residual stress measurement

The measurement of residual stresses was carried out by ISQ on the beam-to-column weld using the Barkhausen's noise technique [BAN07] (see Figure 5-20). In each recorded point, the stress components both in longitudinal and transversal directions of the flange were measured. These points were aligned in the profile flange at selected locations from 10 mm to 250 mm away from the weld. From 10 to 100 mm the points were separated by 10 mm and from 100 to 250 mm and they were separated by 25 mm. Direct measurement on the welds was impossible due to their surface irregularities.

Barkhausen's noise technique does not allow for a direct measurement of stress. The method requires a calibration for a given material in order to establish the correlation of some magnetic parameters with present stress field. Small bars, about 200 mm x 40 mm x 10 mm thick, were machined from the column and beam. The bars were submitted to known tensile and compression loads, and the magnetic field was measured. The correlation between the stress and the magnetic field was established in order to convert the magnetic field measured in the connection into residual stresses. The measurements are given in Figure 5-21 and Figure 5-22.



-----: Position of the residual stress measurement

**Figure 5-20: Position of residual stress measurement**

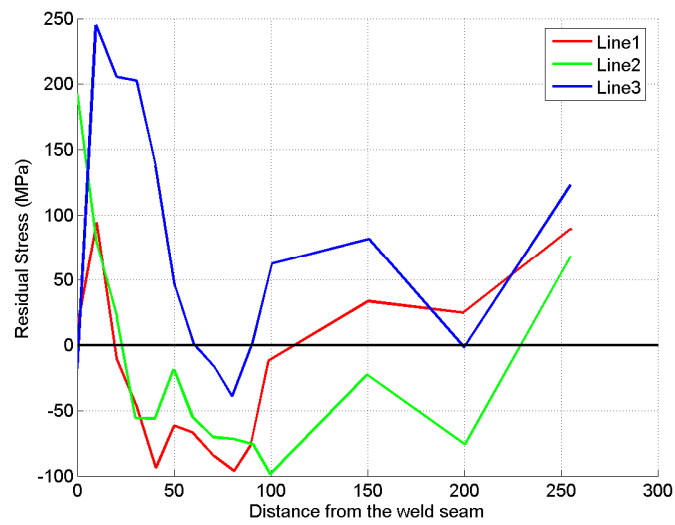


**Figure 5-21: Longitudinal stress measurements**

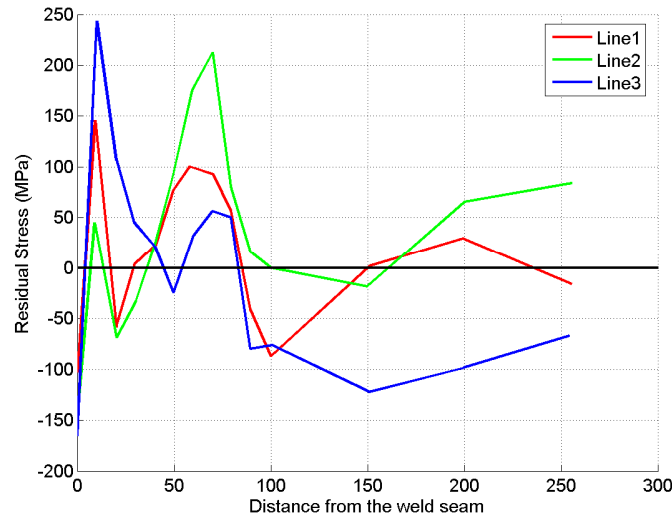


Figure 5-22: Transversal stress measurement

### 5.7.3 The material parameters

The material parameters were provided by Corus, who measured them with using a Gleeble thermomechanical simulator and a dilatometer, which includes the phase transformation effect on S275 grade steel [WEN03]. They provided the flow stress as a function of the strain and the temperature. To model the flow behavior of the base metal and weld metal studied, a correction was carried out in order to obtain the yield stress measured at 20°C by

$$\begin{cases} \sigma_{BM}(T) = \sigma_{275}(T) \frac{\sigma_{yBM}(20^{\circ}\text{C})}{\sigma_{y275}(20^{\circ}\text{C})} \\ \sigma_{WM}(T) = \sigma_{275}(T) \frac{\sigma_{yWM}(20^{\circ}\text{C})}{\sigma_{y275}(20^{\circ}\text{C})} \end{cases} \quad (5.18)$$

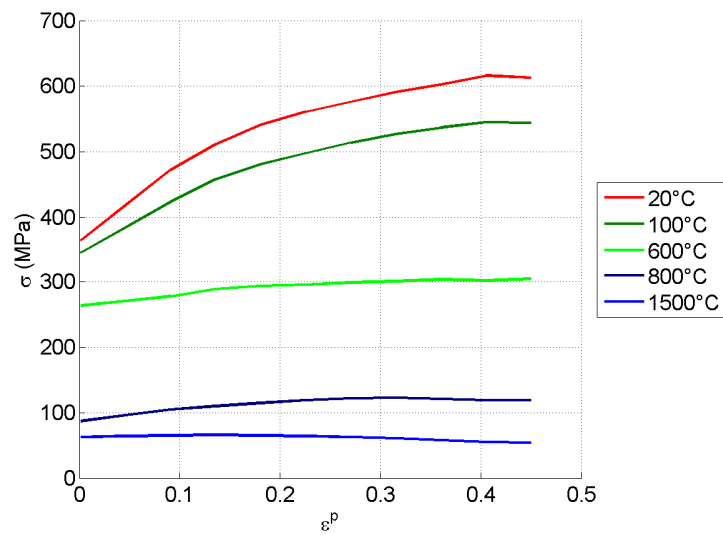
where  $\sigma_{BM}$ ,  $\sigma_{WM}$ , and  $\sigma_{275}$  are the uniaxial stress values for base metal, weld metal and 275 grades respectively,  $\sigma_{yBM}$ ,  $\sigma_{yWM}$ , and  $\sigma_{y275}$  are the initial yield stresses for base metal, weld metal and 275 grades respectively and  $T$  is the temperature. The values of the yield stresses at 20°C were defined in Section 2.5.4. The flow stress as a function of strain and temperature is listed in Table 5-2 to Table 5-3 and illustrated by Figure 5-23 and Figure 5-24.

Young's Modulus and the dilation as a function of the temperature come from the 275 grade as well. The thermal parameters, such as specific heat and conductivity, were identified on 316LNSPH steel grade. These thermomechanical parameters are listed in Table 5-4 and illustrated by Figure 5-25 to Figure 5-28.



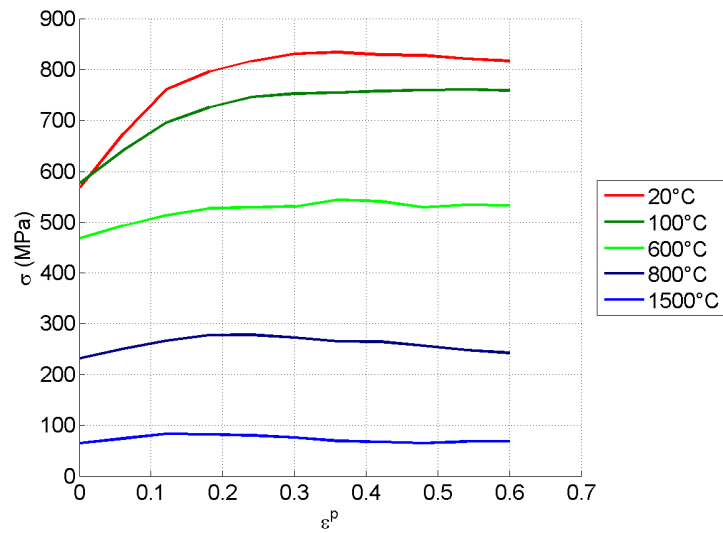
**Table 5-2: Flow stress as a function of strain and temperature for the base Metal**

Strain \ Temperature(°C)	Stress (MPa)													
	20	100	200	300	400	500	600	700	800	900	1000	1100	1300	1400
0.0014	365	346	356	412	403	350	264	139	87	46	38	32	69	63
0.04626	419	385	390	455	441	390	271	146	96	59	47	38	72	64
0.09112	473	424	425	498	479	429	278	153	105	73	56	44	74	65
0.13598	512	458	445	521	506	454	289	159	110	85	63	50	76	66
0.18084	541	481	465	536	531	472	294	160	115	94	68	55	76	65
0.2257	561	498	484	547	550	484	296	161	119	99	72	59	77	64
0.27056	576	514	497	555	560	491	299	163	122	102	74	62	75	63
0.31542	591	527	509	560	571	498	301	163	123	106	78	64	73	61
0.36028	603	537	521	561	588	507	304	165	121	109	85	65	69	58
0.40514	616	545	528	562	601	510	302	167	119	107	87	66	67	55
0.45	613	544	535	561	606	511	305	162	119	106	87	67	64	54

**Figure 5-23: Stress-plastic strain curve as a function of temperature for the base metal**

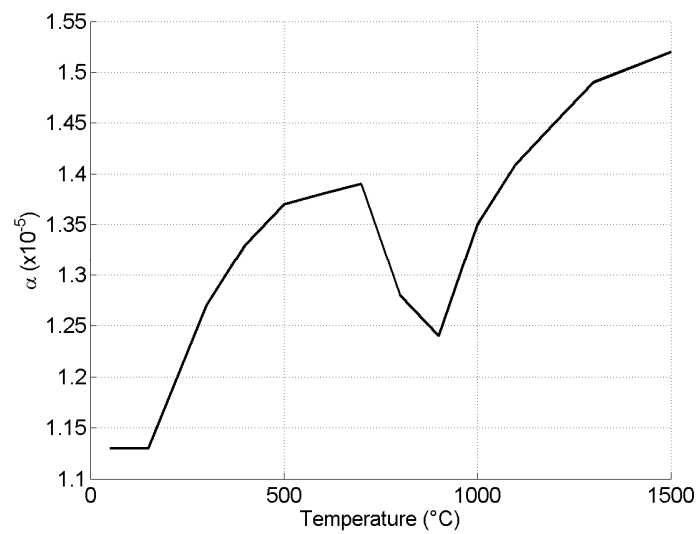
**Table 5-3: Flow stress as a function of strain and temperature for the weld metal**

Strain \ Temperature(°C)	Stress (MPa)														
	20	100	200	300	400	500	600	700	800	900	1000	1100	1200	1300	1400
0.0014	569	578	514	564	542	522	470	352	232	171	138	70	73	65	53
0.06126	674	642	589	629	614	559	494	371	250	195	155	85	85	74	57
0.12112	761	696	655	688	679	594	514	383	266	219	169	99	97	83	61
0.18098	796	726	690	727	717	624	528	389	277	228	175	114	105	82	63
0.24084	817	746	714	746	741	628	530	394	278	235	175	125	108	80	62
0.3007	831	753	730	765	744	634	532	393	272	232	172	129	104	76	58
0.36056	834	755	731	774	747	641	545	403	265	228	167	131	102	69	56
0.42042	829	758	742	780	747	642	542	398	264	221	162	126	103	67	54
0.48028	828	760	744	784	747	635	530	395	256	217	157	119	100	65	51
0.54014	821	761	744	791	748	624	535	387	248	210	157	114	96	68	49
0.6	817	759	743	802	750	624	534	384	242	202	153	111	92	68	47

**Figure 5-24: Stress-plastic strain curve as a function of temperature for the weld metal**

**Table 5-4: Thermo elastic parameters as a function of temperature**

Temperature (°C)	Specific Heat (J.kg <sup>-1</sup> .K <sup>-1</sup> )	Conductivity (J.m <sup>-1</sup> .s <sup>-1</sup> .K <sup>-1</sup> )	Young's Modulus (GPa)	Dilation (x10 <sup>5</sup> )
20	600.73	47.52	200.00	1.13
50	640.78	46.57	198.00	1.13
100	674.15	45.15	179.00	1.13
150	707.53	44.20	180.00	1.18
200	760.93	41.35	178.00	1.27
300	814.32	38.50	176.50	1.33
400	894.42	35.17	175.00	1.37
500	921.12	21.86	153.00	1.38
600	947.82	21.86	100.00	1.39
700	947.82	21.86	8.50	1.28
800	947.82	21.86	9.60	1.24
900	947.82	21.86	2.80	1.35
1000	947.82	21.86	1.00	1.41
1100	947.82	21.86	3.00	1.45
1200	947.82	21.86	4.20	1.49
1300	947.82	21.86	3.90	1.52
1500	600.73	47.52	200.00	1.13

**Figure 5-25: Thermal dilatation as a function of temperature**

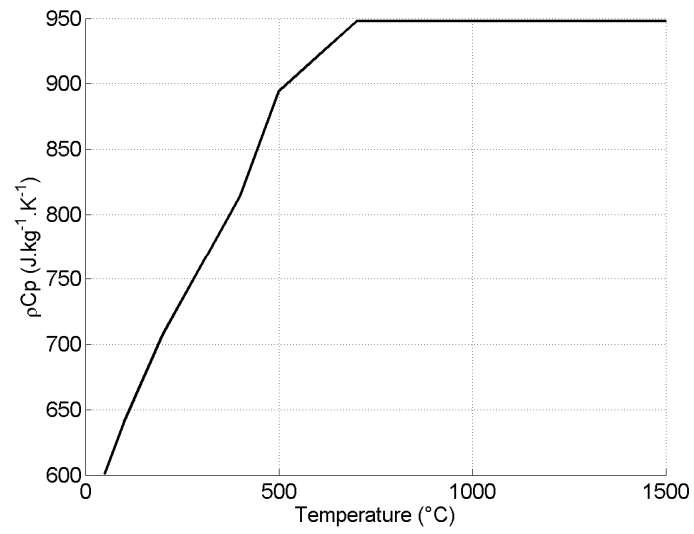


Figure 5-26: Specific heat as a function of temperature

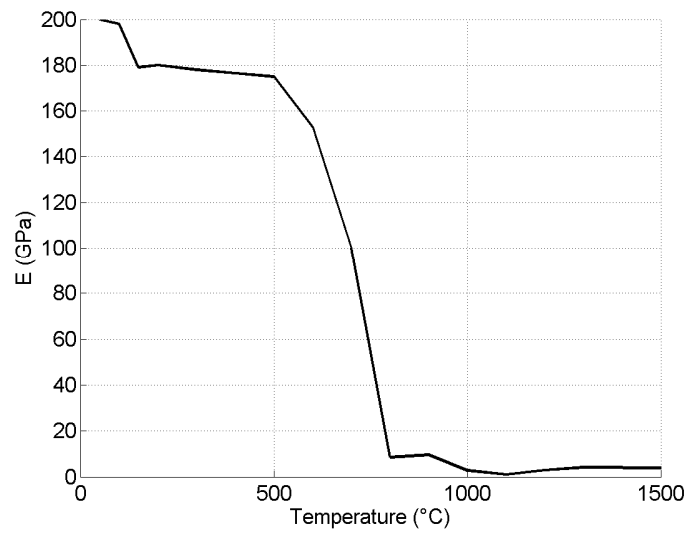


Figure 5-27: Young Modulus as a function of temperature

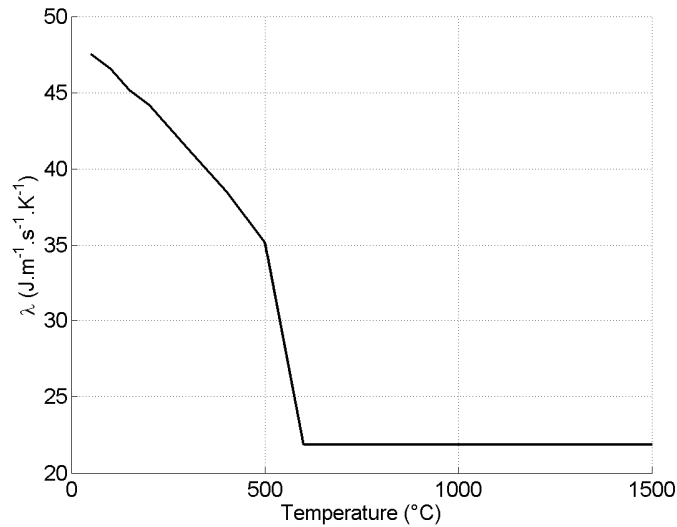


Figure 5-28: Conductivity as a function of temperature

The radiative exchange was taken into account in the convection coefficient. The convection coefficient at room temperature are defined to be  $h=15\text{W.m}^{-2}$ . It was assumed to be constant as no other data were available and  $T_{\text{ext}}=20^\circ\text{C}$  as in [GER05].

#### 5.7.4 FEM modeling description

Due to the tremendous geometry of the connection and the computation time of the 3D welding simulation, only a part of the connection was modeled. One assumes that the welding on one beam flange does not generate residual stresses on the other beam flange. Therefore, only a part of the welding between beam and column flanges was modeled. It was then checked on different geometries. The lengths were sufficiently long to be considered infinite and provided a stationary solution. The thicknesses of the beam and the column flanges remained identical to those of VERAPS ones.

Figure 5-29 shows the mesh and the dimensions of the simplified model used. The thermal mesh contained about 7700 nodes and 9000 elements. The mechanical mesh contained 6500 nodes and 7300 elements. All nodes of the beam and column ends were fixed. The meshes were generated with the 3D mesh generator developed during this research (see Section 6.3.1).

Due to the computation time, it was decided to model only two passes. The parameters of Goldack's heat source model are in Table 5-5. The values of  $f_f$  and  $f_b$  were obtained from the Goldack's paper [GOL84]. The ratio  $c_b/c_f$  is 2 as advised in Goldack's paper. The power and the heat source velocity were taken from Table 5-1. The ideal values of  $a$  and  $b$  are the dimensions of the passes. These values were increased in order to model two passes.

Table 5-5: Heat source parameters

$\eta UI$ (kW)	a (mm)	b (mm)	$c_f$ (mm)	$c_b$ (mm)	$f_f$	$f_b$	v (mm.s-1)
5.5	14	8	10	20	1.4	0.6	3.3

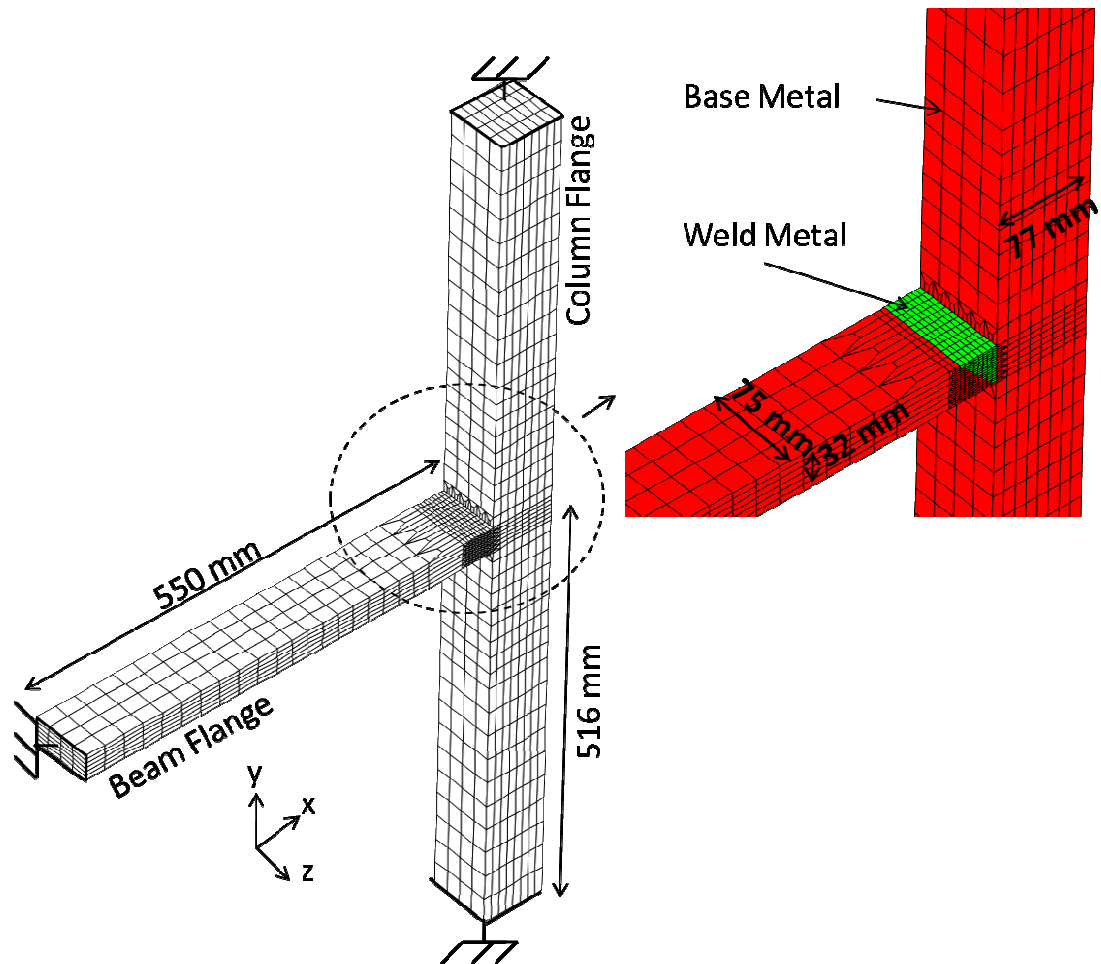


Figure 5-29: Description of beam-to-column flange finite element modeling

### 5.7.5 Results and discussion

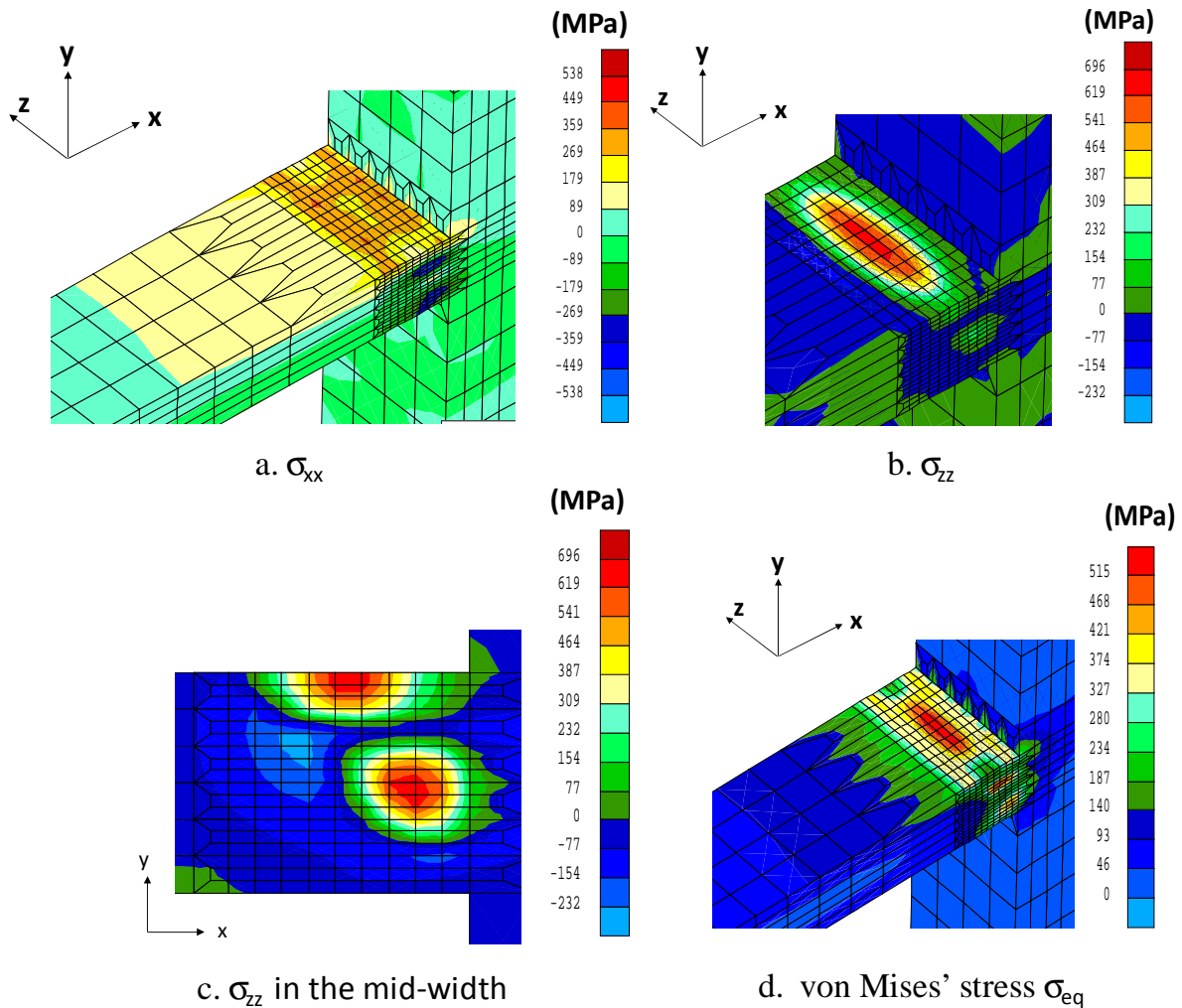


Figure 5-30: Contour plot of the residual stress analysis

The computation was quite-time consuming. Indeed, it required 10 days for only two passes. This limitation explains the author's interest in iterative methods presented in Appendix 1. Figure 5-30 shows the contour plot of the residual stress components. The equivalent von Mises' stress was close to the yielding stress near the path of the heat source. However, the residual stresses seemed to be too concentrated and no stress propagated in the column flange as expected. Figure 5-31 and Figure 5-32 show the comparison of the results of the FEM computation and the experimental measurements on the beam flange's surface. The position where  $x$  is null corresponds to the interface between the beam flange and the welding. The FEM computation provided an equivalent amount of stress but did not succeed in modelling some compression zones in the longitudinal direction. Furthermore, the number of passes modeled seems too low and the boundary conditions were probably not well-adapted in comparison with the reality of the welding process.

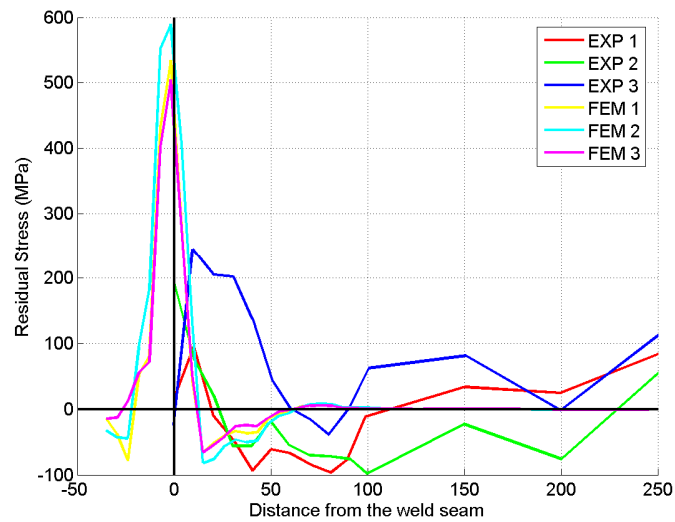


Figure 5-31: Comparison of the longitudinal residual stress between the measurement and simulation of the surface of the beam

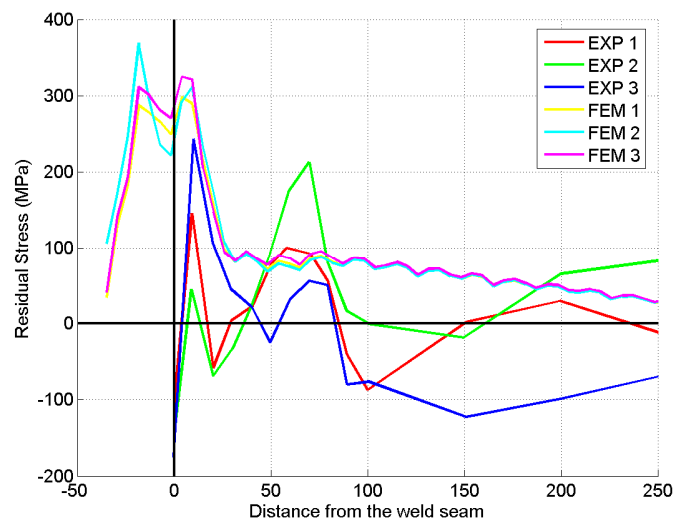


Figure 5-32: Comparison of the transversal residual stress between the measurement and simulation of the surface of the beam

## 5.8 Conclusions

The simulation of the welding process by finite elements presents a number of difficulties. In fact the computation time was significant because of the large dimensions of the flange and the high number of passes. The sequential computation, the birth technique and the use of two different meshes for the thermal and mechanical modeling made it possible to drop this computation time.



Simplified modeling of the welding of a beam flange on a column flange was carried out. First, two passes were modeled instead of 18 passes as in experimental testing. The simulated structures presented a level of residual stress equivalent to that in the experimental measurements. However the residual stress gradient did not correspond to the experimental one.

More work would have been necessary to further develop this method but (as in all research) the time short out and the author chose to focus his effort on applying the damage model, rather than reaching a more representative three-dimensional residual stress field.

The first idea was to look at a two-dimensional simulations to model all the passes, adjust the parameters of the heat source and see if one can modify the parameters to model fewer passes with equivalent energy and predict residual stresses. Then it should be possible to perform three-dimensional modeling with sufficient passes.


The analytical methods or normative approaches do not provide well-balanced three- dimensional residual stresses. Starting with a strongly unbalanced stress field at the initial step did not result in convergence, so the final damage simulations were performed without residual stresses.

Finally the fatigue damage was not coupled with the stress analysis to avoid singularities in the stiffness matrix of the finite element analysis. However, the fatigue damage was then coupled with crack propagation in the cohesive zone model (see Chapter 4.3)



# **Chapter 6**

# **Beam-to-column connection simulations**



## 6.1 Introduction

This chapter discusses the final step of this research study. Its aim is to model the crack's onset and propagation in the large scale cyclic loading tests of a heavy steel weld beam-to-column connection performed at the University of Karlsruhe.

This chapter begins with the definition of a moment resisting frame and the philosophy behind its design. Then the VERAPS connections studied are presented.

Furthermore as the connections simulated had different geometries and types of components a module was developed to generate the 3D mesh of the VERAPS beam-to-column connections. This module is described in this chapter.

Finally, this chapter presents the simulations of the large scale tests performed with the Lagamine code. Firstly, some simulations of different specimens without damage were performed to validate the 3D mesh and the global predicted force. Then, modeling was carried out with only fatigue damage to identify the path of potential cracks for one connection. Finally, a model with the cohesive zone model coupled with fatigue damage was performed. All the numerical analyses have been compared with experimental measurements and observations.

## 6.2 Presentation of the VERAPS connections

### 6.2.1 Introduction

#### 6.2.1.1 The moment resisting frame (MRF)

An earthquake is a tremor of the ground caused by a sudden movement in the earth's crust. Some earthquakes cause slight tremors and others destroy buildings by sideways forces. That's why it is important to design buildings in order to withstand earthquakes in seismic zones. Such a building can be modeled by its frame, which is composed of beams and columns (see Figure 6-1).

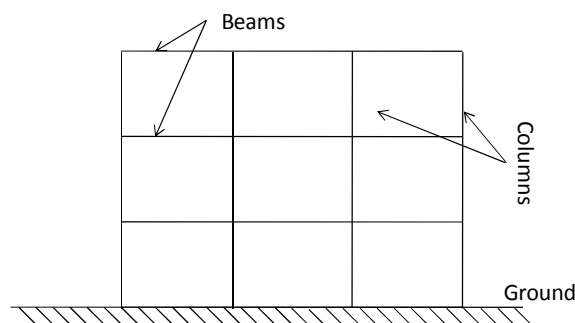


Figure 6-1: Building frame

To avoid irreversible damage, several structural systems have been developed to withstand the sideways forces (see Figure 6-2) described below.

- Brace frame: trussing is used to withstand sideways forces in buildings. Trussing, or triangulation, is formed by inserting diagonal structural members into rectangular areas of a structural frame. It helps to stabilize the frame against sideways forces from earthquakes and strong winds.
- Shear wall: a vertical wall that is used to stiffen the structural frames of buildings. They help frames to withstand sideways earthquake forces.
- Moment resisting frame: the joints, or connections, between columns and beams are designed to be rigid (i.e. the angle between the beam and column end tends to remain constant); therefore the structural members are designed to be strong. They can be manufactured with steel or concrete.

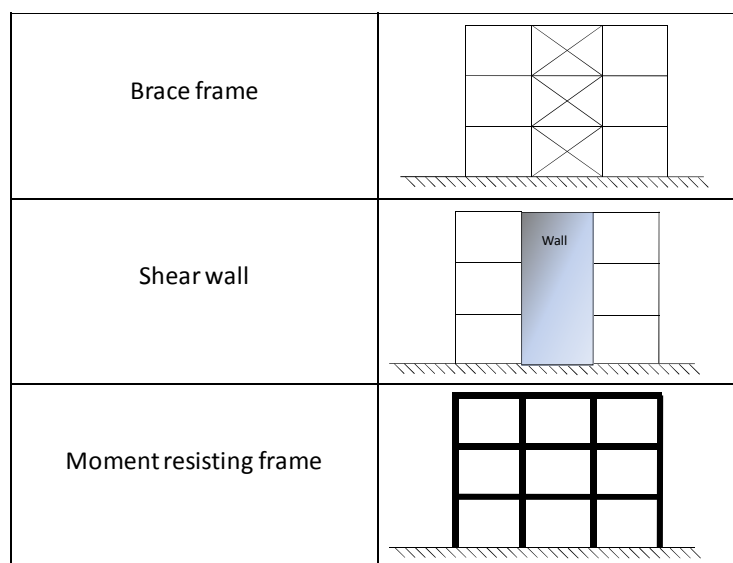


Figure 6-2: Solutions of structural systems to withstand to earthquakes

### 6.2.1.2 The connection ductility of a steel MRF

For a steel moment resisting frame, the dissipation of seismic energy input which plays a fundamental role. This dissipation is dependent on the frame's ductility, which is the ability of the structure to undergo large plastic deformations without losing strength.

The recent earthquakes in Northridge (1994) and Kobe (1995) have seriously compromised this idyllic image of steel as a perfect material for seismic areas. In these quakes, some brittle fractures appeared in the welded beam-to-column connection. Aiming to fill these gaps, the world of civil structural research [MAH98] is moving to give designers constructional rules that will make it possible to design high-ductility structures in seismic areas.

In fact, the connection's ductility depends on all of the component behavior. Their inelastic deformations correspond to plastic hinges at localized positions. The ductility of the structure is linked to the rotational capacity of these plastic hinges. The design philosophy must bear in mind that the inelastic deformations can occur in one or more of the three components of the

connection: the beam end, column end or panel zone. The best solution is for the plastic hinge to develop at the beam end.

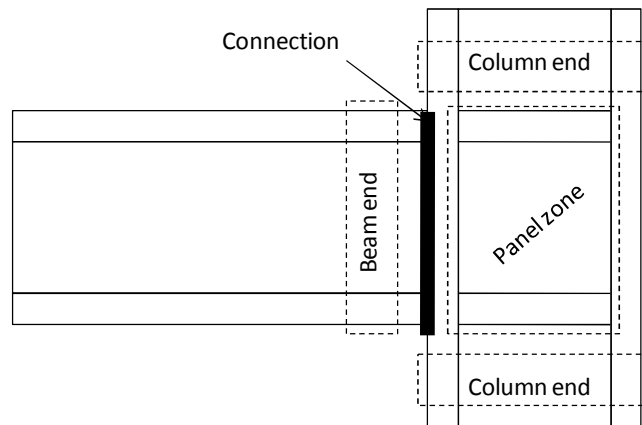


**Figure 6-3: Components of a frame connection**

There are two kinds of beam-to-column connections: welded connection and bolted connection. In the VERAPS project only welded connections are studied. For a welded connection, its ductility is linked to the strength of the shear deformation in the panel, panel crushing or weld fracture [GIO02] (see Figure 6-4). Of these, this thesis focused on modeling the weld fracture.

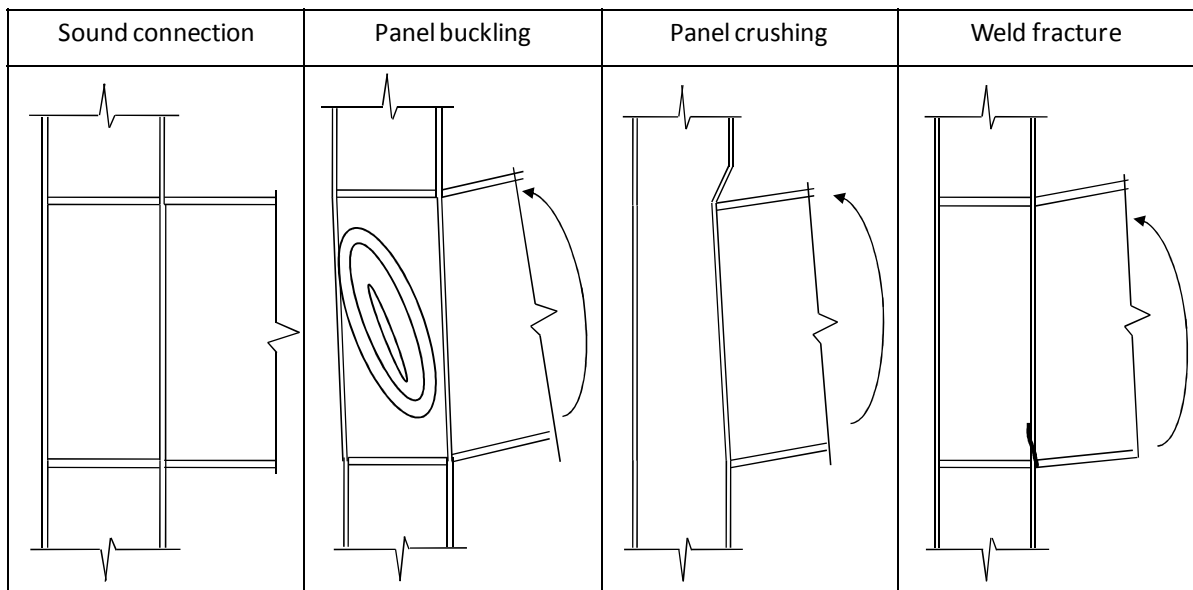


Figure 6-4: Weld connection failure

## 6.2.2 The connection description

Eight large-scale tests were performed with a 6300kN alternating load test frame at the University of Karlsruhe. The frame was oriented for a classic compression-tension test, which gives in the specimen geometry presented in Figure 6-5. Each test sample was subjected to cyclic loading with step-wise deformation cycles increasing up to failure according to the loading procedure of FEMA 350.

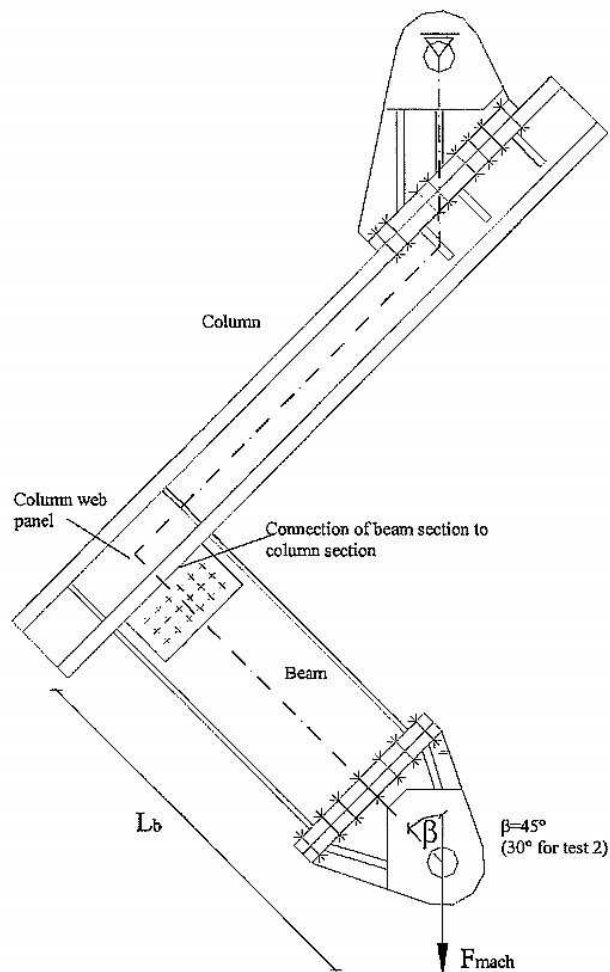


Figure 6-5: Test specimen (from [BAN07])

### 6.2.2.1 The bars

Beams and columns were I sections. The dimensions of beams and columns are defined in Figure 6-6 and Table 6-1. All beams, columns and plates were 355 J0 and J2 grades steel according to the EN10025-2 standard [EN102]. The exact composition can be found in [BAN07]. Varying these dimensions made it possible to test different ratios between plastic joint moment  $M_{pj}$  and beam plastic moment range  $M_{pb}$  (see last column of Table 6-1).



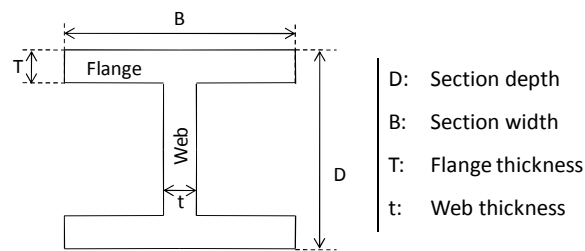


Figure 6-6: Cross section description

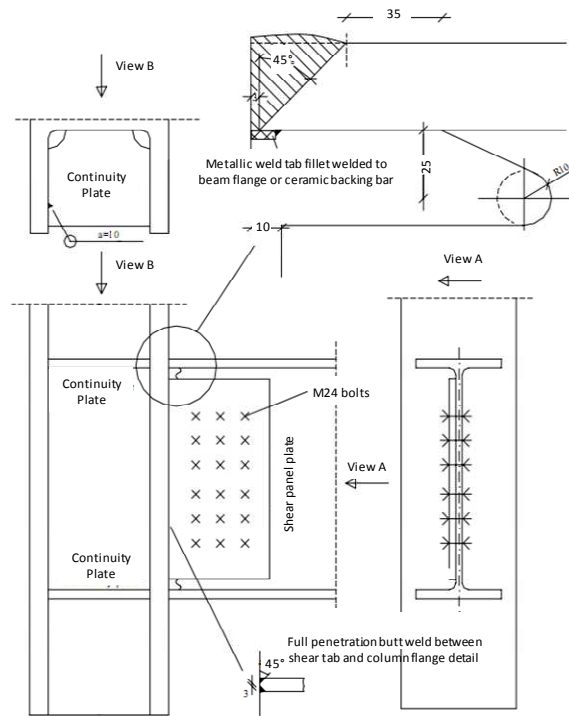
Table 6-1: Cross section dimensions

Test Number	Beam				Column				$M_{pj}/M_{pb}$
	D (mm)	B (mm)	T (mm)	t (mm)	D (mm)	B (mm)	T (mm)	t (mm)	
1	926.6	418.5	32	19.4	514	437	97	60.5	1
2	840.7	292.4	21.7	14.7	514	437	97	60.5	2.25
3	926.6	418.5	32	19.4	498	432	88.9	55.6	0.88
4	918.4	305.5	27.9	17.3	465	421	72.3	45	1.01
5	926.6	307.7	32	19.5	474.6	424	77	47.6	0.91
6	918.4	305.5	27.9	17.3	474.6	424	77	47.6	1.34
7	926.6	307.7	32	19.5	474.6	424	77	47.6	1.19
8	926.6	307.7	32	19.5	474.6	424	77	47.6	1.21

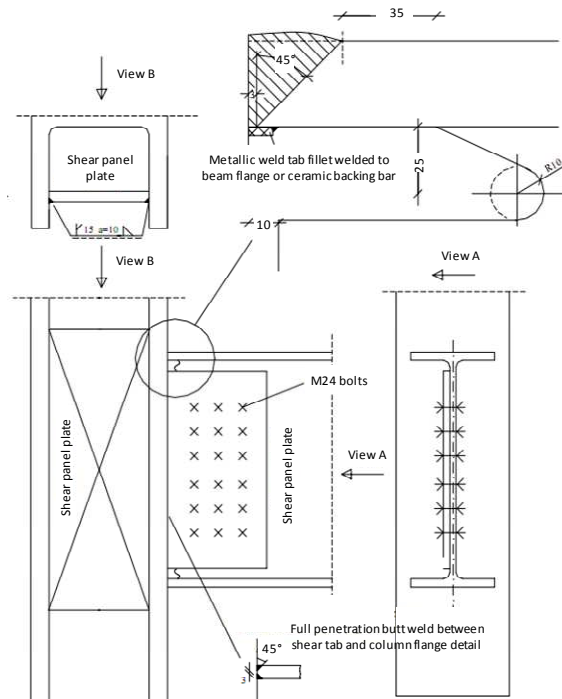
### 6.2.2.2 The stiffeners

Two types of stiffeners of the column panel were manufactured (see Figure 6-7):

- 30-mm-thick transverse stiffeners acting as continuity plates for the beam flanges but bringing no increase in the shear resistance of the panel zone.
- 40-mm-thick extended doubler plates placed parallel to the column web. They acted as stiffeners and as continuity plates and they increased the shear resistance of the panel zone significantly.



a. Conventional continuity plates



b. Modified shear panel zone

Figure 6-7: Details of the connections from [BAN07]

### 6.2.2.3 Connection details

In all specimens, the beam flanges were welded to the column flanges with butt welds. The flange butt welds transmitted the full plastic moment of the section area of the beam flange. For specimens 1, 5, 6 and 7, the beam web was bolted to a shear tab which was welded to the column flange. In specimens 2, 3, 4 and 8 the shear tab was welded and bolted to the beam web. The bolts and the welding of the shear tab are shown in Figure 6-8. The shear tab is welded to the column flange (see Figure 6-7) for all specimens. The bolted shear tab transmitted the plastic moment of the beam web and the corresponding shear.

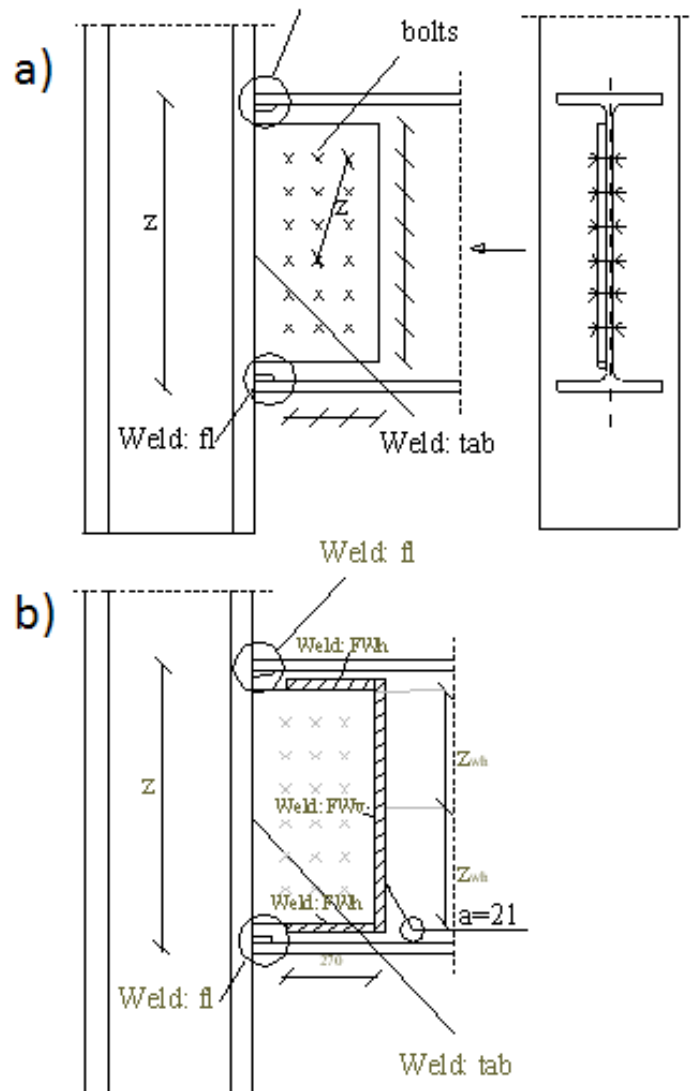


Figure 6-8: Connection Detail with a) bolted shear tab and b) welded and bolted shear tab from [BAN07]

Table 6-2: Joint design description

Specimen Number	Type of reinforcement	Shear tab connection
1	Transverse stiffeners	Bolted
2	Doubler plate	Welded +Bolted
3	Transverse stiffeners	Welded +Bolted
4	Transverse stiffeners	Welded +Bolted
5	Transverse stiffeners	Bolted
6	Doubler plate	Bolted
7	Doubler plate	Bolted
8	Doubler plate	Welded +Bolted

#### 6.2.2.4 The welding

Regarding the welding, the VERAPS connections were manufactured using a range of consumables to cover the full toughness range, together with three different types of processes:

- MMAW: manual metal arc welding,
- TCMAWAGS: tubular cored metal arc welding with active gas shield,
- MAWWOGS: metal arc welding without gas shield.

The welding parameters of these processes are summarized in Table 6-3 below.

Near the weld butt, a hole was machined on the beam web to allow access for the welding process (see Figure 6-7). The dimensions of the weld access holes complied with FEMA requirements.

Some characteristic flaws, such as a lack of fusion, were artificially added during the welding process. During the welding process of the beam flange to the column flange, a backing bar in steel or ceramic was installed below the butt weld to support the welding at the beginning. It was removed at the end of the welding process.

**Table 6-3: Welding parameters**

Specimen Number	Consumable EN Designation	Welding process	Pre-heat (°C)	Nr of passes	Heat Input (kJ.mm <sup>-1</sup> )	Electrode diameter (mm)	Comment
1	440G425MG3Si1	TCMAWAGS	20-40	17	1.6	1.2	
2	440G425MG3Si1	TCMAWAGS	20-40	10	1.5	1.2	
3	EN758T42	MAWVOGS	70-120	21	1.6	2.0	No gas shield
4	499E380RR12	MMAW	70-120	31	1.0	2.5-4	
5	499E424B73H5	MMAW	40	18	1.9	3.2-5	Lack of fusion
6	758T352YN2	MAWVOGS	20-40	10	1.7	1.6	without active gas shield weld flaw
7	499E42B73H5	MMAW	20-40	12	2.3	3.2-5	High heat input
8	758T424NiYN1	MAWVOGS	20-40	10	2.3	20-40	Without active gas shield Ni consumables weld flaw

### 6.2.3 The test procedure

Loading protocols used in the tests performed are related to the behavior of a structure which undergoes an earthquake. The aim was to check the ductility required in cyclic plastic conditions. Of course, in reality this ductile behavior depends on the earthquakes which are presumably represented and the protocol should in principle be related to the seismicity of the zone, since the duration of an earthquake is proportional to its magnitude. However, such a loading would be very difficult to apply. The protocols are rather arbitrarily defined as far as the number of cycles at a given level of deformation is concerned.

FEMA 350 [FEM00] gives criteria for the seismic evaluation of a moment-resisting steel frame. Different prequalifications for connection types are given as well as parametric limitations on their applicability. For connections outside the applicability of the prequalification, a test procedure has been defined.

In FEMA 350 [FEM00] and AISC 2002 [AIS02] procedures for a moment-resisting frame, the loading sequence for beam-to-column connections is explicit. Rotations expressed in radians are imposed. The rotation,  $\theta$ , is defined by Equation (6.1) and Figure 6-9.

$$\theta = \frac{\Delta u}{L_b} \quad (6.1)$$

where  $\Delta u$  is the vertical displacement of the beam end and  $L_b$  is the beam cantilever's length.

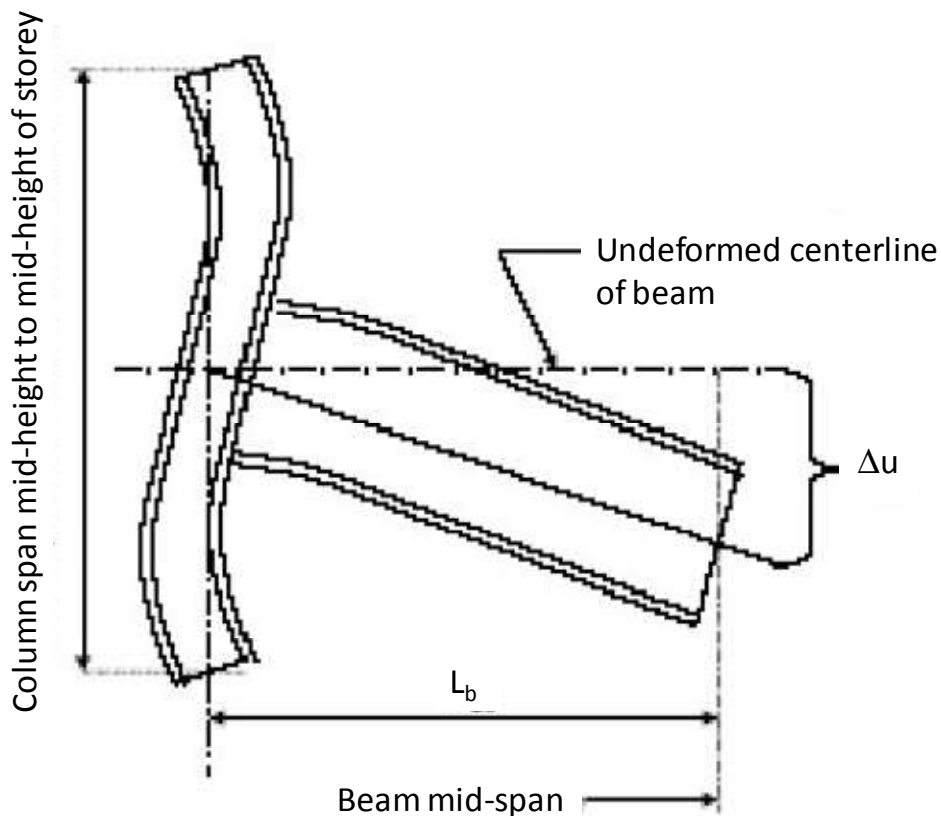


Figure 6-9: Definition of connection rotation from FEMA 350 [FEM00]

The protocol imposes the number and the amplitude of cyclic rotations defined in Table 6-4 until macrocracks are observed. If no macrocracks appear after the total number of cycles, the rotation amplitude is incremented by 0.01 radians, with two cycles of loading at each rotation level.

**Table 6-4: Cyclic rotation imposed on the connection according to FEMA 350**

Step	Number of cycles	Rotation amplitude (rad)
1	6	0.00375
2	6	0.00500
3	6	0.00750
4	4	0.010
5	2	0.015
6	2	0.020
7	2	0.30

Figure 6-5 shows the test configuration for the 8 connections in the VERAPS project. In contrast to various tests performed in FEMA 289 [FEM97], the beam section was not only subjected to shear forces but also axial forces. Therefore VERAPS' beam cantilever was shorter than FEMA's and the rotation amplitude was modified in such a way that the first two steps were in the elastic loading range.

The experimental device imposed a cyclic displacement which caused a reaction moment in the beam section. The beam's elastic limit moment,  $M_{be}$ , was computed before each cyclic test. In a static elastic load step 0, the connection was loaded up to 70% of the elastic limit load,  $F_e$ , determined by:

$$F_e = \frac{M_{be}}{L_b \sin \beta} \quad (6.2)$$

where the angle,  $\beta$ , is defined in Figure 6-5. Then, the connection was released. The machine force,  $F$ , was measured as a function of the imposed machine displacement,  $\Delta u$  (see Figure 6-10).

The stiffness,  $K_e$ , was identified by the tangent of the force displacement curve:

$$K_e = \frac{F}{\Delta u} \quad (6.3)$$



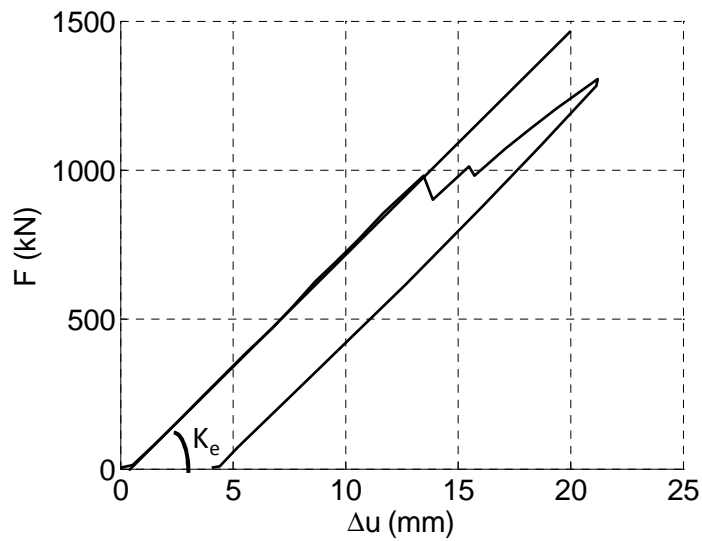


Figure 6-10: Identification of  $K_e$  for the specimen 1

Thus the elastic limit displacement,  $\Delta u_e$ , was found by:

$$\Delta u_e = \frac{F_e}{K_e} \quad (6.4)$$

Consequently, in load step 1, the specimen was loaded with the amplitude ranging between 62% and 74% of  $\Delta u_e$ . For the subsequent step, the displacement's amplitude was defined according to the rotation,  $\theta$ , in the FEMA 350 [FEM00] scheme. The steps were repeated until components in the connection failed or a load decrease of at least 10 % was observed.

During the test, the displacement was imposed and the machine's force was measured. For this purpose, some actuator and strain gauges were installed on the connection.

#### 6.2.4 Test results

Table 6-5 describes the different type of cracks observed in the connections after testing. The other aspects of the results have been summarized in [BAN07].

**Table 6-5: Results of VERAPS experiments**

Specimen Number	Failure description
1	Tearing of beam web cut out
2	Beam flange buckling and shear tab weld cracking
3	Weld cracking of in bottom flange; fracture from sub-surface weld flaw
4	Lamellar tear in column HAZ; flange weld fracture, brittle 'divot' type in column HAZ
5	Weld fracture
6	From weld toe in top flange, high deformation in beam flange; ductile tearing from access hole
7	Ductile tearing from access hole; no fracture of HAZ or weld metal
8	Crack from shear tab-column flange weld; no flange weld cracking found

## 6.3 FEM simulations

### 6.3.1 Mesh Generator

For this project a 3D mesh generator was developed. Indeed the geometry of each component was rather complex (e.g. web access hole or shear tab weld). In addition, each specimen had different dimension and different type of reinforcement (e.g. transverse stiffeners or a doubler plate). Therefore, meshing all specimens involved a great deal of work. The decision was made to develop a module based on the dimensions and the stiffener type as data which could generate all meshes. Consequently, the meshing work was performed only once.

#### 6.3.1.1 Characteristics

A three-dimensional structured mesh generator for Lagamine code was developed, using the language FORTRAN 95. The structure under investigation was divided into blocks and areas. The blocks were defined by 8 nodes and the areas by 4. The subdivision was defined in a local triad ( $\underline{e}_x$ ,  $\underline{e}_y$ ,  $\underline{e}_z$ ). The mesh nodes were generated by interpolation between the nodes defining the block. Different kinds of blocks could be meshed, as follow:

- the simple block,
- the transition block,
- the simple area,
- the transition area.

The simple block (see Figure 6-11) is a hexahedral block composed of  $N_x \times N_y \times N_z$  elements where  $N_x$  is the number of hexahedral elements in the  $\underline{e}_x$  direction,  $N_y$  is the number of elements in the  $\underline{e}_y$  direction and  $N_z$  is the number of elements in the  $\underline{e}_z$  direction.

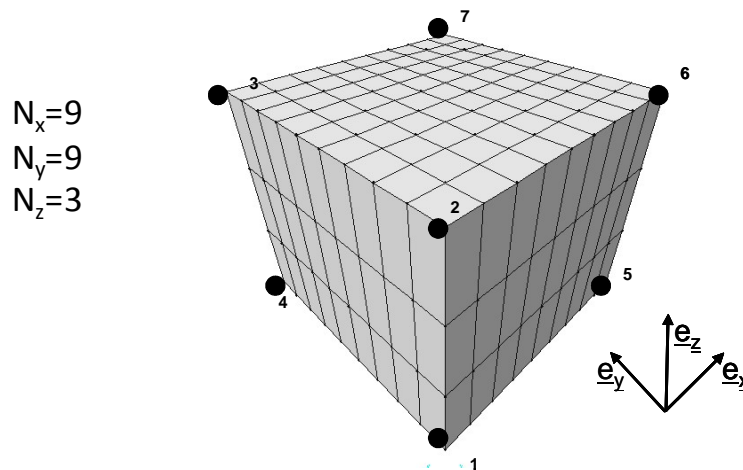


Figure 6-11 Simple bloc

The transition block (see Figure 6-13) allows the mesh to be refined in one direction. It uses the method to pass from one to three element subdivisions (see Figure 6-12):

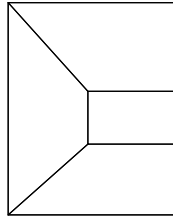


Figure 6-12: Methods to pass from one to three element subdivisions

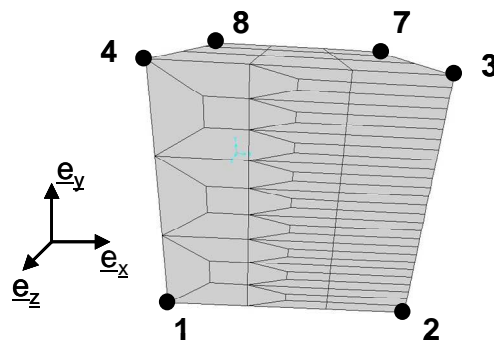


Figure 6-13: Transition block to be finer in the  $e_y$  direction

The simple area (see Figure 6-14) is a quadrilateral area composed of  $N_x \times N_y$  blocks.

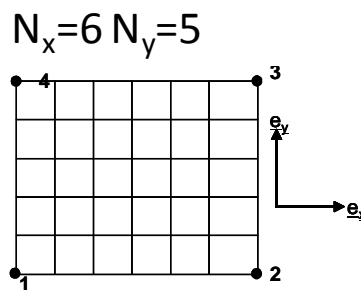


Figure 6-14: Simple area

The transition area (see Figure 6-15) is quadrilateral area that makes it possible to refine a mesh in one direction. Like the transition block, it uses the methods to pass from one to three element subdivisions (see Figure 6-12):

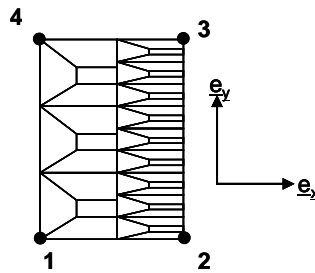


Figure 6-15: Transition block to be finer in the  $e_y$  direction

Once all blocks have been defined, the module generates the nodes and elements in each block. The nodes with the same positions are merged at the interface between 2 adjacent blocks. A group of blocks can be generated by axial symmetry from defined blocks. For example, the blocks can be defined for a fourth of a beam. The nodes and elements of the three fourth remaining fourth parts are generated by symmetry with the nodes and elements of the defined quarter.

The definition of the mesh is set in a data file (\*.msh). Then, the program generates a data file (\*.lag) which is to be used in the compilation by the Lagamine pre-processor, PREPRO, so that one can see the mesh with the Lagamine postprocessor, DESFIN. It also generates a file (\*.leq) where the positions of the nodes and the connectivity table are defined; therefore, it can be used to generate a complete data file for Lagamine or another FEM code with another program (e. g. Matlab or Fortran) to define the constitutive law or the boundary conditions, for example.

### 6.3.1.2 Adaptation to the VERAPS connection

A numerical module allows a \*.msh file to be generated containing the needed data to generate a mesh for a T weld beam-to-column connection. The data of this module is made up of the dimension of the beam and the column (see Figure 6-6).

Then one enters the type of reinforcement, as presented in 6.2.2.2:

- transverse stiffeners,
- doublers plates.

Thus the meshes generated of the connections in this study were composed of approximately 13000 nodes and 8500 elements. The elements are mechanical solid 8-nodes BWD3D [LI97] of mixed type available in the Lagamine code. Figure 6-16 and Figure 6-17 present the meshes of test 5 with transverse stiffeners and test 6 with an improved doubler.

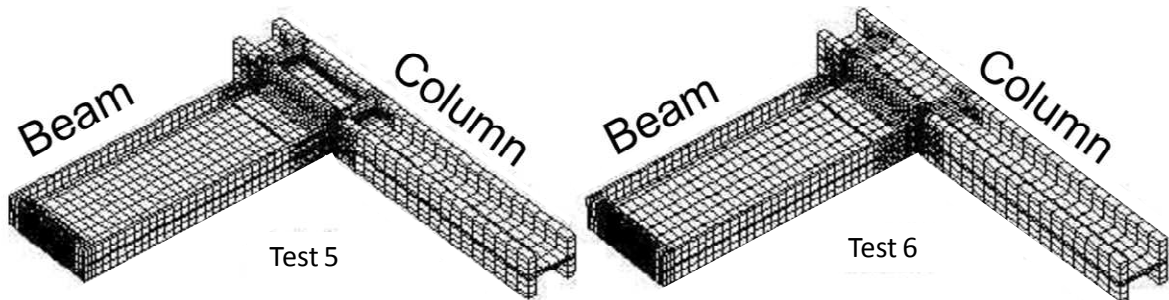


Figure 6-16: Mesh of two beam-to-column connections tested by Karlsruhe

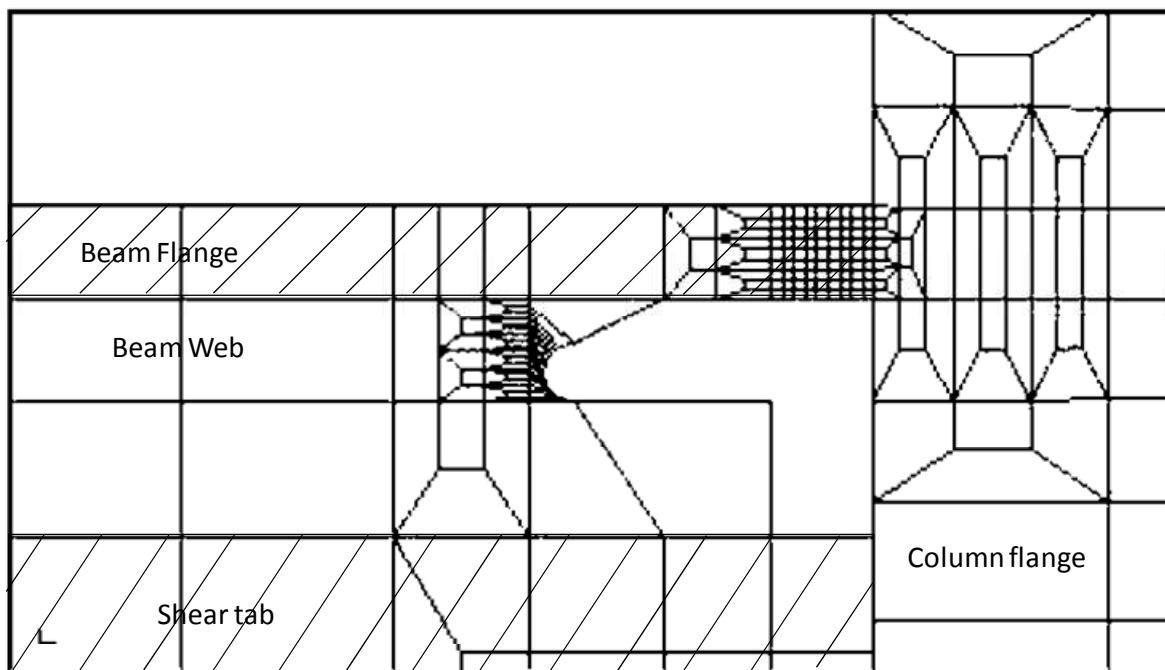


Figure 6-17: Mesh of the connection around the welding

A plate was added to the end of the beam to stiffen it and avoid yielding due to imposed displacement. The beam support was equivalent to a rolling bearing whereas the column support was equivalent to a hinge. Displacements are imposed on three node lines close to the centre of the web at the end of the beam. Therefore, the rotation was free and no physical plasticity was allowed at this point. The boundary conditions are described in Figure 6-18.

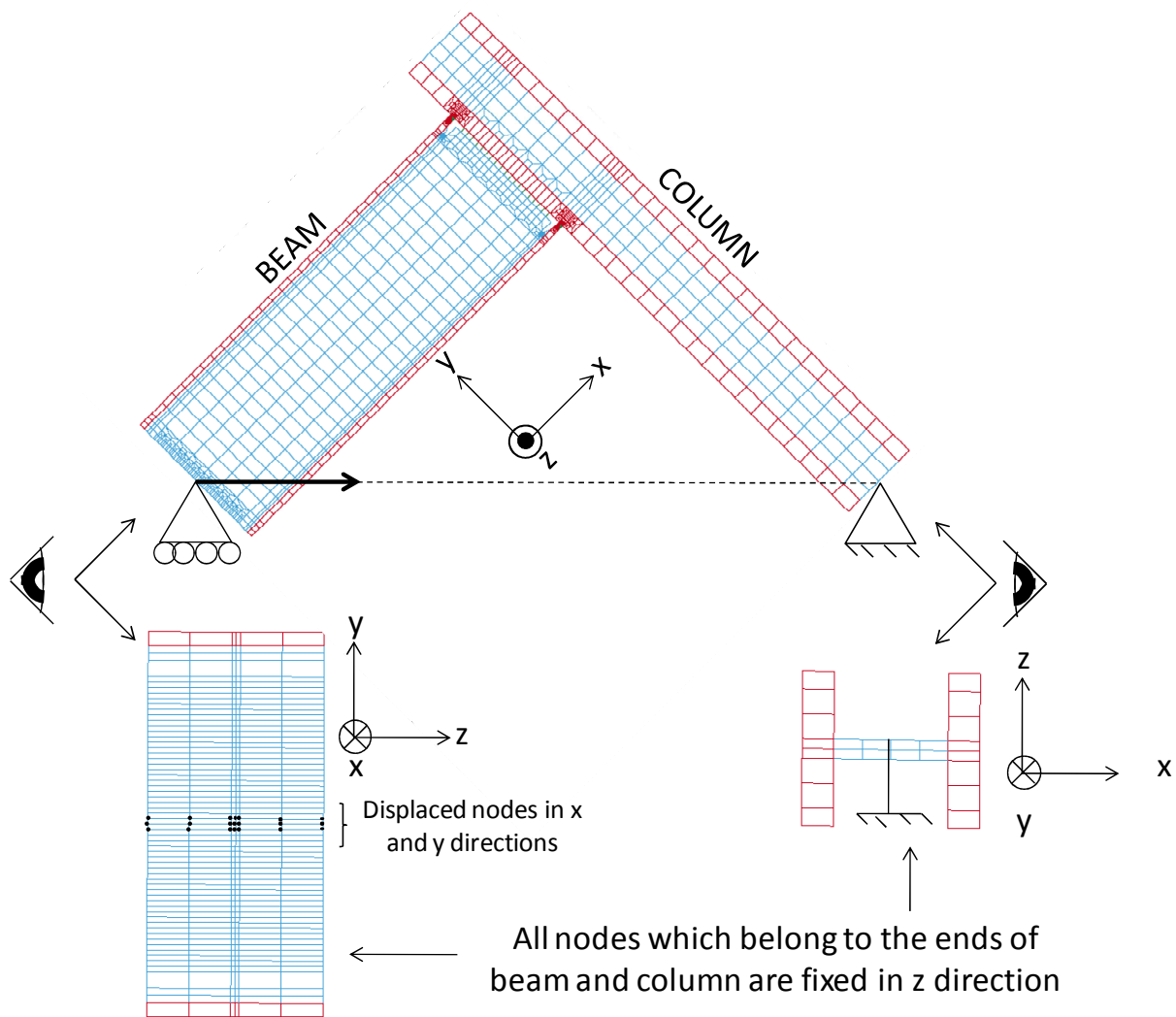


Figure 6-18: Boundary condition of the connection modeling

The constitutive laws for each material were calibrated (see Chapter 2.5.4). As a result, the constitutive laws used were different for the flanges, the web and the welding (see Figure 6-19).

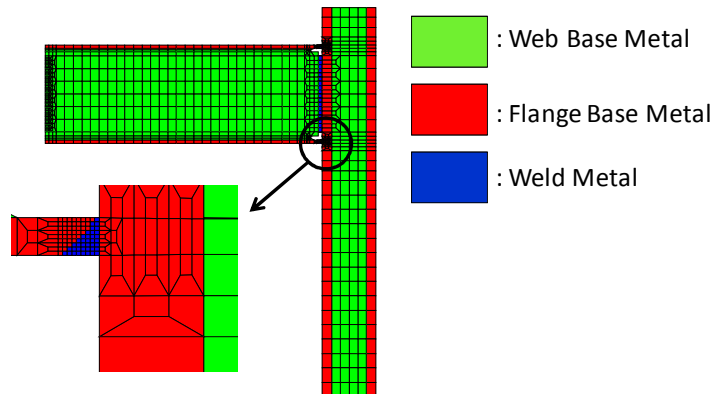


Figure 6-19: Position of the different sets of hardening coefficient

The mesh did not model the bolts of the shear tab. Instead, the connection between the shear tab and the beam web was complete because the nodes were merged at the interface between the two components. The weld metal material of the shear tab-to-column flange and the beam flange-to-column flange connections were modeled.

### 6.3.2 Simulations without damage

The aim of this modeling was to validate the model by predicting the mechanical behavior of the connection before damage phenomena. Moreover, Corus required the longitudinal stresses through the beam flange, welding metal and column flange for different rotations,  $\theta$ , for three connections with different levels of plastic moment ratios, as these results served as input data for the RAP analysis.

#### 6.3.2.1 Static loading

Only static displacement was imposed up to a high level of rotation. During these simulations, no damage neither crack propagation was modeled and the residual stresses were not taken into account in the initial state.

Connections n°1, n°5 and n°6 were modeled under static conditions. The data regarding dimensions, reinforcement and connections are summarized in Table 6-1 and Table 6-2 (see 6.2.2.1 and 6.2.2.3).

Figure 6-20 to Figure 6-22 show the beam end's moment as a function of the imposed displacement predicted by the FEM analysis, measured during step 0 (see 6.2.3) for the different specimens. As can be seen, the elastic stiffness of the connection assessed by FEM analysis or experimentally measured were equivalent. A similar observation can be made for connections 5 and 6.



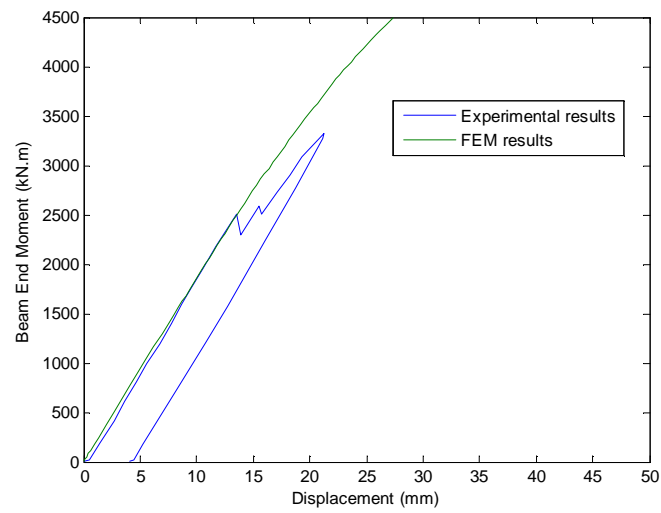


Figure 6-20: Beam end moment vs. imposed displacement curve for specimen 1

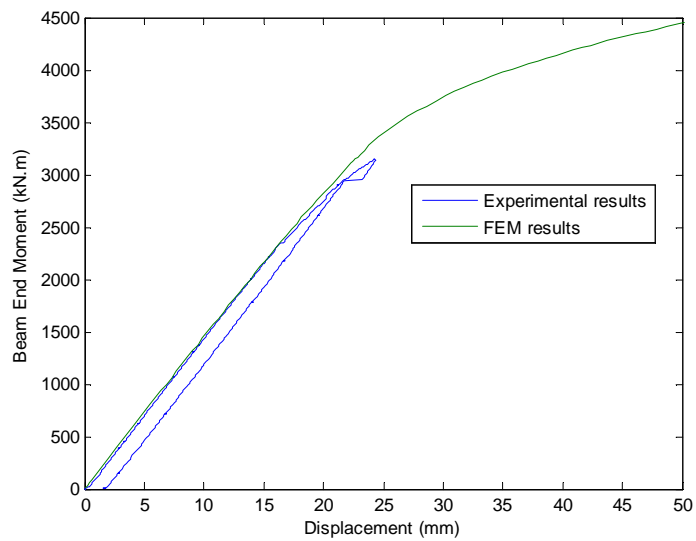


Figure 6-21: Beam end moment vs. imposed displacement curve for specimen 5

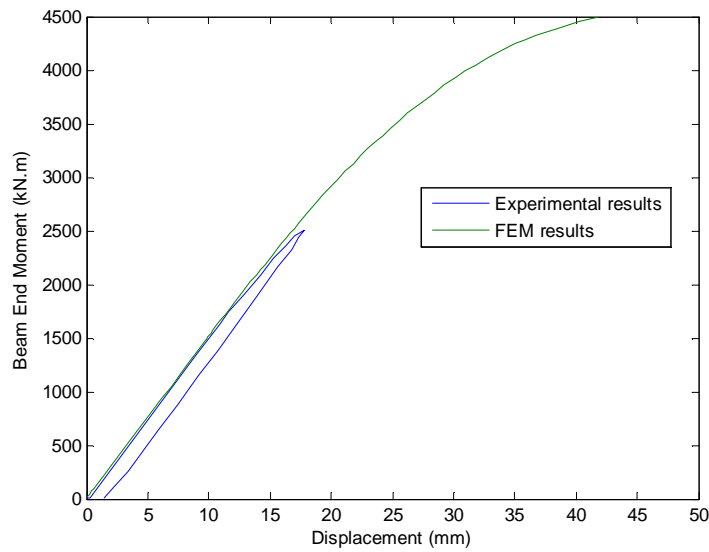


Figure 6-22: Beam end moment vs. imposed displacement curve for specimen 6

Figure 6-23, Figure 6-24 and Figure 6-25 show the stress fields in the longitudinal direction of the beam,  $\sigma_{xx}$ , in the longitudinal direction,  $\sigma_{yy}$ , of the column, and the equivalent von Mises',  $\sigma_{eq}$ , when the imposed displacement was equal to 100 mm for connection 1. It was verified that on the one hand, the beam's upper flange was under tension and the beam's lower flange was under compression; on the other hand, the left column's flange was in compression and the right column's flange was under tension.

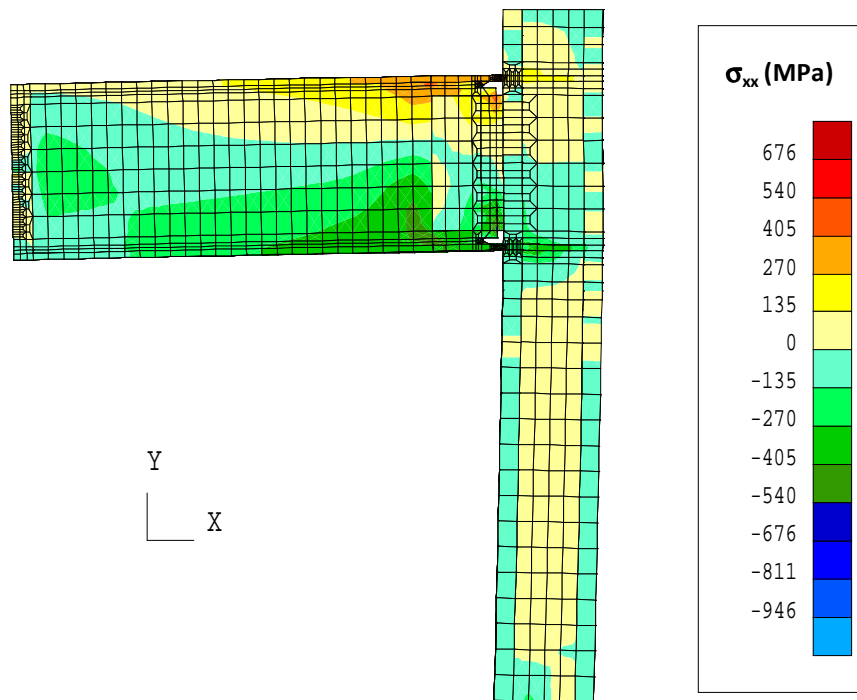


Figure 6-23: Longitudinal stress in the beam for specimen 1 (100 mm displacement)

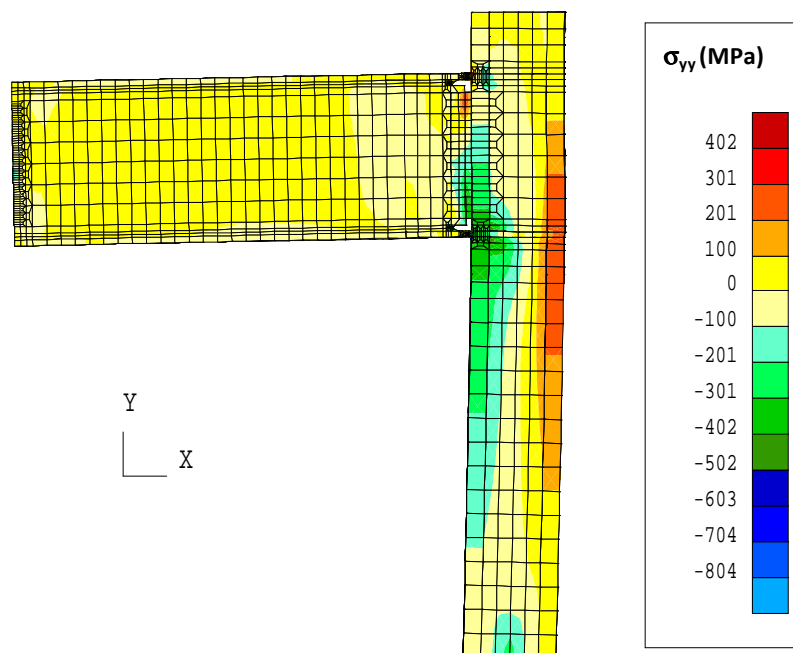


Figure 6-24: Longitudinal stress in the column for specimen 1 (100 mm displacement)

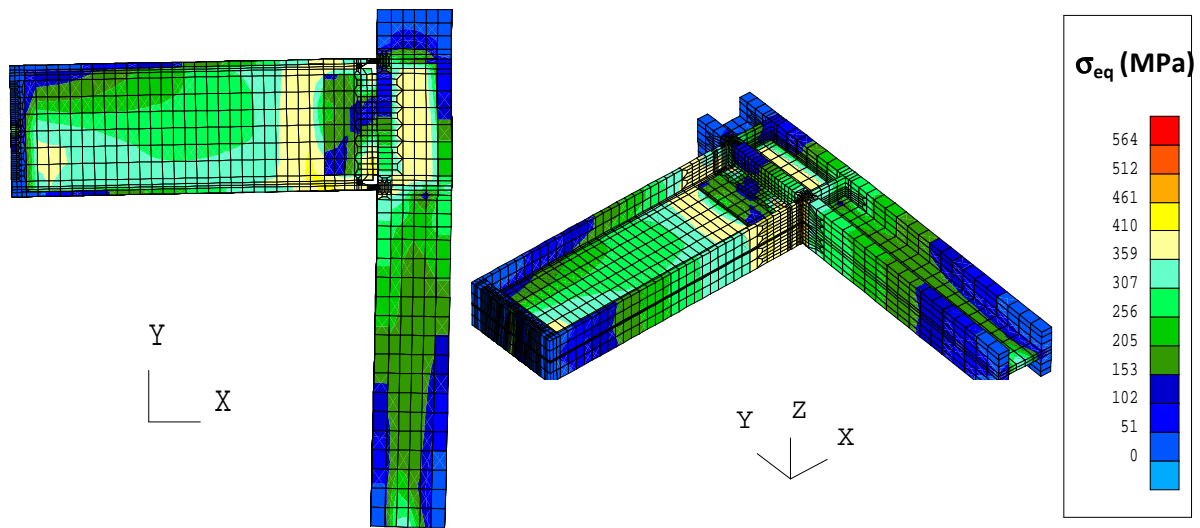


Figure 6-25: Equivalent von Mises Stress for specimen 1 (100 mm displacement)

### 6.3.2.2 Cyclic loading

Table 6-6 summarizes the loading step of connection 3. For the cyclic loading, only specimen 3 was modeled. However, the bolts which joined the beam and column and the loading devices slid during the experiments. The University of Karlsruhe provided the imposed displacement for each cycle by taking into account this sliding. These displacements were then imposed.

Table 6-6: Loading definition of the connection 3

Step	Number of cycles	Displacement amplitude (mm)
1	6	17.6
2	6	24
3	6	35
4	4	47.0
5	1	70.6

Figure 6-26 illustrates the comparison of the beam end's moment rotation curve between the FEM analysis and the experimental measurements. The distortion on the experimental curve is due to the sliding of the bolts. Firstly, it can be noted that the elastic stiffness of the FEM curve was equivalent to the experimental one for steps 1 and 2. Then a plastic zone appears during step 3. The maximum beam end's moment was higher than the experimental one but the hysteresis areas were equivalents. For steps 4 and 5, the maximum beam end's moment was weaker than the previous step, though the maximum rotation increased for the experimental curve. This must have been due to internal damage. Indeed, the FEM analysis without damage does not model the modified behavior. At the end of the simulation, the deformed shape presented buckling at the beam end (see Figure 6-27).

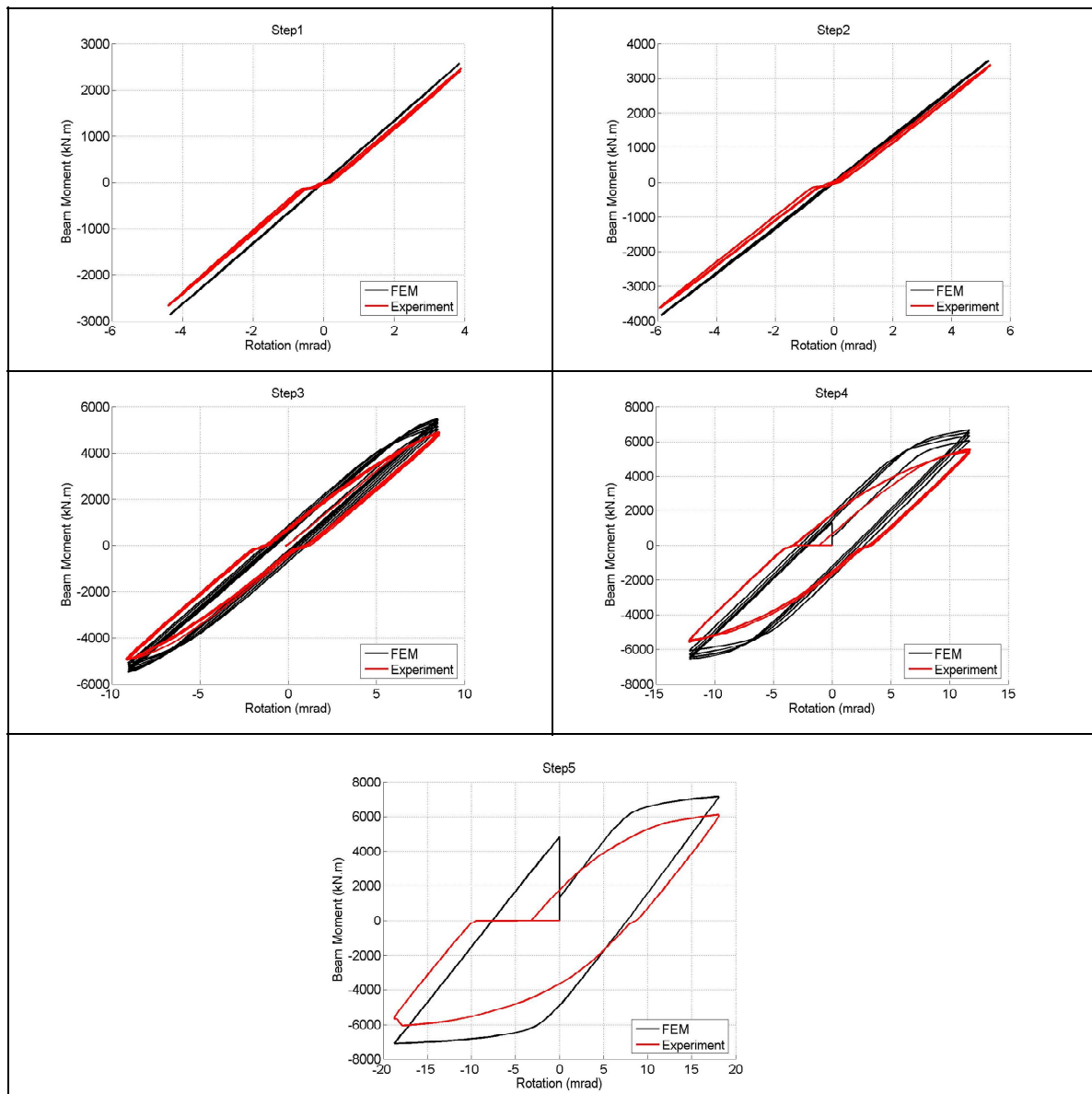


Figure 6-26: Comparison of the beam end's moment rotation between FEM analysis and experimental measurement (specimen 3)

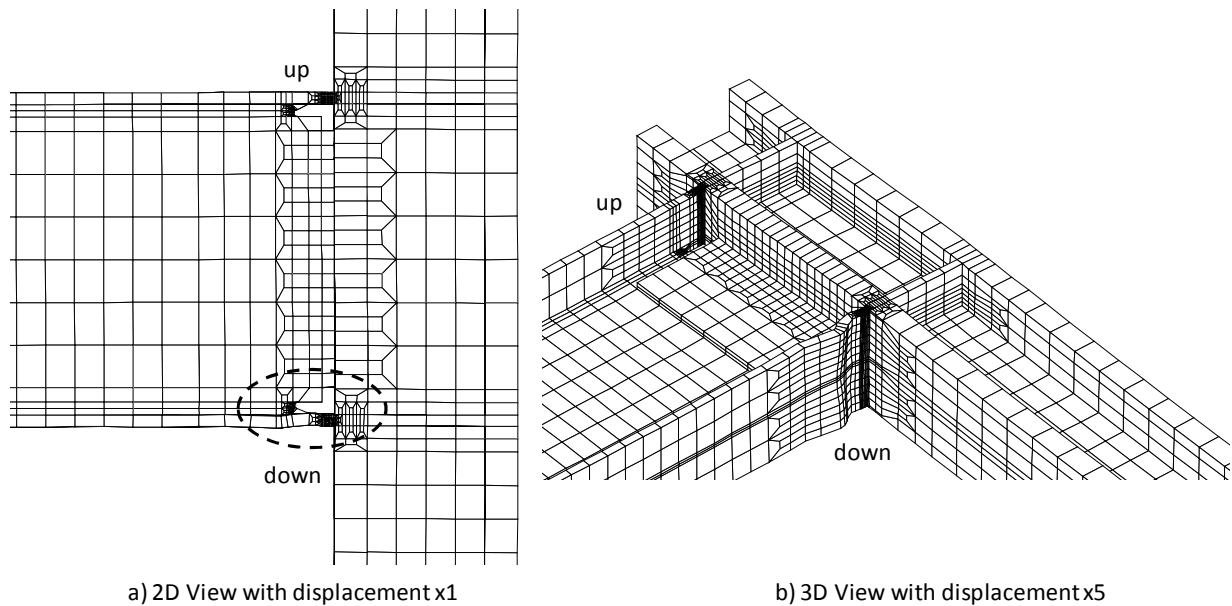


Figure 6-27: Buckling observation at the end of step 5 (specimen 3)

### 6.3.3 Cyclic loading with fatigue damage

The aim of this modeling was to assess the amount of damage due to cyclic loading. The model used was the fatigue continuum damage model of Lemaître and Chaboche (see Chapter 3.5). The model was not coupled with the mechanical aspect that is the fatigue damage did not affect the mechanical behavior. Consequently, one can see the highest damaged zone on the connection to identify the potential crack path but no modification in the predicted stresses and forces. The parameters of the fatigue continuum damage model were calibrated (see Chapter 3.7) for the base metal in the webs and flanges and for the weld metal.

The first zones where fatigue damage began are at the spot of the flange weld metal and near the weld access holes. Indeed, the damage increased at the end of step 1 (see Figure 6-28 and Figure 6-29).

In terms of the weld access hole, the mesh does not seem to be optimal. The solid elements were too elongated in one direction and the proportions of the element's dimensions were not respected. The damage followed one direction but it could be due to the shape of the element. However, many cracks appeared in this zone for some specimens (6 and 7) but not for specimen 3 (see Table 6-5).

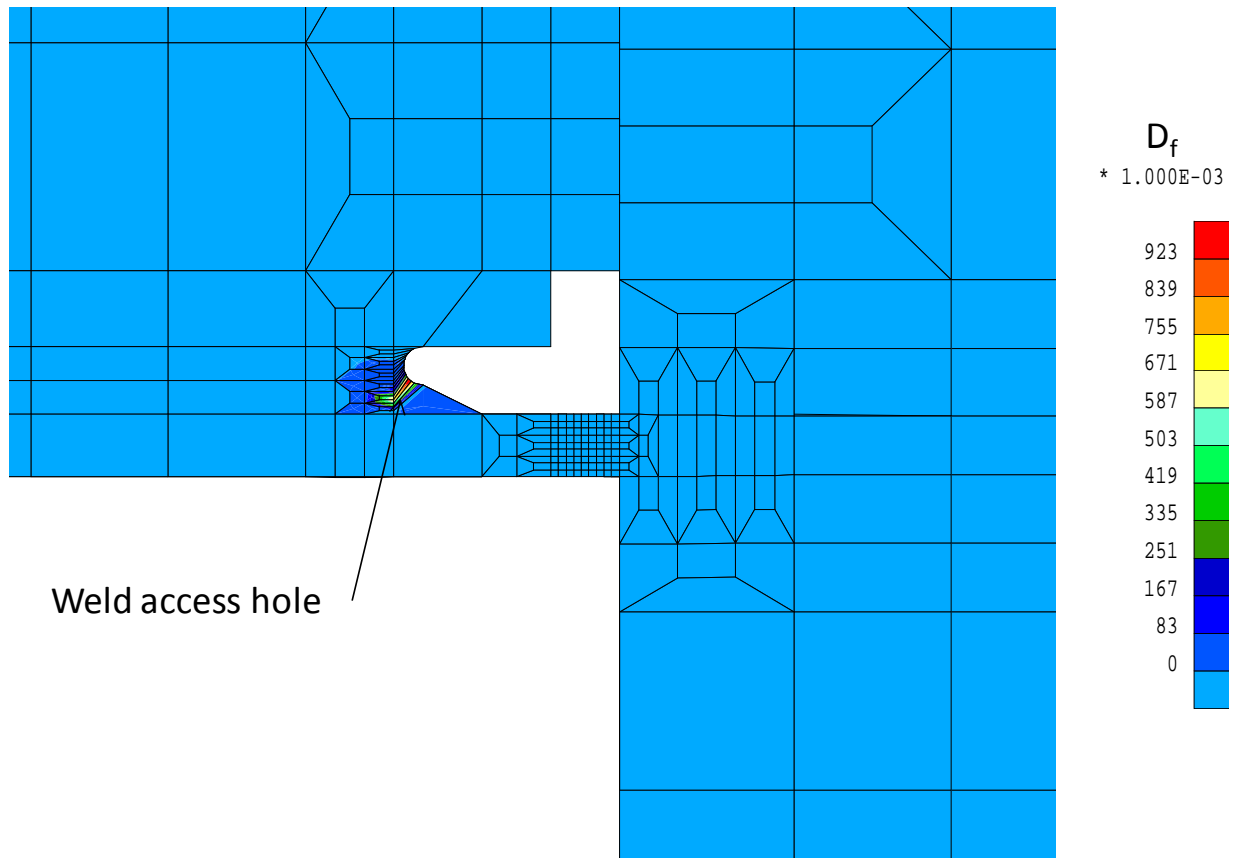


Figure 6-28: Fatigue damage at the end of the step 1 in the weld access hole

Regarding the beam end flange, the damage initiated and was concentrated at the interface between the weld metal and the column flange. In fact, this type of behavior occurred when the moment was as its highest as was the longitudinal stress. In addition, it was the zone where the macrocrack appeared. In the weld flange, the damage increased in the beam flange near the interface between the base metal and the weld metal.

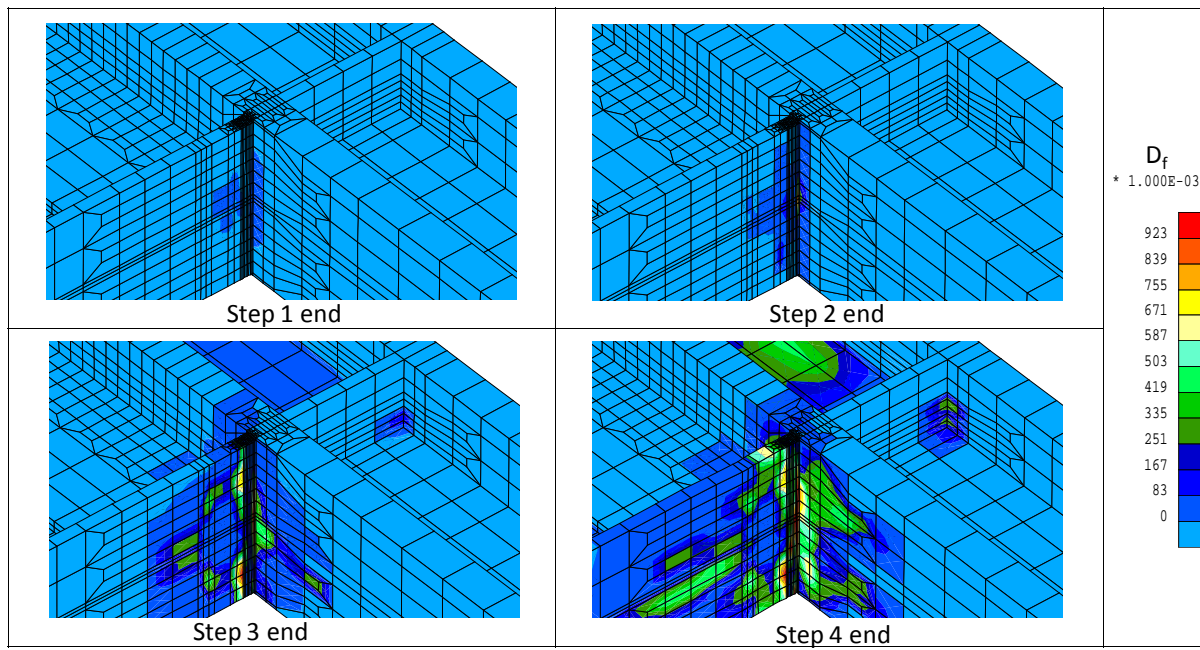


Figure 6-29: Evolution of the fatigue damage near the lower weld flange



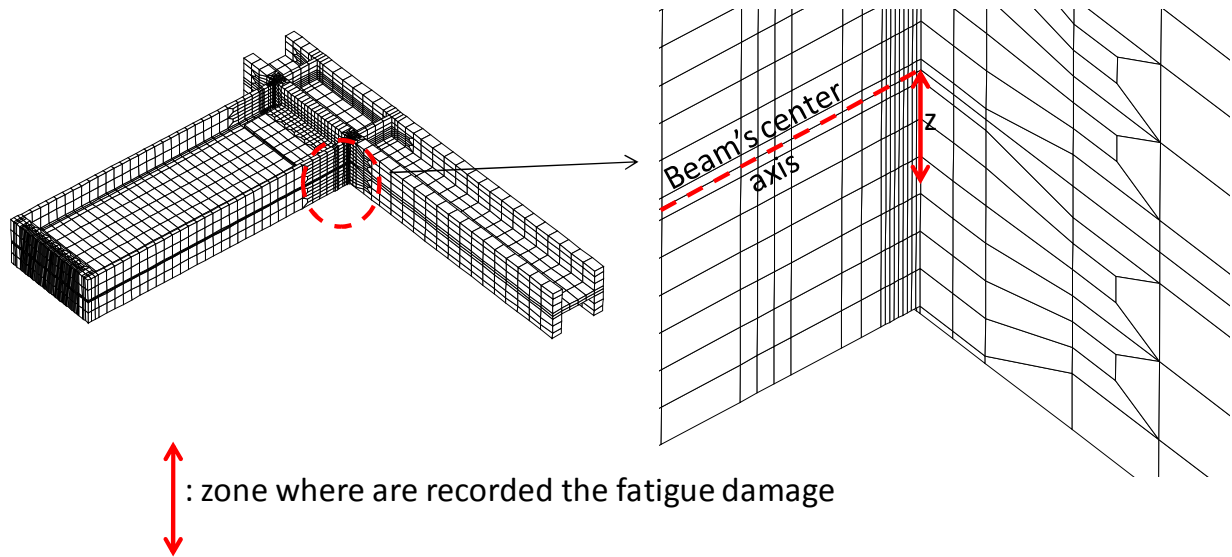


Figure 6-30: Location of elements where the fatigue damage where recorded

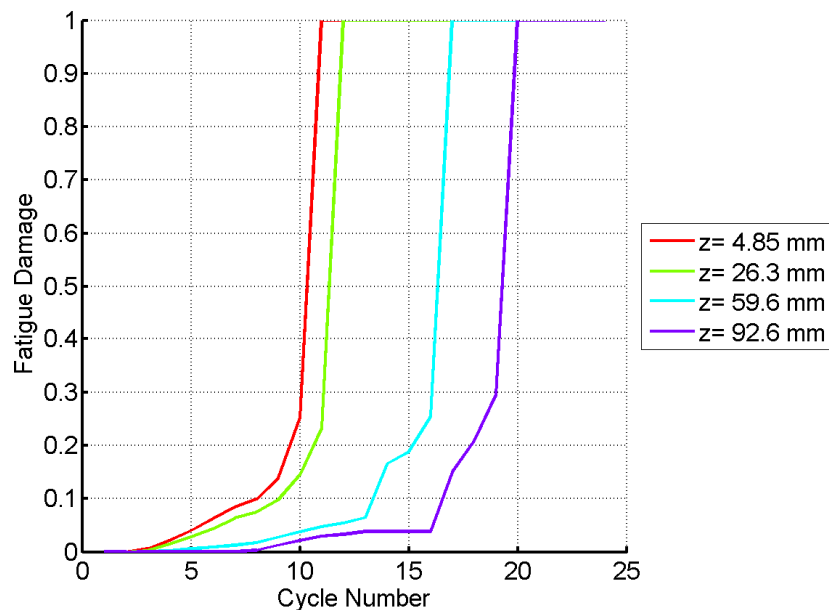


Figure 6-31: Evolution of damage in weld metal elements along the transverse direction of the beam

Figure 6-31 shows the evolution of the fatigue damage over cycle in the weld metal elements which are at the interface between the weld metal and the column flange (see Figure 6-30). The coordinate,  $z$ , is the distance from the beam center. The damage evolves quickly in this modeling. By instance, the damage passed from 20% to 100% for some elements in one cycle which could result convergence problem. Lemaître and Chaboche's model seemed to present some difficulties in modelling the damage evolution in the LCF condition.

To conclude, the zones, where damage was the highest, were at the interfaces between the weld metal and the column flange and at the weld access hole. Due to the poor quality of the mesh and as no macrocracks were observed in this zone, it was decided to apply the cohesive zone at this location. Instead, it was decided to not apply cohesive zone model to the interface between the weld metal and the base metal in the beam flange end.

### 6.3.4 Cyclic loading with the cohesive zone model and fatigue damage

The aim of this simulation was to model the crack's propagation at the connection and observe its impact on the moment rotation curve. Some CZM3D cohesive elements, developed in this thesis (see Chapter 4.4) were defined in the mesh at the interface between the weld metal and the base metal in the beam flange end (see Figure 6-32).

The constitutive law of this element was a bilinear Crisfield law which was identified for the base and weld metals (see Chapter 4.7.5). At the interface of two materials, the parameters of the weld metal were chosen. Indeed the weld metal is less resistant to crack propagation and the crack seemed to propagate through the weld metal according to experimental observations.

The computation stopped after eleven cycles (at the end of the second step according to Table 6-6) due to convergence problems. Figure 6-33 shows the location in the connection where the cracks initiated. The Figure 6-34 illustrates the crack's initiation at the end of the computation. The displacement was multiplied by 50 in order to the crack was visible. Figure 6-35 presents the longitudinal stress field for the beam. The stress began relaxing at the crack initiation. The improvement of the computation is currently performed to model all cycles.

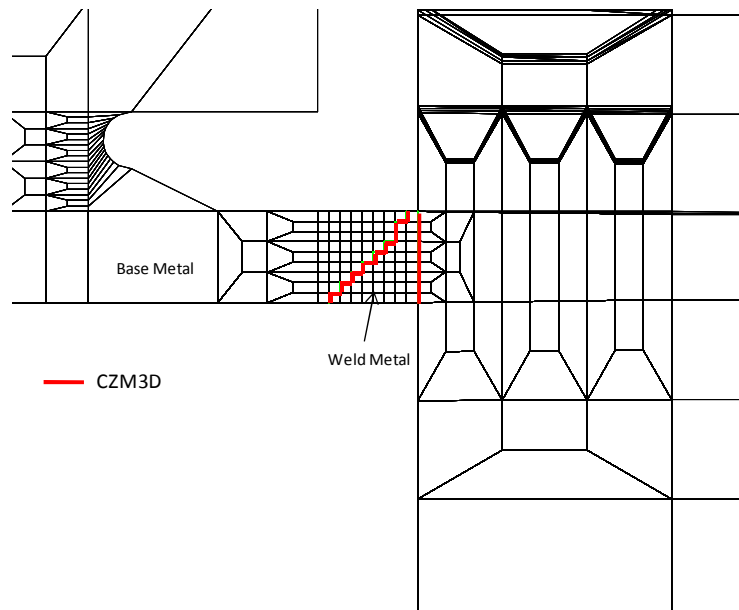


Figure 6-32: Location of the cohesive elements

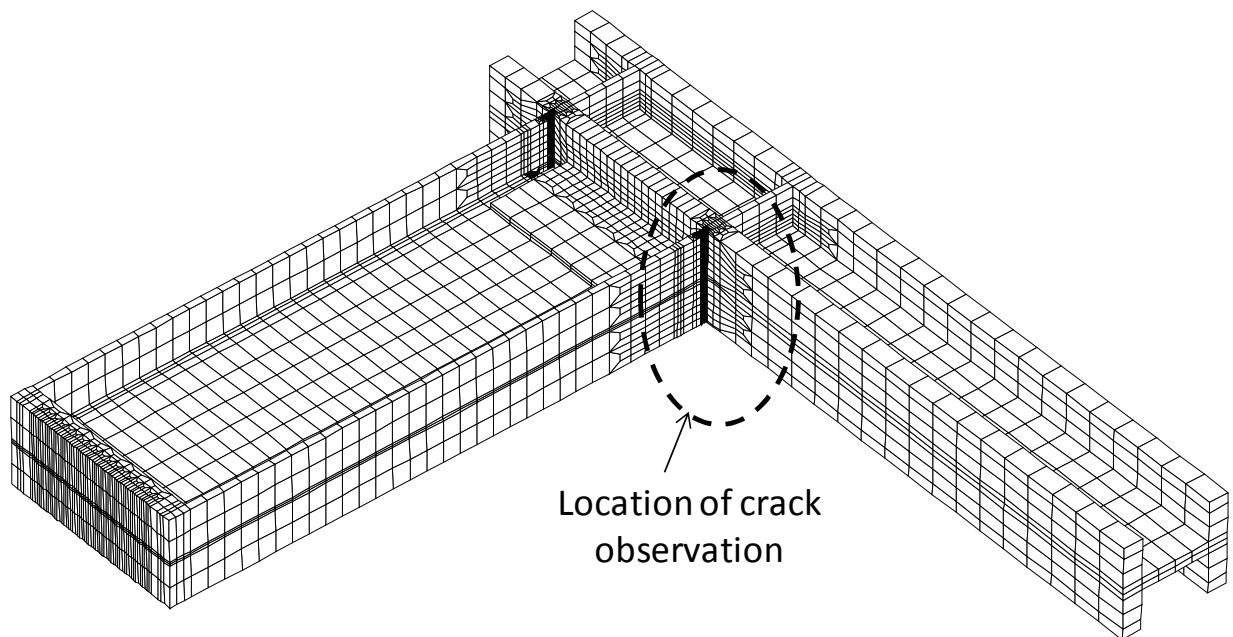
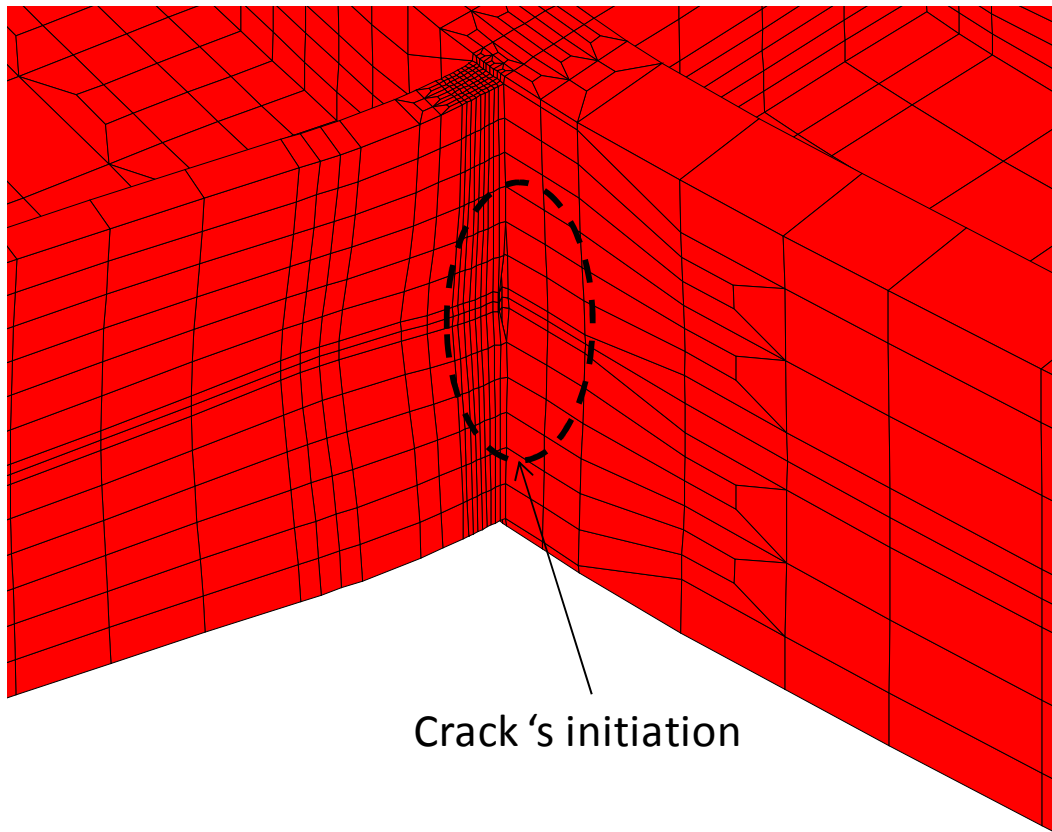


Figure 6-33: Zone in the connection where crack was observed



**Figure 6-34: Crack initiation after 10 cycles (displacement x50)**

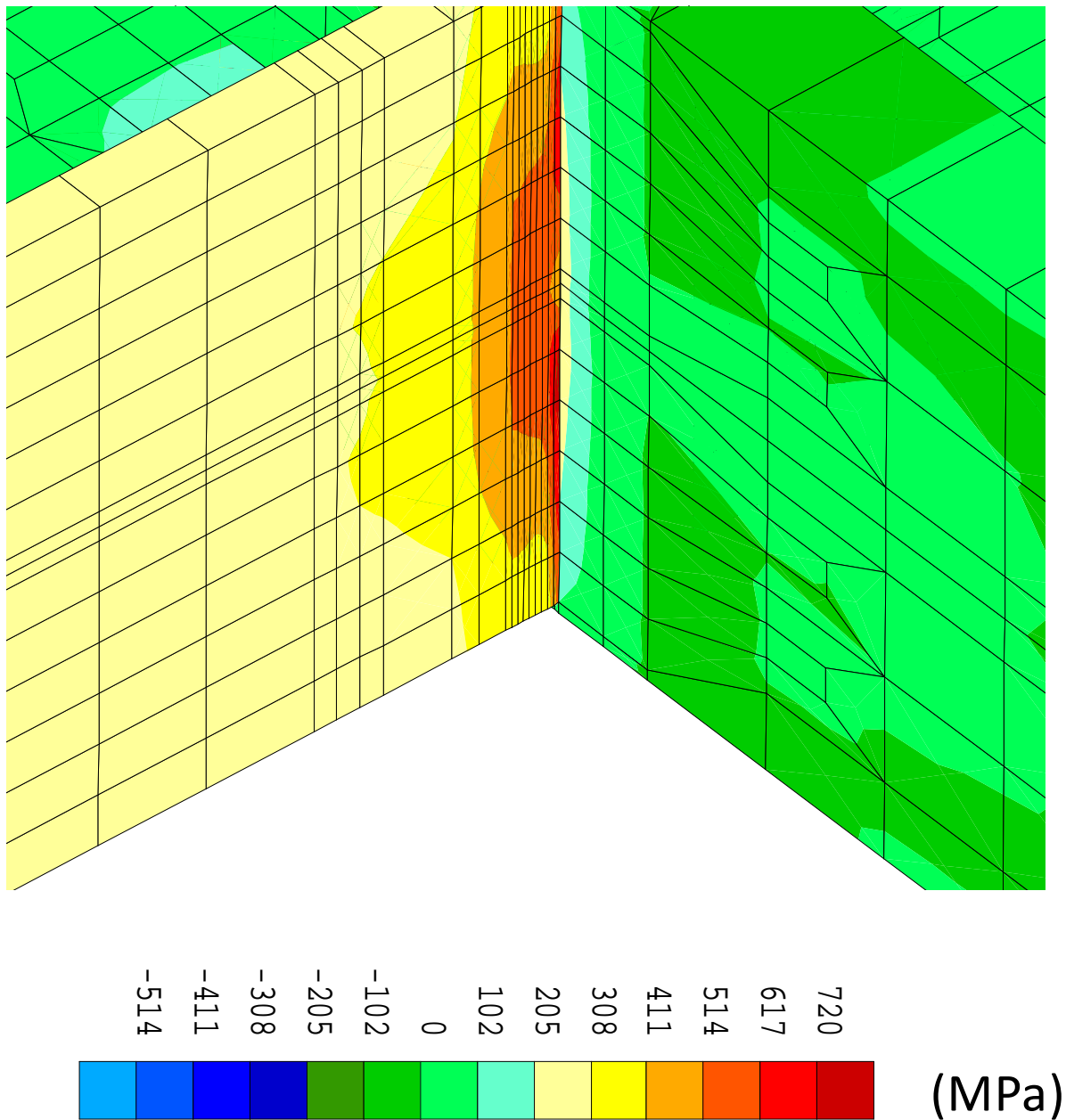


Figure 6-35: Longitudinal stress for the beam flange plot after 10 cycles (displacement x1)

## 6.4 Conclusion

This chapter presents the modeling of the large-scale test performed by the University of Karlsruhe on beam-to-column connections under cyclic loading, a test designed to investigate the onset and propagation of cracks at the connection level.

A three-dimensional structured mesh generator was developed. One drawback of this development is that the program is less user-friendly than a commercial one. However this

generator made it possible to automatically refine with the transition blocks. It has been adapted to the VERAPS project so that one could generate the eight beam-to-column connections of the project with little data.

To test the performance of the meshes, 3 connection tests were modeled under static loading conditions and compared with the University of Karlsruhe's results. The agreement of the elastic stiffness in the moment displacement curve helped us to validate the model in terms of the mesh, material parameters, and boundary conditions. This modeling enabled the longitudinal stress to be assessed through the beam flange, weld butt and column flange and provided these data to Corus for their RAP analysis.

The first computation with the cohesive zone model was performed under cyclic loading conditions for one specimen. The elastic stiffness of its moment rotation was found to be equivalent to the experimental one. Also, the hysteresis loop had an equivalent area. The continuum damage model makes it possible to identify the zone where the greatest damage by fatigue happened: in front of the weld access hole and near the welding connection. However, the mesh presented some problems close to the weld access hole. So, the mesh has to be refined in this zone. Lemaître and Chaboche's model seemed to present some difficulty modelling the damage evolution in the LCF condition, in so far the damage evolved too quickly. Then, a computation with cohesive zone elements was carried out. The computation ended only at the end of the step 2 due to convergence problem. However, the crack began initiating.

# **Chapter 7**

# **Conclusions and**

# **Perspectives**



The aim of this PhD thesis was to model the large scale tests of heavy steel welded beam-to-column connections submitted to cyclic loading. The propagation of a crack in these connections, due to the displacement cycles applied and to fatigue damage, was simulated. In addition to this overall aim, the model had to satisfy two criteria: the modeling should be feasible using commercial codes and it should not require too many parameters. As different factors were taken into account and tested, this study was divided into different steps. The following section discusses the conclusions of the different steps of this work.

In Chapter 2, the constitutive law for the base metal and for the weld metal was described. The metal's behavior was considered to be elastoplastic with isotropic hardening and using von Mises' yield criterion. The parameters of this law were identified from tensile tests on samples extracted from different locations on the connections. More specifically, a set of parameters for the constitutive law was defined for the flanges, the webs and the weld metals. Identifying these sets was a relatively simple task. For all the different steels, Young's modulus was fixed at the classic value for steel (205 GPa) because the available small strain measurements were not accurate enough. It would have been interesting to observe the influence of the use of a mixed (isotropic and kinematic) hardening on the model. However, the quality of the stress-strain measurements during cyclic tensile tests was not sufficiently accurate to be of use. Moreover, the heat-affected zone's behavior was not ascertained, though heat-affected zones are locations where cracks can develop. Experimental identification of this zone would be too difficult a task because of its smallness and because the HAZ's behavior depends on the welding process. Another solution would have been to model the metallurgical modification of the HAZ as in [HAB89]. However, these types of models require many parameters and their identification requires multiple tests. Nevertheless, it could be worth the effort to develop these models in future to better simulate cracks.

Chapter 3 presents Lemaître and Chaboche's fatigue continuum damage model with a multiaxial Sines' criterion, which was implemented in the Lagamine code to take fatigue into account in the crack's propagation. The parameters of this model were obtained from the Wöhler's curve generated by cyclic tensile tests on base and weld metals. However, the number of points was insufficient and they only defined the LCF state. An increase in the number of points would have improved the identification of these parameters, particularly in the HCF state. In addition, the tests were also limited with respect to uniaxial loading. Several multiaxial criteria, such as Crossland's or Dang Van's, could be investigated for tests performed to generate a multiaxial state. Still, this study was the first one in the field of the fatigue damage modeling in the Lagamine team. Following up on this thesis, Mr. Abdeljalil Kalifa Marmi from the ArGENCo Department is working on the assessment of fatigue life on a titanium alloy and aims to identify and validate accurate multiaxial criteria [MAR09].

The crack's propagation was modeled with the cohesive zone model, discussed in Chapter 4. This model was used to simulate crack propagation for a ductile fracture under cyclic loading and could be coupled with fatigue damage. For this model, a two-dimensional and, then, a three-dimensional cohesive element were implemented in the finite element code Lagamine. This implementation has already been performed in commercial codes, such as ABAQUS [GAO04] or Zebulon [BOU06]. For its implementation in the Lagamine code, Xu and Needleman's cohesive law was first implemented. One drawback of this law is its low number of parameters: maximum cohesive stress and the separation,  $\delta_n$ , which together define the energy and the initial stiffness of



the cohesive law. Another degree of freedom would be necessary to affect the initial stiffness independently. Therefore, a bilinear Crisfield's model was used. An inverse method for the identification of the cohesive parameters was developed based on the results of three-point bend testing carried out by Corus. In the first step, a parametric study was performed to understand the effect of varying each parameter on the strength of the cracked component. In the second step, these parameters were adjusted until the numerical results approximated the experimental results. However, this identification concerned only mode I. It would also have been interesting in analyzing mode II and mode III. In addition, after a literature review, it was found that triaxiality affects the cohesive parameters [CHE05]. Unfortunately, the available experimental results did not allow this phenomenon to be studied. Another drawback of the cohesive zone is that the crack's path should be known before the mesh generation. One possible solution to this constraint is to develop a remeshing method, which adds cohesive elements according to a crack criterion. In addition, it is important to note that these cohesive elements will be used in other current researches, such as:

- the DINOSAURE project, which aims to model the coating of nanometric film of composite structures;
- Dr. Ben Bettaieb's post-doctoral project dedicated to a three-dimensional formability criterion of metallic materials during the forming process. The damage is simulated by Gurson's law [BEN08], which is used for crack detection. However, the use of a cohesive model would be used to model crack propagation;
- the study of biomechanics, which could also use cohesive models.

Clearly, this tool's addition to the Lagamine code will find numerous applications.

Chapter 5 outlines the development of a method to compute a balanced residual stress field resulting from the welding process. The finite element welding model generated many problems, namely due to the structure's size and the high computation time. Indeed, the thickness of the beam was considerable, as was the number of passes. Recently, an iterative solver module has been implemented in the Lagamine code, which could speed up the simulations (see Appendix 1). In addition, some assumptions were made to reduce the computation time. A sequential thermomechanical analysis requires less CPU time than a coupled one. Specifically, the use of different meshes for the thermal analysis (fine mesh and larger time step) and for the mechanical analysis (coarser mesh and fine time step) optimized the computation time. Also, a birth technique simulated the weld metal supply and avoided convergence problems due to heating. This was applied only to the mechanical analysis but it would be worthwhile using it on both analyses to avoid error in thermal conduction phenomena. A three-dimensional coupled thermo-elastoplastic constitutive law was implemented by the author in the Lagamine code. The heat source was modeled by Goldack's model. A simulation was performed with two equivalent passes to model the welding process of one VERAPS connection. However, the results of the analyses performed were not accurate enough. This part of the thesis was unfortunately not fulfilled. This way of generating accurate three-dimensional residual stresses was still lengthy and could not be performed within the time devoted to this thesis. The focus of this work was damage modeling, not welding simulations, so the following ideas remain to be developed. To tackle the difficulty of the high number of passes, it was chosen to group several passes into one pass, but the parameters of the heat sources needed to be identified. Due to the time-consuming nature of three-dimensional computations, two-dimensional simulations should be carried out in order to model all the passes, and in turn, to adjust the parameters of this heat source. The goal of

these two-dimensional simulations is to check if one could determine parameters to model fewer passes with equivalent energy and residual stresses predicted. Then, this would make it possible to perform three-dimensional modeling with a lower number of passes. Also, an adaptive remeshing would be interesting with the method described in Appendix 2. In this case, at the beginning, only coarse elements would exist. Then, all elements close to the heat source would be remeshed as finer elements.

After the tools were developed and calibrated, the final step of the thesis, described in Chapter 6, was the simulation of the welded beam-to-column connections submitted to cyclic loading. As eight connections with different dimensions and reinforcements were tested, a three-dimensional structural mesh generator module was developed to carry out the meshwork easily. The input parameters were composed of the dimensions of the beam and the column. However, the meshes in the weld access hole location were not fine enough. Indeed, the zone presented stress concentrations where cracks could initiate. Different simulations were performed. The first simulations in static condition enabled Corus to evaluate the rotation capacity of three connections by RAP analysis by providing the longitudinal stresses through the beam flange, the welding and the column flange. The longitudinal stresses along the beam flange, the welding and the column flange were provided for different levels of rotation. Three simulations (specimens 1, 5 and 6) with different levels of the plastic moment ratio were carried out. The beam end moment versus rotation curves were compared with the experimental measurements from the University of Karlsruhe. The initial elastic slopes of the moment versus rotation curves generated by finite elements and experiments were equivalent, which validated the model. Afterward, specimen 3 was simulated under cyclic loading. Its fatigue damage was computed without affecting the mechanical stiffness to avoid convergence problems. Determining the crack's path is generally a difficult task, but the fatigue damage in this case was an interesting indicator, as validated by experimental observations. With this information, a mesh with cohesive elements was defined to model crack propagation. One simulation with crack propagation was performed but stopped before the end of the test proceeding due to convergence problem. Perhaps other fatigue damage model could be coupled with the cohesive zone model which evolves at each time step, such as models suggested by Bouvard [BOU06] or Roe and Sigmund [ROE03], contrary to Lemaître and Chaboche which evolves at each cycle. An adaptive remeshing would have made it possible to perform the computation in one simulation. However, no simulation with residual stresses as initial values was performed since no accurately balanced residual stress fields were obtained in the previous chapter. However, the impact of the residual stresses on the simulation of the crack's propagation would certainly be interesting to investigate further. In summary, the method developed in this thesis will help engineers to model crack propagations in beam-to-column connections submitted to cyclic loading. After complete validations of each step with experimental results, as discussed above, the finite element analysis could be an interesting counterpart to an analysis of or experiments on risk assessment profiles.

# **Appendix 1**

## **Iterative solvers**



## A1.1 Introduction

In finite element codes, large linear systems have to be solved. Indeed, the nodal position corrections (see Chapter 2.3),  $(\underline{x})_{N \times 1}$ , to reduce the out-of-balanced forces,  $(\underline{F})_{N \times 1}$ , are computed at each iteration with the following equation:

$$\underline{\underline{K}} \underline{x} = \underline{F} \quad (\text{A1.1})$$

where  $(\underline{\underline{K}})_{N \times N}$  is the tangent stiffness matrix of the structure and  $N$  is the dimension of the system.  $N$  can become very large, particularly if the analysis is three dimensional. Therefore, solving Equation (A1.1) represents most of the CPU time of the simulation. That's why it is important to make it possible to solve it rapidly and efficiently. Currently the Lagamine code solves the system directly by computing the inverse  $\underline{\underline{K}}^{-1}$  with the LU factorization method. This method gives the real solution but takes time in simulations with a large number of degrees of freedom.

The usual solution to reduce the solving time in three-dimensional finite element modeling is to use an iterative resolution method. The iterative methods can be classified into two types: stationary (e.g. Jacobi's or Gauss-Seidel's Method) and non-stationary (the Conjugate Gradient method). The method chosen is the Generalized Minimal Residual (GMRES), which is a derivative of the Conjugate Gradient method. To speed up the resolution, the iterative method was coupled with a preconditioning method.

Firstly, this appendix presents the direct method present in Lagamine. Then, the stationary and non-stationary methods are described such as the GMRES method. The preconditioning method which accompanies the GMRES method is explained. Moreover, the appendix describes the necessary modifications on Lagamine. A validation and performance study was performed on different large simulations and their results are shown hereafter.

## A1.2 Direct methods in Lagamine finite element code

Before this study, only direct methods were available in the Lagamine code, namely the LU factorization. This involves factoring the tangent stiffness matrix by:

$$\underline{\underline{K}} = \underline{\underline{L}} \underline{\underline{U}} \quad (\text{A1.2})$$

where  $\underline{\underline{U}}$  is an upper triangular matrix and  $\underline{\underline{L}}$  is a lower triangular matrix.

The advantages of this method are: the computation of the inverse of  $\underline{\underline{L}}$  and  $\underline{\underline{U}}$  are easier than to find the inverse of  $\underline{\underline{K}}$  and it is parallizable. The computation of the inverse of  $\underline{\underline{K}}$  is performed like this:

$$\underline{\underline{K}} = \underline{\underline{L}}^{-1} \underline{\underline{U}}^{-1} \quad (\text{A1.3})$$

In Lagamine, different methods use this factorization. The differences in these methods come from the storage method used during the solving process of the stiffness matrix.

Indeed, for finite element problems, the tangent stiffness matrices are sparse, i.e. the non-zero elements are concentrated around the diagonal (see Figure A1-1). Consequently, it is not necessary to store all the components which are null.

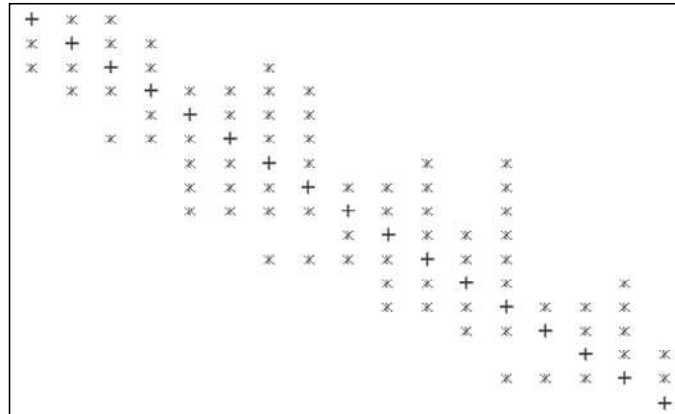


Figure A1-1: Sparse matrix example

The first storage method is the skyline method. In each column, a maximum bandwidth around the diagonal is estimated and only a limited band is stored. The estimation is based on the connection between nodes in all elements. This method is simple and the stiffness matrix is easy to manipulate. However, many zero components remain in the band. Therefore, an optimization of the numbering must be performed during the meshing or a renumbering must be performed. Two are available: an oil spot and directional method (see Lagamine's user guide for details).

The second storage method is the Compressed Sparse Row (CSR). In each column only the non-zero components are stored. Consequently, some pointer arrays make it possible to recover the exact position in the matrix. This method optimizes the memory required to store the tangent stiffness matrix. However, this matrix is harder to manipulate than the skyline one.

The use of the method depends on the size of the system. Some numerical tests show that for small systems always provide a quicker answer with the skyline method. However if the system holds many degrees of freedom, the CSR method seems preferable.

### A1.3 Stationary methods

The principle of the stationary method is the definition of a function,  $f$ , such that

$$\underline{x} = f(\underline{x}) \quad (\text{A1.4})$$

where  $\underline{x}$  is the solution and a stationary point of the function,  $f$ .

Given a starting point,  $\underline{x}_0$ , the following iterative algorithm is used

$$\underline{x}_{n+1} = f(\underline{x}_n). \quad (\text{A1.5})$$

The definition of the function,  $f$ , is carried out by the division of the tangent stiffness matrix:

$$\underline{\underline{K}} = \underline{\underline{M}} - \underline{\underline{N}} \quad (\text{A1.6})$$

where  $\underline{\underline{M}}$  is a non-singular matrix and easy to invert. According to (A1.1), the function,  $f$ , is defined by

$$\underline{x} = \underline{\underline{M}}^{-1} \underline{\underline{N}} \underline{x} + \underline{\underline{M}}^{-1} \underline{\underline{F}} = f(\underline{x}). \quad (\text{A1.7})$$

Therefore, the algorithm is

$$\begin{cases} \underline{x}_0 \text{ chosen,} \\ \underline{x}_{n+1} = f(\underline{x}_n) = \underline{M}^{-1} \underline{N} \underline{x}_n + \underline{M}^{-1} \underline{F}. \end{cases} \quad (\text{A1.8})$$

In order to study convergence, an error by iteration,  $\underline{e}_n$ , is defined. This is the difference between  $\underline{x}_n$  and the exact solution,  $\underline{x}$ :

$$\underline{e}_n = \underline{x}_n - \underline{x}. \quad (\text{A1.9})$$

The problem is that the solution  $\underline{x}$  is unknown. Thus one defines the residual,  $\underline{r}_n$ , by

$$\underline{r}_n = \underline{F} - \underline{K} \underline{x}_n. \quad (\text{A1.10})$$

The residual,  $\underline{r}_n$ , is a transformation of the error  $\underline{e}_n$  in the space of  $\underline{F}$  by multiplying by  $\underline{K}$ :

$$\underline{K} \underline{e}_n = \underline{K}(\underline{x}_n - \underline{x}) = \underline{K} \underline{x}_n - \underline{F} = -\underline{r}_n. \quad (\text{A1.11})$$

Consequently, the residual is a good indicator to see if one is close to or far from the target solution. The algorithm continues until the residual reaches a level of tolerance,  $\varepsilon$ :

$$\frac{\|\underline{r}_n\|_2}{\|\underline{F}\|_2} < \varepsilon \quad (\text{A1.12})$$

where  $\|\dots\|_2$  is the second-order norm.

To study convergence, the error must also be analyzed. For the stationary method the error is

$$\underline{e}_n = \underline{M}^{-1} \underline{N} \underline{x}_{n-1} - \underline{M}^{-1} \underline{F} - \underline{x} = \underline{M}^{-1} \underline{N} (\underline{x}_{n-1} - \underline{x}) = \underline{M}^{-1} \underline{N} \underline{e}_{n-1} = (\underline{M}^{-1} \underline{N})^n \underline{e}_0 = \underline{B}^n \underline{e}_0 \quad (\text{A1.13})$$

where  $\underline{B} = \underline{M}^{-1} \underline{N}$ .

The aim of this algorithm is that the error must converge to zero after several iterations:

$$\lim_{n \rightarrow \infty} \underline{e}_n = \lim_{n \rightarrow \infty} (\underline{B}^n \underline{e}_0) = 0 \quad (\text{A1.14})$$

The choice of  $\underline{x}_0$  affects the number of iterations required to converge to  $\underline{x}$ . However, its effect are less important than that of the effect of  $\underline{B}^n$ . The convergence to  $\underline{B}^n$  depends on the spectral radius of  $\underline{B}$ ,  $\rho(\underline{B})$ , which is the highest eigenvalue of the matrix. The spectral radius must be less than 1.

The famous stationary method divides the matrix in this way:

$$\underline{K} = \underline{D} - \underline{E} - \underline{F} \quad (\text{A1.15})$$

where  $\underline{D}$  is a matrix which contains the diagonal elements,  $\underline{E}$  the upper part and  $\underline{F}$  the lower part of the tangent stiffness matrix.

The first method is the Jacobi's method which uses  $\underline{M}=\underline{D}$  and  $\underline{N}=\underline{E}+\underline{F}$ . This method can be parallelizable. The second famous method is the Gauss-Scheidel's method which uses  $\underline{M}=\underline{D}-\underline{E}$  and  $\underline{N}=\underline{F}$ . This method converges more quickly than the Jacobi's methods. The stationary

methods works well but can fail for some finite positive stiffness matrices. These methods are described in [SAA03].

## A1.4 Krylov subspace methods

### A1.4.1 Some definitions

Two vectors,  $\underline{u}$  and  $\underline{v}$ , are considered conjugate or K-orthogonal if

$$\underline{u}^T \underline{K} \underline{v} = 0 \quad (\text{A1.16})$$

Solving Equation (A1.1) is equivalent to finding the minimum of the function,  $f$ , which is the quadratic form:

$$f(\underline{x}) = \frac{1}{2} \underline{x}^T \underline{K} \underline{x} - \underline{F}^T \underline{x} \quad (\text{A1.17})$$

In this case, the residual,  $\underline{r}$ , is the opposite of the gradient of  $f$  at the  $\underline{x}$  value.

$$\underline{r} = \underline{F} - \underline{K} \underline{x} = -\nabla f \quad (\text{A1.18})$$

### A1.4.2 The conjugate gradient method

#### A1.4.2.1 Principles of the method

One starts at an arbitrary point  $\underline{x}_0$  and takes a set of steps  $\underline{x}_1, \underline{x}_2 \dots$  until  $\underline{x}_i$  is close enough to the solution  $\underline{x}$ . The set follows the form

$$\underline{x}_{n+1} = \underline{x}_n + \alpha_n \underline{p}_n \quad (\text{A1.19})$$

where  $\underline{p}_n$  is a direction vector and  $\alpha_n$  is the norm of the descent to reach the solution.

The optimal,  $\alpha_n$ , which minimizes  $f$  over  $\underline{x}_n$ , is found when the directional derivative is equal to zero:

$$\begin{aligned}
\frac{df(\underline{x}_{n+1})}{d\alpha_n} &= 0 \\
\underline{\nabla}f^T \frac{d\underline{x}_{n+1}}{d\alpha_n} &= 0 \\
-\underline{r}_{n+1}^T \underline{p}_n &= 0 \\
(\underline{F} - \underline{K}\underline{x}_{n+1})^T \underline{p}_n &= 0 \\
(\underline{F} - \underline{K}(\underline{x}_n - \alpha_n \underline{p}_n))^T \underline{p}_n &= 0 \\
(\underline{r}_n - \alpha_n \underline{K}\underline{p}_n)^T \underline{p}_n &= 0 \\
\alpha_n &= \frac{\underline{p}_n^T \underline{r}_n}{\underline{p}_n^T \underline{K}\underline{p}_n}
\end{aligned} \tag{A1.20}$$

Consequently, for a given  $\underline{p}_n$ , the optimal norm,  $\alpha_n$ , is known. Now the direction vector must be chosen. In the beginning the best solution is to follow the steepest descent, which is the residual due to its definition (Equation (A1.18)) :

$$\underline{p}_0 = \underline{r}_0 = \underline{F} - \underline{K}\underline{x}_0 \tag{A1.21}$$

The following direction,  $\underline{p}_{n+1}$ , follows the descent direction and is a conjugate of  $\underline{p}_n$ .

$$\begin{cases} \underline{p}_{n+1} = \underline{r}_n + \beta_n \underline{p}_n \\ \underline{p}_{n+1}^T \underline{K}\underline{p}_n = 0 \end{cases} \tag{A1.22}$$

$$\beta_n = -\frac{\underline{p}_n^T \underline{K}\underline{r}_n}{\underline{p}_n^T \underline{K}\underline{p}_n}$$

#### A1.4.2.2 Krylov's subspace

The subspace span  $D_n$ ,  $[p_0, p_1, \dots, p_n]$ , is a  $K$ -orthogonal basis. Recalling that  $\underline{p}_{i-1} \in D_n$ , this fact implies that each new subspace  $D_{n+1}$  are formed from the union of the previous subspace  $D_n$  and the subspace  $\underline{K}D_n$ . Hence,

$$\begin{aligned}
D_n &= \text{span}\{\underline{p}_0, \underline{K}\underline{p}_0, \underline{K}^2 \underline{p}_0, \dots, \underline{K}^{n-1} \underline{p}_0\} \\
D_n &= \text{span}\{\underline{r}_0, \underline{K}\underline{r}_0, \underline{K}^2 \underline{r}_0, \dots, \underline{K}^{n-1} \underline{r}_0\}
\end{aligned} \tag{A1.23}$$

This subspace is called Krylov's subspace, a subspace created by repeatedly applying a matrix to a vector. It has a pleasing property: because  $\underline{K}D_n$  is included in  $D_{n+1}$ , the fact that the next residual  $\underline{r}_{n+1}$  is orthogonal to  $D_{n+1}$  implies that  $\underline{r}_{n+1}$  is  $\underline{K}$ -orthogonal to  $D_n$ .



### A1.4.2.3 Convergence consideration

In theory, the exact solution can be found in  $N$  iterations, where  $N$  is the dimension of the linear system. The error can be computed as

$$\underline{e}_n = \underline{x}_n - \underline{x} = \underline{x}_{n-1} + \alpha_{n-1} \underline{p}_{n-1} - \underline{x} = \underline{x}_0 + \sum_{i=0}^{n-1} \alpha_i \underline{p}_i - \underline{x} = \underline{e}_0 + \sum_{i=0}^{n-1} \alpha_i \underline{p}_i \quad (\text{A1.24})$$

The initial error can be expressed as a linear combination of a target direction  $[\underline{p}_0, \underline{p}_1, \dots, \underline{p}_N]$ .

$$\underline{e}_0 = \sum_{j=0}^{N-1} \delta_j \underline{p}_j \quad (\text{A1.25})$$

The values of  $\delta_j$  can be computed by multiplying (A1.25) by  $\underline{p}_n^T \underline{K}$

$$\begin{aligned} \underline{p}_n^T \underline{K} \underline{e}_0 &= \sum_{j=0}^{N-1} \delta_j \underline{p}_n^T \underline{K} \underline{p}_j \\ \underline{p}_n^T \underline{K} \underline{e}_0 &= \delta_n \underline{p}_n^T \underline{K} \underline{p}_n \\ \delta_n &= \frac{\underline{p}_n^T \underline{K} \underline{e}_0}{\underline{p}_n^T \underline{K} \underline{p}_n} \\ \delta_n &= \frac{\underline{p}_n^T \underline{K} \left( \underline{e}_0 + \sum_{i=0}^{n-1} \alpha_i \underline{p}_i \right)}{\underline{p}_n^T \underline{K} \underline{p}_n} (*) \\ \delta_n &= \frac{\underline{p}_n^T \underline{K} \underline{e}_n}{\underline{p}_n^T \underline{K} \underline{p}_n} \\ \delta_n &= -\frac{\underline{p}_n^T \underline{r}_n}{\underline{p}_n^T \underline{K} \underline{p}_n} \\ \delta_n &= -\alpha_n \end{aligned} \quad (\text{A1.26})$$

Line (\*) is possible due to the  $\underline{K}$ -orthogonality of  $\underline{p}_i$  vectors.

In conclusion, a component of the initial error,  $\underline{e}_0$ , is removed at each iteration in the  $D_N$  span; therefore, after  $N$  iterations the exact solution is identified. In fact if the relations in (A1.24) and (A1.26) give

$$\begin{aligned}
\mathbf{e}_n &= \mathbf{e}_0 + \sum_{i=0}^{n-1} \alpha_i \mathbf{p}_i \\
\mathbf{e}_n &= -\sum_{j=0}^{N-1} \alpha_j \mathbf{p}_j + \sum_{i=0}^{n-1} \alpha_i \mathbf{p}_i \\
\mathbf{e}_n &= -\sum_{j=n}^{N-1} \alpha_j \mathbf{p}_j
\end{aligned} \tag{A1.27}$$

Then  $\mathbf{e}_n=0$  after  $N$  iterations.

However if the dimension is very large, then the computation time becomes prohibitive. One prefers to find an approximate solution and stop the iteration when the residual is sufficiently reduced. The stop criterion is

$$\frac{\|\mathbf{r}_n\|_2}{\|\mathbf{r}_0\|_2} < \varepsilon \tag{A1.28}$$

where  $\varepsilon$  is a convergence coefficient chosen by the user.

One can define a  $\mathbf{K}$  norm by  $\|\mathbf{v}\|_{\mathbf{K}} = \mathbf{v}^T \mathbf{K} \mathbf{v}$ . [SHE94] shows that

$$\|\mathbf{e}_n\|_{\mathbf{K}} \leq 2 \left( \frac{\sqrt{\gamma}-1}{\sqrt{\gamma}+1} \right)^n \|\mathbf{e}_0\|_{\mathbf{K}} \quad \text{with } \gamma = \frac{\lambda_{\max}}{\lambda_{\min}} \tag{A1.29}$$

where  $\lambda_{\max}$  and  $\lambda_{\min}$  are the maximum and the minimum eigenvalues of  $\mathbf{K}$  respectively.

In practice, the conjugate gradient converges better if the distribution of the eigenvalues are clustered and low or if the starting point is close to the exact solution. The conjugate gradient method converges better than the stationary method because it tends to reduce the residual. However, the conjugate gradient can fail if the stiffness matrix is nonsymmetrical or non definite and positive.

**A1.4.2.4 Algorithm**

In summary the algorithm of the conjugate gradient is:

$$\begin{aligned}
 \underline{r}_0 &= \underline{F} - \underline{K}\underline{x}_0; \\
 \underline{p}_0 &= \underline{r}_0; \\
 \text{do while } \|\underline{r}_n\|_2 &> \varepsilon \|\underline{r}_0\|_2 \\
 &\left\{ \begin{array}{l}
 \alpha_n = \frac{\underline{p}_n^T \underline{r}_n}{\underline{p}_n^T \underline{K} \underline{p}_n}; \\
 \underline{x}_{n+1} = \underline{x}_n + \alpha_n \cdot \underline{p}_n; \\
 \beta_n = -\frac{\underline{p}_n^T \underline{K} \underline{r}_n}{\underline{p}_n^T \underline{K} \underline{p}_n}; \\
 \underline{p}_{n+1} = \underline{r}_n + \beta_n \underline{p}_n; \\
 \underline{r}_{n+1} = \underline{F} - \underline{K}\underline{x}_{n+1};
 \end{array} \right. \\
 \text{end}
 \end{aligned}$$

**A1.4.3 Arnoldi's method**

Arnoldi's [SAA03] procedure is an algorithm for building an orthonormal basis of the Krylov subspace. One variant of this algorithm is

$$\begin{aligned}
 \underline{p}_0 &= \frac{\underline{r}_0}{\|\underline{r}_0\|_2} \\
 \text{do } j=1, m \\
 &\left\{ \begin{array}{l}
 \text{do } i=1, j \\
 \{ \underline{h}_{ij} = \underline{p}_i^T \underline{K} \underline{p}_j \\
 \text{end do} \\
 \underline{w}_j = \underline{K} \underline{p}_j - \sum_{k=1}^j \underline{h}_{kj} \underline{p}_k \\
 \underline{h}_{j+1,j} = \|\underline{w}_j\|_2 \\
 \text{If } \underline{h}_{j+1,j} = 0, \text{ then Stop} \\
 \underline{p}_{j+1} = \frac{\underline{w}_j}{\underline{h}_{j+1,j}}
 \end{array} \right. \tag{A1.30} \\
 \text{End do}
 \end{aligned}$$

One may define some matrices:

$$\underline{P}_n = [\underline{p}_1, \underline{p}_2, \dots, \underline{p}_n] \tag{A1.31}$$

where  $(\underline{P}_n)_{N \times n}$  contains the vector of Krylov's subspace.

$$\left(\overline{\underline{H}}_k\right)_{ij} = \begin{cases} h_{ij} & \text{if } 1 \leq j \leq k, 1 \leq i \leq j+1 \\ 0 & \text{otherwise} \end{cases} \quad (\text{A1.32})$$

where  $\overline{\underline{H}}_n$  has a dimension  $(n \times (n+1))$

The superior Hessenberg matrix,  $(\underline{H}_n)_{n \times n}$ , is the matrix  $\overline{\underline{H}}_n$  after having removed the last line.

$$\overline{\underline{H}}_n = \begin{bmatrix} \underline{H}_n \\ 0 \dots 0 h_{n+1,n} \end{bmatrix}$$

Saad [SAA86] demonstrated that

$$\underline{\underline{K}}\underline{\underline{P}}_n = \underline{\underline{P}}_{n+1} \overline{\underline{H}}_n \quad (\text{A1.33})$$

#### A1.4.4 GMRES method

This method was developed by Saad [SAA86]. It searches at each iteration,  $n$ , for the vector  $\underline{z}_n$ , which belongs to  $D_n$  and minimizes the residual.

$$\underline{x}_n = \underline{x}_0 + \underline{z}_n = \underline{x}_0 + \underline{\underline{P}}_n \underline{y}_n \quad (\text{A1.34})$$

Therefore one defines the following function:

$$\begin{aligned} J(\underline{y}) &= \|\underline{r}_n\|_2 \\ J(\underline{y}) &= \|\underline{F} - \underline{\underline{K}}\underline{x}_n\|_2 \\ J(\underline{y}) &= \|\underline{F} - \underline{\underline{K}}(\underline{x}_0 + \underline{\underline{P}}_n \underline{y})\|_2 \\ J(\underline{y}) &= \|\underline{r}_0 - \underline{\underline{K}}\underline{\underline{P}}_n \underline{y}\|_2 \\ J(\underline{y}) &= \|\beta \underline{p}_1 - \underline{\underline{K}}\underline{\underline{P}}_n \underline{y}\|_2 \quad \text{with } \beta = \frac{\underline{r}_0}{\|\underline{r}_0\|_2} \\ J(\underline{y}) &= \|\beta \underline{p}_1 - \underline{\underline{P}}_{n+1} \overline{\underline{H}}_n \underline{y}\|_2 \quad (*) \\ J(\underline{y}) &= \|\beta \underline{\underline{P}}_{n+1} \underline{e}_1 - \underline{\underline{P}}_{n+1} \overline{\underline{H}}_n \underline{y}\|_2 \quad \text{with } \underline{e}_1 = [1, 0, \dots, 0] \text{ dimension } ((n+1) \times 1) \\ J(\underline{y}) &= \|\underline{\underline{P}}_{n+1} (\beta \underline{e}_1 - \overline{\underline{H}}_n \underline{y})\|_2 \\ J(\underline{y}) &= \|\beta \underline{e}_1 - \overline{\underline{H}}_n \underline{y}\|_2 \quad \text{because } \underline{\underline{P}}_{n+1} \text{ is orthonormal} \end{aligned} \quad (\text{A1.35})$$

Line (\*) comes from the relation in (A1.33).

Consequently,

$$\underline{y}_n = \min_{\underline{y} \in D_n} J(\underline{y}) = \min_{\underline{y} \in D_n} \|\beta \underline{e}_1 - \overline{\underline{H}}_k \underline{y}\|_2. \quad (\text{A1.36})$$

Minimizing  $\underline{y}_n$  is not time-consuming since it requires the solution of an  $n \times (n+1)$  least-square problem where  $n$  is typically small.

If  $n=N$ , the solution obtained is the correct solution because the residual is minimized on  $\mathbb{R}^N$ .

The GMRES algorithm is performed as follows

- Step 0: Choose  $\underline{x}_0$  and compute  $\underline{r}_0$  and  $\underline{p}_1$ ,  $n=1$ ;
- Step 1: Perform Arnoldi's algorithm;
- Step 2: Identify  $\underline{y}_n$  by minimizing  $J(\underline{y})$  and compute  $\underline{x}_{n+1}$ . If  $\underline{r}_n$  respects the convergence criterion, stop; else  $n=n+1$  and go on to step 1.

This method converges forever because it searches for the optimal direction to optimize the residual. However, the bigger  $n$  is, the more expensive the algorithm is, because the dimension of  $\underline{P}_{k+1}$  increases and the multiplication matrix procedure requires more steps. To tackle these difficulties, one imposes a maximum number of iteration  $n_{\max}$ . Then, Krylov's subspace is constructed with the dimension  $n_{\max}$  associated with  $\underline{r}_0$  and  $\underline{K}$ . If  $\underline{x}_{n_{\max}}$  does not respect the convergence criterion, the algorithm is relaunched with  $\underline{x}_0$  equal to  $\underline{x}_{n_{\max}}$ . This algorithm is called GMRES( $n$ ).

This algorithm is described below.

Step 0: Choose  $\underline{x}_0$  and compute  $\underline{r}_0 = \underline{F} - \underline{K}\underline{x}_0$ ,  $\underline{p}_0 = \frac{\underline{r}_0}{\|\underline{r}_0\|_2}$

Step 1:

do  $j=1, n$

$\left\{ \begin{array}{l} \text{do } i=1, j \\ \left\{ \begin{array}{l} \underline{h}_{ij} = \underline{p}_i^T \underline{K} \underline{p}_j \\ \text{end do} \\ \underline{w}_j = \underline{K} \underline{p}_j - \sum_{k=1}^j \underline{h}_{kj} \underline{p}_k \\ \underline{h}_{j+1,j} = \|\underline{w}_j\|_2 \\ \text{If } \underline{h}_{j+1,j} = 0, \text{ then Stop} \\ \underline{p}_{j+1} = \frac{\underline{w}_j}{\underline{h}_{j+1,j}} \end{array} \right. \end{array} \right.$

end do

Step2: Identify  $\underline{y}_n$  which minimizes  $J(\underline{y})$  and compute  $\underline{x}_n = \underline{x}_0 + \underline{P}_n \underline{y}_n$

Step3: Compute  $\underline{r}_n = \underline{F} - \underline{K}\underline{x}_n$ . If  $\underline{r}_n$  respects the convergence criterion, then stop, else goto Step1

with  $\underline{x}_0 = \underline{x}_n$  and  $\underline{p}_0 = \frac{\underline{r}_n}{\|\underline{r}_n\|_2}$

## A1.5 Preconditioning

Preconditioning is a technique to speed up convergence for iterative methods. The convergence depends on the distribution and the eigenvalues of the stiffness matrix,  $\underline{\mathbf{K}}$ . Suppose that  $\underline{\mathbf{M}}$  is a symmetric, positive-definite matrix that approximates  $\underline{\mathbf{K}}$ , but is easier to invert. Equation (A1.1) can be indirectly solved by solving

$$\underline{\mathbf{M}}^{-1} \underline{\mathbf{K}} \underline{\mathbf{x}} = \underline{\mathbf{M}}^{-1} \underline{\mathbf{F}} \quad (\text{A1.37})$$

If the set of eigenvalues of  $\underline{\mathbf{M}}^{-1} \underline{\mathbf{K}}$  is lower and better clustered than the set of  $\underline{\mathbf{K}}$ , then the number of iterations to solve (A1.37) will be lower than the iteration number of (A1.1).

There are different ways of building  $\underline{\mathbf{M}}$ . The simplest way of defining a preconditioner is to perform an incomplete LU factorization of the original matrix  $\underline{\mathbf{K}}$ . This entails a decomposition of the form

$$\underline{\mathbf{K}} = \underline{\mathbf{L}}_0 \underline{\mathbf{U}}_0 - \underline{\mathbf{R}} \quad (\text{A1.38})$$

where  $\underline{\mathbf{L}}_0$  and  $\underline{\mathbf{U}}_0$  have the same nonzero structure as the lower and upper parts of  $\underline{\mathbf{K}}$ , respectively, and  $\underline{\mathbf{R}}$  is the residual error of the factorization. This incomplete factorization, known as ILU(0), is rather easy and inexpensive to compute.

This approach involves preserving the matrix structure of the original matrix  $\underline{\mathbf{K}}$  and dropping any fill-in elements that are generated with  $\underline{\mathbf{L}}$  and  $\underline{\mathbf{U}}$  in the position where the elements of  $\underline{\mathbf{K}}$  vanish (see Figure A1-2). Therefore one defines the set,  $Z_0$ , of row/column couple (i,j) that respects the following condition:

$$Z_0 = \{(i, j) \mid 1 \leq i, j \leq N, K_{ij} \neq 0\} \quad (\text{A1.39})$$

The algorithm is

$$\begin{array}{l} \text{for } i=1:N \\ \quad \left\{ \begin{array}{l} \text{for } j=1:N \\ \quad \left\{ \begin{array}{l} \text{if } (i, j) \in Z_0 \text{ then} \\ \quad \left\{ \begin{array}{l} s_{ij} = K_{ij} - \sum_{k=1}^{\min(i,j)-1} L_{ik} U_{kj} \\ \text{if } (i \leq j) \text{ then } L_{ij} = s_{ij} \\ \text{else } U_{ij} = \frac{s_{ij}}{L_{ii}} \end{array} \right. \\ \quad \end{array} \right. \\ \quad \end{array} \right. \\ \quad \end{array} \\ \text{end} \end{array} \quad (\text{A1.40})$$

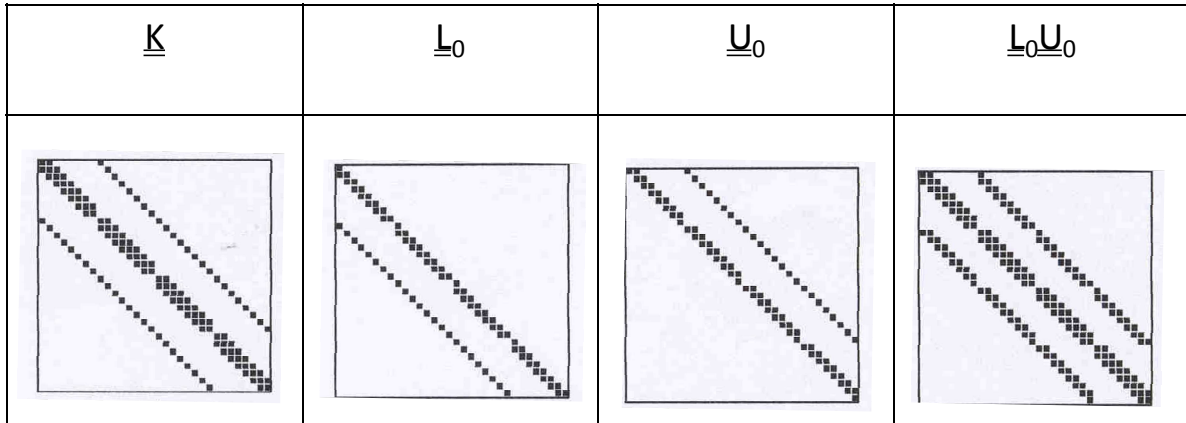


Figure A1-2: Example of ILU(0) factorization

However the ILU(0) often causes a crude approximation and requires many iterations to converge. So, it is necessary to improve the fill-in with the new set:

$$Z_1 = \{(i, j) | 1 \leq i, j \leq N, K_{ij} \neq 0 \text{ and } (\underline{L}_0 \underline{U}_0)_{i,j} \neq 0\} \quad (\text{A1.41})$$

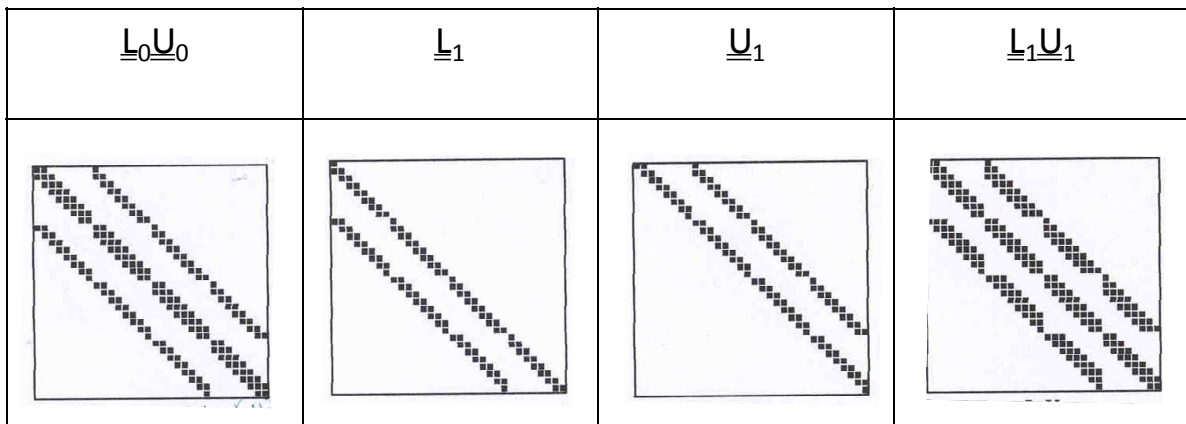


Figure A1-3: Example of ILU(1) factorization

This method is called ILU(1) (see Figure A1-3). One can generalize this with the method ILU(k) where the set is defined by

$$Z_k = \{(i, j) | 1 \leq i, j \leq N, K_{ij} \neq 0 \text{ and } (\underline{L}_{k-1} \underline{U}_{k-1})_{i,j} \neq 0\} \quad (\text{A1.42})$$

This algorithm requires fewer iteration than ILU(0) to converge. However, there are three drawbacks:

- The number of non-zero components cannot be predicted.
- The CPU time of this algorithm can be long.
- The algorithm can drop large elements and so  $\underline{R}$  is not small.

To tackle these difficulties one combines this method with the threshold strategy. This method is called ILUT. The components are dropped as a function of their position and with their value. If the value of an element out of the diagonal is less than a threshold, then it is considered null.

## **A1.6 Implementation in Lagamine**

### **A1.6.1 GMRES module description**

The GMRES method was developed by Y. Saad. It offers a FORTRAN open source tool kit, called SPARKIT, which contains applications to manipulate a sparse matrix. A file called GMRES.F contains the following subroutines which come from SPARKIT:

- Pgmres : GMRES solver,
- ILU(0): simple preconditioner,
- ILUT: improved preconditioner.

### **A1.6.2 Input parameters**

GMRES requires some input parameters:

- im : dimension of the Krylov subspace,
- maxits: maximum of iteration,
- eps: tolerance convergence coefficient.

Likewise, the ILUT(k, $\epsilon$ ) preconditioning requires some input parameters:

- lfill: number of incomplete LU factorization steps (=k),
- droptol: tolerance coefficient to drop elements ( $=\epsilon$ ).

The drawback of GMRES is that the calibration of the parameters to speed up the solving process is a difficult task.

## **A1.7 Validation of the GMRES method in Lagamine**

The GMRES method was tested on two models which had significant number of degrees of freedom. These models were launched on two operating systems: Windows XP on a PC and LINUX on a machine called Nick2.

### **A1.7.1 Indentation test**

This model simulates an indentation in the surface of a material sample [GER07] (see Figure A1-4). The model was three dimensional with three degrees of freedom. The sample was modeled by 1879 nodes and 1772 elements. The total number of degrees of freedom was 5506.



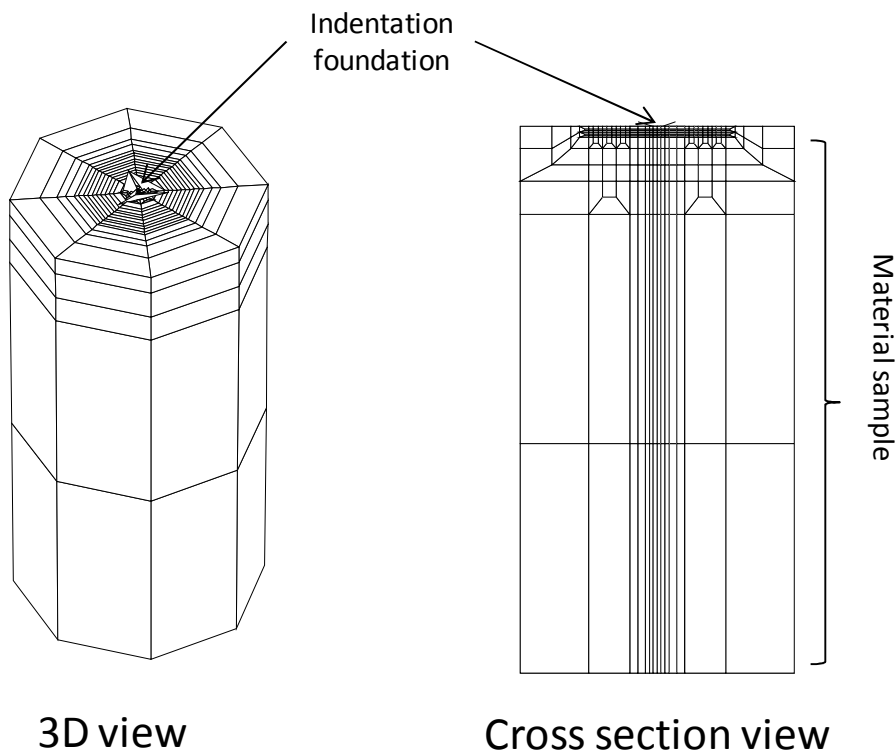


Figure A1-4: Indentation test modeling mesh

The computation was launched with the three methods with Windows XP. Only 10% of the simulation has been performed. The parameters for the iterative method are given in the table below.

Table A1-1: Iterative resolution parameters for indentation simulation

im	eps	lfil	droptol
250	1E-4	25	1E-2

The results are summarized on the followed table:

Table A1-2: Comparison of CPU time for indentation simulation SPIF modeling

METHOD	CPU time
DIRECT LU Skyline	39 min 58s
DIRECT LU CSR	1 h 5 min 28s
Iterative method	5 min 0 s

### A1.7.2 Incremental forming modeling

The modeling is the forming of sheet metal by an incremental single point process [HEN09] (see Figure A1-5). The sheet was circular and only a quarter was modeled thanks to symmetry. The model was three dimensional and the nodes had six degrees of freedom (3 translations and 3 rotations). The mesh contained 4450 nodes and 4506 elements. The total number of degrees of freedom was 26392.

The computation was launched with the three methods with Windows XP. Only 0.1 s of computation was simulated. The results are summarized on the following table.

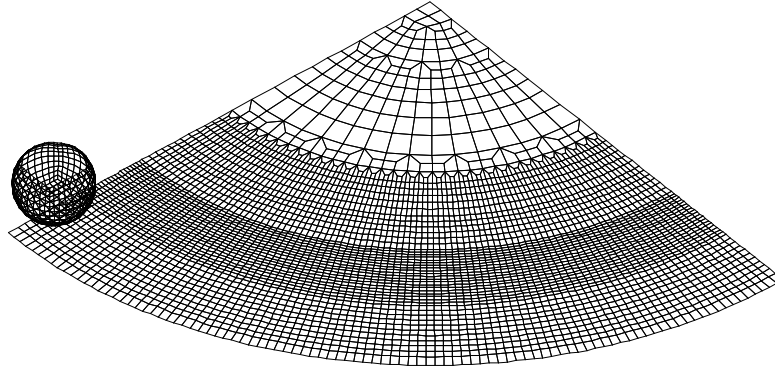


Figure A1-5: SPIF process modeling mesh

Table A1-3: Comparison of CPU time for SPIF simulation

METHOD	OS	CPU time
DIRECT LU Skyline	PC	1h 3 min 20 s
	Nick2	21 min 24 s
DIRECT LU CSR	PC	1h 12m 30s
	Nick2	13 min 22 s
Iterative method	PC	13 min 51 s
	Nick2	7 min 40 s

Table A1-4: Iterative resolution parameters for the SPIF simulation

im	eps	lfil	droptol
2000	1E-4	50	1E-6

## A1.8 Conclusions

After a literature review, GMRES method was implemented in the Lagamine code. The advantage of this method that it works well on a non-symmetric sparse matrix. This method is coupled with a preconditioned ILU method to speed up the convergence. The language is free open-source in FORTRAN. The drawbacks of this method are the need to calibrate the parameters to reach a satisfactory gain in computation time.

The method was experimented on two simulations which contained many degrees of freedom. The gain in computation time was significant. In addition, this method was used for the identification of the cohesive parameters. In the inverse method, many 3D simulations were performed. Finally, this method helps us to gain computation time.

# **Appendix 2**

# **Adaptive remeshing**



This chapter describes a remeshing method which was developed during this PhD work period. This method was applied in the ALECASPIF project (An **AL**uminum alloy improved by the **ECAP** Processing and Shaped by the Incremental Forming **SPIF**). Some incremental forming SPIF process is modeled by finite elements. However, due to a high level of strain concentration in all parts of the structure in different moments, the mesh must be very fine and the computation, as a result, time becomes prohibitive. The work completed the Christophe Henrard's PhD from the ArGEnCo Department [HEN09].

That's why a remeshing method was developed by the author. This method is explained in this thesis because the method could be used in the case of remeshing with cohesive zone model or welding process. This appendix consists of the paper presented during the Numisheet Conference 2008 at Interlaken.

## ADAPTIVE REMESHING FOR INCREMENTAL FORMING SIMULATION

Cedric Lequesne<sup>1\*</sup>, Christophe Henrard<sup>1</sup>, Chantal Bouffieux<sup>1</sup>, Joost R. Duflo<sup>2</sup>,  
Anne Marie Habraken<sup>1</sup>

<sup>1</sup>University of Liege, ArGEnCo, Liege, Belgium

<sup>2</sup>Katholieke Universiteit Leuven, PMA, Leuven, Belgium

**ABSTRACT:** Incremental forming of aluminium sheets has been modelled by finite element simulations. However the computation time was prohibitive because the tool deforms every part of the sheet and the mesh along the tool path must be very fine. Therefore, an adaptive remeshing method has been developed. The elements that are close to the tool are divided into smaller elements in order to have a fine mesh where high deformations occur. Consequently, some new nodes become inconsistent with the non-refined neighbouring elements. To overcome that problem, their displacements are constrained, i.e. dependent on their master nodes displacements. The data concerning these new nodes and elements are stored in a linked list, which is a fundamental data structure. It consists of a sequence of cells, each containing data fields and a pointer towards the next cell. The goal of this article is to explain the developments performed in the finite element code, to validate the adaptive remeshing technique and to measure its efficiency using the line test simulation. During this test, which is a simple incremental forming test, a clamped sheet is deformed by a spherical tool moving along a linear path.

**KEYWORDS:** Remeshing, Finite Element Simulation, Incremental Forming

### 1 INTRODUCTION

Single point incremental forming (SPIF) is a sheet metal forming process that is very appropriate for rapid prototyping because it does not require any dedicated dies or punches to form a complex shape. Instead, it uses a standard smooth-end tool mounted on a numerically controlled multi-axis milling machine. The tool follows a complex tool-path and progressively deforms a clamped sheet into its desired shape ([1], [2]).

Simulating this process is a complex task. First, the tool diameter is small compared to the size of the metal sheet. Moreover, during its displacement, the tool deforms almost every part of the sheet, which implies that small elements are required everywhere on the sheet. For implicit simulations, the computation time is thus prohibitive. In this paper, the simulations were performed using the finite element code Lagamine [3] developed at the University of Liege. In order to decrease the simulation time, a new method using an adaptive remeshing has been developed.

This article starts with an introduction to the adaptive remeshing method implemented in the

finite element code used. Then, it describes the reference simulation, the line test, used throughout this paper in order to assess the performance of this method.

### 2 ADAPTIVE REMESHING

#### 2.1 SPIF PROCESS MODELLING

The metal sheet is modelled with 4-node shell elements with six degrees of freedom for each node – three translations and three rotations – called COQJ4 [4]. Some elements contain contact element using a classical penalty method [5]. The tool is modelled using an undeformable spherical foundation.

#### 2.2 REMESHING METHOD

The zone where high deformations occur is always close to the current location of the tool. Therefore, the chosen remeshing method is a refinement without transition which moves along with the tool. The coarse elements, close to the tool, are divided into a fixed number of small new elements. Some new nodes can become inconsistent with the neighbouring coarse elements.

---

\* Corresponding author: B 52/3, Chemin des Chevreuils, 1, 4000 Liege, Belgium, +32 (0) 4 366 91 40, +32 (0) 4 366 91 92, cedric.lequesne@ulg.ac.be

Numisheet 2008

September 1 - 5, 2008 – Interlaken, Switzerland

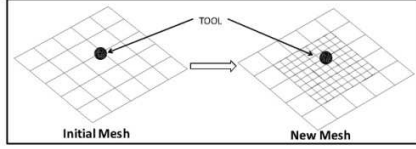


Figure 1: Remeshing method

### 2.3 NEIGHBOURHOOD CRITERION

The elements are refined in the tool neighbourhood. The criterion defining the size of the neighbourhood is:

$$D^2 \leq \alpha(L^2 + R^2) \quad (1)$$

where  $D$  is the shortest distance between the centre of the spherical tool and the nodes of the element,  $L$  is the longest diagonal of the element,  $R$  is the radius of the tool and  $\alpha$  is a neighbourhood coefficient chosen by the user. Consequently, every coarse element which respects the criterion is deactivated and refined in several new smaller elements. It becomes a "cell". In each cell some new objects are generated (nodes, elements, ...).

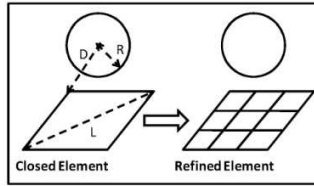


Figure 2: Element refinement

## 2.4 NEW NODES

### 2.4.1 Generation of new nodes

Each new node is located between two old nodes,  $A$  and  $B$ . Its degree of freedom is computed by interpolation:

$$\underline{q}_p = \left(1 - \frac{p}{n+1}\right) \underline{q}_A + \left(\frac{p}{n+1}\right) \underline{q}_B \quad (2)$$

where  $n$  is the number of new nodes between  $A$  and  $B$ ,  $p$  is the new node number,  $\underline{q}_p$ ,  $\underline{q}_A$  and  $\underline{q}_B$  are respectively the degrees of freedom of the node  $p$ ,  $A$  and  $B$ .

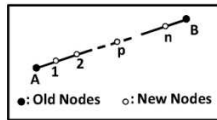


Figure 3: Generation of new nodes.

### 2.4.2 Constrained nodes

This method created some nodes which are incompatible with the non-refined neighbouring element. They must be constrained so that they remain in the same relative positions between two old master-nodes. Consequently there are two types of degrees of freedom  $\underline{q}$ : unconstrained,  $\underline{q}_r$  and constrained,  $\underline{q}_s$ :

$$\underline{q} = \begin{bmatrix} \underline{q}_r \\ \underline{q}_s \end{bmatrix} \quad (3)$$

The constrained degrees of freedom are computed in function of the unconstrained degrees of freedom:

$$\underline{q}_s = \underline{N} \underline{q}_r \quad (4)$$

where  $\underline{N}$  is an interpolation matrix which contains similar formulae as equation (2). It is then possible to rewrite equation (3) without  $\underline{q}_s$ :

$$\underline{q} = \underline{A} \underline{q}_r \text{ with } \underline{A} = \begin{bmatrix} \underline{I} \\ \underline{N} \end{bmatrix} \quad (5)$$

where  $\underline{I}$  is an identity matrix.

In order to identify the equilibrium state, the out-of-balance forces matrix  $\underline{F}$  and the stiffness matrix  $\underline{K}$  are modified using the same master-slave relation [6]:

$$\underline{F}_r = \underline{A}^T \underline{F} \quad (6)$$

$$\underline{K}_r = \underline{A}^T \underline{K} \underline{A} \quad (7)$$

where  $\underline{F}_r$  is the out-of-balance forces array and  $\underline{K}_r$  is the stiffness matrix of the unconstrained degrees of freedom.

## 2.5 NEW ELEMENTS

The new nodes are known but the variables must be transferred from the coarse elements to the new smaller elements. The transfer method used [7] is simpler to implement and requires less computation time than classical ones. The idea is to interpolate a variable (stresses, strains ...) from neighbouring integration points using a weighted-average formula. The value of a variable  $Z_j$  in a new integration point  $j$  is computed as equation (8):

$$Z_j = \begin{cases} \frac{\sum_k Z_k + CZ_p}{\sum_k R_{kj}^n + R_{pj}^n} & \text{if } R_{pj} > R_{\min} \\ \sum_k \frac{1}{R_{kj}^n} + \frac{C}{R_{pj}^n} & \\ Z_p & \text{if } R_{pj} \leq R_{\min} \end{cases} \quad (8)$$

Numisheet 2008

September 1 - 5, 2008 – Interlaken, Switzerland

where  $k$  are the integration points where the variable  $Z_k$  is known,  $p$  is the closest integration point to the new integration point  $j$  where the variable is  $Z_p$ ,  $R_{kj}$  and  $R_{pj}$  are the distance between  $k$  and  $j$ ,  $p$  and  $j$  respectively,  $C$  is a user-defined constant used to amplify the influence of the closest integration point  $p$ ,  $n$  is a interpolation exponent which must be an even number. All the points for which  $R_{kj} > R_{max}$  are ignored. After a trial-and-error procedure, the best set of threshold values were found to be:  $C=5$ ,  $n=4$ ,  $R_{max}=1.5d$  where  $d$  is a diagonal of the new element and  $R_{min}=10^{-5}D$  where  $D$  is a diagonal of the rectangle in which the work piece is inscribed.

**2.6 REACTIVATION OF COARSE ELEMENT**

If a cell does not respect the neighbourhood criterion anymore, the new fine elements are removed and the coarse element is reactivated. However the shape prediction could be less accurate if the distortion is important on the location of the coarse element. Consequently, an additional criterion is used.

To assess the distortion, a distance,  $d$ , between the current position of every new node,  $\underline{X}_v$ , and a virtual position,  $\underline{X}_i$ , is computed, as illustrated in Figure 4. The virtual position would be the position of the node if it had the same relative position in the plane described by the coarse element. This position is calculated by interpolation with the four nodes positions,  $\underline{X}_i$ , of the coarse element.

$$\underline{X}_v = \sum_{i=1,4} H_i(\xi, \eta) \underline{X}_i \tag{9}$$

where  $H_i$  is the interpolation function,  $\xi$  and  $\eta$  are the initial relative position of the node in the cell. The criterion for reactivating a coarse element is:

$$d \leq d_{max} \text{ with } d = |\underline{X}_c - \underline{X}_v| \tag{10}$$

where  $d_{max}$  is the maximum distance chosen by the user. If the criterion is not respected for a node, then the coarse element is not reactivated and remains a cell with fine elements.

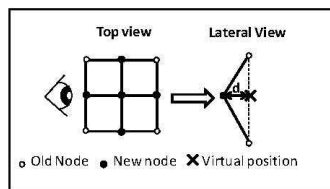


Figure 4: Example of assessment of distortion in a cell

**2.7 LINKED LIST**

In computer science, a linked list [8] is a data structure. It consists of a sequence of objects, each containing arbitrary data fields and one reference ("link") pointing towards the next object. The principal benefit of a linked list over a conventional array is that the order of the linked items may be different from the order in which they are stored in memory or on disk. The list of items can be scanned in a different order. Linked lists facilitate the insertion and removal of objects at any point in the list. During the SPIF process many elements are refined and coarsened, so that many cells are created and removed. This data storage method is appropriate for this purpose. A cell contains the information about new nodes, new element and constrained edges.

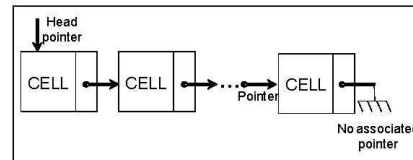


Figure 5: Linked list

**3 REFERENCE SIMULATION: LINE TEST**

**3.1 THE LINE TEST DESCRIPTION**

The validation of the new approach is performed on the so-called line test simulation. This simple SPIF test is presented in Figure 6. A square metal sheet of an aluminium alloy AA3003-O with a thickness of 1.2 mm is clamped along its edges. The spherical tool radius is 5 mm. The displacement of the tool is composed of five steps with an initial position tangent to the surface of the sheet: a first indent of 5 mm (step1), a line movement at the same depth along the X-axis (step 2), then a second indent up to the depth of 10 mm (step 3) followed by a line at the same depth along the X-axis (step 4) and the unloading (step5).

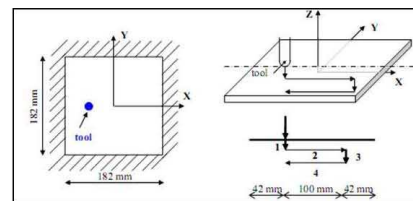


Figure 6: Schematic presentation of the line test

Numisheet 2008

September 1 - 5, 2008 – Interlaken, Switzerland

**3.2 FEM DESCRIPTION**

**3.2.1 Description of the constitutive law**

The elastic range is described by the Hooke's law. For the plastic part, the yield locus,  $F_{Hill}$ , is described by Hill'48 law:

$$F_{Hill}(\underline{\sigma}) = \frac{1}{2} [(H+G)\sigma_{11}^2 + (H+F)\sigma_{22}^2 + 2H\sigma_{11}\sigma_{22} + 2N\sigma_{12}^2] - \sigma_F^2 = 0 \quad (11)$$

where  $\sigma_F$  is the yield stress and F, G, H and N are Hill's coefficients. The hardening equation is described by the Swift law:

$$\sigma_F = K (\epsilon_0 + \epsilon^p)^n \quad (12)$$

where  $\epsilon^p$  is the plastic strain,  $\epsilon_0$  is the initial strain before yielding, K is an hardening coefficient and n is an hardening exponent. The parameters of this modelling are summarized in Table 1 to 3.

**Table 1:** Hooke's law parameters

E (MPa)	$\nu$
72600	0.36

**Table 2:** Hill'48 law parameters

F	G	H	N
1.22	1.19	0.81	4.06

**Table 3:** Swift law parameters

$\epsilon_0$	K (MPa)	n
0.00057	183	0.229

**3.2.2 Boundary Conditions**

The geometry and the loading are symmetrical about the X-axis, so that only half of the sheet is modelled. Consequently, the displacements and rotations around the X- and Z-axis are fixed for every node along the X-axis. Moreover, the nodes along the edges are fixed to model the clamping of the sheet.

**3.2.3 The meshes**

Two types of meshes are tested. The first is the reference. It is used without adaptive remeshing and contains 884 elements. The second is used with adaptive remeshing and contains 314 elements.

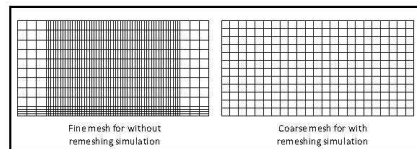


**Figure 7:** Meshes

**3.2.4 The remeshing parameters**

Every coarse element that needs to be refined is divided into four new elements. The neighbourhood coefficient,  $\alpha$ , is equal to 2 and the maximum relative distance,  $d_{max}$ , is 0.1 mm.

**3.3 RESULTS**

**3.3.1 Mesh evolution**

Figure 8 shows the evolution of the mesh during the simulation. During step 1, only the elements close to the tool are refined. During the other steps, the tool moves further away. Therefore, some refined elements are removed but those where the distortion is important remain refined. Finally at the end of the simulation the mesh is fine only where the distortion is high.

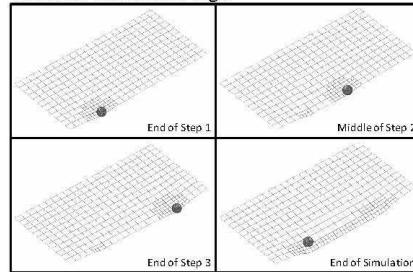


**Figure 8:** Evolution of the mesh

**3.3.2 Comparison with the reference**

The main outputs of the SPIF simulation are the final shape of the sheet and the evolution of the tool force during the simulation. Figure 9 shows the final shape of the sheet in a cross-section along the symmetric axis in the middle of the thickness for the reference and the remeshed simulation. Figure 10 shows the evolution of the tool force during the simulations. The results are quite similar. The oscillations of the force are due to the penalty method. They are higher with remeshing because the mesh used here is coarser than the reference.

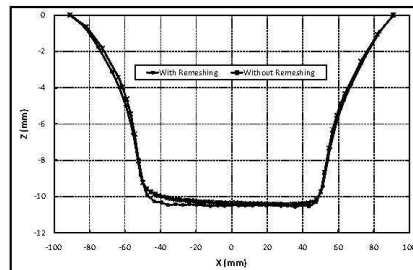


**Figure 9:** Shape in a cross-section at the end of the line test



Numisheet 2008

September 1 - 5, 2008 – Interlaken, Switzerland

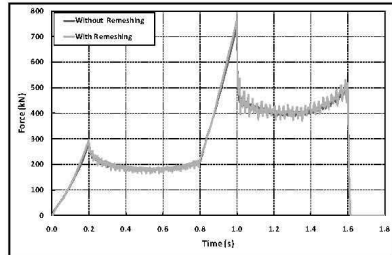


Figure 10: Evolution of tool force during the line test

#### 4 CONCLUSIONS

This paper presents the validation of the adaptive remeshing technique applied on the SPIF process. This method has the advantage to decrease the number of nodes while giving quite accurate results.

In the future the same technique will be used to simulate more complex SPIF process and decrease the time computation.

#### 5 ACKNOWLEDGEMENT

The authors of this article would like to thank the Institute for the Promotion of Innovation by Science and Technology in Flanders (IWT) and the Belgian Federal Science Policy Office (Contracts IAP P6-24 and TAP2 ALECASPIF P2/00/01) for their financial supports.

As Research director, A.M. Habraken would like to thank the Fund for Scientific Research (FNRS, Belgium) for its support.

#### 6 REFERENCES

- [1] Henrard C., Habraken A.M., Szekeres A., Dufloy J.R., He S., Van Bael A. and Van Houtte P.: *Comparison of FEM Simulations for the Incremental Forming Process*. Advanced Materials Research, 6-8: 533-542, 2005.
- [2] Jeswiet J., Micari F., Hirt G., Bramley A., Dufloy J. and Allwood J.: *Asymmetric Single Point Incremental Forming of Sheet Metal*. CIRP Annals, 54(2): 623-649, 2005.
- [3] Cescotto S. and Grober H.: *Calibration and Application of an Elastic-Visco-Plastic Constitutive Equation for Steels in Hot-Rolling conditions*. Engineering Computations, 2: 101-106, 1985.
- [4] Jetteur P. and Cescotto S.: *A Mixed Finite Element for the Analysis of Large Inelastic Strains*. International Journal for Numerical Methods in Engineering, 31: 229-239, 1991.
- [5] Habraken A.M. and Cescotto C.: *Contact between Deformable Solids, the Fully*

*Coupled Approach*. Mathematical and Computer Modeling, 28(4-8): 153-169, 1998.

- [6] Driessen B. J., *A direct stiffness modification approach to attaining linear consistency between incompatible finite element meshes*. The Information Bridge, 2000.
- [7] Habraken A.M., *Contribution to the modelling of metal forming by finite element model*. Ph D thesis of University of Liege, 1989.
- [8] Newell, Allen and Shaw, *Programming the Logic Theory Machine*. Proceedings of the Western Joint Computer Conference: 230-240, 1957.



# Appendix 3 References





[AIS02] AISC, *Seismic provisions for structural steel buildings*, American Institute for Steel Construction, 2002.

[ALI00] C. Aliaga, *Simulation numérique par éléments finis en 3D du comportement thermomécanique au cours du traitement thermique d'aciers: application à la trempe de pièces forgées ou coulées*, Ecole Nationale Supérieure des Mines de Paris., 2000.

[ANV06] M. Anvari, I. Scheider and C. Thaulow, *Simulation of dynamic ductile crack growth using strain-rate and triaxiality-dependent cohesive elements*, Engineering Fracture Mechanics, 73, (15), 2210-2228, 2006.

[BAN07] A. Bannister, *VERAPS: Validation and Enhancement of Risk Assessment Procedure for Seismic connection*, Report EUR, Publication Office, Publications.Europa.eu, 2007.

[BAR62] G. I. Barenblatt, *Mathematical theory of equilibrium cracks in brittle fracture*, Advances in Applied Mechanics, VII, 55-129, 1962.

[BAR98] J. D. Barnichon, *Finite element modelling in structural and petroleum geology*, University of Liège, 1998.

[BEL91] T. Belytschko and L. P. Bindeman, *Assumed Strain Stabilization of the 4-Node Quadrilateral with 1-Point Quadrature for Nonlinear Problems*, Computer Methods in Applied Mechanics and Engineering, 88, (3), 311-340, 1991.

[BEN08] M. Ben Bettaieb, X. Lemoine, L. Duchêne and A. M. Habraken, *Study of Bendability of Steel Sheets*, Pietrzyk M., J. Kusiak, J. Majtaet al, Verlag Stahleisen, Steel Research International, Germany, 2008.

[BOG08] F. Bogard, P. Lestriez and Y. Q. Guo, *Numerical modeling of fatigue damage and fissure propagation under cyclic loadings*, International Journal of Damage Mechanics, 17, (2), 173-187, 2008.

[BOU06] J. L. Bouvard, *Modélisation de la propagation de fissure dans les aubes de turbines monocristalline*, Ecole Nationale Supérieur des Mines, 2006.

[BRO95] W. Brocks, D. Z. Sun and A. Honig, *Verification of the transferability of micromechanical parameters by cell model calculations with visco-plastic materials*, International Journal of Plasticity, 11, (8), 971-989, 1995.

[BSI91] BSI, *British Standard: Fracture mechanics toughness tests. Method for determination of  $K_{Ic}$ , critical CTOD and critical J values of metallic materials*, BS 7448-1:1991, 1991.

[BUN00] H. J. Bunge, K. Pöhlandt, A. E. Tekkaya and D. Banabic, *Formability of Metallic Materials*, Springer, 2000.

[CAM96] G. T. Camacho and M. Ortiz, *Computational modelling of impact damage in brittle materials*, International Journal of Solids and Structures, 33, (20-22), 2899-2938, 1996.

[CAS06] S. Casotto, *Prediction of geometrical distortions and microstructure of hot-rollers steel ring during cooling*, Università degli studi di Padova, 2006.

[CAS04] S. Castagne, F. Pascon, G. Bles and A. M. Habraken, *Developments in finite element simulations of continuous casting*, Journal De Physique Iv, 120, 447-455, 2004.

[CES85] S. Cescotto and H. Grober, *Calibration and Application of an elastic viscoplastic constitutive equation for steels in hot rolling conditions*, Engineering Computations, 2, (2), 101-106, 1985.

[CES97] S. Cescotto and K. Li, *Introduction d'un modèle elastoplastique avec ecrouissage mixte dans la sous-routine ARB2E, ARB2A du programme Lagamine*, Internal Report, MSM, University of Liege, 1997.

[CHA01] J. L. Chaboche, F. Feyel and Y. Monerie, *Interface debonding models: a viscous regularization with a limited rate dependency*, International Journal of Solids and Structures, 38, (18), 3127-3160, 2001.

[CHA04] P. H. Chang and T. L. Teng, *Numerical and experimental investigations on the residual stresses of the butt-welded joints*, Computational Materials Science, 29, (4), 511-522, 2004.

[CHA02] W. S. Chang and S. J. Na, *A study on the prediction of the laser weld shape with varying heat source equations and the thermal distortion of a small structure in micro-joining*, Journal of Materials Processing Technology, 120, (1-3), 208-214, 2002.

[CHA87] R. Charlier, *Approche unifiée de quelques problèmes non linéaires de mécanique des milieux continus par la méthode des éléments finis (grandes déformations des métaux et des sols, contact unilatéral de solides, conduction thermique et écoulements en milieu poreux)*, University of Liège, 1987.

[CHE05] C. R. Chen, O. Kolednik, J. Heerens and F. D. Fischer, *Three-dimensional modeling of ductile crack growth: Cohesive zone parameters and crack tip triaxiality*, Engineering Fracture Mechanics, 72, (13), 2072-2094, 2005.

[CHE03] C. R. Chen, O. Kolednik, I. Scheider, T. Siegmund, A. Tatschl and F. D. Fischer, *On the determination of the cohesive zone parameters for the modeling of micro-ductile crack growth in thick specimens*, International Journal of Fracture, 120, (3), 517-536, 2003.

[CHE98] G. Cheng and A. Plumtree, *A fatigue damage accumulation model based on continuum damage mechanics and ductility exhaustion*, International Journal of Fatigue, 20, (7), 495-501, 1998.

[CLA04] M. Clarin, *High strength steel: Local buckling and residual stresses* Lulea University of Technology, 2004.

[COF53] L. F. J. Coffin, *A study of the effect of cyclic thermal stresses on a ductile metal*, 1953.

- [COR03] A. Cornec, I. Scheider and K. H. Schwalbe, *On the practical application of the cohesive model*, Engineering Fracture Mechanics, 70, (14), 1963-1987, 2003.
- [CRO56] B. Crossland, *Effect of large hydrostatic pressures on the torsional fatigue strength of an alloy steel*, International Conference on Fatigue on Metals, London, 1956.
- [DAN93] K. Dang Van, *Micro-macro approach in high-cycle multiaxial fatigue*, D. L. M. a. R. Ellis, ASTM, Advances in Multiaxial Fatigue San Diego, California, 1993.
- [DUC05a] L. Duchene, P. de Montleau, F. El Houdaigui, S. Bouvier and A. Habraken, *Analysis of texture evolution and hardening behavior during deep drawing with an improved mixed type FEM element*, L. M. Smith, F. Pourboghrat, J.-W. Yoon and T. B. Stoughton, 6th Numisheet conference, Detroit, USA, 2005.
- [DUC05b] L. Duchene and A. M. Habraken, *Analysis of the sensitivity of FEM prediction to numerical parameters in deep drawing simulations*, European Journal of Applied Mathematics A/solids, 24, (4), 614-629, 2005.
- [DUC08] L. Duchene, T. Lelotte, P. Flores, S. Bouvier and A. M. Habraken, *Rotation of axes for anisotropic metal in FEM simulations*, International Journal of Plasticity, 24, (3), 397-427, 2008.
- [DUG60] D. S. Dugdale, *Yielding of steel sheets containing slits*, Journal of the Mechanics and Physics of Solids, 8, pp. 100–108, 1960.
- [DYD96] M. Dyduch, *Adaptive methods in finite element simulation of metal forming process*, University of Liege, 1996.
- [EN102] EN10025-2:2002, *Hot-rolled products of structural steel*, European Committee for Standardization, 2002.
- [ERI05] M. Erinc, P. J. G. Schreurs and H. B. H. Geers, *Cohesive zones for fatigue damage in solder joint*, 11th International Conference on Fracture, Turin, Italy, 2005.
- [FEM97] FEMA, *Connection test summaries*, 1997.
- [FEM00] FEMA, *Recommended seismic design criteria for new steel moment-frame buildings*, 2000.
- [FRI75] E. Friedman, *Thermo-mechanical analysis of the welding process using the finite element method*, ASME J. Pressure Vessel Technology, 97, (3), 206–213, 1975
- [GAO04] Y. F. Gao and A. F. Bower, *A simple technique for avoiding convergence problems in finite element simulations of crack nucleation and growth on cohesive interfaces*, Modelling and Simulation in Materials Science and Engineering, 12, (3), 453-463, 2004.

[GER07] A. F. Gerday, N. Clement, P. J. Jacques, T. Pardoën and A. M. Habraken, *Inverse modeling of nanoindentation tests to identify Ti-555 behavior*, M. S. Niinomi, M. Akiyama, M. Ikeda, Hagiwara and K. Maruyama, *Ti-2007 Science and Technology*, 2007.

[GER05] D. Gery, H. Long and P. Maropoulos, *Effects of welding speed, energy input and heat source distribution on temperature variations in butt joint welding*, *Journal of Materials Processing Technology*, 167, (2-3), 393-401, 2005.

[GEU98] P. H. Geubelle and J. S. Baylor, *Impact-induced delamination of composites: a 2D simulation*, *Composites Part B-Engineering*, 29, (5), 589-602, 1998.

[GIO02] V. Gioncu and F. M. Mazzolani, *Ductility of seismic resistance steel structures*, Taylor & Francis, 2002.

[GOL84] J. Goldack, A. Chakravarti and M. Bibby, *A new finite element model for welding heat source*, *Metallurgical Transaction B*, 15, 299-305, 1984.

[HAB89] A. M. Habraken, *Contribution à la modélisation du formage des métaux par la méthode des éléments finis*, Université de Liège, 1989.

[HAB90] A. M. Habraken and S. Cescotto, *An automatic remeshing technique for finite element simulation of forging processes*, *International Journal for Numerical Methods in Engineering*, 30, (8), 1503-1525, 1990.

[HAB98] A. M. Habraken and S. Cescotto, *Contact between deformable solids: The fully coupled approach*, *Mathematical and computer modelling*, 28, (4-5), 153-169, 1998.

[HAM08] L. Hamitouche, M. Tarfaoui and A. Vautrin, *An interface debonding law subject to viscous regularization for avoiding instability: Application to the delamination problems*, *Engineering Fracture Mechanics*, 75, (10), 3084-3100, 2008.

[HEN09] C. Henrard, *Numerical Simulations of the Single Point Incremental Forming Process*, University of Liège, 2009.

[HEN07] C. Henrard, B. Bouffieux, L. Duchene, J. R. Duflou and A. M. Habraken, *Validation of an new finite element for incremental forming simulation using a dynamic explicit approach*, *Key engineering materials*, 304, 495-502, 2007.

[HIL48] R. Hill, *A theory of the yielding and plastic flow of anisotropic metals*, *Proceedings of the Royal Society* 193, (281-297), 1948.

[KAC86] L. M. Kachanov, *Introduction to continuum damage mechanics*, Martinus Nijhoff Publishers, 1986.

[KEL99] K. Keller, S. Weihe, T. Siegmund and B. Kroplin, *Generalized Cohesive Zone Model: incorporating triaxiality dependent failure mechanisms*, *Computational Materials Science*, 16, (1-4), 267-274, 1999.



- [KRU78] G. W. Krutz and L. J. Segerlind, *Finite element analysis of welded structures*, Welding Journal Research, 57, 211s-216s, 1978.
- [LEH08] A. Lehtovaara and R. Rabb, *A numerical model for the evaluation of fretting fatigue crack initiation in rough point contact*, Wear, 264, (9-10), 750-756, 2008.
- [LEM96] J. Lemaitre and J. L. Chaboche, *Mécanique des matériaux solides*, Dunod, 1996.
- [LI 03] H. Li and N. Chandra, *Analysis of crack growth and crack-tip plasticity in ductile materials using cohesive zone models*, International Journal of Plasticity, 19, (6), 849-882, 2003.
- [LI97] X. K. Li and S. Cescotto, *A mixed element method in gradient plasticity for pressure dependent materials and modelling of strain localization*, Computer Methods in Applied Mechanics and Engineering, 144, (3-4), 287-305, 1997.
- [MAH98] S. A. Mahin, *Lessons from damage steel buildings during the Northridge earthquake*, Engineering Structures, 20, (4-6), 1998, 1998.
- [MAN53] S. S. Manson, *Behaviour of material under conditions of thermal stress*, 1953.
- [MAN81] S. S. Manson, Halford, G. R., *Practical implementation of the double linear damage rule and damage curve approach for treating cumulative fatigue damage* International Journal of Fracture, 17, (2), 169-192, 1981.
- [MAR09] A. K. Marmi, A. M. Habraken and L. Duchene, *Multiaxial fatigue damage modelling at macro scale of Ti-6Al-4V alloy*, International Journal of Fatigue, In Press, Accepted Manuscript, 2009.
- [MAT01] C. G. Matos and R. H. Dodds, *Probabilistic modeling of weld fracture in steel frame connections - part I: quasi-static loading*, Engineering Structures, 23, (8), 1011-1030, 2001.
- [MI 98] Y. Mi, M. A. Crisfield, G. A. O. Davies and H.-B. Hellweg, *Progressive delamination using interface elements*, Journal of composite materials, 32, (14), 1246-1272, 1998.
- [MIN45] M. A. Miner, *Cumulative Damage in Fatigue*, Journal of Applied Mechanics, Trans. ASME, 12, A159-A164, 1945.
- [MOR687] J. Morrow, *Fatigue Design Handbook*, Advances in Engineering, 21-29, 1968.
- [MOS99] P. Mosbah, S. Shima, A. M. Habraken and R. Charlier, *Numerical simulation of compact process of a multispeed part with comparison to experiments*, Journal of the Japan Society of Powder and Powder metallurgy, 46, 696-704, 1999.
- [PAL24] A. Palmgren, *Durability of Ball Bearings*, ZVDI, 14, 339-341, 1924.

- [PAP97] I. V. Papadopoulou, P. Davoli, C. Gorla, M. Filippini and A. Bernasconi, *A comparative study of multiaxial high-cycle fatigue criteria for metals*, International Journal of Fatigue, 19, (3), 219-235, 1997.
- [PAS03] F. Pascon, *2D1/2 Thermal-Mechanical Model of Continuous Casting of Steel Using Finite Element Method*, University of Liege, 2003.
- [PAV69] V. Pavelic, R. Tanbakuchi, O. A. Uyehera and P. S. Myers, *Experimental and computed temperature histories in gas tungsten-arc welding of thin plates*, Welding Journal Research, 48, 295-305, 1969.
- [RAH00] P. Rahulkumar, A. Jagota, S. J. Bennison and S. Saigal, *Cohesive element modeling of viscoelastic fracture: application to peel testing of polymers*, International Journal of Solids and Structures, 37, (13), 1873-1897, 2000.
- [RIC68] J. R. Rice, *A path Independent Integral and the Approximate Analysis of Strain Concentration by Notches and Cracks*, Journal of Applied Mechanics, 35, 379-386, 1968.
- [RIC80] J. R. Rice, *The Mechanics of Earthquake Rupture*, A. M. D. a. E. Boschi, International School of Physics 'Enrico Fermi', 1980.
- [ROD04] D. M. Rodrigues, L. F. Menezes and A. Loureiro, *The influence of the HAZ softening on the mechanical behaviour of welded joints containing cracks in the weld metal*, Engineering Fracture Mechanics, 71, (13-14), 2053-2064, 2004.
- [ROE03] K. L. Roe and T. Siegmund, *An irreversible cohesive zone model for interface fatigue crack growth simulation*, Engineering Fracture Mechanics, 70, (2), 209-232, 2003.
- [SAA03] Y. Saad, *Iterative methods for sparse linear systems*, SIAM, 2003.
- [SAA86] Y. Saad and M. H. Schultz, *GMRES: a generalised minimal residual algorithm for solving nonsymmetric linear system*, SIAM Journal on Scientific and Statistical Computing, 7, (3), 856-869, 1986.
- [SAIN06] B. Saint-Germain, *Etude expérimentale et numérique des structures mécano-soudées*, Ecole Centrale de Paris, 2006.
- [SHA09] D. G. Shang, *Measurement of fatigue damage based on the natural frequency for spot-welded joints*, Materials and Design, 30, 1008-1013, 2009.
- [SHE02] C. Shet and N. Chandra, *Analysis of energy balance when using cohesive zone models to simulate fracture processes*, Journal of Engineering Materials and Technology-Transactions of the Asme, 124, (4), 440-450, 2002.
- [SHE94] J. Shewchuk, *An introduction to the conjugate gradient method without the agonizing pain*, Technical report, School of Computer Science, Carnegie Mellon University, 1994.

- [SIM86] J. C. Simo and T. J. R. Hughes, *On the variationnal foundations of assumed strain methods*, Journal of applied mechanics, 53, 51-54, 1986.
- [SIN59] G. Sines, *Metal Fatigue*, G. Sines and J.L. Waisman, 1959.
- [SMI70] K. N. Smith, P. Watson and T. H. Topper, *A stress-strain function for the fatigue of metals*, Journal of materials, 5, (4), 767-778, 1970.
- [SUQ87] P. M. Suquet, *discontinuities and Plasticity, Nonsmooth Mechanics and Applications*, Moreau Panagiotopoulos Ed, 1988.
- [TEN04] T. L. Teng and P. H. Chang, *Effect of residual stresses on fatigue crack initiation life for butt-welded joints*, Journal of Materials Processing Technology, 145, (3), 325-335, 2004.
- [TVE04] V. Tvergaard, *Predictions of mixed mode interface crack growth using a cohesive zone model for ductile fracture*, Journal of the Mechanics and Physics of Solids, 52, (4), 925-940, 2004.
- [TVE92] V. Tvergaard and J. W. Hutchinson, *The Relation between Crack-Growth Resistance and Fracture Process Parameters in Elastic Plastic Solids*, Journal of the Mechanics and Physics of Solids, 40, (6), 1377-1397, 1992.
- [WAL01] K. Wallin, *Low-cost J-R curve estimation based on CVN upper shelf energy*, Fatigue & Fracture of Engineering Materials & Structures, 24, (8), 537-549, 2001.
- [WAN04] J. Wang and R. H. Wagoner, *A new hexahedral solid element for 3D FEM simulation of sheet metal forming*, S. Gosh, J. C. Castro and J. K. Lee, The 8th Numiform conference, OH, USA, 2004.
- [WEL61] A. A. Wells, *Unstable crack propagation in metals-cleavage and fast fracture*, *Symposium on Crack Propagation*, Cranfield, 1961.
- [WEN03] S. Wen, S. Church and D. Parker, *Finite element modelling of weld residual stress, distortion and HAZ microstructure*, Corus, Research, Development Technology, Rotherham, England, 2003.
- [WIL99] I. Wilsius, *Etude experimental de la déchirure ductile basée sur des approches locales en mécanique de la rupture*, Université des Sciences et Technologique, 1999.
- [WOH55] A. Wöhler, *Theorie rechteckiger eiserner Brückenbalken mit Gitterwänden und mit Blechwänden*, Zeitschrift für Bauwesen, 5, 121-166, 1855.
- [XU 93] X. P. Xu, Needleman, A., *Void nucleation by inclusion debonding in a crystal matrix*, Modelling and Simulation in Materials Science and Engineering, 1, 111-132, 1993.
- [ZHA00] J. Zhang and P. Dong, *Residual stresses in welded moment frames and implications for structural performance*, Journal of Structural Engineering-Asce, 126, (3), 306-315, 2000.

[ZAH09] Y.-H. Zhang and S. J. Maddox, *Investigation of fatigue damage to welded joints under variable amplitude loading spectra*, International Journal of Fatigue, 31, 138-152, 2009.

[ZHU95] Y. Y. Zhu and S. Cescotto, *Unified and Mixed Formulation of the 4-Node Quadrilateral Elements by Assumed Strain Method - Application to Thermomechanical Problems*, International Journal for Numerical Methods in Engineering, 38, (4), 685-716, 1995.

# Abstract

During the earthquake in Japan and California in the 1990s, some weld beam-to-column connections had some cracks in heavy rigid frame steel building. Consequently it is required to assess the performance of the welded connection in term of rotation capacity and crack propagation strength. Some experimental tests have been performed. The weld connections were submitted to cyclic loading with increasing amplitude until macro crack event. However the crack phenomenon depends on many parameters: the geometry, the material, the welding process. For this reason, it is interesting to develop a finite element modeling of this connection to complete these experiments and perform a parametric study. The welded connection is modeled by three dimensional mixed solid elements. The constitutive law is elastoplastic with isotropic hardening identified for the base metal and the weld metal. The crack propagation is modeled by cohesive zone model. The parameters of the cohesive zone model have been identified by inverse method with the modeling of three points bending tests of a pre-cracked sample performed on the base and weld metal. The fatigue damage generated by the cyclic loading is computed by the fatigue continuum damage model of Lemaitre and Chaboche and it is coupled with the cohesive zone model. The damage and the crack propagation depend on the residual stresses generated by the welding process. They have been computed by a simulation of this process with a thermo mechanical finite element analysis. This thesis presents the used models and the results compared with the experimental tests.